Magnetic approaches to form and to stimulate three-dimensional tissue models

Gaëtan Mary

Université de Paris
Ecole doctorale Physique en Île-de-France - ED n°564
Laboratoire Matière et Systèmes Complexes, UMR 7057

MAGNETIC APPROACHES TO FORM AND TO STIMULATE THREE-DIMENSIONAL TISSUE MODELS

Par Gaëtan Mary

Thèse de doctorat de **Biophysique**

Dirigée par Claire Wilhelm
Et par Myriam Reffay

Soutenance prévue le 27 Février 2020

Devant un jury composé de :

Mathilde Badoual
Directrice de recherche ; Université Paris Diderot ; Examinatrice
Timo Betz
Professor ; Münster University ; Rapporteur
Jean-Baptiste Manneville
Directeur de recherche ; Institut Curie ; Examinateur
Fabien Montel
Chargé de recherche ; ENS Lyon ; Rapporteur
Myriam Reffay
Maître de conférence ; Université Paris Diderot ; Co-directrice
Claire Wilhelm
Directrice de recherche ; Université Paris Diderot ; Directrice

Titre :
Approches magnétiques pour la formation et la stimulation à trois dimensions de modèles de tissus biologiques

Résumé :
Cette thèse présente l'utilisation de force magnétiques dans le but de former et de stimuler mécaniquement des agrégats multicellulaires. Ces structures 3D, composées de cellules jointes les unes aux autres, sont considérées comme des bons modèles de tissus biologiques. Ici, des cellules magnétiques sont utilisées afin de créer des agrégats magnétiques présentant des formes et des tailles contrôlées, et de les soumettre à des contraintes mécaniques sans aucune matrice extérieure. Trois sujets sont abordés: (i) le magnétisme induit est utilisé afin de réaliser de la rhéologie tissulaire (ii) le magnétisme induit est utilisé afin d'appliquer une large contrainte anisotropique à des modèles de tumeurs cancéreuses (iii) enfin, le magnétisme induit est utilisé afin d'améliorer la différenciation d'agrégats composés de précurseurs de tissus musculaires squelettiques et cardiaques.

Mots clefs :
biophysique ; tissus ; rhéologie ; magnétisme ; nanoparticules ; différenciation ; cancer

Title :

Magnetic approaches to form and to stimulate three-dimensional tissue models

Abstract :
This thesis presents the use of magnetic forces as a tool to form and to mechanically stimulate multicellular aggregates. These 3D structures, composed of interconnected cells, are considered as relevant models of biological tissues. Herein, magnetic cells are spatially controlled to create magnetic multicellular aggregates presenting specific shapes and sizes, and to subject them to remote mechanical stimuli without any external scaffold. Three different subjects are addressed: (i) the use of magnetic approaches to perform tissue rheology (ii) the use of magnetic forces to apply large anisotropic deformation on tumor models (iii) finally, the use of magnetic forces to enhance the differentiation of multicellular aggregates composed of cardiac muscle and skeletal muscle precursors.

Keywords :
biophysics; tissues; rheology; magnetism; nanoparticles; differentiation; tumor

Contents

CHAPTER 2 : MAGNETIC COMPRESSION OF MOUSE COLON CANCER CELL SPHEROIDS

CHAPTER 3.0 : CARDIAC AND SKELETAL TISSUE ENGINEERING

CHAPTER 3.5 : MAGNETIC STRETCHING OF SKELETAL MUSCLE PRECURSORS

1 - Preface

A proper understanding of the regulation of a biological tissue is critical in various fields such as development, biophysics, regenerative medicine and cancerology. Indeed, the disruption of the tissue organization gives rise to severe diseases, in which cancer is a crying example. On the other hand, tissue engineering, which aims in re-creating partially or totally a damaged tissue, requires a perfect comprehension of the chemical and physical cues surrounding the tissue repair. Yet, a biological tissue is a complex system, which function arises both from its macroscopic organization and its microscopic constituents. Regarding this inherent complexity, biologists and physicists focused in creating more controlled models, enabling to mimic the organization and/or the behaviour of a native tissue. A current challenge to tackle is the creation of such tissue models through the control of the cell spatial organization. A first step in making a tissue model is the creation of a 2D structure, for instance using microstructured substrates. However, if such 2D culture allows to study fundamental aspects such as collective migration effects, they are far from reproducing the native architecture of a tissue. In this context, multicellular aggregates represent powerful tools for mimicking a biological tissue. Yet, creating such structures without the need for a supporting matrix is currently a challenge.

Moreover, mechanical forces are now admitted to be key regulating factors in development, cancer progression and stem cell differentiation. Besides, applying controlled mechanical forces at such small and large scale - that can be found in the range of a few micrometres to a few millimetres – represents another challenge by itself.

As they allow the application of controlled remote distant forces, magnetic forces represent good candidates to address both these challenges. In the recent years, different approaches have been proposed to subject cells to magnetic forces. For instance, magnetic particles can be adsorbed on the cell membrane, or aggregates composed of a mixture of cells and cell-sized magnetic particles can be created. Yet, concerns about the cytotoxicity of such approaches and the integrity of hybrid structures have been raised. In the host team, the internalization of magnetic iron oxide nanoparticles has been shown to be fully cytocompatible and to enable the spatial control of cells, at the 2D and the 3D scale. Besides, such method can be used in order to apply controlled magnetic forces on the so-formed aggregates.

Iron oxide nanoparticles are widely used in biomedical research and bioengineering. If they were first introduced as contrast agents in Magnetic Resonance Imaging, they are now used as targeting agents or heating agents for cancer treatment. While concerns about the increasing use of nanoparticles are regularly raised both by specialists and public opinion, most works have demonstrated the iron oxide nanoparticles cytocompatibility, validating the use of such technologies for in-vitro and in-vivo models.

This PhD aims in contributing to three different fields using mechanical stimulation of tissue models through the use of magnetic forces. The magnetic forces will be used to apply mechanical forces on different tissue models. Hence, the three experimental parts of this manuscript can be read separately. This manuscript starts with a general introduction which presents the use of multicellular aggregates as tissue model, common ground of all presented works. Additionally, this chapter will present the cell magnetic labelling, also common to all aspects of the thesis, and which allows to form and to subject multicellular aggregates to remote various forces. The three following chapters of the manuscript will then address the following themes:

Chapter 1: The use of magnetic multicellular aggregate as a tool to investigate the rheology of tissue models. An introduction will present the tools and the main results of the current data about the rheology of tissue models, from the single cell to the 3D scale of a tissue. The experimental work will be presented in the form of an article. It first introduces innovative magnetic method used in order to create unprecedented cylindrical multicellular aggregates. The rheological behaviour of such magnetic tissue models is then investigated through the use of an electromagnet.

Chapter 2: The use of magnetic forces as a tool to apply large anisotropic deformation on tumor models. First, an introduction will present how tumor progression and growth are intrinsically linked to a constantly evolving mechanical map. Then, we will address how surgical intervention can give rise to additional mechanical stress, and we will introduce a magnetic tumor model used to mimic such interventions. The experimental work will be presented in the form of an article. Using a permanent magnet, 1 mm tumor models will be subjected to large anisotropic deformation. We will present our results on the in-vitro and in-vivo behaviours triggered by this magnetic deformation.

Chapter 3: Finally, we will present how magnetic multicellular aggregates can be powerful tools in order to functionalize tissue models composed of cardiac and skeletal muscle precursors First, an introduction will present the different cell models available for tissue engineering and cell therapy. We will then discuss the current methods available to subject multicellular aggregates to controlled mechanical forces, in order to enhance the differentiation toward a final lineage. In this context, magnetic forces allow such stimulation without the use of external scaffolds. Two different projects will be presented. The first one, presented in the form of an article, will present the use of cyclic magnetic stimulation to enhance the differentiation of Embryonic Stem Cells multicellular spheroids toward cardiomyogenesis. The second one will present the first results on the use of a magnetic stretcher as a tool to align at the 3D scale skeletal muscle precursors.

2 - General introduction: from the single cell to tissue models

The different projects presented in this manuscript are based on the use of magnetic forces in order to create biological tissue models, and to subject them to mechanical stimuli. To introduce such projects, this chapter aims at presenting the structure of a biological tissue, and how multicellular aggregates can be used as tissue models. We will first present the cell, and how it interacts with its microenvironment to build the 3D structure of a biological tissue. Then, we will describe the main techniques currently used to make multicellular aggregates, which are widely accepted as good models of biological tissues. We will present the main features of such objects, and how they are found at the crosstalk of biophysics, cancerology and tissue engineering. Finally, as it gathers the different projects addressed in this manuscript, we will highlight how magnetic cells can be powerful tools in order to subject the tissue models to remote forces, and the method used to magnetise them.

Content

2.1 - Biological tissues

Tissues are complex, 3D-architectured materials composed of cells bound together and to the Extracellular Matrix (ECM), which composition, structure and function are intrinsically linked. For instance, conjunctive tissues such as cartilage are composed of a dense ECM, whereas epitheliums are mainly composed of joint cells. In this paragraph, we will briefly describe the main features of adherent cells, and we will address how they interact in order to create a tissue. Finally, regarding the complexity of the tissue structure, we will present multicellular aggregates, currently used as in-vitro tissue models.

2.1.1) The cell

The cell represents the basic brick of a biological tissue. They are dense colloidal suspensions composed of proteins separated from the external environment by a bilipid layer called plasma membrane. Through the intermediary of transmembrane proteins connected to the cytoskeleton, the membrane works as a sensor of the cell microenvironment, enabling the cells to adapt to external stimuli such as mechanical forces or substrate rigidity. Such adaptability is directly related to the cytoskeleton properties, which is responsible for both the cell shape and the cell mechanical features. As it will be fundamental for the following chapter, we are going to detail its main characteristics.

The cell cytoskeleton is a dense and dynamic network, composed of protein filaments (Figure 2-1). The network expands all over the cell structure and it is constantly renewing. In order to polymerise or depolymerise this dynamic network, the cell consumes energy in the form of ATP molecules. This is essential for critical cell properties such as contractility, motility, and division. Additionally, cell cytoskeleton participates in intracellular trafficking through molecular motors. It contains three different types of filaments (1):

Microfilaments (or actin filaments): they take place on the cell cortex, below the plasma membrane. This is a semi-flexible structure (persistence length of 17 μm, F-actin filament presenting sizes in the range of 6 to 8 nm). Molecular motors (Myosins) connect the F-actin filaments together. By sliding the actin filaments, the myosins provide the force generation and contractility properties of the entire network. Additionally, actin filaments form stress fibres between adhesive regions, pre-stressing the cytoskeleton by generating forces on cell adhesion points.

Intermediate filaments Situated between the actin and the microtubules, intermediate filaments are considered as the general scaffold of the cells, surrounding and anchoring the nucleus and the organelles. The network is composed of 10 nm filaments. Depending of the cell type, the nature of the intermediate filaments may change, and can be used as a marker of differentiation.

Microtubules Microtubule polymerization starts at the centrosomes, and they generally join the plasma membrane. The network is composed of larger hollow filaments (25nm, with a 14 nm lumen) stiffer than the others filaments (persistence length of a few millimetres). Microtubules are involved in cell division, cell polarity, and internal trafficking. The dynamic polymerization is able to produce critical forces during the cell division.

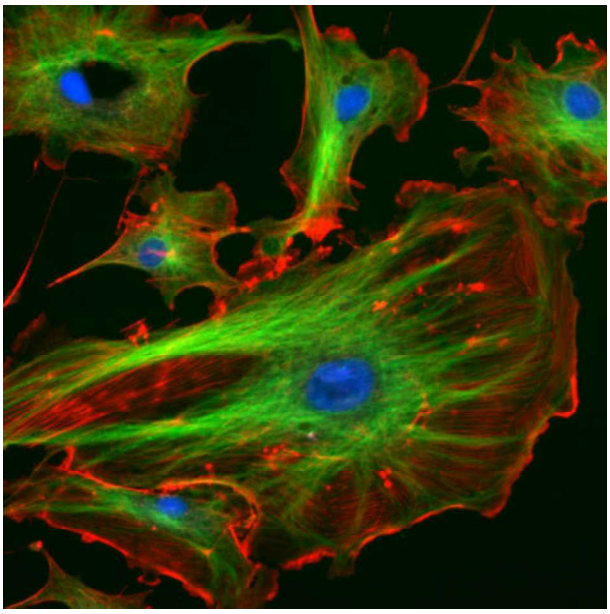

Figure 2-1: Cytoskeleton organization of an eukaryotic cell. The nucleus is labelled in blue, the microtubules in green and the microfilaments in red (from Wikipedia).

Through specific transmembrane proteins, the cell is connected to its microenvironment. These proteins are directly bound the cytoskeleton, allowing the cell to probe its microenvironment and to adapt to external mechanical stimuli. Such binding is critical in order to form the 3D structure of a biological tissue.

2.1.2) Cell adhesion

Two types of interactions can be distinguished: interactions between the cell and its substrate, and cell-cell interactions.

Cell-Cell Adhesion

The cell-cell junctions are mainly driven by four protein families (Figure 2-2) (2) (3): the cadherins, the selectins, the immunoglobulins (Ig), and the integrins. These junctions can be symmetrical (the cadherins are linked to the extracellular binding domain of another cadherin) or asymmetrical (the integrins bound to specific proteins placed on the membrane of another cell), and the proteins are linked to the cell cytoskeleton, enabling the transduction and the propagation of mechanical signals between the cells. Besides, they allow the binding to cell belonging to the same type (homotypic adhesion) or belonging to different cell types (heterotypic adhesion).

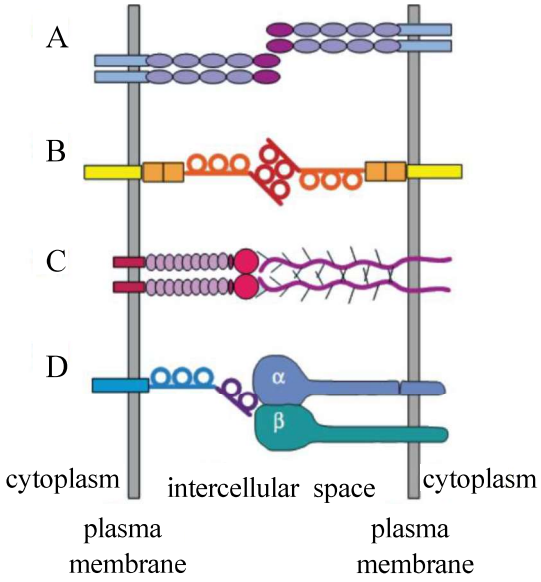

Figure 2-2: Transmembrane proteins responsible for the cell-cell adhesion. A) Cadherin; **B)** Immunoglobulines; **C)** Selectins; **D)** Integrins. Adapted from (10).

The cadherin family represents the most studied proteins. The bound between the extracellular domains is Ca^{2+} dependent, and calcium depletion lowers or disrupts the cell adhesion (4). Depending on the tissue, different types of cadherins have been identified. For instance, E-cadherins are found in epithelial tissues, whereas N-cadherins are found in mesenchymal tissues (such as skeletal tissues). Cadherin secondary structure is shared

between the different types, and the cadherins are connected to the cytoskeleton through α-catenin and the β-catenin (6). Through these proteins, the cell mechanically interacts and influences the surrounding cells, and the cell can modify its adhesive properties to adapt to the external stimuli (7). Intercellular adhesions are dynamic processes, which mature through the recruitment of adhesion proteins in a contact region named Adherent Junction (8). An increase in the cadherin density directly enhances the cell-cell adhesion (9), stabilising the global structure of the tissue.

Cell-substrate adhesion

Cells interact with their substrate through a specific family of transmembrane proteins, called integrins (Figure 2-3). The interaction is based on the structural complementarity between the extracellular domain of the integrin, and specific proteins of the ECM, such as fibronectin (11), collagen and laminin. The intracellular domain is linked to the actin cytoskeleton. Via the focal adhesions, this interaction enables the cell to probe and to adapt to the mechanical properties of the ECM (12).

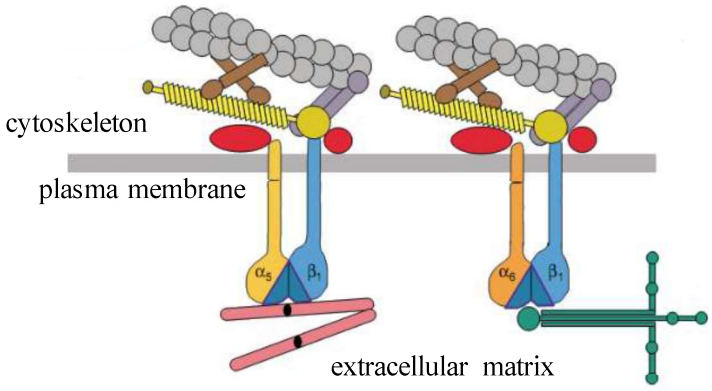

Figure 2-3: Cell-ECM junctions through integrins. Transmembrane integrins (α and β domains are represented) bind the cytoskeleton (through proteins such as a-actinin in red) to specific proteins of the extracellular matrix (fibronectin in pink or laminin in green). Adapted from (10).

2.1.3) Extracellular Matrix

The ECM is a dense network, composed of interconnected macromolecules, such as proteins (collagen, elastin, fibronectin and laminin) and polysaccharides (glycosaminoglycan) (13). In conjunctive tissues, the cells secrete their own ECM. This is for instance the main function of

highly specialized cells such as fibroblasts (14). The ECM structures the tissue, and its composition and organization depends on the nature of such tissue.
ECM regulation is a key factor for the tissue integrity, and can be disturbed during cancer progression (15). Additional, through chemical factors (16) mechanical inductions, the ECM regulates cellular processes. For instance, ECM stiffening is associated with malignancy (17).
Therefore, a biological tissue is composed of single or many cell types, embedded in the ECM. Cell-Cell adhesion and Cell-ECM adhesion give the global structure of the tissue.

2.2 - From the cell to tissue models

As cell cohesion occurs on an adherent substrate, the cells form a 2D layer that can be used as a tissue model for instance mimicking an epithelium. This type of model has also implications in the understanding of wound healing (18), development (19) and finds various analogies with cancer metastatic process (20). However, 2D-cultures are far from reproducing the cell-cell and cell-ECM interactions found in a tissue (21) (22). On the other hand, multicellular aggregates are composed of 3D assemblies of cell, which integrity is driven by the cell-cell junctions (Figure 2-4). They can be composed of different cell types (co-culture), and depending of the maturation time, cells can express their own ECM, therefore getting closer to native tissues. Therefore, multicellular aggregates are now accepted as good models of biological tissues (23).

As multicellular aggregates are used in the different projects presented in this manuscript, we will first describe in this paragraph the current tools available to create such 3D structures. Then, we will address their main features and applications in many fields. Overall, it evidences the need for tools enabling the application of controlled forces on multicellular aggregates, yet hardly achievable at the scale of such 3D structure.

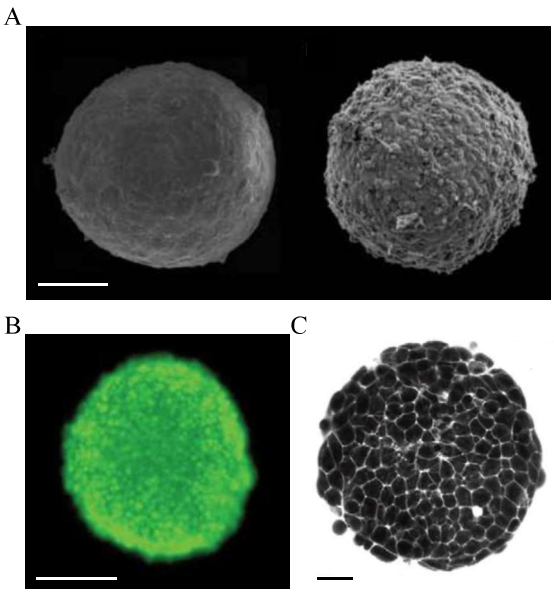

Figure 2-4: Multicellular aggregates. A) Scanning electron pictures of multicellular spheroids. Left picture: spheroid composed of human umbilical vein smooth muscle cells. Right picture: spheroid composed of Chinese hamster ovary cells. The different aspect of the surface comes from differences in the cell-cell adhesion, stronger on the left spheroid. Scale bar 100 μm. Adapted from (24). **B)** Immunofluorescence picture of mouse colon cancer spheroid (CT26 cell line). The cells express a cytoplasmic GFP marker. Scale bar: 150 μm. Adapted from (25) **C)** Bi-photonic pictures of mouse teratocarcinoma stem cell spheroid (F9 cell line). The intercellular space is labelled using sulforhodamine B. Scale bar: 10 μm. Adapted from (26).

2.2.1) Formation of multicellular aggregates

Methods to form multicellular aggregates mainly rely on locally increasing the cell density of a controlled cell suspension, in order to favour the cell-cell adhesion (Figure 2-5) (23) (27):

Non-adhesive substrate Cell-cell adhesions can be favoured by seeding cells on non-adhesive substrates, which can be shaken in order to enhance the spheroid formation. Yet, the size and the shape of the obtained spheroids cannot be controlled.

Hanging Drops and Microwells Gravity is the first force that can be used to condense cell suspensions. Cells can be seeded in Hanging Drops (small pending drops presenting volumes in the range of 10 to 30 μl), or inside microwells. The first method requires several time-consuming steps, while the later requires expensive commercial devices.

Microfluidic devices can be developed in order to seed the cells in controlled hollow structures, but they require elaborated set-ups (28).

Active methods Finally, external forces can be applied on the cells to favour the formation of a 3D culture. Centrifugation, shear forces in large spinning flasks (29), or remote forces such as electric (30), acoustic (32) or magnetic forces (31) (33) (34) can be used.

All these techniques rely on the formation of a small assembly of cells (typically a few thousands), which growth arises from the cell proliferation. Therefore, such techniques require a few days in order to obtain multicellular spheroids presenting diameters in the range of 100 μm to 500 μm.

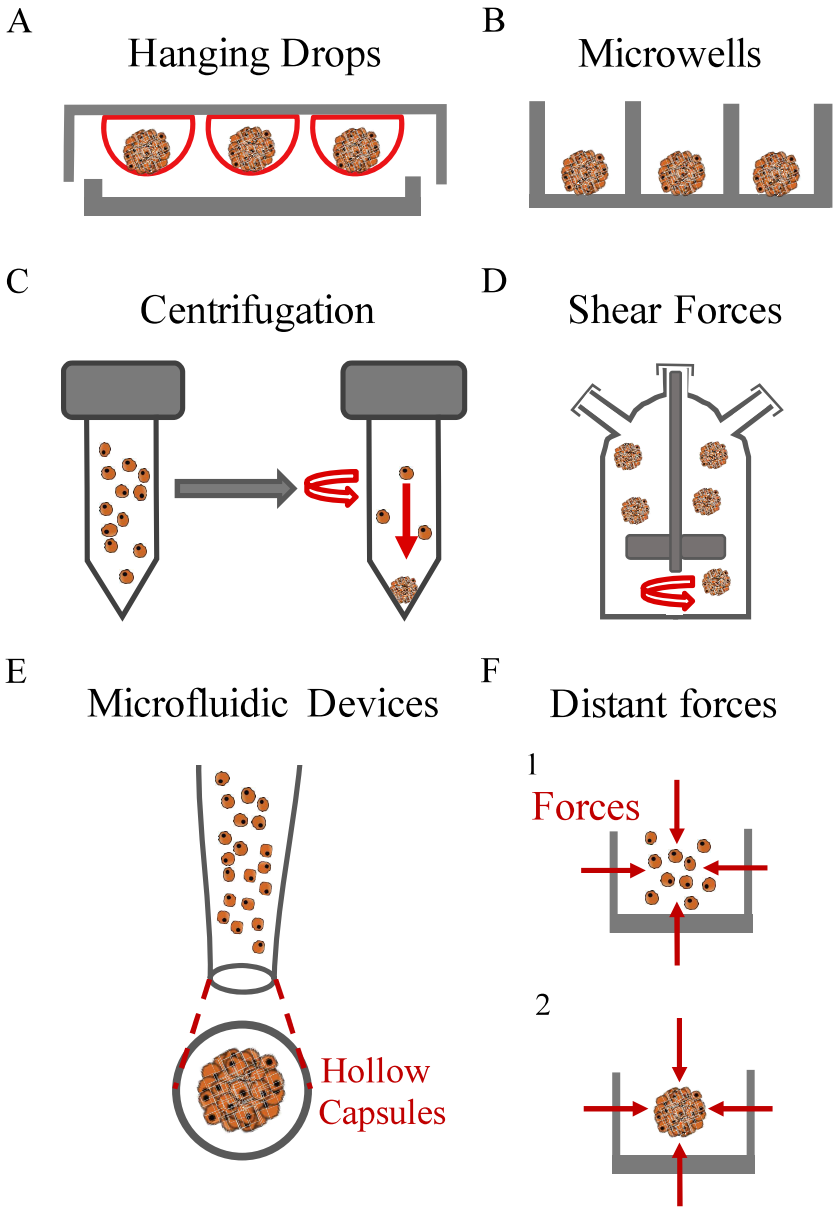

Figure 2-5: Formation of multicellular spheroids. The different approaches aim in locally increasing the cell density of a small number of cells (in the range of a thousand to a few thousands). Cell cohesion and cell proliferation give rise to the spheroid growth. Adapted from (23).

In the team, such size and time limitations were recently overcome by François Mazuel who developed an innovative method termed Magnetic Molding (35). Herein, cells are magnetically labelled using superparamagnetic iron oxides. The magnetic cells are then attracted in spheroidal agarose molds, which can be tuned in order to present diameter in the range of 500 μm to a few millimetres. After a night, the obtained multicellular spheroids can be removed from the molds, and present sizes in the same range than their molds. Hence, this method allows the quick formation (within a night) of unprecedented-sized spheroids. This method is used in the chapters 1 and 2 of this manuscript, in order to create large magnetic aggregates.

2.2.2) Main features of multicellular aggregates

Such formed multicellular spheroids present interesting features arising from their 3D structure (Figure 2-6). First, they are by nature avascular structures, giving rise to gradients of metabolic elements such as ATP, glucose or dioxygen. As such gradient can lead to the apparition of a necrotic core, spheroids are usually limited to diameters below 500 μm (36).
Resulting from these gradients, three distinct regions are usually found in spheroids (37): (i) the periphery, were the cells are proliferating (ii) the core, that can be necrotic due to cell apoptosis (iii) and a transition region in between, where quiescent cells can be observed. Besides, both metabolic gradients and evolution of cell density lead to cell movements, that can be observed radially from the shell to the core (or inversely) of the aggregate, or only observed on the spheroid surface (38) (39) (40).
If mechanical gradients were suspected in spheroids, they were difficult to measure until the recent development of methods using deformable cell-size like hydrogel probes inserted inside the spheroids, and reproducing the cell-cell adhesions. These methods allow mapping the evolution of mechanical stresses inside a spheroid (41) (42). It is now accepted that a compressive stress increases toward the spheroid core, whereas tensile forces can be measured on the shell.

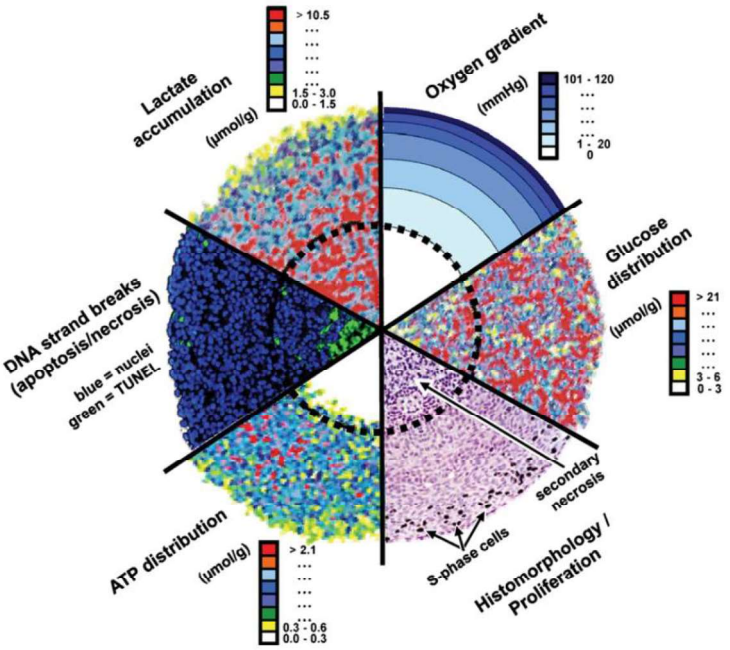

Figure 2-6: Due to their 3D-structure, multicellular spheroids present gradients in metabolic elements and phenotypes. Extracted from (36).

2.2.3) Applications of multicellular spheroids

As they mimic the organization of an in-vitro tissue model, multicellular spheroids have found applications in various fields, from fundamental projects in biophysics, to applications in regenerative medicine. In this paragraph, we will present some applications of the multicellular spheroids, which are directly related to the projects presented in this manuscript.

2.2.3.1) Biophysics

Multicellular spheroids represent simple tissue models, were the number of cells, the composition, and the maturation can be fully controlled. Therefore, they represent key object for the characterization of mechanical properties of tissues, have been of deep interests in biophysics. Using theoretical and experimental concepts developed for soft matter and rheology of more common materials, physicists have been implicated in the understanding of their mechanical properties (43), leading to describing multicellular aggregates as visco-elastic materials. Yet, investigating the mechanical properties of tissue models requires the development of tools enable to subject such multicellular aggregates to controlled deformations. This matter will be addressed in detail in the Chapter 1 of this manuscript.

2.2.3.2) Cancer models

Avascular cancer spheroids reproduce some features of growing tumor. For instance, necrotic cores are usually found in growing spheroids. Moreover, multicellular spheroids have been widely used as models for cancer therapy, such as drug screening (44). In the team, avascular tumor models are used to test the potential application of therapy involving hyperthermia through the injection of nanoparticles (45). Additionally, these tumor models have been used in order to understand fundamental characteristics of the tumor progression. During metastasis, the cells have to escape the tumor, and they have to migrate in order to invade the host (46). In-vitro models using avascular spheroids have highlighted striking characteristic of this process, such as cell migration (47), cell-ECM interactions (48) or cancer cell-fibroblasts interactions (49).

Besides, physicists are now fully implicated in the field. Indeed, in order to grow, the tumor has to push on the tissue host. This growth in confined environment gives rise to a new mechanical map (50), which reciprocally affects the tumor and the host tissue (51). If in-vitro models have been developed in order to understand the effects of mechanical compression of tumor models, at the 3D scale, it cannot be achieved without the intermediate of an external ECM-like matrix. This matter will be addressed in the Chapter 2 of this manuscript.

2.2.3.3) Tissue engineering and Functionalization

Multicellular spheroids find direct applications in fundamental study of the development (52), but also in regenerative medicine. This field aims in partially or totally recreating tissues and/or organs. Multicellular aggregates can then be used as elementary building blocks for the creation of larger structures. Multicellular spheroids can indeed be fused together in order to form a controlled and complex architecture (53). Figure 2-7 presents two examples of such structures: a branched vascular tree model, and a ring assembly composed of multicellular spheroids.

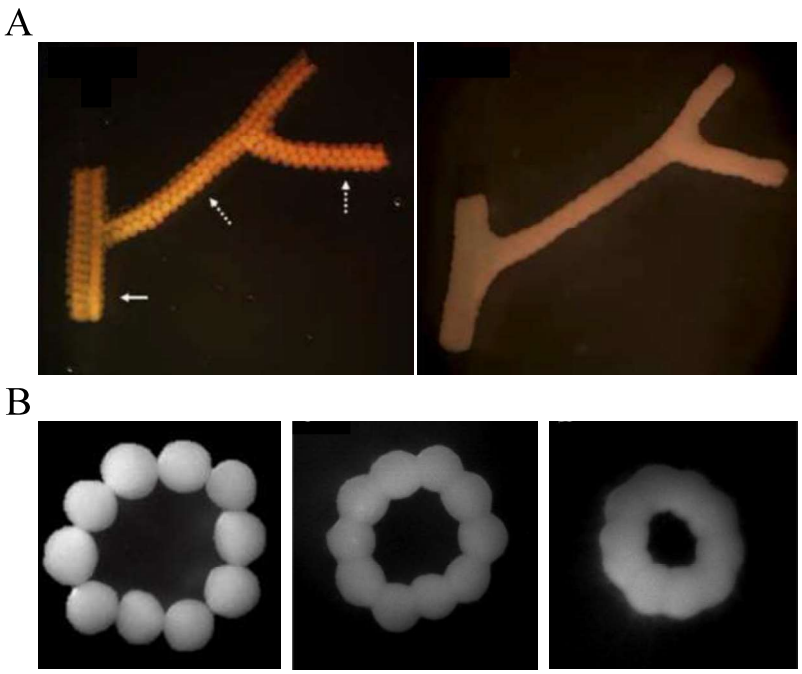

Figure 2-7: Bioprinting uses multicellular spheroids as elementary building blocks to create larger structures. A) Branched segment of a vascular tree model, created with 300 um spheroids of human skin fibroblasts (CRL-2522 cell line). Left picture presents the initial seeding. Right picture presents the structure after 7 days of maturation. Adapted from (24). **B)** Evolution of the fusion of ring vascular tissue model. Adapted from (53).

If a complete replacement of a damaged organ is still far from being achieved (54), the controlled environment of a multicellular spheroid has allowed many discoveries. Multicellular spheroids represent the first structure that can be used to culture stem cells at a 3D scale. Such multicellular aggregates are usually termed Embryonic Body (EB), and have been shown to spontaneously differentiate toward the three embryonic germ layers (55). In particular, EBs seeded on adhesive substrate can present spontaneous beating, indicating a functionalization toward a cardiac tissue model (56). Yet, the resulting differentiation is incomplete, and results in immature cardiomyocyte (57). To tackle this limitation, mechanical stimulations have succeeded in enhancing the functionalization of stem cells derived engineered tissues. For instance, cyclic stretching enhanced the differentiation toward cardiac tissue (58), constant strains enhanced the differentiation toward skeletal muscle (59), and a compressive loading enhanced the differentiation toward cartilage tissues (60) (61). However, the lack of tools to apply mechanical forces on multicellular aggregates is crying, and most of the mechanical methods are based on applying the forces indirectly to an external supportive matrix called scaffold (62). This matter will be developed in the last chapter of this manuscript.

2.3 - Motivation: Applying mechanical forces on 3D tissue models

These three different fields highlight the need of tools to apply controlled forces at the 3D scale of multicellular aggregates. In this context, magnetic forces represent good candidates as they enable the application of remote distance forces, through the versatility of a magnetic field. Indeed, the geometry and the intensity of such field can be easily tuned. In the different projects addressed in this manuscript, we propose the use of magnetic forces for two purposes. First, magnetic forces are used to spatially control the 3D assembly of cells, therefore allowing the formation of magnetic multicellular aggregates. Second, the magnetism thus induced will be used as a tool to apply controlled mechanical stimulations on different tissue models. To do so, cells are magnetically labelled using iron oxide nanoparticles. In the final paragraph of this introduction, we address the main features of this magnetic labelling.

2.4 - Magnetic formation and stimulation of multicellular spheroids

In order to subject cells to remote magnetic forces, one needs to associate them with magnetic particles. Mainly, magnetic labelling methods rely on the use of magnetic nanoparticles (NPs). By definition, NPs are natural or manufactured object presenting sizes in the range of 1 to 100 nm. Both the involved sizes (in the range of biological polymers such) and their large surface/volume ratio enable these objects to develop interactions with the living (63). Through endocytosis, the NPs are internalized in the cells. The induced magnetism allows to easily control their position and their aggregation via remote magnetic forces.

2.4.1) Magnetic labelling of the cells

Three different approaches have been developed in order to magnetically label the cells (64):

(i) Magnetic NPs can be functionalized in order to express specific proteins, such as antibodies, immunoglobulin or specific peptides. Therefore, the NPs are targeting specific membrane receptors, triggering the endocytosis. This approach can be used to label specific cells (65).

(ii) Magnetic NPs can be coated with a polymer, such as dextran, and functionalized with a transfection agent to induce the endocytosis of the complex. Commonly used agents are: the protamine sulphate (66), the poly-L-Lysine (PLL) (67) and the

lipofectamine (68). These NPs were first developed in the late 80s as contrast agents to perform Magnetic Resonance Imaging (MRI) on the liver (69). Yet, the use of these NPs is limited because of the presence of transfection agents. Precipitation of the NPs can occur, or the dextran can be absorbed on the membrane surface, therefore causing serious cytotoxicity (70).

(iii) The last approach consists in using non-functionalized NPs, which can be coated with carboxydextran (71), or with negative molecules such as citrate. Via the negative charges of the citrate groups, this coating stabilizes the NPs in solution.

This last approach has been used in the different projects presented in this manuscript. Indeed, these NPs allow a rapid magnetization of the cells, and are shown to be cytocompatible with various cell lines.

2.4.2) Iron Oxide Nanoparticles

In this manuscript, the same nanoparticles have been used. The NPs are iron oxide nanoparticles γ-Fe_2O_3 (9 nm, polydispersity of 30%), coated with citrate groups. They are provided by the PHENIX laboratory (UMR 8234). They are synthetized using co-precipitation of Fe^{2+} and Fe^{3+} ions, according to the Massart's procedure (72). As mentioned above, the NPs are coated with negative anionic citrate groups (at physiological pH). These negatives charges increase the repulsive electrostatic interactions between the particles, avoiding the flocculation of the suspension through the attractive Van Der Waals interactions (73).

The chosen NPs are superparamagnetic objects. Each NP carries a permanent moment, but due thermal agitation, no magnetization is measured in the absence of an external magnetic field. On the other hand, under an external magnetic field, the magnetic moments align, and a macroscopic magnetic moment can be measured (74). The resulting moment depends on the intensity of the external field. Magnetization curve of a typical suspension will be presented in the Chapter 1 of this manuscript.

2.4.3) Cell internalization

The cells are labelled using NPs suspended in culture medium. For short time incubation (typically between 30min to 2h), RPMI culture medium supplemented with free citrate ions (in order to avoid the desorption of the coating) is used. The free citrate contributes to the stabilisation of the NPs, and assure the internalization of single particles. The negative charges of the coating allow the spontaneous adsorption on the cell membrane, enabling the internalization through non-specific endocytosis pathways (75). Following the adsorption, membrane invagination is triggered, and the NPs are internalized in lipid vesicles. Intracellular trafficking leads to the transport and the fusion of thus formed vesicles to the cellular endosomes. The internalization process in presented in the Figure 2-8.

The amount of NPs can be easily controlled using two parameters: the concentration of the labelling solution, and the labelling time. An increase of both parameters leads to an increase in the number of NPs per cells, enabling the control of the induced magnetism. Moreover, we observe a saturation of magnetic labelling for long-time incubation, or for concentrated solutions. For the different projects, the labelling conditions have been adapted in order to assure cell viability, and to provide a chosen and controlled magnetism.

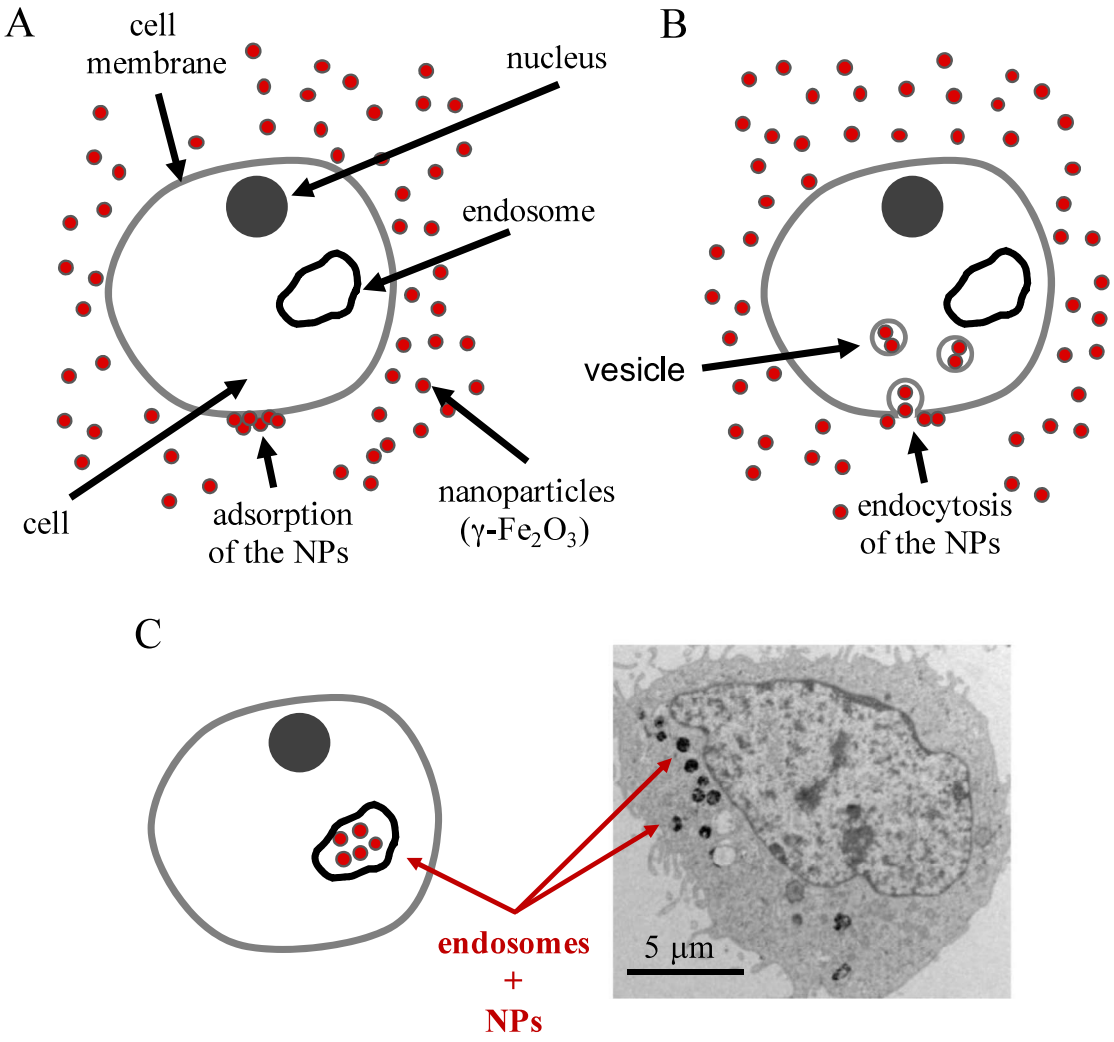

Figure 2-8: Internalization of the NPs. A) The cells are labelled with a solution of NPs. The anionic coating allows the NP adsorption on the cellular membrane. **B)** Through the invagination of the membrane, the NPs are internalized within vesicles. **C)** Via cellular trafficking, the loaded vesicles fuse with the cellular endosomes. On the right, a Transmission Electron Microscopic picture is shown. Due to the electronic density of the iron, the NPs are visible inside the endosomes.

2.4.4) Cell cytotoxicity

Concerns about the toxicity of NPs are widely addressed (76). Indeed, due to the sizes involved, these objects are susceptible to diffuse through biological membranes, and to interact with cell metabolism. Surface reactivity can lead to the generation of free radicals, and to trigger cellular stress and cytotoxicity. This issue is a growing society concern, as we are subjected to increasing NP expositions (through pollution, through the increase of NPs in commercial products etc.) (77).

Several studies have shown that the internalisation of NPs does not interfere with Mesenchymal Stem Cell (MSC) (78) (79) or embryonic stem cells (ESCs) differentiation (80). This subject has been widely studied on previous works the group. Studies based on several cell lines demonstrate that the magnetic labelling does not interfere with cell metabolism (64) (81), or does not interfere with stem cell differentiation (82). As the iron is an essential metabolic element, iron oxide NPs are quickly (in the range of a week) depredated through metabolic pathways (75). The becoming of the degradation products is currently studied (83).

In our model systems, cytotoxicity of the magnetic labelling has been addressed using conventional cytotoxicity assays such as metabolic assays (alamarBlue reagent). As our final goal is to apply controlled mechanical forces on tissue models, we have been focused on compromising between cell magnetic labelling, and cell toxicity. This will be particularly addressed in the Chapter 2 of this manuscript.

2.5 - Conclusion

To conclude, a biological tissue is a complex 3D architecture, which can be partially mimicked in-vitro through the formation of multicellular aggregates. Such tissue models find applications in various fields, such as biophysics, cancerology and tissue engineering. Herein, we propose the use of magnetic cells, as an-all-in-one tool to form magnetic multicellular aggregate, and to subject them to remote magnetic forces. Such magnetic stimulations will be used in the Chapter 1 to investigate the rheology of tissue models, in the Chapter 2 to apply large deformation on tumor models, and finally in the Chapter 3 to enhance the differentiation of cardiac precursors and the organization of skeletal precursors. For each chapter, the mechanical cues implicated in the belonging field will be first addressed.

References

1. Fletcher DA, Mullins RD. Cell mechanics and the cytoskeleton. Nature. 2010 Jan;463(7280):485–92.
2. Takeichi M. Functional correlation between cell adhesive properties and some cell surface proteins. The Journal of Cell Biology. 1977 Nov 1;75(2):464–74.
3. Rutishauser U, Thiery JP, Brackenbury R, Sela BA, Edelman GM. Mechanisms of adhesion among cells from neural tissues of the chick embryo. Proceedings of the National Academy of Sciences. 1976 Feb 1;73(2):577–81.
4. Kim SA, Tai C-Y, Mok L-P, Mosser EA, Schuman EM. Calcium-dependent dynamics of cadherin interactions at cell-cell junctions. Proceedings of the National Academy of Sciences. 2011 Jun 14;108(24):9857–62.
5. Kalluri R, Weinberg RA. The basics of epithelial-mesenchymal transition. J Clin Invest. 2009 Jun 1;119(6):1420–8.
6. Drees F, Pokutta S, Yamada S, Nelson WJ, Weis WI. α-Catenin Is a Molecular Switch that Binds E-Cadherin-β-Catenin and Regulates Actin-Filament Assembly. Cell. 2005 Dec;123(5):903–15.
7. Jamora C, Fuchs E. Intercellular adhesion, signalling and the cytoskeleton. Nat Cell Biol. 2002 Apr;4(4):E101–8.
8. Yap AS, Brieher WM, Gumbiner BM. Molecular and functional analysis of cadherin-based adherens junctions. Annu Rev Cell Dev Biol. 1997 Nov;13(1):119–46.
9. Steinberg MS, Foty RA. Intercellular adhesions as determinants of tissue assembly and malignant invasion. :5.
10. Hynes RO. Cell adhesion: old and new questions. Trends in Cell Biology. 1999 Dec;9(12):M33–7.
11. Ruoslahti E. Fibronectin in cell adhesion and invasion. Cancer Metast Rev. 1984;3(1):43–51.
12. Elosegui-Artola A, Bazellières E, Allen MD, Andreu I, Oria R, Sunyer R, et al. Rigidity sensing and adaptation through regulation of integrin types. Nature Mater. 2014 Jun;13(6):631–7.
13. Frantz C, Stewart KM, Weaver VM. The extracellular matrix at a glance. Journal of Cell Science. 2010 Dec 15;123(24):4195–200.
14. Cole MA, Quan T, Voorhees JJ, Fisher GJ. Extracellular matrix regulation of fibroblast function: redefining our perspective on skin aging. J Cell Commun Signal. 2018 Mar;12(1):35–43.
15. Kalluri R. The biology and function of fibroblasts in cancer. Nat Rev Cancer. 2016 Sep;16(9):582–98.
16. Hynes RO. The Extracellular Matrix: Not Just Pretty Fibrils. Science. 2009 Nov 27;326(5957):1216–9.
17. Wullkopf L, West A-KV, Leijnse N, Cox TR, Madsen CD, Oddershede LB, et al. Cancer cells' ability to mechanically adjust to extracellular matrix stiffness correlates with their invasive potential. Discher D, editor. MBoC. 2018 Oct;29(20):2378–85.
18. Sakar MS, Eyckmans J, Pieters R, Eberli D, Nelson BJ, Chen CS. Cellular forces and matrix assembly coordinate fibrous tissue repair. Nat Commun. 2016 Apr;7(1):11036.
19. Cetera M, Ramirez-San Juan GR, Oakes PW, Lewellyn L, Fairchild MJ, Tanentzapf G, et al. Epithelial rotation promotes the global alignment of contractile actin bundles during Drosophila egg chamber elongation. Nat Commun. 2014 Dec;5(1):5511.
20. Giampieri S, Manning C, Hooper S, Jones L, Hill CS, Sahai E. Localized and reversible TGFβ signalling switches breast cancer cells from cohesive to single cell motility. Nat Cell Biol. 2009 Nov;11(11):1287–96.
21. Abbott A. Biology's new dimension. Nature. 2003 Aug;424(6951):870–2.
22. Griffith LG, Swartz MA. Capturing complex 3D tissue physiology in vitro. Nat Rev Mol Cell Biol. 2006 Mar;7(3):211–24.
23. Lin R-Z, Chang H-Y. Recent advances in three-dimensional multicellular spheroid culture for biomedical research. Biotechnol J. 2008 Oct;3(9–10):1172–84.
24. Norotte C, Marga FS, Niklason LE, Forgacs G. Scaffold-free vascular tissue engineering using bioprinting. Biomaterials. 2009 Oct;30(30):5910–7.
25. Kopanska KS, Alcheikh Y, Staneva R, Vignjevic D, Betz T. Tensile Forces Originating from Cancer Spheroids Facilitate Tumor Invasion. Engler AJ, editor. PLoS ONE. 2016 Jun

7;11(6):e0156442.
26. Vasilica Stirbat T, Tlili S, Houver T, Rieu J-P, Barentin C, Delanoë-Ayari H. Multicellular aggregates: a model system for tissue rheology. Eur Phys J E. 2013 Aug;36(8):84.
27. Cui X, Hartanto Y, Zhang H. Advances in multicellular spheroids formation. J R Soc Interface. 2017 Feb 28;14(127):20160877.
28. Alessandri K, Sarangi BR, Gurchenkov VV, Sinha B, Kiessling TR, Fetler L, et al. Cellular capsules as a tool for multicellular spheroid production and for investigating the mechanics of tumor progression in vitro. Proceedings of the National Academy of Sciences. 2013 Sep 10;110(37):14843–8.
29. Sakai Y, Naruse K, Nagashima I, Muto T, Suzuki M. Large-scale preparation and function of porcine hepatocyte spheroids. Int J Artif Organs. 1996 May;19(5):294–301.
30. Sebastian A, Buckle A-M, Markx GH. Formation of multilayer aggregates of mammalian cells by dielectrophoresis. J Micromech Microeng. 2006 Sep 1;16(9):1769–77.
31. Ino K, Ito A, Honda H. Cell patterning using magnetite nanoparticles and magnetic force. Biotechnol Bioeng. 2007 Aug 1;97(5):1309–17.
32. Chen K, Wu M, Guo F, Li P, Chan CY, Mao Z, et al. Rapid formation of size-controllable multicellular spheroids via 3D acoustic tweezers. Lab Chip. 2016;16(14):2636–43.
33. Anil-Inevi M, Yaman S, Yildiz AA, Mese G, Yalcin-Ozuysal O, Tekin HC, et al. Biofabrication of in situ Self Assembled 3D Cell Cultures in a Weightlessness Environment Generated using Magnetic Levitation. Sci Rep. 2018 Dec;8(1):7239.
34. Haisler WL, Timm DM, Gage JA, Tseng H, Killian TC, Souza GR. Three-dimensional cell culturing by magnetic levitation. Nat Protoc. 2013 Oct;8(10):1940–9.
35. Mazuel F, Reffay M, Du V, Bacri J-C, Rieu J-P, Wilhelm C. Magnetic Flattening of Stem-Cell Spheroids Indicates a Size-Dependent Elastocapillary Transition. Physical Review Letters [Internet]. 2015 Mar 4 [cited 2017 Jan 16];114(9). Available from: http://link.aps.org/doi/10.1103/PhysRevLett.114.098105
36. Hirschhaeuser F, Menne H, Dittfeld C, West J, Mueller-Klieser W, Kunz-Schughart LA. Multicellular tumor spheroids: An underestimated tool is catching up again. Journal of Biotechnology. 2010 Jul 1;148(1):3–15.
37. Fang G, Lu H, Law A, Gallego-Ortega D, Jin D, Lin G. Gradient-sized control of tumor spheroids on a single chip. Lab Chip. 2019;10.1039.C9LC00872A.
38. Dorie MJ, Kallman RF, Rapacchietta DF, Van Antwerp D, Huang YR. Migration and internalization of cells and polystyrene microspheres in tumor cell spheroids. Experimental Cell Research. 1982 Sep;141(1):201–9.
39. Pettet G. The Migration of Cells in Multicell Tumor Spheroids. Bulletin of Mathematical Biology. 2001 Mar;63(2):231–57.
40. Delarue M, Montel F, Caen O, Elgeti J, Siaugue J-M, Vignjevic D, et al. Mechanical Control of Cell flow in Multicellular Spheroids. Phys Rev Lett. 2013 Mar 26;110(13):138103.
41. Dolega ME, Delarue M, Ingremeau F, Prost J, Delon A, Cappello G. Cell-like pressure sensors reveal increase of mechanical stress towards the core of multicellular spheroids under compression. Nat Commun. 2017 Apr;8(1):14056.
42. Lee W, Kalashnikov N, Mok S, Halaoui R, Kuzmin E, Putnam AJ, et al. Dispersible hydrogel force sensors reveal patterns of solid mechanical stress in multicellular spheroid cultures. Nat Commun. 2019 Dec;10(1):144.
43. Gonzalez-Rodriguez D, Guevorkian K, Douezan S, Brochard-Wyart F. Soft Matter Models of Developing Tissues and Tumors. Science. 2012 Nov 16;338(6109):910–7.
44. Nunes AS, Barros AS, Costa EC, Moreira AF, Correia IJ. 3D tumor spheroids as in vitro models to mimic in vivo human solid tumors resistance to therapeutic drugs: NUNES ET AL. Biotechnology and Bioengineering. 2019 Jan;116(1):206–26.
45. Espinosa A, Kolosnjaj-Tabi J, Abou-Hassan A, Plan Sangnier A, Curcio A, Silva AKA, et al. Magnetic (Hyper)Thermia or Photothermia? Progressive Comparison of Iron Oxide and Gold Nanoparticles Heating in Water, in Cells, and In Vivo. Adv Funct Mater. 2018 Sep;28(37):1803660.
46. Sahai E. Illuminating the metastatic process. Nat Rev Cancer. 2007 Oct;7(10):737–49.
47. Paul CD, Mistriotis P, Konstantopoulos K. Cancer cell motility: lessons from migration in confined spaces. Nat Rev Cancer. 2017 Feb;17(2):131–40.

48. He X, Lee B, Jiang Y. Cell-ECM Interactions in Tumor Invasion. In: Rejniak KA, editor. Systems Biology of Tumor Microenvironment [Internet]. Cham: Springer International Publishing; 2016 [cited 2019 Nov 28]. p. 73–91. Available from: http://link.springer.com/10.1007/978-3-319-42023-3_4
49. Attieh Y, Clark AG, Grass C, Richon S, Pocard M, Mariani P, et al. Cancer-associated fibroblasts lead tumor invasion through integrin-β3–dependent fibronectin assembly. J Cell Biol. 2017 Nov 6;216(11):3509–20.
50. Northcott JM, Dean IS, Mouw JK, Weaver VM. Feeling Stress: The Mechanics of Cancer Progression and Aggression. Front Cell Dev Biol. 2018 Feb 28;6:17.
51. Broders-Bondon F, Nguyen Ho-Bouldoires TH, Fernandez-Sanchez M-E, Farge E. Mechanotransduction in tumor progression: The dark side of the force. J Cell Biol. 2018 May 7;217(5):1571–87.
52. Schell JP. Spontaneous Differentiation of Human Pluripotent Stem Cells via Embryoid Body Formation. In: Human Stem Cell Manual [Internet]. Elsevier; 2012 [cited 2019 Nov 28]. p. 363–73. Available from: https://linkinghub.elsevier.com/retrieve/pii/B9780123854735000230
53. Mironov V, Visconti RP, Kasyanov V, Forgacs G, Drake CJ, Markwald RR. Organ printing: Tissue spheroids as building blocks. Biomaterials. 2009 Apr;30(12):2164–74.
54. Colombo F, Sampogna G, Cocozza G, Guraya S, Forgione A. Regenerative medicine: Clinical applications and future perspectives. J Microsc Ultrastruct. 2017;5(1):1.
55. Itskovitz-Eldor J, Schuldiner M, Karsenti D, Eden A, Yanuka O, Amit M, et al. Differentiation of Human Embryonic Stem Cells into Embryoid Bodies Comprising the Three Embryonic Germ Layers. Mol Med. 2000 Feb;6(2):88–95.
56. Kehat I, Kenyagin-Karsenti D, Snir M, Segev H, Amit M, Gepstein A, et al. Human embryonic stem cells can differentiate into myocytes with structural and functional properties of cardiomyocytes. J Clin Invest. 2001 Aug 1;108(3):407–14.
57. Leitolis A, Robert AW, Pereira IT, Correa A, Stimamiglio MA. Cardiomyogenesis Modeling Using Pluripotent Stem Cells: The Role of Microenvironmental Signaling. Front Cell Dev Biol. 2019 Aug 9;7:164.
58. Shimko VF, Claycomb WC. Effect of Mechanical Loading on Three-Dimensional Cultures of Embryonic Stem Cell-Derived Cardiomyocytes. Tissue Engineering Part A. 2008 Jan;14(1):49–58.
59. Heher P, Maleiner B, Prüller J, Teuschl AH, Kollmitzer J, Monforte X, et al. A novel bioreactor for the generation of highly aligned 3D skeletal muscle-like constructs through orientation of fibrin via application of static strain. Acta Biomaterialia. 2015 Sep;24:251–65.
60. O'Conor CJ, Case N, Guilak F. Mechanical regulation of chondrogenesis. Stem Cell Res Ther. 2013 Jul 1;4(4):61.
61. Fayol D, Frasca G, Le Visage C, Gazeau F, Luciani N, Wilhelm C. Use of Magnetic Forces to Promote Stem Cell Aggregation During Differentiation, and Cartilage Tissue Modeling. Adv Mater. 2013 May 14;25(18):2611–6.
62. Besser RR, Ishahak M, Mayo V, Carbonero D, Claure I, Agarwal A. Engineered Microenvironments for Maturation of Stem Cell Derived Cardiac Myocytes. Theranostics. 2018;8(1):124–40.
63. Whitesides GM. The "right" size in nanobiotechnology. Nat Biotechnol. 2003 Oct;21(10):1161–5.
64. Wilhelm C, Gazeau F. Universal cell labelling with anionic magnetic nanoparticles. Biomaterials. 2008 Aug;29(22):3161–74.
65. Xu H, Aguilar ZP, Yang L, Kuang M, Duan H, Xiong Y, et al. Antibody conjugated magnetic iron oxide nanoparticles for cancer cell separation in fresh whole blood. Biomaterials. 2011 Dec;32(36):9758–65.
66. Arbab AS, Yocum GT, Kalish H, Jordan EK, Anderson SA, Khakoo AY, et al. Efficient magnetic cell labeling with protamine sulfate complexed to ferumoxides for cellular MRI. Blood. 2004 Aug 15;104(4):1217–23.
67. Kostura L, Kraitchman DL, Mackay AM, Pittenger MF, Bulte JWM. Feridex labeling of mesenchymal stem cells inhibits chondrogenesis but not adipogenesis or osteogenesis. NMR Biomed. 2004 Nov;17(7):513–7.
68. Farrell E, Wielopolski P, Pavljasevic P, van Tiel S, Jahr H, Verhaar J, et al. Effects of iron

oxide incorporation for long term cell tracking on MSC differentiation in vitro and in vivo. Biochemical and Biophysical Research Communications. 2008 May;369(4):1076–81.
69. Stark DD, Weissleder R, Elizondo G, Hahn PF, Saini S, Todd LE, et al. Superparamagnetic iron oxide: clinical application as a contrast agent for MR imaging of the liver. Radiology. 1988 Aug;168(2):297–301.
70. Montet-Abou K, Montet X, Weissleder R, Josephson L. Cell internalization of magnetic nanoparticles using transfection agents. Mol Imaging. 2007 Feb;6(1):1–9.
71. Singh N, Jenkins GJS, Asadi R, Doak SH. Potential toxicity of superparamagnetic iron oxide nanoparticles (SPION). Nano Reviews. 2010 Jan;1(1):5358.
72. Massart R. Preparation of aqueous magnetic liquids in alkaline and acidic media. IEEE Trans Magn. 1981 Mar;17(2):1247–8.
73. Kotsmar C, Yoon KY, Yu H, Ryoo SY, Barth J, Shao S, et al. Stable Citrate-Coated Iron Oxide Superparamagnetic Nanoclusters at High Salinity. Ind Eng Chem Res. 2010 Dec 15;49(24):12435–43.
74. Neuberger T, Schöpf B, Hofmann H, Hofmann M, von Rechenberg B. Superparamagnetic nanoparticles for biomedical applications: Possibilities and limitations of a new drug delivery system. Journal of Magnetism and Magnetic Materials. 2005 May;293(1):483–96.
75. Mazuel F, Espinosa A, Luciani N, Reffay M, Le Borgne R, Motte L, et al. Massive Intracellular Biodegradation of Iron Oxide Nanoparticles Evidenced Magnetically at Single-Endosome and Tissue Levels. ACS Nano. 2016 Aug 23;10(8):7627–38.
76. Ajdary M, Moosavi M, Rahmati M, Falahati M, Mahboubi M, Mandegary A, et al. Health Concerns of Various Nanoparticles: A Review of Their in Vitro and in Vivo Toxicity. Nanomaterials. 2018 Aug 21;8(9):634.
77. Bundschuh M, Filser J, Lüderwald S, McKee MS, Metreveli G, Schaumann GE, et al. Nanoparticles in the environment: where do we come from, where do we go to? Environ Sci Eur. 2018 Dec;30(1):6.
78. Qi Y, Feng G, Huang Z, Yan W. The application of super paramagnetic iron oxide-labeled mesenchymal stem cells in cell-based therapy. Mol Biol Rep. 2013 Mar;40(3):2733–40.
79. Ito A, Hibino E, Honda H, Hata K, Kagami H, Ueda M, et al. A new methodology of mesenchymal stem cell expansion using magnetic nanoparticles. Biochemical Engineering Journal. 2004 Aug;20(2–3):119–25.
80. Au K-W, Liao S-Y, Lee Y-K, Lai W-H, Ng K-M, Chan Y-C, et al. Effects of iron oxide nanoparticles on cardiac differentiation of embryonic stem cells. Biochemical and Biophysical Research Communications. 2009 Feb;379(4):898–903.
81. Frasca G, Du V, Bacri J-C, Gazeau F, Gay C, Wilhelm C. Magnetically shaped cell aggregates: from granular to contractile materials. Soft Matter. 2014;10(28):5045.
82. Du V, Luciani N, Richard S, Mary G, Gay C, Mazuel F, et al. A 3D magnetic tissue stretcher for remote mechanical control of embryonic stem cell differentiation. Nat Commun. 2017 Dec;8(1):400.
83. Van de Walle A, Plan Sangnier A, Abou-Hassan A, Curcio A, Hémadi M, Menguy N, et al. Biosynthesis of magnetic nanoparticles from nano-degradation products revealed in human stem cells. Proc Natl Acad Sci USA. 2019 Mar 5;116(10):4044–53.

CHAPTER 1: RHEOLOGY OF MULTICELLULAR AGGREGATES

3 - State of the art: from single-cell rheology to tissue-model rheology

Through the eyes of a physicist, a biological tissue can be seen as a multi-scaled, active 3D material. Hence, using simple models such as multicellular aggregates, biophysicists have been focused in understanding the mechanical properties of such a complex system. This chapter aims in presenting the main features of the rheology of tissue models. As the cell represents the elementary brick of a tissue, we will first describe the tools available to perform single cell rheology. Then, we will address the general consensus adopted on the cell mechanics. Finally, we will stress that such a rheological behaviour has been found in tissue models at the 2D scale, but not at the 3D scale.

Content

3.1 - Single cell rheology

Single cell represents the elemental constituent of a tissue, and its mechanical properties have been widely studied. In this chapter, we present the main features of the rheological properties of the cell.

3.1.1) The cell as a material

In a biological tissue, due to various stimuli such as cell-cell adhesion, cell –substrate adhesion or cell division, a cell is constantly submitted to physical constraints. This dynamic behaviour is shown to be critical to the cell viability, migration, or differentiation. The mechanical properties of a cell are mainly due to the organization and the active properties of its cytoskeleton (1). Strikingly, a cell appears softer than it constitutive components. For instance, actin filaments present Young's modulus close to the gigapascal (2), whereas cells present Young's modulus in the range of a hundred to a thousand of kilopascals, many orders of magnitude below thus found in common materials (Figure 3-1). Such difference can be explained by the multi-scale architecture of the cell, the inter-connexion of the different components, and by the dynamical processes that lower the overall rigidity of the cell (3).

Generally, the cell is described as a viscoelastic material presenting active features. Its rheology is characterized by a power-law response, that is strikingly conserved between various cell types and various cell components. The following chapter presents current methods enabling the study of single cell mechanics, and the main features of the cell rheological behaviour.

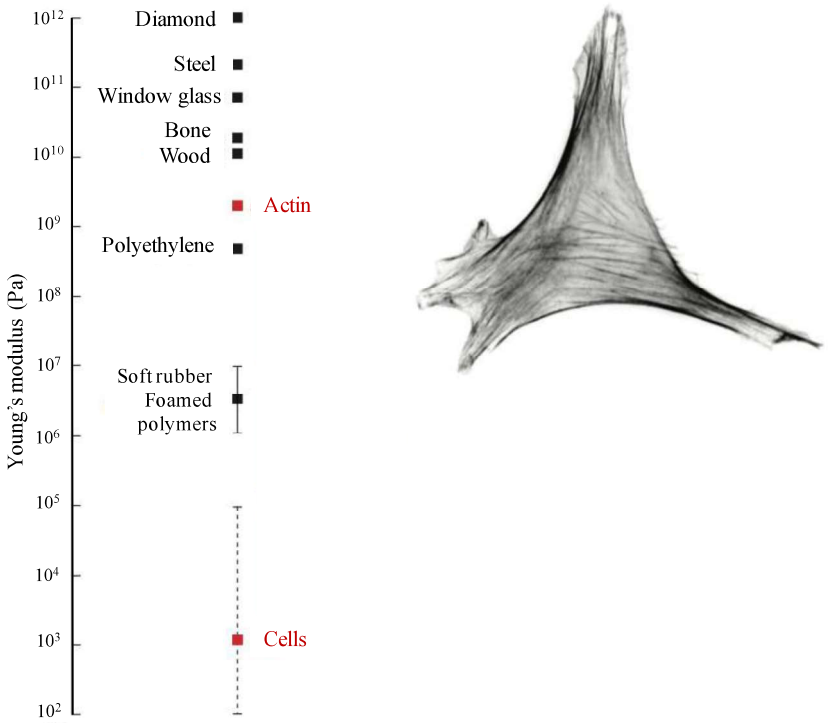

Figure 3-1: Cell Young's modulus compared to various materials. Cells present soft Young's modulus in a broad range from a hundred to a few thousands pascals. The cell appears softer than its own constituents (actin Young's modulus is shown). The right picture presents the actin skeleton of a fibroblast. Adapted from (3).

3.1.2) Probing the cell

To assess the mechanical properties of a material, one can apply controlled forces to the object and measure the resulting deformations, or on the contrary measure the force required to create a known deformation (4). At the scale of a single cell, new tools have been developed in order to measure thus weak involved deformations (at the scale of the nm) and forces (at the scale of the pN). Depending on the chosen technology, the size of the probe, its functionalization and the frequency range available, one can investigate different aspects of the cell rheology. Doing so, the global cell rheology, or contribution of the different cell components on its overall mechanics can be addressed (5). Herein, we present some classical technics used to probe the behaviour a cell under a controlled mechanical stress:

- Atomic force microscopy (AFM) This method consists in applying a local controlled force at the surface of a cell (8). The tip is pressed against the cell, and the deflection of the cantilever is monitored. This tip can be functionalized in order to interact with chosen cell elements. Such method presents high spatial and temporal resolutions.

- Optical and magnetic tweezers Theses techniques are based on trackers that can be stimulated using a controlled force developed thanks to an optical trap or a magnetic gradient. The monitoring of the bead displacement allows measuring the mechanical properties of the material (9). Alternatively, magnetic twisting cytometry consists in applying rotating magnetic moments (10). These two methods allow the application of forces in the range of 1 to 500 pN. Their main drawback is the resulting heating of the cell due to laser focusing for optical trap and the limitation to unidirectional forces in the case of magnetic tweezers.

- Parallel plate rheometer This method has been developed in the laboratory by Atef Asnacios (Figure 3-2). A single cell is placed between two glass microplates. One microplate is rigid, and the other acts as a calibrated cantilever. By stretching the cell, creep experiment of the whole cell can be performed (11). Plus, oscillating stimulations can be imposed (12) (13). Contrarily to the previously exposed methods, the parallel plate rheometer allows measuring the rheological properties of the entire cell, in a various range of frequencies. As presented later in this manuscript, this set-up was used in order to compare the rheological behaviour of single F9 cells, with the behaviour of multicellular aggregates composed of the same cells.

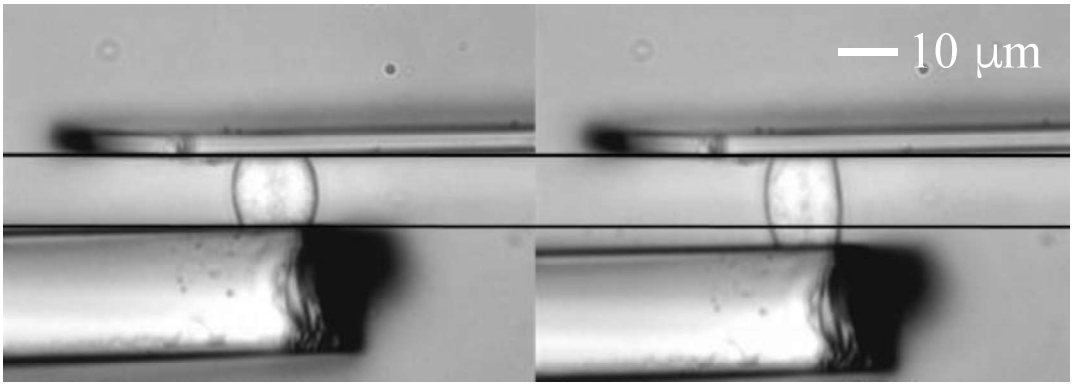

Figure 3-2: Creep experiment of C2-7 cell using the Parallel Plate Rheometer. Using a constant force, the cell is stretched between two glass microplates. The thick bottom plate shifts in order to compensate the cell deformation, maintaining a fixed deflexion of the thin upper plate. The left picture presents the beginning of the stretching, and the right picture presents the cell after 30s. Extracted from (11).

Altogether, these technics allowed unravelling the mechanical properties, at the single cell level.

3.1.3) The mechanical consensus on adherent cells

The different tools allow probing the mechanical properties of the multiscale object that represents a cell. In spite of discrepancies on the absolute values of the different parameters (which may depend on the method, on the cell component, on the cell line etc.), the literature seems to agree with a few mechanical behaviours conserved within the cells:

- Cells present a power-law rheology.
- Cells are prestressed structures.
- Cells show non-linear mechanical behaviour once subjected to large deformations or long time scale stimuli. Stress stiffening, as well as fluidization have been demonstrated.

3.1.3.1) Power law rheology

The mechanical behaviour of cells subjected to a constant stress (stretching or compression), has been addressed using several tools on various cell lines. Remarkably, a general answer has been described as a power-law behaviour.

In an experiment called creep experiment, a cell is subjected to a constant force F, and the resulting deformation $\delta(t)$ is monitored over time. The creep function of the cell $J(t)$ is defined as:

$$J(t) = \frac{\delta(t)}{F} = j_0\left(\frac{t}{\tau_0}\right)^{\alpha}$$

The display of J as a function of time, at log-log scale, is characterised by a straight line with a slope equal to α. The prefactor j_0 is the compliance of the cell, and reflects the inverse of the stiffness. The timescale τ_0 is arbitrarily put to 1s, and the exponent a reflects the mechanical behaviour of the cell. For instance, for $\alpha = 0$, we obtain $\frac{\delta(t)}{F} = j_0$, which corresponds to a purely elastic material. On the other hand, for $\alpha = 1$, we obtain $\frac{\delta(t)}{F} = j_0 \frac{t}{\tau_0}$, which corresponds to the viscous response of a Newtonian fluid. In the like of viscoelastic materials, cells present an intermediate state, and show a typical range of α between 0.1 and 0.5. The Figure 3-3 presents the creeping experiment of a F9 cell (measured with the magnetic tweezers method) and two materials representing the limit states (3).

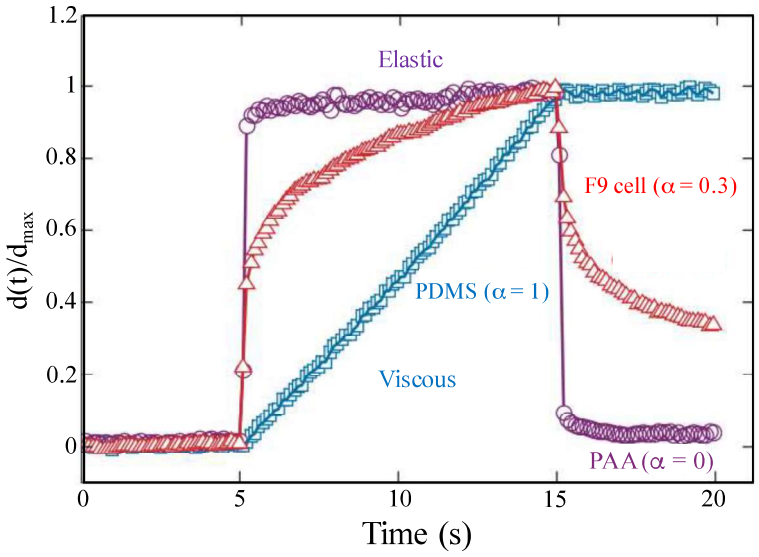

Figure 3-3: Power-law behaviour of a F9 cell. The red line presents the creep experiment of a F9 cell subjected to a constant force during 10s. This response is characteristic of a power-law rheology with an exponent α close to 0.3. This rheological behaviour is compared to two limit cases: a purely viscous (polydimethylsiloxane, PDMS in cyan) or a purely elastic material (polyacrylamide-bis-acrylamide, PAA in purple). These two responses correspond respectively to an exponent α equal to 0 and to 1. Adapted from (3).

The power law can be transcribed for sinusoidal varying forces. The complex modulus G^* of the cell is described as a function of the stimulation pulsation ω, and corresponds to the ratio of the displacement divided by the applied shear:

$$G^*(\omega) = \frac{\delta(\omega)}{\sigma(\omega)} = |G^*(\omega)|\, e^{i\phi(\omega)}$$

In the previous formula, $|G^*(\omega)|$ the norm, and $\phi(\omega)$ the phase. For a power-law response, the expression of the complex modulus becomes:

$$G^*(\omega) = \frac{\delta(\omega)}{\sigma(\omega)} = \frac{\Gamma(1-\alpha)}{j_0} = (i\omega\tau_0)^\alpha$$

$$|G^*(\omega)| = \frac{1}{j_0}\Gamma(1-\alpha)\omega^\alpha {\tau_0}^\alpha$$

$$\phi(\omega) = \frac{\alpha\pi}{2}$$

With Γ the gamma function and i the imaginary number. Therefore, $|G^*(\omega)|$ also follows a power-law with the same exponent α, and the phase is constant and fixed by α.

Interestingly, the power law behaviour is conserved for different cell lines and for different cell components (Table 3-1). Also, such behaviour is conserved for a large range of

stimulation frequencies (roughly between 0.01 Hz to 1 kHz) (14) (15). This behaviour characterised by a scale-free power-law rheology, is now admitted as a universal law of the cell rheology.

System	Alpha	Complex Modulus (Pa)	Methods	Ref
Myoblast (C2-7 cell line)	0.24		Parallel plates	(11)
Myoblast (C2 cell line)	0.21 – 0.29	570 - 1060	Optical Tweezers - Microplates	(16)
Alveolar epithelial (A549)	0.18- 0.22	160	Optical Tweezers	(16)
Macrophages	0.20 – 0.25		Microplates	(16)
Fibroblast (L929 + primary cells)	0.15 – 0.26	170	Optical Tweezers-Microplates	(16)
Canin Kydney (MDCK cell line)	0.18		Optical Tweezers-Microplates	(16)
Cytoplasm	0.15	1 Pa	Force spectrum microscopy	(17)
Various reconstituted Actin Gels	0.05 – 0.15		Diffusing wave spectroscopy	(18)

Table 3-1: Power-law rheology is conserved for various cell lines, and different cellular component. The different cell lines present an exponent α in a range of 0.15 to 0.3. If the cytoplasm presents an exponent α in the same range, lower values have been measured for reconstituted actin gels (between 0.05-0.15). This weaker power-law reflects a more elastic material, and is related to the dynamics of the cross-linked reconstituted gels. In the cell, actin filaments are bound to the cell walls, and interact with the organelles, lowering the overall dynamics compared to reconstituted gels (18).

The power-law response reflects a broad distribution of relaxation time. Due to the multiscale architecture of a cell, the mechanical behaviour cannot be described by a finite number of relaxation times. Therefore, classic models cannot describe such rheology. In (16), Balland et al. proposed a model of the cytoskeleton viewed as an infinite assembly of Kelvin-Voigt units, each of the unit presenting a different relaxation time, resulting in the final mechanical behaviour of the cell.

If the power law behaviour is conserved for a large range of frequencies, the value of the exponent α may change. At high frequencies, the cytoskeleton dominates the mechanical response, by imposing a viscous dissipation due to the fluctuations of its filaments. For freely dissipating filaments, theoretical models predict a power law exponent of ¾ (19). Rheological experiments performed on actin polymers confirmed this value (20). Such a value is measured

in cells subjected to high frequency stimulations (21). At very low frequencies, cells present a weaker power-law, with an exponent α between 0.05 and 0.15. If the origin of this weak power-law is yet to be clarified in cells, such behaviour could be due to the dynamics of the proteins composing the cells (18). For time scales in a range of 0.1s to 100s, the power-law exponent is found between 0.15 and 0.3.

3.1.3.2) The cell as a Soft Glassy Material

The power-law rheology is typical of various soft materials such as foams, emulsions, pastes and slurries (22). In such materials, the microscopic components are not able to move freely, which does not allow to reach the thermodynamic equilibrium. They are metastable materials, and their rheological properties arise from the microscopic rearrangements of their components. The power-law rheology can be explained by the complexity of the material energy landscape. Fabry et al. (15) introduced this model to describe the rheology of the cell, for which the energy landscape comes from the ATP consumption of its components.

3.1.3.4) The tensegrity model: the cell is prestressed

Due to the contractility of the actomyosin complex, the cell can be considered as a prestressed material (23). Through the cell adhesions, such contractility results in an intrinsic tension of the cell cortex. Kollmannsberger et al. experimentally linked the prestressed state of the cell with the values of j_0 and α (26). For instance, a cell presenting a higher cortical tension appears stiffer (24), and is characterized by a lower value of the power-law exponent (25). Such a prestressed state can be seen as a way for the cell to adapt to the microenvironment (3).

3.1.3.5) Non-linear behaviour

The response of the cell to high mechanical stresses is non-linear (27). Both the stiffness and the exponent α increase with the mechanical stress (28), indicating both the stiffening and the fluidization of the cell under high constraints. The consequent fluidization depends on the initial cytoskeleton prestress: stiffer or more contractile cells fluidify more than softer or less contractile cells (28) (29).

3.1.3.6) Cytoskeleton contribution

Several studies have submitted cells to drugs impacting the cytoskeleton networks. In such conditions, the power-law behaviour is conserved, and if the stiffness is affected, small effects are noted on the power-law exponent.

For instance, the cytochalasin D, an inhibitor of the actin polymerisation, was used to disrupt the actin network of different cell types (30). In response to the drug, the authors noticed a softening of the cells, and an increase of the value of the power-law exponent. In addition, cells subjected to latrunculin A – a drug that induced the depolymerisation of the F-actin - showed a softening (400% softer) and an increase of the exponent α (from 0.2 to 0.27) (31). Blebbistatin, that inhibits the myosin II, was used on myoblasts to disturbed their contractility (32). In response, the authors reported a softening of the cells, and a decrease of the exponent α.

Therefore, if the disruption of the actin network or the disturbing of the contractility of the cells is reported to impact the two parameters, the effects vary regarding the type of cells or of the type of stimulation (18).

3.2 - Mechanics of cell monolayers

Scaling up toward a tissue model, cell monolayers appear as good candidates to take into account cohesiveness and collective effects that can be driven by cell assemblies (33). Measuring the rheology of 2D cell monolayers requires imposing forces to such a structure. Two approaches have been developed: one can measure the local properties of the structure, or investigate the overall rheology of the 2D tissue model.

3.2.1) Probing the mechanical properties of an epithelium

Two kinds of tools have been implemented to characterize the rheology of a 2D monolayer. The first ones highlight the relations between the cell and the tissue, as they focus on investigating the local rheology of cells taken in a global 2D structure. The same tools than the one developed for single cell rheology are used (such as AFM (34) or optical tweezers (35)). Plus, local measurements of cell-cell tensions using FRET probes allow looking at the force transmission through the cell-cell junctions (36). If these tools enable the mapping of

the local mechanical properties of 2D monolayers, they are not suitable for unravelling the overall mechanics of the structure.

3.2.2) Rheological behaviour of a whole epithelium

The tools mentioned above are powerful tools to investigate local mechanical behaviours inside the monolayer. The characterization of the overall rheology of such 2D models has been addressed in a very few studies.

To do so, Harris et al. developed a stretching device enabling to stretch a whole suspended epithelium (37). This device allowed to perform creep experiment on the epithelium, without any substrate (Figure 3-4). By applying a constant stress of a few kPa, they demonstrated that the epithelium rheological behaviour is a power law with an exponent equal to 0.15, slightly lower than the ones found for single cells. The relaxation also exhibits such a power-law response with an exponent close to 0.3 (38). This technique requires large deformation, implying that non-linear regimes are investigated.

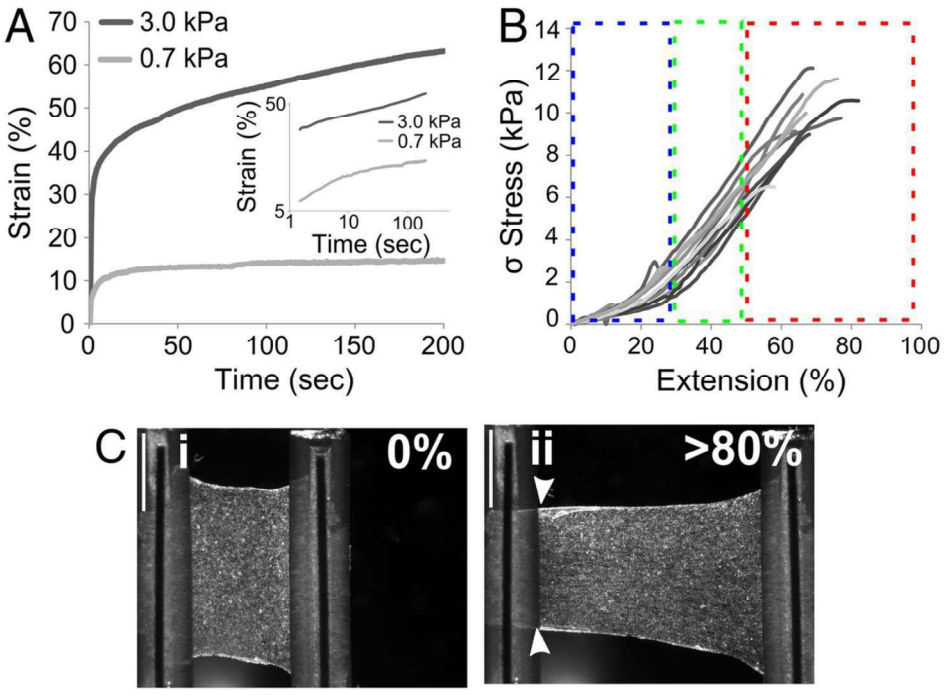

Figure 3-4: Creep function of a suspended monolayer. A) Mechanical response of a monolayer subjected to constant stresses (3 and 0.7 kPa). Such response is characteristic of a power-law rheology. **B)** Under stress, three different regimes are observed: the flattening, the extension and the plasticity of the monolayer. **C)** Bright field imaging of the monolayer stretching. Under a constant strain, the monolayer is stretched up to 80% of its initial length. Extracted from (37)

Strikingly, these experiments demonstrate that in the like of the single cell, a monolayer also presents a power-law rheology. As the power-law response arises from the multi-scale organization of the material, it is not surprising to obtain such a rheology at the scale of a 2D tissue model. Yet, such result was never observed before. In the next paragraph, we will stress that this response has never been observed at the scale of a multicellular aggregates.

3.3 - Mechanics of 3D tissue models

Several studies have been focused on investigating the mechanical properties of multicellular aggregates. Historically, biological tissues and multicellular aggregates have been compared to liquids (39). The analogy arises from the nature of the cell-cell adhesion. Indeed, in the like of particles composing a liquid, cells interact through attractive adhesions. Recent works have refined this model, demonstrating the active visco-elastic properties of multicellular aggregates. Such as common viscoelastic materials, tissue models can be described by a surface tension, an elastic modulus and an effective viscosity.

3.3.1) Tools to probe a multicellular aggregate

In order to measure such parameters, new tools have been developed, enabling to submit the tissue models to know forces (such as centrifugation (40) or magnetic forces (41)) or to controlled deformations. Such deformations can be applied locally through micropipette aspirations (42), or at the global scale of the spheroid using parallel plates (43) (44).
However, such tools cannot provide an insight on the dynamic properties of a 3D tissue model.

3.3.2) Mechanical properties of a 3D tissue

The previous experiments have been able to address the mechanical behaviour of soft biological tissue models, but only at rest. They can be completed by dynamics measurements using shear rheometers on spheroids (49). However, the results were obtained for hundreds of F9 spheroids at the same time (Figure 3-5). Because of such a large number, absolute measurements were not possible.

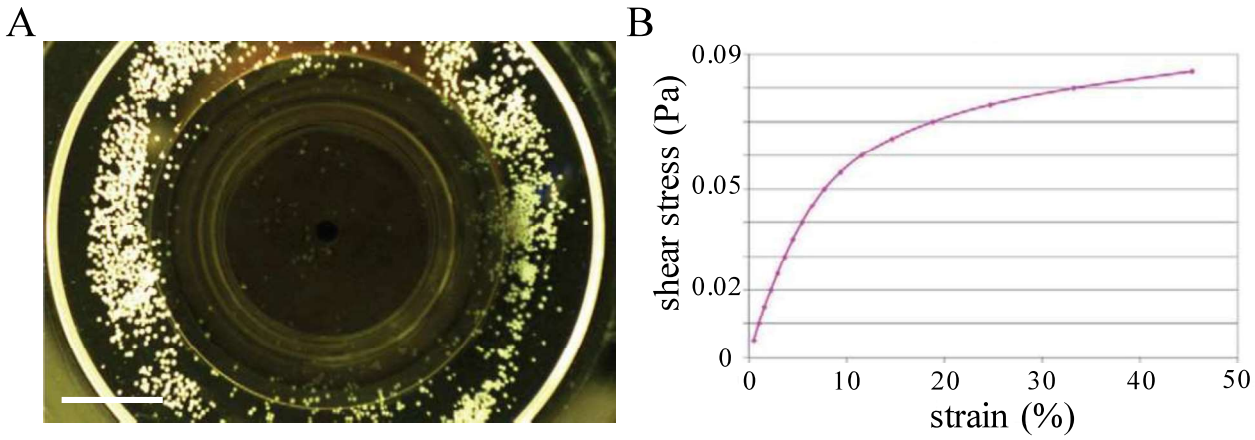

Figure 3-5: Rheology of F9 spheroids. A) Several hundreds of multicellular spheroids are placed in a classic shear rheometer. Scale bar: 1 cm. **B)** The tissue models were subjected to pulses (3s) of increasing imposed shear stresses. The curve represents the imposed shear stress as a function of the measured maximum strain. Adapted from (49).

Strikingly, the mechanical properties of multicellular aggregates depend on the time scale of the stimulation. At short time scale, a tissue model is purely elastic, and becomes visco-elastic at long time scales (50). We are going to briefly summarize these time-dependent behaviours.

From a few seconds to the minute: elastic behaviour Subjected to small or to short-time deformations, the response is elastic and reversible (50) (51) (42). This response comes mainly from the properties of the cell cytoskeleton. As for the single cell scale, the elastic modulus depends on the stress applied and on the rheological history of the aggregate (52).

From the minute to an hour: viscoelastic behaviour For longer deformations, the aggregate recovery takes longer. The answer is viscoelastic (42) (53) (43). The rheological behaviour is characterised by a surface tension, an elastic modulus and a viscosity.

These viscoelastic properties come from the multi-scale architecture of the tissue. If the elastic properties come mainly from the cell cytoskeleton, the viscosity comes from the cell arrangements. Historically, these rearrangements were evidenced by Philips and Steinberg (53). By fixing chicken embryos subjected to short or long centrifugations, they demonstrated that the short centrifugations (minutes) lead to deformed cells, whereas long centrifugations (hours) lead to the recovery of the cell shape. Such a recovery is due to the cell relaxation during long centrifugations. More recently, cell rearrangements have been directly pictured in aggregates subjected to constrictions inside microfluidic devices (54). The rearrangement of

cells, consisting in a swap of the neighbouring cells, is called T1 transition (Figure 3-6) (55). The same rearrangements can be found in embryo, but also in model materials such as foams (54).

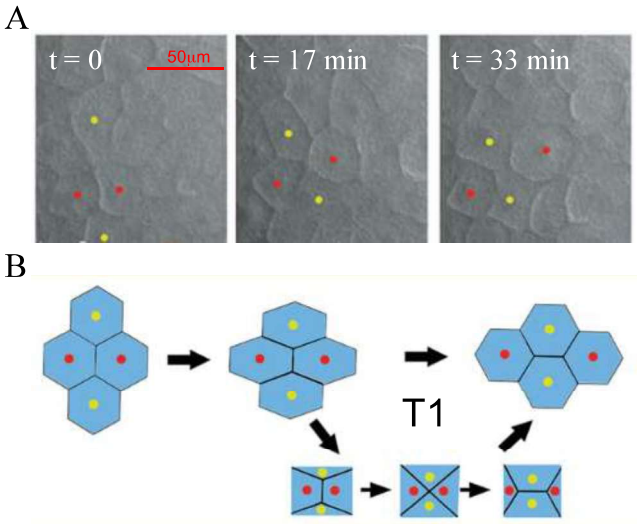

Figure 3-6: T1 transition in a tissue. A) Illustration of a spontaneous T1 transition filmed on an explant of a Xenopus embryonic tissue. The transition corresponds to a swap of the neighbouring cells. Originally, the two cells tagged with the red dots are in contact. After the T1 transition, the cells tagged with the yellow dots are in contact. **B)** Scheme of the cell swapping during the T1 transition. To undergo such a transition, energy barriers need to be overcome in order to swap the cell contact lines. Adapted from (55).

Others models aim in refining the viscoelastic behaviour of a tissue by describing it as a visco-elasto-plastic behaviour (56). In this model, plasticity occurs when the aggregate is subjected to a stress higher than a yield stress. For instance, such behaviour characterizes the decrease of the effective viscosity with the increase of the stress applied to multiple aggregates placed in a rheometer. A yield point was observed for cells subjected to strains close to 12% (51). This yield stress corresponds to the energy sufficient to break the cell adhesion bonds (56), or the energy necessary to induce cell rearrangements (51).

For a few hours: viscous behaviour For stimulations of a few hours, a tissue can be seen as viscous fluid, characterized by its effective viscosity. For F9 aggregates, the effective viscosity is reported in a range of a few10^5 Pa.s (57). This viscous behaviour arises from the cell-contour fluctuations, enabling the cells to overcome the energetic barriers necessary to rearrange (58), and therefore relaxing the stress. It results in a slow fluidization of the material (51).

For day-long stimulations For longer stimulations, cell divisions and cell death influence the rheological behaviour. Mathematical models demonstrate that the fluctuations and rearrangements due to cell divisions and apoptosis tend to fluidify the tissue (59).

Active response

Additionally to these passive behaviours, active answers have been highlighted. For instance, an aggregate subjected to a pipette aspiration presents a surface tension increasing with the applied pressure, and also demonstrates a pulsatile response (52).

Subjected to compressive stress, cell division (60) (61) and cell movements inside the tissue can be impacted (62). In particular, the effects of a compressive stress on the biological response of a growing tumor will be discussed in details in the chapter 2 of this manuscript.

Unravelling the cell contribution on the global mechanics

A very few studies have been focused on the effect of cell adhesion on the global mechanics of an aggregate. Mainly, these experiments have been focused on the effects on the surface tension of the tissue (63) and the viscosity (42).

Additionally, a few works have been focused on the contribution of the cytoskeletal components on the whole aggregate rheology. For instance, depletion of the α-actinin, a protein binding the actin cytoskeleton to the cadherins, impacts the surface tension and the viscosity of the aggregate (57).

3.4 - Conclusion: What about the dynamic behaviour at the 3D scale?

As presented above, the power-law behaviour of a single cell has been widely studied. In particular, the power-law response of the cell and the cells components is widely observed and accepted. Scaling up, this behaviour was highlighted in suspended monolayers subjected to creep experiments. But, the lack of evidence of such behaviour at the scale of a 3D tissue model is crying. Indeed, very few studies report a power-law for extracted tissues. For instance, rheological experiments performed with a classic rheometer on animal organs or tissue extracts (such as liver tissues (68), adipose tissue (69) or human brain slides (70)),

highlighted power-law behaviours with an exponent close to 0.2 (45) (46). But, this behaviour has never been demonstrated with multicellular aggregates.

This stresses a crying lack of tools allowing to unravel the dynamical response of multicellular aggregates.

3.6 - Proposed approach

Herein, we propose the use of magnetic forces in order to investigate the dynamical properties of multicellular aggregates. Previously in the group, François Mazuel developed an all-in-one tool in order to create large magnetic spheroids, and to subject them to a magnetic flattening (41). If this method allows measuring the surface tension of an aggregate, the short-time deformations are yet to be unravelled. In order to study the dynamical behaviour of multicellular aggregates, Francois Mazuel developed and characterized the magnetic rheometer, composed of an electromagnet instead of a permanent magnet. Such a tool allows to subject magnetic multicellular aggregates to remote varying magnetic field.

François Mazuel developed and characterized the magnetic rheometer during his PhD. Herein, I present the final version of the project, in which I was first involved as a Master 2 student. In particular, I was interested in two major issues:

- First, I investigated the contribution of cell cytoskeleton on the aggregate rheology. If the actin depletion impacts both the cell stiffness and the cell power-law exponent, such contribution has never been demonstrated at the 3D scale. To do so, F-actin was disturbed using latrunculin A, and I investigated the impact on the rheology of a multicellular aggregate.
- Second, as cell-cell adhesion is the hallmark of cell assembly, I tested if a change in the cell cohesiveness would impact the overall rheology of a multicellular aggregate. To do so I investigated both the influence of a cadherin depletion (through the use of egtazic acid, EGTA), and the influence of an enhanced cell-cell adhesion thanks to the maturation of the multicellular aggregates.

In the next paragraph, the project is presented in the form of an article.

References

1. Kasza KE, Rowat AC, Liu J, Angelini TE, Brangwynne CP, Koenderink GH, et al. The cell as a material. Curr Opin Cell Biol. 2007 Feb;19(1):101–7.
2. Gardel ML, Kasza KE, Brangwynne CP, Liu J, Weitz DA. Chapter 19 Mechanical Response of Cytoskeletal Networks. In: Methods in Cell Biology [Internet]. Elsevier; 2008 [cited 2019 Nov 19]. p. 487–519. Available from: https://linkinghub.elsevier.com/retrieve/pii/S0091679X08006195
3. Kollmannsberger P, Fabry B. Linear and Nonlinear Rheology of Living Cells. Annu Rev Mater Res. 2011 Aug 4;41(1):75–97.
4. Moeendarbary E, Harris AR. Cell mechanics: principles, practices, and prospects: Cell mechanics. Wiley Interdiscip Rev Syst Biol Med. 2014 Sep;6(5):371–88.
5. Matellan C, del Río Hernández AE. Where No Hand Has Gone Before: Probing Mechanobiology at the Cellular Level. ACS Biomater Sci Eng. 2019 Aug 12;5(8):3703–19.
6. Lee H, Ferrer JM, Nakamura F, Lang MJ. Passive and active microrheology for cross-linked F-actin networks in vitro. 2011;24.
7. Crocker JC, Ho BD. Multiple-Particle Tracking and Two-Point Microrheology in Cells. :38.
8. Luo Q, Kuang D, Zhang B, Song G. Cell stiffness determined by atomic force microscopy and its correlation with cell motility. Biochim Biophys Acta BBA - Gen Subj. 2016 Sep;1860(9):1953–60.
9. Falleroni F, Torre V, Cojoc D. Cell Mechanotransduction With Piconewton Forces Applied by Optical Tweezers. Front Cell Neurosci. 2018 May 14;12:130.
10. Coughlin MF, Bielenberg DR, Lenormand G, Marinkovic M, Waghorne CG, Zetter BR, et al. Cytoskeletal stiffness, friction, and fluidity of cancer cell lines with different metastatic potential. 2013;25.
11. Desprat N, Richert A, Simeon J, Asnacios A. Creep Function of a Single Living Cell. Biophys J. 2005 Mar;88(3):2224–33.
12. Mitrossilis D, Fouchard J, Pereira D, Postic F, Richert A, Saint-Jean M, et al. Real-time single-cell response to stiffness. Proc Natl Acad Sci. 2010 Sep 21;107(38):16518–23.
13. Wu P-H, Aroush DR-B, Asnacios A, Chen W-C, Dokukin ME, Doss BL, et al. A comparison of methods to assess cell mechanical properties. Nat Methods. 2018 Jul;15(7):491–8.
14. Hoffman BD, Massiera G, Van Citters KM, Crocker JC. The consensus mechanics of cultured mammalian cells. Proc Natl Acad Sci. 2006 Jul 5;103(27):10259–64.
15. Fabry B, Maksym GN, Butler JP, Glogauer M, Navajas D, Fredberg JJ. Scaling the Microrheology of Living Cells. Phys Rev Lett [Internet]. 2001 Sep 13 [cited 2017 Jan 16];87(14). Available from: http://link.aps.org/doi/10.1103/PhysRevLett.87.148102
16. Balland M, Desprat N, Icard D, Féréol S, Asnacios A, Browaeys J, et al. Power laws in microrheology experiments on living cells: Comparative analysis and modeling. Phys Rev E [Internet]. 2006 Aug 9 [cited 2017 Jan 16];74(2). Available from: http://link.aps.org/doi/10.1103/PhysRevE.74.021911
17. Guo M, Ehrlicher AJ, Jensen MH, Renz M, Moore JR, Goldman RD, et al. Probing the Stochastic, Motor-Driven Properties of the Cytoplasm Using Force Spectrum Microscopy. Cell. 2014 Aug;158(4):822–32.
18. Hoffman BD, Crocker JC. Cell Mechanics: Dissecting the Physical Responses of Cells to Force. Annu Rev Biomed Eng. 2009 Aug;11(1):259–88.
19. Gittes F, MacKintosh FC. Dynamic shear modulus of a semiflexible polymer network. Phys Rev E. 1998 Aug 1;58(2):R1241–4.
20. Gardel ML, Shin JH, MacKintosh FC, Mahadevan L, Matsudaira PA, Weitz DA. Scaling of F-Actin Network Rheology to Probe Single Filament Elasticity and Dynamics. Phys Rev Lett. 2004 Oct 29;93(18):188102.
21. Deng L, Trepat X, Butler JP, Millet E, Morgan KG, Weitz DA, et al. Fast and slow dynamics of the cytoskeleton. Nat Mater. 2006 Aug;5(8):636–40.
22. Sollich P. Rheological constitutive equation for a model of soft glassy materials. Phys Rev E. 1998 Jul 1;58(1):738–59.
23. Ingber DE. Cellular tensegrity: defining new rules of biological design that govern the cytoskeleton. :15.
24. Wang N, Naruse K, Stamenovic D, Fredberg JJ, Mijailovich SM, Tolic-Norrelykke IM, et al.

Mechanical behavior in living cells consistent with the tensegrity model. Proc Natl Acad Sci. 2001 Jul 3;98(14):7765–70.
25. Stamenović D, Suki B, Fabry B, Wang N, Fredberg JJ, Buy JE. Rheology of airway smooth muscle cells is associated with cytoskeletal contractile stress. J Appl Physiol. 2004 May;96(5):1600–5.
26. Kollmannsberger P, Fabry B. Active soft glassy rheology of adherent cells. Soft Matter. 2009;5(9):1771.
27. Fernández P, Pullarkat PA, Ott A. A Master Relation Defines the Nonlinear Viscoelasticity of Single Fibroblasts. Biophys J. 2006 May;90(10):3796–805.
28. Kollmannsberger P, Mierke CT, Fabry B. Nonlinear viscoelasticity of adherent cells is controlled by cytoskeletal tension. Soft Matter. 2011;7(7):3127–32.
29. Bursac P, Lenormand G, Fabry B, Oliver M, Weitz DA, Viasnoff V, et al. Cytoskeletal remodelling and slow dynamics in the living cell. Nat Mater. 2005 Jul;4(7):557–61.
30. Smith BA, Tolloczko B, Martin JG, Grütter P. Probing the Viscoelastic Behavior of Cultured Airway Smooth Muscle Cells with Atomic Force Microscopy: Stiffening Induced by Contractile Agonist. Biophys J. 2005 Apr;88(4):2994–3007.
31. Laudadio RE, Millet EJ, Fabry B, An SS, Butler JP, Fredberg JJ. Rat airway smooth muscle cell during actin modulation: rheology and glassy dynamics. Am J Physiol-Cell Physiol. 2005 Dec;289(6):C1388–95.
32. Balland M, Richert A, Gallet F. The dissipative contribution of myosin II in the cytoskeleton dynamics of myoblasts. Eur Biophys J. 2005 May;34(3):255–61.
33. Trepat X, Wasserman MR, Angelini TE, Millet E, Weitz DA, Butler JP, et al. Physical forces during collective cell migration. Nat Phys. 2009 Jun;5(6):426–30.
34. A-Hassan E, Heinz WF, Antonik MD, D'Costa NP, Nageswaran S, Schoenenberger C-A, et al. Relative Microelastic Mapping of Living Cells by Atomic Force Microscopy. Biophys J. 1998 Mar;74(3):1564–78.
35. Bambardekar K, Clément R, Blanc O, Chardès C, Lenne P-F. Direct laser manipulation reveals the mechanics of cell contacts in vivo. Proc Natl Acad Sci. 2015 Feb 3;112(5):1416–21.
36. Jurchenko C, Salaita KS. Lighting Up the Force: Investigating Mechanisms of Mechanotransduction Using Fluorescent Tension Probes. Mol Cell Biol. 2015 Aug 1;35(15):2570–82.
37. Harris AR, Peter L, Bellis J, Baum B, Kabla AJ, Charras GT. Characterizing the mechanics of cultured cell monolayers. Proc Natl Acad Sci. 2012 Oct 9;109(41):16449–54.
38. Khalilgharibi N, Fouchard J, Asadipour N, Barrientos R, Duda M, Bonfanti A, et al. Stress relaxation in epithelial monolayers is controlled by the actomyosin cortex. Nat Phys. 2019 Aug;15(8):839–47.
39. Steinberg MS. Reconstruction of Tissues by Dissociated Cells. Science. 1963 Aug 2;141(3579):401–8.
40. Kalantarian A, Ninomiya H, Saad SMI, David R, Winklbauer R, Neumann AW. Axisymmetric Drop Shape Analysis for Estimating the Surface Tension of Cell Aggregates by Centrifugation. Biophys J. 2009 Feb;96(4):1606–16.
41. Mazuel F, Reffay M, Du V, Bacri J-C, Rieu J-P, Wilhelm C. Magnetic Flattening of Stem-Cell Spheroids Indicates a Size-Dependent Elastocapillary Transition. Phys Rev Lett [Internet]. 2015 Mar 4 [cited 2017 Jan 16];114(9). Available from: http://link.aps.org/doi/10.1103/PhysRevLett.114.098105
42. Guevorkian K, Colbert M-J, Durth M, Dufour S, Brochard-Wyart F. Aspiration of Biological Viscoelastic Drops. Phys Rev Lett. 2010 May 24;104(21):218101.
43. Forgacs G, Foty RA, Shafrir Y, Steinberg MS. Viscoelastic Properties of Living Embryonic Tissues: a Quantitative Study. Biophys J. 1998 May;74(5):2227–34.
44. Foty RA, Forgacs G, Pfleger CM, Steinberg MS. Liquid properties of embryonic tissues: Measurement of interfacial tensions. Phys Rev Lett. 1994 Apr 4;72(14):2298–301.
45. Nicolle S, Vezin P. A strain-hardening bi-power law for the nonlinear behaviour of biological soft tissues. J Biomech. 2010;6.
46. Marion G, W.M PG, A.J AP, W.J OC, P.T BF. Linear viscoelastic behavior of subcutaneous adipose tissue. Biorheology. 2008;(6):677–688.
47. Budday S, Sommer G, Haybaeck J, Steinmann P, Holzapfel GA, Kuhl E. Rheological characterization of human brain tissue. Acta Biomater. 2017 Sep;60:315–29.
48. Madsen C, Cox T. Relative Stiffness Measurements of Tumour Tissues by Shear Rheology.

BIO-Protoc [Internet]. 2017 [cited 2019 Oct 16];7(9). Available from: https://bio-protocol.org/e2265
49. Vasilica Stirbat T, Tlili S, Houver T, Rieu J-P, Barentin C, Delanoë-Ayari H. Multicellular aggregates: a model system for tissue rheology. Eur Phys J E. 2013 Aug;36(8):84.
50. Yu M, Mahtabfar A, Beelen P, Demiryurek Y, Shreiber DI, Zahn JD, et al. Coherent Timescales and Mechanical Structure of Multicellular Aggregates. Biophys J. 2018 Jun;114(11):2703–16.
51. Marmottant P, Mgharbel A, Kafer J, Audren B, Rieu J-P, Vial J-C, et al. The role of fluctuations and stress on the effective viscosity of cell aggregates. Proc Natl Acad Sci. 2009 Oct 13;106(41):17271–5.
52. Guevorkian K, Gonzalez-Rodriguez D, Carlier C, Dufour S, Brochard-Wyart F. Mechanosensitive shivering of model tissues under controlled aspiration. Proc Natl Acad Sci. 2011 Aug 16;108(33):13387–92.
53. Phillipsj HM, Steinberg MS. Embryonic tissues as elasticoviscous liquids. :20.
54. Tlili S. Biorhéologie in vitro : de la cellule au tissu [Internet] [PhD Thesis]. 2015. Available from: http://www.theses.fr/2015USPCC146
55. David R, Luu O, Damm EW, Wen JWH, Nagel M, Winklbauer R. Tissue cohesion and the mechanics of cell rearrangement. Development. 2014 Oct 1;141(19):3672–82.
56. Preziosi L, Ambrosi D, Verdier C. An elasto-visco-plastic model of cell aggregates. J Theor Biol. 2010 Jan;262(1):35–47.
57. Stirbat TV, Mgharbel A, Bodennec S, Ferri K, Mertani HC, Rieu J-P, et al. Fine Tuning of Tissues' Viscosity and Surface Tension through Contractility Suggests a New Role for α-Catenin. Heisenberg C-P, editor. PLoS ONE. 2013 Feb 4;8(2):e52554.
58. Schötz E-M, Lanio M, Talbot JA, Manning ML. Glassy dynamics in three-dimensional embryonic tissues. J R Soc Interface. 2013 Dec 6;10(89):20130726.
59. Ranft J, Basan M, Elgeti J, Joanny J-F, Prost J, Julicher F. Fluidization of tissues by cell division and apoptosis. Proc Natl Acad Sci. 2010 Dec 7;107(49):20863–8.
60. Desmaison A, Guillaume L, Triclin S, Weiss P, Ducommun B, Lobjois V. Impact of physical confinement on nuclei geometry and cell division dynamics in 3D spheroids. Sci Rep. 2018 Dec;8(1):8785.
61. Desmaison A, Frongia C, Grenier K, Ducommun B, Lobjois V. Mechanical Stress Impairs Mitosis Progression in Multi-Cellular Tumor Spheroids. Engler AJ, editor. PLoS ONE. 2013 Dec 3;8(12):e80447.
62. Delarue M, Montel F, Caen O, Elgeti J, Siaugue J-M, Vignjevic D, et al. Mechanical Control of Cell flow in Multicellular Spheroids. Phys Rev Lett. 2013 Mar 26;110(13):138103.
63. Foty RA, Steinberg MS. Cadherin-mediated cell-cell adhesion and tissue segregation in relation to malignancy. Int J Dev Biol. 2004;48(5–6):397–409.

4 - Article: *Magnetic Remote Stimulation of multicellular aggregates: non-linear power law rheology at the tissue scale*

Magnetic remote stimulation of multicellular aggregates: non-linear power law rheology at the tissue scale

Gaëtan Mary[1‡], François Mazuel[1‡], Vincent Nier[2], Florian Fage[1] , Louisiane Devaud[1], Jean-Claude Bacry[1], Atef Asnacios[1], Cyprien Gay[1], Philippe Marcq[2], Claire Wilhelm[1*] and Myriam Reffay[1*]

1 Laboratoire Matière et Systèmes Complexes, UMR 7057, CNRS and Université Paris Diderot, 75205 Paris cedex 13, France
2 Laboratoire Physico Chimie Curie, Institut Curie, PSL Research University, Sorbonne Université, CNRS, 26 rue d'Ulm, 75005 Paris, France
‡ These authors contributed equally to this work
* Authors for correspondence: myriam.reffay@univ-paris-diderot.fr,

Abstract

Tissues are subjected to stress stimuli whatever their function is. Stress is a potential stimulus for their differentiation or remodelling. While cell rheology has been extensively studied, mechanical tissue behavior under deformations is still unknown. Here, we report that submitted to a compression driven by magnetic intracellular forces, multicellular aggregates respond a power-law response with non-linearites leading to tissue fluidization at high stress. Due to the versatility of the magnetic rheometer accessible stimulations, creep functions as well as harmonic functions or broad spectrum stimulations have been tested to corroborate this result. Remarkably, tissue dynamics reproduces the feautures of single cell rheology and respond in the same way to cytoskeleton perturbation. However cell-cell adhesion function in tissue compliance is fundamental. Magnetic rheometer appears as an essential tool that can be correlated with advanced inference methods to provide in a single experiment the broad spectrum of model tissue rheology.

Introduction

Exploring and modelling the mechanical and rheological behaviors of biological tissues is a field of increasing interest with key issues at stake ranging from developmental biology to tumor invasion, tissue engineering and biomedical aspects [1, 2, 3]. Biological tissues are complex 3D cellular, heterogeneous and active materials. Their intrinsic complexity makes them challenging to characterize as this necessarily entails to perfectly control and reproduce the tissue microscopic and macroscopic architecture. In that sense, multicellular aggregates are considered the most relevant models of biological tissues for quantitative exploration [4]. Organized in three dimensions and usually made of a single type of cells, their cell number, cell-cell interactions, and overall size are well-controlled. Unlike animal embryos, no genetic pathway is involved. All these features make them simple, well-controlled system of choice, as testified by its widespread current use in developmental biology [5], organogenesis, cancer [6, 7], drug screening and biophysical research [7, 8, 9, 10].

Concepts from soft condensed matter physics have often successfully explained tissue behavior [11], for instance cell sorting [12], spreading, and cell diffusion as well as in modelling the reshaping and movements within a physically stimulated tissue [13, 14, 15, 16, 17]. Of note, tissue rheology is generally found to be time-dependent, *i.e.* elastic on short time scales (seconds to minutes) [18, 19] yet viscous on longer time scales (minutes to hours), up to even longer time scales (days) where cell division and death also contribute to tissue fluidization [20]. Rheology should also exhibit these multiscale contributions as both intracellular and intercellular parameters are involved [4].

The mechanical features of single living cells have been analyzed and scrutinized, evidencing remarkable dynamical behaviors. In particular, despite the variety of experimental approaches

[21, 22, 23, 24], a consensus has emerged to describe the cellular creep function as a power-law response over a large range of frequency and time. Such power-law ousts the spring-dashpots models to impose the image of a cell with no dominating timescale [25] but rather a continuum of relaxation time and processes. Single cells could then be described as a material characterized by two parameters only: the power-law exponent reflecting the viscous versus elastic contribution to the dynamics (in the range $0.15 - 0.3$ for cells, thus closer to a solid than to a liquid behaviour) and the pre-factor scaling its stiffness value. Both depend however on the level of applied stress, with some demonstration of stress-stiffening [26, 27] as well as of stress-softening [24], with attempts as well to reconcile the two opposite observations [28]. Cell monolayers also seem to behave rheologically as single cells during relaxation [29].

However a remaining challenge is to understand the link between cellular and aggregate rheology that is to say how these single cells mechanical properties are translated at the tissue scale. Power-law was indeed rarely measured at the tissue scale as the only studies concern whole organs[30][31]. They reported powerlaws with exponent close to 0.2. However it was never evidenced in the simplest tissue model of multicellular aggregates only made of the assembly of multiple cells. The rheology of multicellular aggregates should be influenced by the intercellular junctions [32]. Cell-cell adhesions themselves exhibits viscoelastic properties [33] but the link between cellular and junctional contribution is not straightforward to infer.

Herein we propose to tackle the issue of multicellular aggregate dynamics by applying remote magnetic forces over the whole tissue. It first requires to magnetize the tissue to be probed and magnetic nanoparticles are perfect candidates to do so. They can be easily internalized within the cells prior to the formation of the multicellular aggregates thus conferring bulk magnetization to the model tissue. External magnetic field applied at distance, with no contact, then create internal controlled stresses to probe the aggregate mechanical properties[18]. Electromagnetic stimulations provide a wide range of possible stimulations. Besides, the all-in-one magnetic approach is also essential to initially magnetically form the multicellullar aggregate by magnetic molding[18]. The designed cylindrical shape is fundamental to quantitatively analyze the mechanical response with an unprecedented high precision. Doing so we measured the creep function at the tissue level and evidenced a robust power-law behavior confirmed by harmonic stimulation and comparison with microplates set-up. Moreover the range of applied stress reveals non-linearity in the mechanical response. Going further, the versatility of the magnetic stimulation, allowing any type of temporal stimulation, led us to apply a large spectrum input signal to model the full rheological behavior of a multicellular aggregate in a single acquisition and corroborate the nonlinear power-law rheology.

A magnetic rheometer at the tissue scale

In order to measure rheological parameters of a whole multicellular aggregate, our goal is to be able to stimulate this material mechanically with an arbitrary signal. We choose to remotely apply magnetic forces on all cells through internalized magnetic nanoparticles [34]. Our previous works have evidenced that incorporating magnetic nanoparticles does not modify the cell biological activity [35]. The tissue can be stimulated at will as the magnetic cellular force is created by an electromagnet whose magnetic field can be varied in a time-dependent manner.

For simplicity, we decide to test the aggregate's rheological response in the most linear geometry. We use a magnetically inspired molding strategy [18] and design cylindrical multicellular aggregates, thus ensuring a constant contact surface area. The resulting cylindrical aggregates (Figure 1a-b) have a typical diameter of 2 mm and a typical height $h_0 = 0.8$ mm (which corresponds to about 10^6 cells). They display well developed cell-cell adhesions (Figure 1c). Note that in the case of a multicellular spheroid, the contact area would change during the force application and the interpretation of the measurements would then require additional care.

The magnetic field and gradient were optimized to apply a homogeneous body force. To

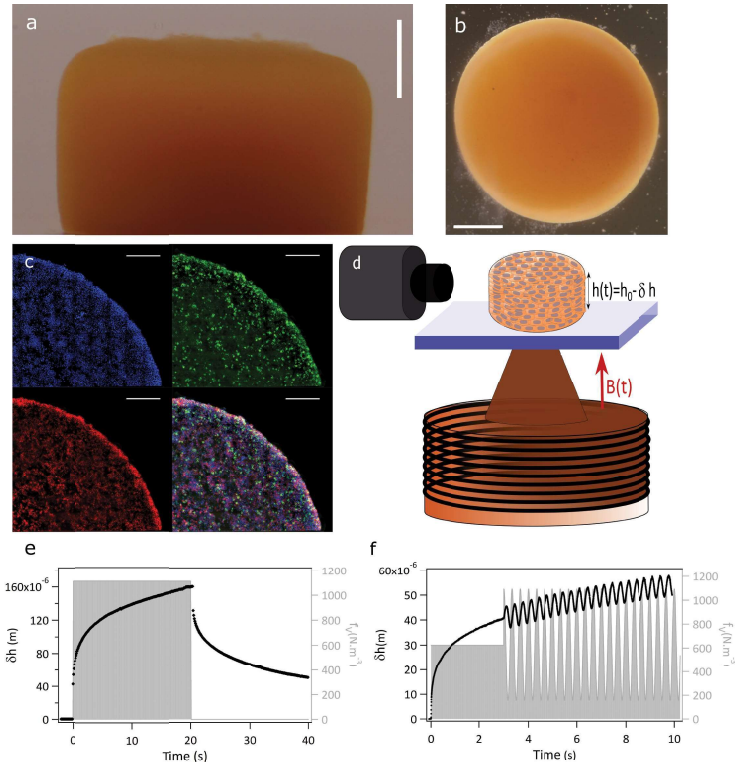

Figure 1: **A magnetic rheometer. a-b** Side and top view of a magnetic cylindrical multicellular aggregate of 900 μm radius (scale bar: 500 μm). **c** Quarter sections of a cylindrical aggregate stained with SiR-actin (red), E-cadherin antibody (green) and DAPI (blue) (Scale bars: 100 μm). **d** Schematics of the magnetic rheometer. An aggregate is seeded in a 37°C thermostated cuve filled with culture medium. The sides of the cuve are sealed with glass to allow fast camera imaging. An electromagnet composed of a central soft iron polar piece surrounded by a coil is positioned underneath to generate the magnetic field. The current supplied to the coil is delivered by an amplified signal generator. Imaging and magnetic signals are synchronized. **e-f** Magnetic forces per unit volume imposed to the whole aggregate (in gray) and measured deformation of the aggregate (in black) are superimposed. The versatility of the rheometer allows to use various imposed signals, here a step (**e**) and a sinusoid (**f**).

this end, we create a magnetic field B with a homogeneous gradient $\mathrm{d}B/\mathrm{d}z$ up to $30\,\mathrm{T.m^{-1}}$. The magnetic volume force $f_V = M_V(B)\,\mathrm{d}B/\mathrm{d}z$ is thus homogeneous, with a maximum value around $2.5\,\mathrm{kN.m^{-3}}$. The stress in the aggregate is linear with the altitude above the contact surface. In the following, the notation σ refers to the stress at the bottom of the cylinder: $\sigma = \sigma(z=0) = \int_{z=0}^{z=h} f_V(z)\,\mathrm{d}z$. The stress σ is around 2 Pa for the maximal force. Herein, aggregates are submitted to various force signals: steps, ramps, sinusoidal and broad spectrum signals with frequencies ranging from 0.125 to 10 Hz (Figure 1e-f).

This set-up (Figure 1d, see also Materials and Methods) is both very sensitive and highly versatile. Displacements are recorded by fast camera imaging and quantified by image analysis. They vary in response to the magnetic field stimulation chosen at will and imposed through the electromagnet. The threshold of detection in displacement is of the order of 0.5 μm. In the present use, the aggregate height h varies by at most 5%.

Here, measurements were carried out on F9 murine cells [36]. However, the magnetic rheometer use can be extended to other cell types, provided the cells are able to form multicellular structures and have a sufficient magnetic potency based on endocytosis.

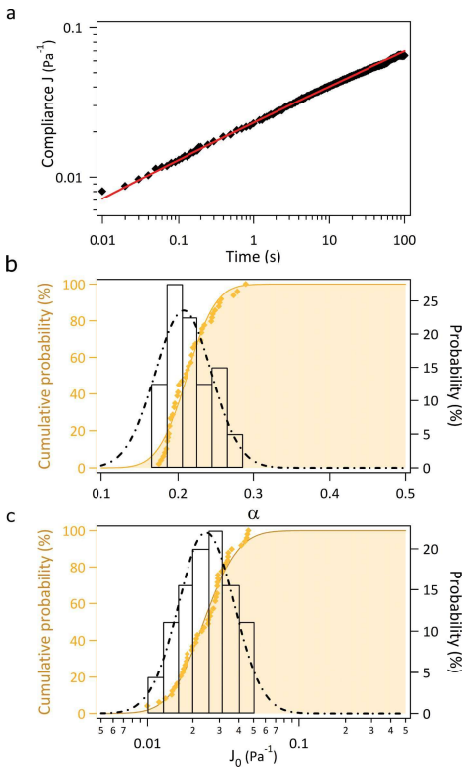

Figure 2: **Creep function and power-law rheology.** **s** Creep function of a multicellular aggregate submitted to a step of a $1.125\,\mathrm{kN.m^{-3}}$ force per unit volume, plotted in logarithmic scale. Experimental data (black crosses) are fitted with a power-law of time $J(t) = J_0\,(t/\tau)^{\alpha}$. **b-c** Cumulative distribution finction (orange diamond) and histogram (in black) of the exponent α (**b**) and of the compliance J_0 presented in logarithmic scale (**c**). The cumulative distribution functions of the exponent and of the logarithm of the compliance are fitted by an error function while their histograms are described by a normal distribution.

Power-law rheology of multicellular aggregates

Taking advantage of the versatility of the magnetic rheometer, we first use two classical signals: steps and sinusoids.

The creep function of the multicellular aggregates is first recorded by applying a force step of $1.125\,\mathrm{kN.m^{-3}}$, equivalent to a stress step of $\sigma \equiv h_0\, f_V = 1\,\mathrm{Pa}$, and by measuring the induced deformation (Supplemental Movie 1). From the height, $h(t) = h_0 - \delta h(t)$ (see Figure 1d), we compute the creep function

$$J(t) = \frac{\delta h(t)/h_0}{\sigma(t)} \tag{1}$$

Over four orders of magnitude (0.01 to 100 s), the creep function displays a power law behavior (Figure 2a), *i.e.*:

$$J(t) = J_0(t/\tau)^{\alpha}, \tag{2}$$

with exponent $\alpha = 0.22 \pm 0.02$ and compliance $J_0 = 0.021 \pm 0.005\,\mathrm{Pa^{-1}}$. The parameter τ is set to 1 s by convention.

Since measurements repeated on one single aggregate led to very small variations (below 5 %) of α and J_0, we repeated the same assay over 40 aggregates in order to sample the distribution of both the exponent α and the prefactor J_0. Figures 2b and c show their histograms and cumulative histograms (with J_0 in logarithmic scale). The latter are fitted by an error function, yielding the average values as well as the standard deviation. We find $\alpha = 0.212 \pm 0.005$ and

$J_0 = (2.36 \pm 0.1)\,10^{-2}\,\mathrm{Pa}^{-1}$. The corresponding normal and log-normal probability laws for α and J_0 respectively [37, 23] are plotted in Figures 2b and c. The dispersion between several measurements for the same aggregate is smaller than the variability between different aggregates, the magnetic rheometer thus is able to test aggregates discrepancies with high precision and these value reflects the inherent distribution of aggregates properties.

To confirm this power-law rheological response, we then apply a sinusoidal force signal with amplitude σ_{osc} at angular frequency ω to access the complex compression modulus $E^*(\omega)$. As nanoparticles are superparamagnetic, no pushing forces are possible thus to create a sinusoidal force, a pre-stress has first to be applied then a sinusoidal signal is superimposed(Figure 1f). Assuming a linear response, the measured displacement can be interpreted as the superposition of the creep function for the initial step and the response δh_{osc} to an oscillatory signal. As an example, Figure 3a presents the height $h(t)$ of the aggregate in response to a sinusoidal stress oscillating at 3 Hz. Figure 1f shows the corresponding displacement $\delta h(t)$. Fig 3b provides $\delta h_{\mathrm{osc}}(t)$ obtained by subtraction. The amplitude $\delta\bar{h}_{\mathrm{osc}}$ and phase φ of $\delta h_{\mathrm{osc}}(t)$ are used to compute the complex compression viscoelastic modulus $E^* = |E^*|\,e^{i\varphi}$ with amplitude $|E^*| = \sigma_{\mathrm{osc}}/(\delta\bar{h}_{\mathrm{osc}}/h_0)$. Figure 3c displays $|E^*|$ and φ as a function of frequency $\omega/(2\pi)$ ranging from 0.1 to 10 Hz. The phase shift is independent of frequency while the amplitude has a power-law dependence on frequency over two orders of magnitude.

As expected, this result is consistent with the creep response under constant applied stress. Indeed, in the linear regime, and for $J(t)$ obeying Eq. (2), the complex modulus reads [23]:

$$E^*(\omega) = \frac{(i\omega)^\alpha}{J_0\,\Gamma(1+\alpha)} \tag{3}$$

with Γ the Euler gamma function. Hence, in particular, $|E^*| \propto \omega^\alpha$ and $\varphi = \alpha\pi/2$. From the oscillatory experiment, we find $\alpha = 0.22 \pm 0.02$ and $J_0 = 0.016 \pm 0.005\mathrm{Pa}^{-1}$, both in agreement with the values extracted from the creep experiment. Agreement between these two rheometry protocols has been observed at single cell level [23] but is confirmed with aggregates on magnetic rheometer. It stands for the signature of an intrinsic property of multicellular mechanics.

Power-law rheology of single cells

A power-law behaviour has also been observed at the single-cell level in a similar frequency range for many different cell types [23]. In particular, α and $\log(J_0)$ are distributed according to a normal law [37, 23].

In order to compare the rheology of individual F9 cells to that of their multicellular assemblies, we now probe them in a uniaxial stretching rheometer [38]. Briefly, a single magnetically labelled F9 cell is stretched between two glass microplates, a rigid one and a flexible one whose stiffness was previously calibrated. The force applied to the cell together with its deformation, here in the $10 - 50\,\%$ range, are simultaneously measured at different frequencies up to 0.5 Hz.

The results are shown in Figure 3c. The stiffness found for single F9 cells was around 240 Pa, leading to $J_0 = (8 \pm 0.6)\,10^{-3}\,\mathrm{Pa}^{-1}$, while the exponent $\alpha = 0.27 \pm 0.03$ is consistent with that measured for F9 cellular aggregates.

Single cells appear slightly less elastic-like than the multicellular aggregates. The multicellular organization in aggregate thus softens the whole tissue material compared to its cellular components, it may be related with their ability to reorganize while being solicited probably for the same reason that a cotton ball is soft to the touch while each fiber has a high Young modulus. Besides, the elastic modulus of the individual cell is not the only component of the aggregate softness, and cell-cell movements also have a key role however in the range of applied frequencies they are not fully tested as they imply some slower processes when adhesion is important. The evolution of α and $|E|$ differs from the one obtained for aggregates at frequencies above 1 Hz (data not shown), the increase of the phase shift at these frequencies has to be related with

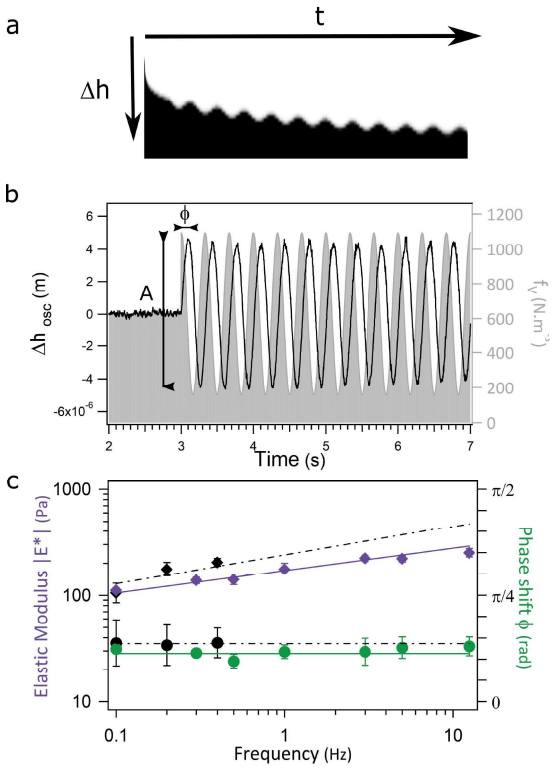

Figure 3: **Harmonic regime and comparison with single cell rheology.** **a** Kymograph of the upper interface of the aggregate submitted first to a force step of 834 $\mathrm{N.m^{-3}}$ and then to a force oscillation at a frequency 0.3Hz and with an amplitude 280 $\mathrm{N.m^{-3}}$ around the step force. **b** Extracted oscillatory contribution of the deformation (in black) superimposed with the harmonic part of the applied force. Phase shift φ and amplitude A are measured at each frequency. **c** Frequency dependence of the modulus (dark purple diamonds) and phase (dark green circles) of the complex viscoelastic modulus E^* of the aggregate. Experimental data are fitted by a power law for the modulus (purple solid line) and by a constant for the phase shift (green solid line) giving an exponent $\alpha = 0.22$ and a stiffness $E_0 = 160$ Pa. Results obtained for F9 single cells with nanoparticles using microplate experiments are included for comparison (black symbols).)

fluidization processes that are not tested with the magnetic rheometer as deformations rate are smaller with this set-up.

Contribution of individual cell mechanics and cell-cell contacts

The magnetic rheometer provides a high precision over the determination of J_0 and α thus appearing as an appealing tool to decipher for the role of cell-cell contacts and the contribution of cell constituents such as cytoskeleton on the rheological behavior of the entire aggregate. The creep functions of cell aggregates formed under various conditions are compared. First by varying the maturation time (from 16hours to 48hours) (Figure 4a-b) and by adding EGTA to inhibit the formation of intercellular adhesions (Figure 4c), we explore the role of cell-cell contacts. Interestingly, increasing the maturation time provides different cell organization, cells are more densely packed in the center of the aggregate, while at shorter time, cohesion occurs mainly at the periphery. Under the action of EGTA, a Ca-chelator decreasing the forces of intercellular adhesion while not acting on mechanical single cell features [24], the aggregates appeared looser, with cadherins less expressed. Surprisingly, the exponent α is not significantly modified by the

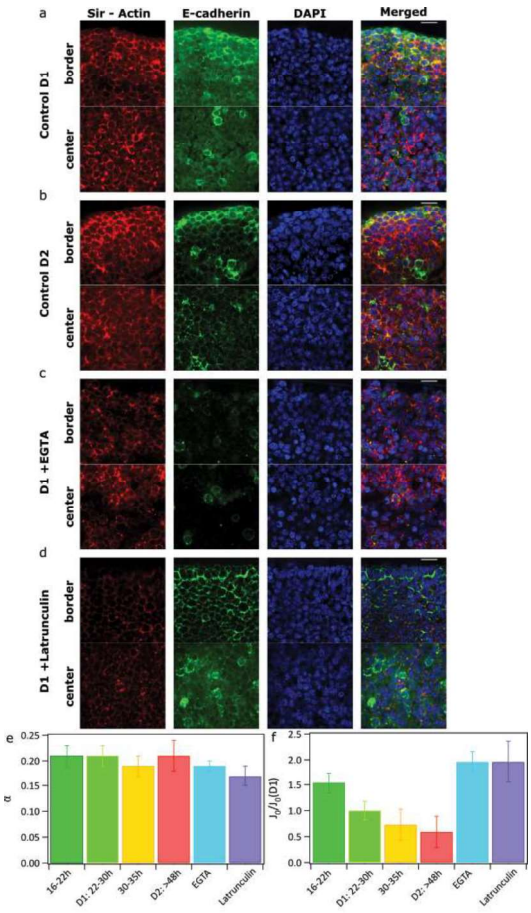

Figure 4: **Contribution of cell-cell contacts and cell cytoskeleton on aggregates rheology. a-d** Immunofluorescence images of aggregates both in the center and on the periphery Scale bars indicate 20 μm. Nuclei (DAPI labelling), cadherins (GFP E-cadherin antibody) and actin filaments (SiR-Actin) are labelled. **b-c** Impact of maturation time (from 16 to 48 hours), and disruptive agents (EGTA and latrunculin A) on the exponent α (**b**) and compliance (**c**), expressed in fold increase compared to the value at day 1 maturation time (24 hours), chosen as standard.

degree of cell-cell adhesion (Figure 4e), while the stiffness depends on the cell-cell contacts in the structure (Figure 4f): the less cohesive it is (short maturation time, and under the action of EGTA), the softer is the aggregate. That means that cell-cell adhesions are necessary to create a stiffer structure which is quite logical as it inhibits rapid local cell rearrangements. The comparison with the individual F9 cells has to be underlined: while individual cells are stiffer than the aggregate, the structure in aggregate provides more softness probably related with the cell-to-cell rearrangements but these ones are blocked by cell-cell junctions. Thus while the power-law behavior is kept at the aggregates levels, mechanisms involved seem different than the one at the cellular scale.

The magnetic rheometer provides a high precision determination of both J_0 and α. It thus appears to be an appealing tool to decipher the role of cell-cell contacts and the contribution of cell constituents such as cytoskeleton in rheological behavior. To address this, the creep functions of cell aggregates formed under various conditions are compared. We first investigate the role of cell-cell contacts in aggregate mechanics by varying the aggregate maturation time (48 h instead of 24 h as before - Figure 4a-b-), or by adding EGTA to inhibit the formation of intercellular adhesions (Figure 4c). Interestingly, increasing the maturation time provides also different cell organization, with cells more densely packed in the center of the aggregate, while at shorter time,

cohesion occurs mainly at the periphery. Under the action of EGTA, a Ca-chelator decreasing the forces of intercellular adhesion while not acting on mechanical single cell features [24], the aggregates appeared looser, with cadherins less expressed. Surprisingly, the exponent α is not significantly modified by the degree of cell-cell adhesion (Figure 4e), while the stiffness depends on the cell-cell contacts in the structure (Figure 4f): the less cohesive it is (short maturation time, and under the action of EGTA), the softer is the aggregate. That means that cell-cell adhesions are necessary to create a stiffer structure which is quite logical as it inhibits rapid local cell rearrangements. The comparison with the individual F9 cells has to be underlined: while individual cells are stiffer than the aggregate, the structure in aggregate provides more softness probably related with the cell-to-cell rearrangements but these ones are blocked by cell-cell junctions. Thus while the power-law behavior is kept at the aggregates levels, mechanisms involved seem different than the one at the cellular scale.

We next investigated the role of the actin cell cytoskeleton, by submitting the aggregates to latrunculin A (1 μM), an inhibitor of actin polymerization. On single cells, it was reported that latrunculin A softens the cells by 2 to 5-fold, depending on cell type and inhibitor concentration [39, 25, 24]. On the aggregates, the dense cortical actin meshwork visible on normal cells is disrupted and small patches appear (Figure 4d). Here again, no significant changes were found on the α exponent (Figure 4e). By contrast, latrunculin-treated aggregates exhibit a two-fold higher compliance (Figure 4f). Interestingly, it reproduces the behavior of single cells. Changes of individual cell mechanics thus have a straight impact on aggregate stiffness.

Non-linear behavior of cell aggregates

Importantly, the regime of small deformations studied so far does not preclude the presence of non-linearities within this range. Knowing the power-law compliance given by Eq. (2), we expect that the response to a force ramp $\sigma(t) = \dot{\sigma}_0\, t$ should be:

$$\frac{\delta h(t)}{h_0} = \int_0^t J(t')\dot{\sigma}_0\, \mathrm{d}t' = \frac{1}{1+\alpha}\, J_0\, \dot{\sigma}_0 \tau \left(\frac{t}{\tau}\right)^{1+\alpha} \propto t^{1+\alpha} \tag{4}$$

it is described by a time-dependent power law with exponent $1 + \alpha$.

We further test the linearity of the multicellular aggregate response by probing them with a force ramp (Figure 5a). For volume forces below $1.2\,\mathrm{kN.m^{-3}}$, we observe no apparent deviation from linearity. Above, the observed deformation is smaller than expected from the linear regime. Such stress stiffening is confirmed by recording the creep responses to different force steps varying from 556 to $2225\,\mathrm{N.m^{-3}}$. Each aggregate was submitted to increasing force steps (Figure 5c), with 30 min pause in between to let the structure returns to its undisturbed state (tested with a series of identical force steps, leading to the same response). Whatever the force applied, the creep compliance still follows a power law. Yet, prefactor J_0 is decreasing with force (Figure 5e), confirming stress stiffening while the power law exponent is almost invariant. Stress stiffening was previously reported for complex polymeric materials as well as living cells [40, 41, 42]. For polymers, alignment over the direction of the applied force leads to an increased resistance, which contributes to the stiffening of the network. This contribution is implied at the cellular scale. Herein, at the tissue scale, cell-cell arrangements might also play a role as stress can disrupt a dhesion and facilitate in turn cell-to-cell movements.

All-in-one rheology inference

The classical use of step force signal (confirmed by ramp and oscillatory signals) has helped determine the rheological features of these multicellular aggregates, including the non-linearity of

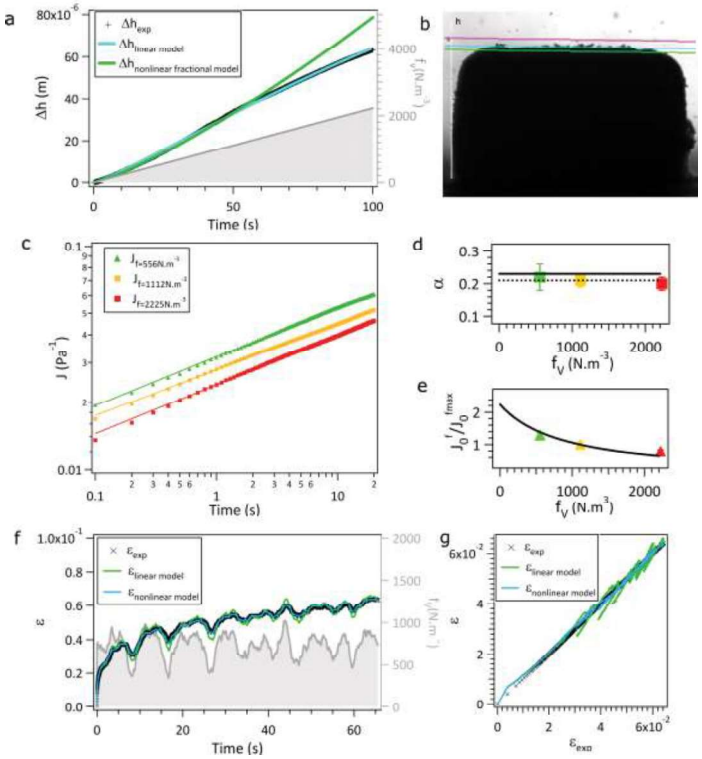

Figure 5: **Non linearity of the rheological parameters.** **a** Displacement (black crosses) of the upper surface of the aggregate submitted to a ramp force increasing from 0 to 2225 $\mathrm{N.m^{-3}}$ in 100s (grey signal). The expected linear answer is superimposed in green while the nonlinear fractional model prediction is in blue. **b** Image of the whole aggregate and superposition of the levels obtained at the end of the ramp assuming the nonlinear fractional model or the linear one. The pink line marked the initial upper surface. (scale bar: 500 mm). **c** Creep functions obtained for three different forces per unit volume ($f_V = 556, 1112, 2225\,\mathrm{N.m^{-3}}$). **d-e** Variation of the exponent α and the compliance J_0 fitted from the three creep functions with the applied force per unit volume. These results are compared with the nonlinear fractional model prediction in black. The mean value of α is also included as a dotted line. **f** Strain response of the aggregate (black crosses) to a broad spectrum signal (indicated in grey). The linear and the nonlinear fractional model fits are superimposed in green and blue respectively. **g** Comparison of the linear and nonlinear fractional models strains with the experimental data.

the power-law response. In addition, we also stimulated the same system with a broad spectrum signal in order to confirm the above results through an independent measurement. The broad spectrum method, suggested theoretically by some of us [in preparation], consists in applying a multi-frequency input signal (see Materials and Methods for details) and to use both the input and output signals to infer the rheological differential equation that relates them. These signals and their time derivatives form a trajectory in the system phase space. Using a broad spectrum signal rather than a sinusoidal one allows us to explore the phase space efficiently and to thus sketch the manifold that corresponds to the constitutive equation we wish to determine.

This all-in-one rheology inference method requires only one experiment, since various, possibly non-linear, rheological models can be tested and compared quantitatively once the experiment is already completed (see Materials and Methods for details). The magnetic rheometer offers a unique possibility to test this method as its electromagnetic stimulation allows any time and frequency dependent signal to be applied.

Limiting our investigations to simple viscoelastic models with at most four parameters, a nonlinear fractional model is identified as the best model using the Akaike Information Criterion (AIC, Figure 5f and Supplementary Figure S4). This best fit corresponded to a power law creep function with a force-dependent compliance $J(t) = \frac{J_0}{1+a_1\sigma}\left(\frac{t}{\tau}\right)^{\alpha}$, where τ is an arbitrary time scale (which we take as equal to 1 s). The best parameters obtained to fit the broad spectrum data gave an exponent $\alpha = 0.23$, remarkably close to the one obtained using the step function forcing (Figure 5d). Moreover, the force dependence of the inferred prefactor is in good agreement with the one established using step forcing (Figure 5e). Finally, revisiting the deformations induced by a ramp magnetic force signal, Figure 5a shows that the non-linear model yields a prediction in good agreement with the data.

Taken together, the analysis of all collected data confirms that the rheology of multicellular aggregates is best described by a fractional rheological law with a force-dependent stiffening.

Conclusion

This study describes a unique tool to explore model tissue rheology: the magnetic rheometer. Magnetically formed cylindrical aggregates are deformed by remote magnetic forces with various stimulation patterns from force step to random signals. It brings out striking features of the mechanical properties of multicellular arrangements with a high precision not suffering from cell to cell variability of single cell experiment. First the compliance of such structure presents a power law behavior whatever the stimulation type: the creep function of the aggregate is a time dependent power law while the viscoelastic complex modulus is a frequency dependent power law with the same exponent α and equivalent stiffness. Such power-law behavior of aggregates is the hallmark of a continuous distribution of relaxation times, already identified at the individual cell level. Interestingly these multiple relaxation processes represent an intrinsic feature of tissues at various spatial scales for the multicellular organization to the cytoskeleton network. The value of α around 0.2 puts model tissues in the same range as individual cells in term of dynamics however the global structure tends to increase the stiffness. A power law exponent of 0 indicates a purely elastic solid while an exponent of 1 is representative of a purely viscous fluid. The obtained exponent accounts for intermediate viscoelastic behavior. If intracellular cytoskeleton has a role in the aggregates stiffness, the multicellular arrangements are also pointed out: compliance depends on the strength of the cell-cell adhesions.

Besides, while the power-law behavior is conserved whatever the forces applied, stress stiffening is also observed, reflecting more solid-like aggregates when submitted to increasing forces. Finally, a nonlinear fractional model is proposed and is able to describe, within a single experiment, the creep function at any applied forces. Frequency dependence extracted from random signals coupled with inference model thus provides a powerful approach to decipher in a single set of experiment the best rheological model to describe complex materials, such as a model tissue here.

The magnetic rheometer could become a key actor for the mechanical exploration of tissues thanks to its versatility in applied signals (from step to random force signal) as well as biological samples (different cell types, easy inhibitors testing).

References

[1] Valerie Marie Weaver. Cell and tissue mechanics: the new cell biology frontier. *Molecular Biology of the Cell*, 28(14):1815–1818, jul 2017.

[2] Kaoru Sugimura, Pierre-François Lenne, and François Graner. Measuring forces and stresses in situ in living tissues. *Development*, 143(2):186–196, Jan 2016.

[3] Otger Campàs. A toolbox to explore the mechanics of living embryonic tissues. *Seminars in Cell & Developmental Biology*, 55:119–130, Jul 2016.

[4] Tomita Vasilica Stirbat, Sham Tlili, Thibault Houver, Jean-Paul Rieu, Catherine Barentin, and Hélène Delanoë-Ayari. Multicellular aggregates: a model system for tissue rheology. *Eur Phys J E Soft Matter*, 36(8):9898, Aug 2013.

[5] Vicard Du, Nathalie Luciani, Sophie Richard, Gaëtan Mary, Cyprien Gay, François Mazuel, Myriam Reffay, Philippe Menasché, Onnik Agbulut, and Claire Wilhelm. A 3d magnetic tissue stretcher for remote mechanical control of embryonic stem cell differentiation. *Nature Communications*, 8(1), sep 2017.

[6] Ruei-Zhen Lin and Hwan-You Chang. Recent advances in three-dimensional multicellular spheroid culture for biomedical research. *Biotechnology Journal*, 3(9-10):1172–1184, oct 2008.

[7] Sritama Nath and Gayathri R. Devi. Three-dimensional culture systems in cancer research: Focus on tumor spheroid model. *Pharmacology and Therapeutics*, 163:94–108, jul 2016.

[8] X. Cui, Y. Hartanto, and H. Zhang. Advances in multicellular spheroids formation. *Journal of The Royal Society Interface*, 14(127):20160877, feb 2017.

[9] Adam A. Lucio, Alessandro Mongera, Elijah Shelton, Renwei Chen, Adele M. Doyle, and Otger Campàs. Spatiotemporal variation of endogenous cell-generated stresses within 3d multicellular spheroids. *Scientific Reports*, 7(1), sep 2017.

[10] Francesco Pampaloni, Emmanuel G Reynaud, and Ernst H K Stelzer. The third dimension bridges the gap between cell culture and live tissue. *Nat Rev Mol Cell Biol*, 8(10):839–845, Oct 2007.

[11] David Gonzalez-Rodriguez, Karine Guevorkian, Stéphane Douezan, and Françoise Brochard-Wyart. Soft matter models of developing tissues and tumors. *Science*, 338(6109):910–917, Nov 2012.

[12] S. F Gabby Krens and Carl-Philipp Heisenberg. Cell sorting in development. *Curr Top Dev Biol*, 95:189–213, 2011.

[13] H. M. Phillips and M. S. Steinberg. Equilibrium measurements of embryonic chick cell adhesiveness, I. shape equilibrium in centrifugal fields. *Proceedings of the National Academy of Sciences*, 64(1):121–127, sep 1969.

[14] Ali Kalantarian, Hiromasa Ninomiya, Sameh M I Saad, Robert David, Rudolf Winklbauer, and A. Wilhelm Neumann. Axisymmetric drop shape analysis for estimating the surface tension of cell aggregates by centrifugation. *Biophys J*, 96(4):1606–1616, Feb 2009.

[15] G. Forgacs, R.A. Foty, Y. Shafrir, and M.S. Steinberg. Viscoelastic properties of living embryonic tissues: a quantitative study. *Biophys. J.*, 74:2227–2234, 1998.

[16] Karine Guevorkian, Marie-Josée Colbert, Mélanie Durth, Sylvie Dufour, and Françoise Brochard-Wyart. Aspiration of biological viscoelastic drops. *Phys Rev Lett*, 104(21):218101, May 2010.

[17] Tomita Vasilica Stirbat, Abbas Mgharbel, Selena Bodennec, Karine Ferri, Hichem C Mertani, Jean-Paul Rieu, and Hélène Delanoë-Ayari. Fine tuning of tissues viscosity and surface tension through contractility suggests a new role for ±-catenin. *PLoS One*, 8(2):e52554, 2013.

[18] Francois Mazuel, Myriam Reffay, Vicard Du, Jean-Claude Bacri, Jean-Paul Rieu, and Claire Wilhelm. Magnetic flattening of stem-cell spheroids indicates a size-dependent elastocapillary transition. *Physical Review Letters*, 114(9), Mar 2015.

[19] Miao Yu, Aria Mahtabfar, Paul Beelen, Yasir Demiryurek, David I. Shreiber, Jeffrey D. Zahn, Ramsey Foty, Liping Liu, and Hao Lin. Coherent timescales and mechanical structure of multi-cellular aggregates. *Biophysical Journal*, 114(3):652a, 2018.

[20] Jonas Ranft, Markus Basan, Jens Elgeti, Jean-François Joanny, Jacques Prost, and Frank Jülicher. Fluidization of tissues by cell division and apoptosis. *Proc Natl Acad Sci U S A*, 107:20863–20868, Nov 2010.

[21] P-H Wu, D Raz-Ben Aroush, A Asnacios, W-C Chen, ME Dokukin, BL Doss, P Durand-Smet, A Ekpenyong, J Guck, NV Guz, PA Janmey, JSH Lee, NM Moore, A Ott, Y-C Poh, R Ros, M Sander, I Sokolov, JR Staunton, N Wang, G Whyte, and Wirtz. G. A comparison of methods to assess cell mechanical properties. *Nat Meth*, 15:491–498, 2018.

[22] Philip Kollmannsberger and Ben Fabry. Linear and nonlinear rheology of living cells. *Annu Rev Mat Res*, 41:75–97, 2011.

[23] Martial Balland, Nicolas Desprat, Delphine Icard, Sophie Féréol, Atef Asnacios, Julien Browaeys, Sylvie Hénon, and François Gallet. Power laws in microrheology experiments on living cells: Comparative analysis and modeling. *Phys. Rev. E*, 74:021911, 2006.

[24] Xavier Trepat, Linhong Deng, Steven S An, Daniel Navajas, Daniel J Tschumperlin, William T Gerthoffer, James P Butler, and Jeffrey J Fredberg. Universal physical responses to stretch in the living cell. *Nature*, 447(7144):592–595, May 2007.

[25] Ben Fabry, Geoffrey N. Maksym, James P. Butler, Michael Glogauer, Daniel Navajas, Nathan A. Taback, Emil J. Millet, and Jeffrey J. Fredberg. Time scale and other invariants of integrative mechanical behavior in living cells. *Phys. Rev. E*, 68:041914, 2003.

[26] Viola Vogel and Michael Sheetz. Local force and geometry sensing regulate cell functions. *Nat Rev Mol Cell Biol*, 7(4):265–275, Apr 2006.

[27] Benjamin D Matthews, Darryl R Overby, Robert Mannix, and Donald E Ingber. Cellular adaptation to mechanical stress: role of integrins, Rho, cytoskeletal tension and mechanosensitive ion channels. *J Cell Sci*, 119(Pt 3):508–518, Feb 2006.

[28] Lars Wolff, Pablo Fernández, and Klaus Kroy. Resolving the stiffening-softening paradox in cell mechanics. *PLoS One*, 7(7):e40063, 2012.

[29] N Khalilgharibi, J Fouchard, N Asadipour, R Barrientos, M Duda, A Bonfanti, A Yonis, A Harris, P Mosaffa, Y Fujita, A Kabla, Y Mao, B Baum, JJ Munoz, M Miodownik, and G Charras. Stress relaxation in epithelial monolayers is controlled by the actomyosin cortex. *Nat Phys*, 15:839–847, 2019.

[30] S. Nicolle, P. Vezin, and J.-F. Palierne. A strain-hardening bi-power law for the nonlinear behaviour of biological soft tissues. *Journal of Biomechanics*, 43(5):927–932, mar 2010.

[31] Marion Geerligs, Gerrit W M Peters, Paul A J Ackermans, Cees W J Oomens, and Frank P T Baaijens. Linear viscoelastic behavior of subcutaneous adipose tissue. *Biorheology*, 45(6):677–688, 2008.

[32] G Charras and AS Yap. Tensile forces and mechanotransduction at cell-cell junctions. *Curr Biol*, 28:445–457, 2018.

[33] K Bambardekar, R ClÃ©ment, O Blanc, C Chardes, and Lenne PF. Direct laser manipulation reveals the mechanics of cell contacts in vivo. *Proc Natl Acad Sci*, 112:1416–1421, 2015.

[34] C Wilhelm and F Gazeau. Universal cell labelling with anionic magnetic nanoparticles. *Biomaterials*, 29:3161–3174, 2008.

[35] D. Fayol, G Frasca, C LeVisage, F Gazeau, N Luciani, and C Wilhelm. Use of magnetic forces to promote stem cell aggregation during differentiation, and cartilage tissue modeling. *Adv Mater*, 25:2611–2616, 2013.

[36] A Nagafuchi, Y Shirayoshi, K Okazaki, K Yasuda, and M Takeichi. Transformation of cell adhesion properties by exogenously introduced e-cadherin cdna. *Nature*, 329:341–343, 1987.

[37] Nicolas Desprat, Alain Richert, Jacqueline Simeon, and Atef Asnacios. Creep function of a single living cell. *Biophysical journal*, 88(3):2224–2233, 2005.

[38] O. Thoumine and A. Ott. Time scale dependent viscoelastic and contractile regimes in fibroblasts probed by microplate manipulation. *J Cell Sci*, 110:2109–2116, Sep 1997.

[39] A. Berquand, A. Holloschi, M. Trendelenburg, and P. Kioschis. Analysis of cytoskeleton-destabilizing agents by optimized optical navigation and AFM force measurements. *Microscopy Today*, 18(02):34, mar 2010.

[40] Pablo Fernández and Albrecht Ott. Single cell mechanics: stress stiffening and kinematic hardening. *Phys Rev Lett*, 100(23):238102, Jun 2008.

[41] Karen E Kasza, Amy C Rowat, Jiayu Liu, Thomas E Angelini, Clifford P Brangwynne, Gijsje H Koenderink, and David A Weitz. The cell as a material. *Curr. Opinion Cell Biol.*, 19:101–107, 2007.

[42] Daniel A. Fletcher and R. Dyche Mullins. Cell mechanics and the cytoskeleton. *Nature*, 463:485–492, 2010.

[43] Ana Espinosa, Jelena Kolosnjaj-Tabi, Ali Abou-Hassan, Anouchka Plan Sangnier, Alberto Curcio, Amanda K. A. Silva, Riccardo Di Corato, Sophie Neveu, Teresa Pellegrino, Luis M. Liz-Marzán, and Claire Wilhelm. Magnetic (hyper)thermia or photothermia? progressive comparison of iron oxide and gold nanoparticles heating in water, in cells, and in vivo. *Advanced Functional Materials*, 28(37):1803660, jul 2018.

[44] Francesco Mainardi. *Fractional calculus and waves in linear viscoelasticity: An introduction to mathematical models*. Imperial College Press, 2010.

[45] Hirotugu Akaike. A new look at the statistical model identification. *IEEE Transactions on Automatic Control*, 19(6):716–723, 1974.

[46] Kenneth P Burnham and David R Anderson. *Model selection and multimodel inference: a practical information-theoretic approach*. Springer, 2003.

Materials and Methods

Nanoparticles and reagents

The nanoparticles used to magnetically label the F9 cells are citrated iron oxide maghemite (Fe_2O_3) magnetic nanoparticles with a characteristic diameter of 9 nm (polydispersity 28 %). They are superparamagnetic nanoparticles. The magnetization curve is presented in Fig S1.

To inhibit actin filament formation, Latrunculin A (1 μM) purchased from Sigma is used during aggregates formation and stimulation. EGTA (0.4 mM) is added at the same stage to act as a calcium chelator and decrease cell-cell cadherin mediated interacted as well as individual calcium influx.

Immunofluorescence was performed using SiR-actin to stain actin filaments and DAPI to label nuclei. E-cadherin antibody (ECCD-2 from Thermofisher) coupled with a secondary anti-rat GFP antibody is used to enhance this cell-cell adhesion molecule.

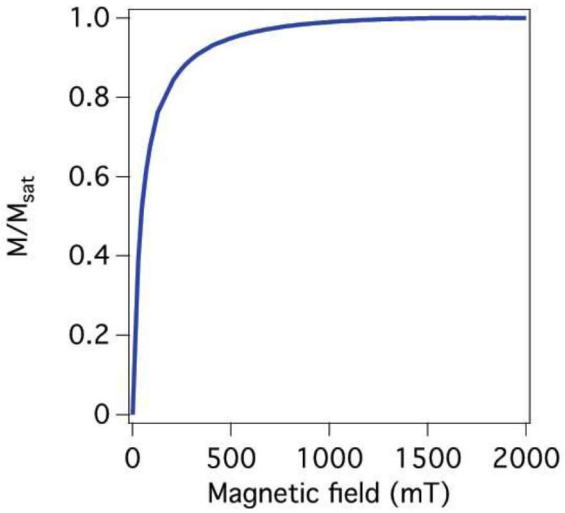

Figure S1: **Magnetization curve of the iron oxide nanoparticles.** The magnetization normalized by the saturation magnetization is plotted as a function of the external magnetic field.

Magnetic cell labeling and cylinder aggregates magnetic formation

F9 murine cells are grown in DMEM supplemented with 5 % fetal bovine serum (FBS) and 1 % antibiotics (penicillin/streptomycin) at 37°C and 5 % CO_2. When cells are at confluence, nanoparticles solution ([Fe] = 5 mM in RPMI) is added for 2 h. Nanoparticles are internalized in cells through endocytosis pathways and are finally localized within intracellular vesicles identified as endosomes [43]. After incubation, cells were washed with fresh RPMI and detached with trypsin to be seeded in 2 % agarose gel cylindrical molds (diameter 2 mm, height 1.5 mm) obtained by forming a network of small magnetic cylinders within an agarose mold. Indeed by removing the magnets below, and taking off the magnetic cylinders within the gel, we achieved to have cylindrical wells to seed cells within. The seeding of cells (1 million) in the wells was then magnetically driven by the magnets below the dish (Fig 1A-C). The resulting cylindrical aggregates were extracted from the well after 16 h (overnight maturation) and resulted in a 2 mm diameter and 0.8 mm high for 106 cells) cylindrical tissue showing important cell-cell adhesions.

At this stage, inhibitors may be added in the solution. One million magnetically labeled cells were deposited in each mold (Figure S2). Cell-cell contacts developed overnight to produce a cohesive cylindrical tissue that can be removed from the mold. The resulting aggregates

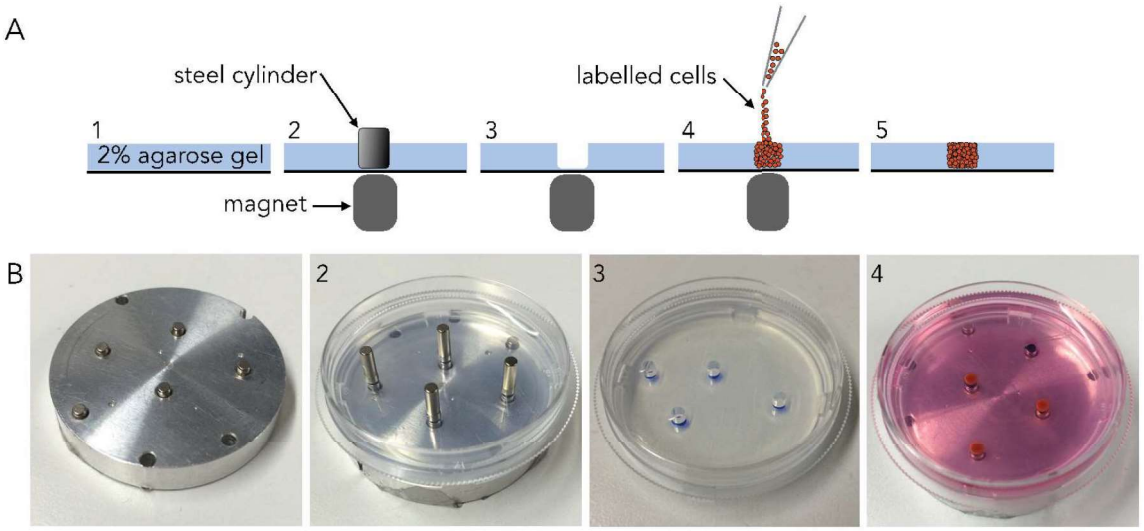

Figure S2: **Magnetic molding of cylindrical multicellular spheroids. a** Schematic representation and **b** pictures of the different steps of the molding protocol. (1) A layer of 2% agarose solution in PBS is poured into a culture dish. (2) A cylindrical permanent magnet is placed under the dish as the agarose is still liquid to attract a calibrated steel cylinder (2 mm in diameter). (3) The agarose solidifies as it cools down and the cylinder is removed to form a cylindrical mold. (4) The dish is filled with DMEM medium without FBS and magnetically labeled cells are deposited in a small volume in the well. The magnet attracts and compacts the cells for 30 seconds before being removed. (5) The dish is incubated at 37°C and 5% CO_2 overnight to allow tissue formation.

(Figure 1a-b) have a reproducible size (2 mm in diameter and around 1 mm in height) and a homogeneous bulk saturation magnetization ($M_V^{\text{sat}} = 103 \pm 16 \text{A.m}^{-1}$) measured with a vibrating sample magnetometer (Quantum Design, Versalab).

Magnetic field applicator

The magnetic field used to deform the magnetized aggregate was generated with an electromagnet composed of a custom-made water-cooled coil (6 Ω, 14 mH) wrapped around a soft iron polar piece (diameter 55 mm, height 85 mm) allowing the passage of a current up to 10A. The shape of the polar piece was optimized (reduction of the diameter from 55 mm to 5 mm of the upper part) to maximize the magnetic field gradient (30T.m^{-1} for the maximum 120 mT magnetic field) and its homogeneity in the aggregate volume. The top of the electromagnet was 3 mm below the center of the aggregate. The electromagnet tension was controlled with a TGA 1242 signal generator (Aim&TTi) and amplifier (Kebco BOP). The magnetic field generated at the center of the aggregate linearly depends on the applied tension (Figure S3a) and the magnetic field gradient was almost constant (less than 10 % variation) whatever the applied tension (Figure S3b) over a size exceeding one millimeter ensuring a homogenous force on cells. Indeed as every cell in the aggregate has a field dependent magnetization, the application of a homogenous magnetic field gradient $\mathrm{d}B/\mathrm{d}z$ results in a magnetic force that reads $f_V = M_V(B)\,\mathrm{d}B/\mathrm{d}z$. In this range of magnetic field(0 to 120 mT), the magnetization curve is not linear thus the effective magnetic force per unit volume derives from:

$$f_V = \left(\frac{M_V}{M_{\text{sat}}}\right)[B(V(t))]\; M_V^{\text{sat}}\,\frac{\mathrm{d}B}{\mathrm{d}z}\,[V(t)] \tag{5}$$

The set up was calibrated and characterized in order to determine the bulk flattening magnetic

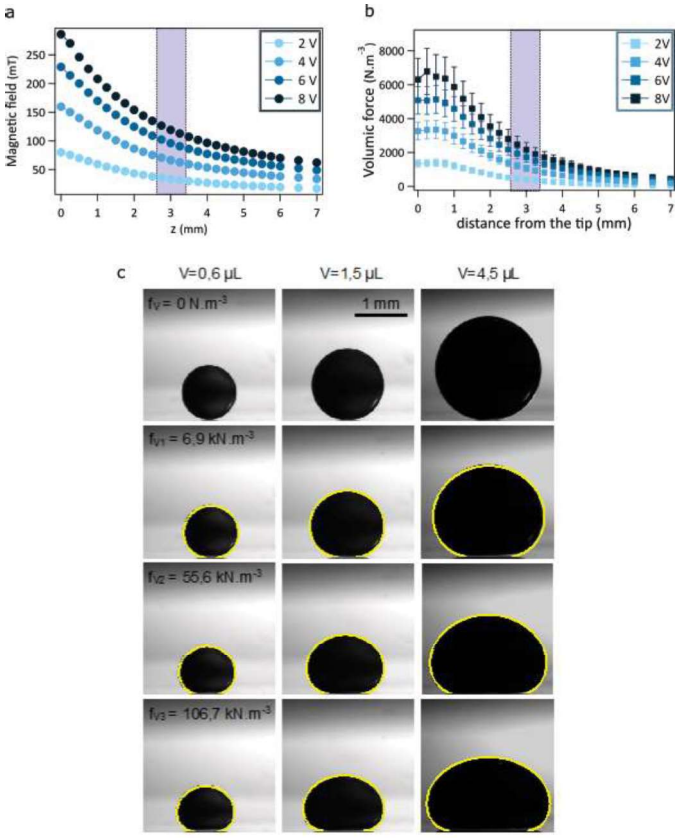

Figure S3: **Calibration of the magnetic field generator. a** Magnetic field created by the electromagnet as a function of the distance to the top of the polar piece for different tensions applied to the amplifier. The center of the aggregate is 3 mm above the electromagnet so the range of the distance of the aggregate is drawn in violet. **b** volumic force extracted from the measures of the magnetic field and the one of the magnetization curve of the aggregate. **c** Ferrofluid drops ([Fe]=1.25 M) of three different volumes ($0.6, 1.5, 4.5\,\mu$L) deposited on a superhydrophobic coated glass surface, in a silicon oil bath, are submitted to increasing magnetic flattening forces (under normal gravity, $f_{V1} = 6.9\,\mathrm{kN.m^{-3}}$, $f_{V2} = 55.6\,\mathrm{kN.m^{-3}}$, $f_{V3} = 106.7\,\mathrm{kN.m^{-3}}$) corresponding to increasing tensions applied to the amplifier (respectively:$0, 1.2, 4.8, 8$ V). Droplets experimental equilibrium profiles are fitted with theoretical capillary profile (yellow), obtained by integrating numerically Laplace equation for capillarity in non-wetting condition (using Matlab's function ode45).

force generated as a function of the applied tension $V(t)$ using the set-up as a tensiometer [18]. Ferrofluid drops (aqueous solution of the nanoparticles used for cell labelling) of various size were deposited on a superhydrophobic surface in a silicon bath were flattened. Fitting each experimental profile with the Laplace equation for capillarity in non-wetting conditions, provided the surface tension and was validated by comparison with classic sessile drop experiment (Fig S3C).

Signal generation and synchronization

The tension signal is transferred to the generator using the Waveform Manager Plus software. To synchronize the deformation signal with the force generation, a LED, powered by a pulse generator that is synchronized with the signal generator (see Figure 1b), was used to overexpose a single image of the movie corresponding to the beginning of the deformation sequence.

Image analysis

Deformations were analyzed using the image correlation based tracking algorithm on ImageJ Tracker_install to measure the displacement of the aggregate upper interface as a function of time ($\Delta h(t)$ in Figure 1E-F). Vibrations of the setup (mainly due to the water circulation use to thermalize the container) were compensated by tracking a fixed point on the container bottom (adsorbed dust for instance) and subtracting its motion from the interface displacement. The precision on the interface displacement is $\pm 0.5\,\mu$m.

Broad spectrum input signal

The stress signal we applied for the all-in-one rheology inference protocol is a superposition of a number of sinusoidal signals:

$$\sigma(t) = \sigma_0 \sum_{i=1}^{n} \rho_i \cos(2\pi f_i t + \phi_i), \tag{6}$$

where σ_0 is used to tune the amplitude. The frequency range is chosen as 0.1-10 Hz. The $n = 32$ frequencies f_i are (logarithmically) equally spaced within this range. The phases ϕ_i are chosen randomly within $[0, 2\pi]$. In order to damp high frequencies, the magnitude of the real prefactor ρ_i is chosen to decrease with the frequency. More precisely, ρ_i^2 is drawn uniformly within $[0, f_{\min}^2/f_i^2]$.

Parametric inference method

A rheological model is defined by a p-dimensional parameter vector $\vec{\theta}$ and by a differential equation of the form $\epsilon(t) = \mathcal{R}(\{\sigma(t')\}_{t'}, \vec{\theta})$, where $\mathcal{R}$ is an integro-differential operator acting on the function $\sigma(t)$. In order to assess to what degree the rheologial model, defined by $\mathcal{R}$, is suitable to describe the experimental data $\{\epsilon_{\exp}(t)\}_t$, we assume that the experimental noise $\phi(t)$ is white and Gaussian (amplitude s) and contributes additively within the measured deformation value:

$$\epsilon_{\exp}(t) = \mathcal{R}(\{\sigma(t')\}_{t'}, \vec{\theta}) + \phi(t)\,. \tag{7}$$

We then determine the values of the parameters $\vec{\theta}$ and s, *i.e.*, $p+1$ real numbers, that maximize the likelihood function

$$L\left(\{\epsilon_{\exp}(t)\}_t \,\middle|\, \{\sigma(t)\}_t, \vec{\theta}\right) = \frac{1}{(2\pi s^2)^{N_t/2}} \exp\left(-\sum_{t=1}^{N_t} \frac{\|\epsilon_{\exp}(t) - \mathcal{R}(\{\sigma(t')\}_{t'}, \vec{\theta})\|^2}{2s^2}\right) \tag{8}$$

for N_t time points. Indeed, the likelihood L indicates how likely it is to observe the actual experimental data $\{\epsilon_{\exp}(t)\}$, given the rheological model (encoded in $\mathcal{R}$), the parameter set $(\vec{\theta}, s)$ and the imposed stress history $\{\sigma(t)\}$. The larger the likelihood, the better the model and its parameters fit the experimental data.

A number of rheological models (see Table 1, first two columns) were tested against the experimental data by maximizing the likelihood. The optimized parameter values for each model are listed (see third column). For fractional models, we used the Caputo version of the fractional derivative [44], defined as:

$$\frac{\mathrm{d}^\alpha \epsilon}{\mathrm{d}t^\alpha} = \frac{1}{\Gamma(1-\alpha)} \int_0^t \frac{\dot{\epsilon}(t')}{(t-t')^\alpha} \mathrm{d}t' \tag{9}$$

Model	Equation	Optimal parameters	p	AIC
Viscous	$\sigma = \eta \frac{\mathrm{d}\epsilon}{\mathrm{d}t}$	$\eta = 518\,\mathrm{Pa.s}$	1	-34 361
Elastic	$\sigma = E\,\epsilon$	$E = 13.5\,\mathrm{Pa}$	1	-39 477
Maxwell	$\frac{\eta}{E}\frac{\mathrm{d}\sigma}{dt} + \sigma = \eta \frac{\mathrm{d}\epsilon}{\mathrm{d}t}$	$E = 20.8\,\mathrm{Pa}$, $\eta = 1222\,\mathrm{Pa.s}$	2	-49 297
Kelvin	$\sigma = \eta \frac{\mathrm{d}\epsilon}{\mathrm{d}t} + E\,\epsilon$	$E = 11.7\,\mathrm{Pa}$, $\eta = 88.8\,\mathrm{Pa.s}$	2	-50 564
Fractional	$\sigma = E\tau^{\alpha}\frac{\mathrm{d}^{\alpha}\epsilon}{\mathrm{d}t^{\alpha}}$	$\alpha = 0.23$, $E = 30.7\mathrm{Pa}$	2	-61 189
N.L. Fract.	$\sigma = (a_0 + a_1\sigma)\,\tau^{\alpha}\frac{\mathrm{d}^{\alpha}\epsilon}{\mathrm{d}t^{\alpha}}$	$\alpha = 0.23$, $a_0 = 16\,\mathrm{Pa}$, $a_1 = 23$	3	-79 664
Burgers	$\frac{\mathrm{d}^2\sigma}{\mathrm{d}t^2} + \left(\frac{E+E_0}{\eta_0} + \frac{E}{\eta}\right)\frac{\mathrm{d}\sigma}{\mathrm{d}t} + \frac{EE_0}{\eta\eta_0}\sigma = E\frac{\mathrm{d}^2\epsilon}{\mathrm{d}t^2} + \frac{EE_0}{\eta_0}\frac{\mathrm{d}\epsilon}{\mathrm{d}t}$	$E = 49$ Pa, $\eta = 2146\,\mathrm{Pa.s}$, $E_0 = 23$ Pa, $\eta_0 = 123\,\mathrm{Pa.s}$	4	-68 232

Table 1: Model selection. First three columns: likelihood maximization and corresponding optimal parameter values. The optimized value of the likelihood (Eq. (8)) combined with the number p of parameters yield the Akaike information criterion (AIC) value (last column). The absolute AIC values are not particularly meaningful, but their relative values provide a comparison between the different models. The non-linear fractional model (lowest AIC value) is optimal among the models tested here. The arbitrary time scale τ is taken as equal to 1s.

Rheological models

Maxwell

$$\eta\frac{d\varepsilon}{dt} = \sigma + \tau\frac{d\sigma}{dt} \tag{10}$$

$$\varepsilon(t) = \frac{\sigma(t)-\sigma(0)}{E} + \int_0^t \frac{\sigma(t')}{\eta}dt' \tag{11}$$

Kelvin-Voigt

$$E\varepsilon + \eta\frac{d\varepsilon}{dt} = \sigma \tag{12}$$

$$\varepsilon(t) = \int_0^t \frac{\sigma(t')}{\eta}e^{-(t-t')/\tau}dt' \tag{13}$$

Zener

$$E_0\varepsilon + (E_0+E)\tau\frac{d\varepsilon}{dt} = \sigma + \tau\frac{d\sigma}{dt} \tag{14}$$

$$\varepsilon(t) = \frac{\sigma(t)-\sigma(0)e^{-\frac{E_0}{E+E_0}t/\tau}}{E+E_0} + \frac{E^2}{(E+E_0)^2}\int_0^t \frac{\sigma(t')}{\eta}e^{-\frac{E_0}{E+E_0}(t-t')/\tau}dt' \tag{15}$$

Anti-Zener

$$(\eta+\eta_0)\frac{d\varepsilon}{dt} + \eta_0\tau\frac{d^2\varepsilon}{dt^2} = \sigma + \tau\frac{d\sigma}{dt} \tag{16}$$

$$\varepsilon(t) = \int_0^t \frac{\sigma(t')}{\eta+\eta_0}dt' + \frac{\eta}{\eta_0}\int_0^t \frac{\sigma(t')}{\eta+\eta_0}e^{-\frac{\eta+\eta_0}{\eta_0}(t-t')/\tau}dt' \tag{17}$$

Burgers

$$\eta\frac{d\varepsilon}{dt}+\eta\tau_0\frac{d^2\varepsilon}{dt^2} = (1+\frac{\eta}{\eta_0})\sigma+(\tau+\tau_0+\frac{\eta}{E_0})\frac{d\sigma}{dt}+\tau\tau_0\frac{d^2\sigma}{dt^2} \quad (18)$$

$$\varepsilon(t) = \frac{\sigma(t)-\sigma(0)}{E}+\int_0^t\frac{\sigma(t')}{\eta}dt'+\int_0^t\frac{\sigma(t')}{\eta_0}e^{-(t-t')/\tau_0}dt' \quad (19)$$

Linear fractional element

$$E\tau^\alpha\frac{d^\alpha\varepsilon}{dt^\alpha} = \sigma \quad (20)$$

$$\varepsilon(t) = \frac{1}{E\tau^\alpha}\int_0^t\frac{(t-t')^{\alpha-1}\sigma(t')}{\Gamma(\alpha)}dt' \quad (21)$$

$$= \frac{1}{E\tau^\alpha}I^\alpha\sigma(t) \quad (22)$$

Model selection

Once the parameter values of each model have been optimized, we need to be able to select the best model. The difficulty is that the various models contain different numbers of parameters. In order to avoid both too simple models and too complex models (since overfitting may reduce reproducibility and/or predictability), we compute for eack model the Akaike information criterion [45] defined as

$$\mathrm{AIC} = -2\log L + 2(p+1)\,. \quad (23)$$

The AIC provides an objective estimation of the quality of each model, penalizing the number of parameters p and favouring a high value of the likelihood function L [46]:

$$\mathrm{AIC}(\mathcal{R}) = \sum_t\frac{\|\epsilon_{\exp}(t)-\mathcal{R}(\{\sigma(t')\}_{t'},\vec{\theta})\|^2}{s^2}+N_t\log(2\pi s^2)+2(p+1) \quad (24)$$

On Fig. 5f, the experimentally measured deformation $\epsilon(t)$ is compared with the predictions provided by both the linear and the non-linear fractional models from the applied stress $\sigma(t)$. The linear fractional model yields reasonable predictions, while the non-linear fractional model predicts an almost exact value for the deformation history (coefficient of determination $R^2 = 0.997$).

5 - Conclusion

Herein, we present the magnetic rheology of multicellular aggregates. We use an electromagnet as a tool to apply remote distance forces on large cylindrical aggregates. We highlight the following results:

- **Cylindrical magnetic multicellular aggregates** Large cylindrical magnetic multicellular aggregates (1 mm x 2 mm) are produced using the magnetic molding method (1). Until now, such method was used to obtain spherical aggregates, but it has been implemented here in order to produce cylindrical aggregates composed of F9 cells. Such shape was allowed thanks to the small surface tension of the F9 cells (close to 5 $mN.m^{-1}$ (2)). This atypical shape avoids the nonlinearities found during the deformation of spheroids.
- **The Magnetic Rheometer** An electromagnet, developed by François Mazuel, is used to create at will remote magnetic forces. Such versatility is used to apply four different mechanical cues: constant constraints, varying constraints, and random constraints.
- **Power-Law Rheology** Constant and frequency stimulations are the basics of any rheological experiments. Through the use of the magnetic rheometer, we demonstrate for the first time the power-law rheology of multicellular aggregates, for a broad frequency range. Thus found power-law behaviour can be characterized by only two parameters: its exponent alpha and its stiffness. Strikingly, the comparison with single cell rheology of the same cells (made using the parallel-plate rheometer developed by Atef Asnacios (3)) demonstrates a same power-law behaviour (with exponents close to 0.2), whereas the tissue appears stiffer than the cell itself.
- **Cell contribution on the global mechanics** We investigate the contribution of cell components on the overall mechanics of the multicellular aggregates. We focus on the cell cytoskeleton, and the cell-cell adhesions. Two methods are used. First, drugs added during the aggregate magnetic molding are used to homogeneously deplete the F-actin and the E-cadherins. Second, aggregate maturation (24h) allows us to unravel the rheology of the same tissue model, presenting an enhanced cohesivity. F-actin and E-cadherins depletion, give rise to softer aggregates, whereas aggregate maturation, through the increase of the cell-cell adhesion, leads to stiffer aggregates. Strikingly, no differences in the power-law behaviour are observed.

- **Non-linearity and random signals** Ramp signals and creep experiments using increasing force intensities highlight a stress stiffening in our tissue models. Plus, the random signal approach, developed by Cyprien Gay and Philip Marc, allows assessing the complete rheological spectrum of the magnetic aggregates using one single signal.

The Conclusion 5-1 presents a graphic summary of thus obtained results.

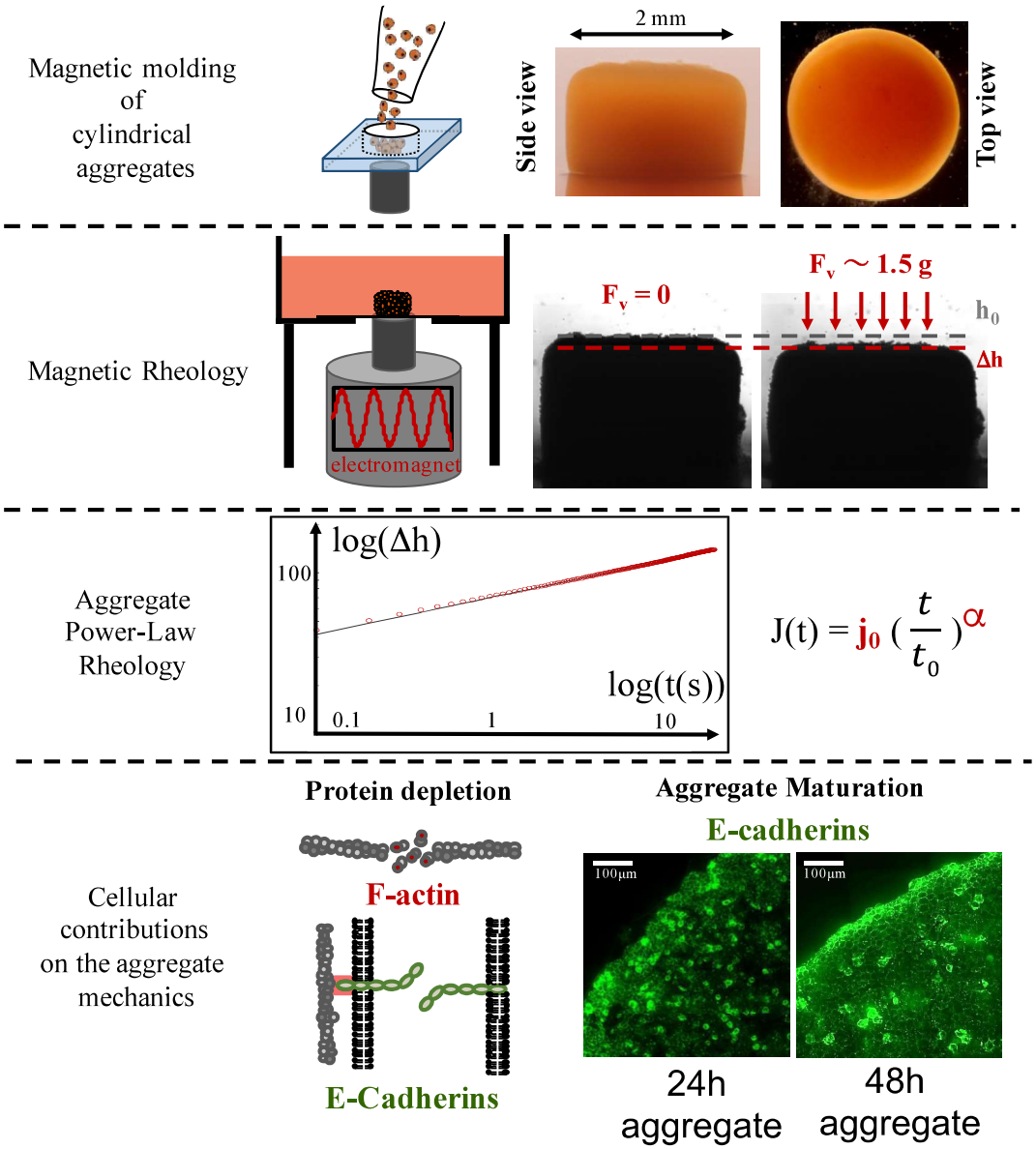

Conclusion 5-1: Conclusion of the Chapter 1. Magnetic molding is used to create unprecedented cylindrical multicellular aggregates. The rheology of thus obtained aggregates in investigated using a homemade set-up: the Magnetic Rheometer. The power-law rheology of multicellular aggregates has been demonstrated. Plus, the contribution of the cell cytoskeleton and the cell-cell adhesion on the global rheology has been addressed.

Perspectives

Further leads are considered for the future of these works.

Cancer Cells

So far, the rheometer has been only used with one cell line (F9 cells). Such a tool could be an ideal tool to work on tumor models. Tumor tissues usually appear stiffer than their native counterpart. Yet, if the comparison of the rheological behaviour of tumor and healthy cancer cells have been widely described (4) (5), it has only been done at the 3D scale on tissue extracts (6).

ECM contribution

As mention above, tumor appear stiffer than their native tissue. Such phenomena is directly linked with an ECM stiffening (7). Yet, it would be interesting to use our set-up in order to measure the evolution of an aggregate rheology, depending on the ECM secretion. However, we would need to culture our aggregates long enough to obtain significant ECM. Depending on the cell line, this could take between a few days (8) to weeks (9). Such long time culture requires NPs that are slowly degraded, which can be for instance by tuning the NPs' coating (10).

Cell mechanics contribution

We would like to investigate the effect of additional cellular component en the global mechanics of the tissue. Cell-cell adhesions have been modified using EGTA as a Ca^{2+} chelating agent, or through a 24h-maturation of the aggregates. Yet, the resulting cell adhesion is not easily adjustable. As it has been used for instance in micropipette aspiration experiments, cell transfection allows a proper tuning of the cell-cell adhesion (11). Such technology could be used with our set-up.

Plus, we would like to investigate the contribution of other cellular components on the global mechanics. For instance, the actomyosin contractility is usually linked with the mechanics of the cell and of the tissue, and can be modified using drugs.

Large deformations

Finally, we highlighted a stress stiffening of our multicellular aggregates. However, it has been done is the regime of small deformations (around 10% of the aggregate initial height). To investigate the large deformation without modifications of the set-up, we consider using NPs presenting higher magnetic susceptibilities, such as iron oxide nanocubes (12).

References

1. Mazuel F, Reffay M, Du V, Bacri J-C, Rieu J-P, Wilhelm C. Magnetic Flattening of Stem-Cell Spheroids Indicates a Size-Dependent Elastocapillary Transition. Physical Review Letters [Internet]. 2015 Mar 4 [cited 2017 Jan 16];114(9). Available from: http://link.aps.org/doi/10.1103/PhysRevLett.114.098105
2. Mgharbel A, Delanoë-Ayari H, Rieu J. Measuring accurately liquid and tissue surface tension with a compression plate tensiometer. HFSP Journal. 2009 Jun;3(3):213–21.
3. Desprat N, Richert A, Simeon J, Asnacios A. Creep Function of a Single Living Cell. Biophysical Journal. 2005 Mar;88(3):2224–33.
4. Jonas O, Mierke CT, Käs JA. Invasive cancer cell lines exhibit biomechanical properties that are distinct from their noninvasive counterparts. Soft Matter. 2011;7(24):11488.
5. Alibert C, Goud B, Manneville J-B. Are cancer cells really softer than normal cells?: Mechanics of cancer cells. Biol Cell. 2017 May;109(5):167–89.
6. Madsen C, Cox T. Relative Stiffness Measurements of Tumour Tissues by Shear Rheology. BIO-PROTOCOL [Internet]. 2017 [cited 2019 Oct 16];7(9). Available from: https://bio-protocol.org/e2265
7. Pickup MW, Mouw JK, Weaver VM. The extracellular matrix modulates the hallmarks of cancer. EMBO Rep. 2014 Dec;15(12):1243–53.
8. Beaune G, Duclos G, Khalifat N, Stirbat TV, Vignjevic DM, Brochard-Wyart F. Reentrant wetting transition in the spreading of cellular aggregates. Soft Matter. 2017;13(45):8474–82.
9. Luciani N, Du V, Gazeau F, Richert A, Letourneur D, Le Visage C, et al. Successful chondrogenesis within scaffolds, using magnetic stem cell confinement and bioreactor maturation. Acta Biomaterialia. 2016 Jun;37:101–10.
10. Plan Sangnier A, Van de Walle AB, Curcio A, Le Borgne R, Motte L, Lalatonne Y, et al. Impact of magnetic nanoparticle surface coating on their long-term intracellular biodegradation in stem cells. Nanoscale. 2019;11(35):16488–98.
11. Guevorkian K, Gonzalez-Rodriguez D, Carlier C, Dufour S, Brochard-Wyart F. Mechanosensitive shivering of model tissues under controlled aspiration. Proceedings of the National Academy of Sciences. 2011 Aug 16;108(33):13387–92.
12. Mazuel F, Espinosa A, Luciani N, Reffay M, Le Borgne R, Motte L, et al. Massive Intracellular Biodegradation of Iron Oxide Nanoparticles Evidenced Magnetically at Single-Endosome and Tissue Levels. ACS Nano. 2016 Aug 23;10(8):7627–38.

CHAPTER 2: MAGNETIC COMPRESSION OF MOUSE COLON CANCER CELL SPHEROIDS

6 - State of the art: Mechanical compression of solid tumors

This chapter present the evolution of the mechanical map arising from the tumor development inside the host tissue. Thus induced mechanical cues impact directly the cancer progression, and a better understanding of the resulting effects is promising for considering new treatments and surgical acts. We will briefly describe the tumor micro-environment, and how the or growth gives rise to an evolving mechanical environment. Then we will present in-vitro models enabling to apply controlled forces on tumor models.

Content

6.1 - Tumor mechanical environment

Cancer comes from malfunctioning cells. They divide continuously and the cell proliferation gives rise to the tumor growth. Additionally to the malfunctioning cells, the tumor stroma is composed of fibroblasts and immune cells, altogether embedded in an ECM made of fibrillar proteins, such as collagen I and fibronectin (1). The tumor stroma is perfused by blood vessels and drained by the lymphatic system (2). In order to grow, the tumor mass has to deform and to disrupt the organization of the healthy surrounding tissue, which in return resists to the expansion. This stress is called externally applied stress, and has been shown to be compressive for the tumor interior, and tensile at the interface between with the host tissue, due to the interaction with the stroma ECM (3) (Figure 6-1).

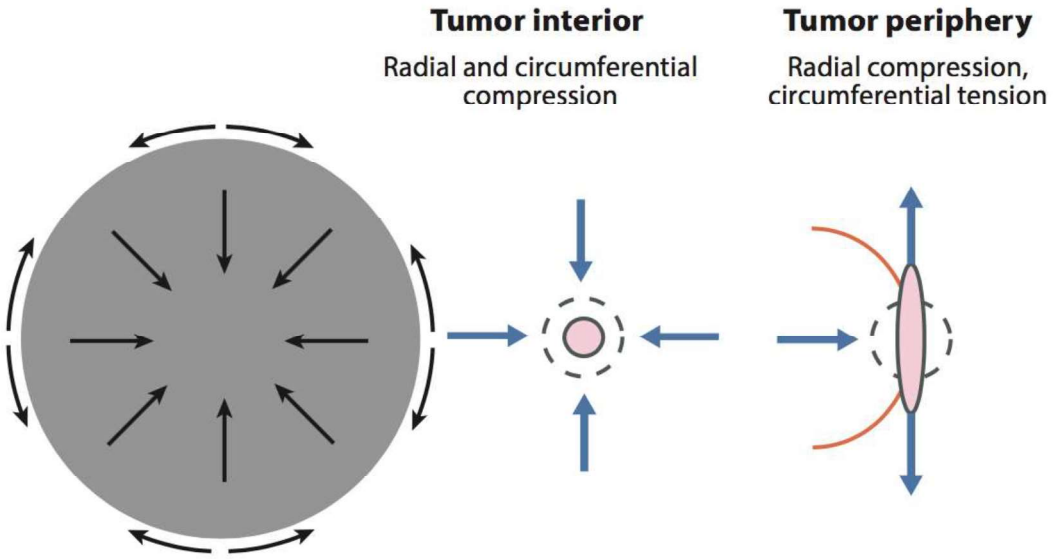

Figure 6-1: As a tumor grows, the surrounding tissue resists the expansion. The external solid stress results in two contributions: a compressive contribution toward the centre of the tumor, and a tensile contribution at the interface with the stroma. Adapted from (2).

The growth-induced stress is the first mechanical stimulation applied to the tumor. But, as the tumor grows and matures, the mechanical map surrounding the tumor evolves constantly. We are going to briefly address its main features.

6.1.1) Tumor stiffening

Whereas single cancer cells appear softer than their normal counterparts (4), solid tumors appear stiffer than their normal tissue. For instance, as the elastic modulus of a normal breast is typically close to 3 kPa, elastic moduli of breast cancers have been measured in a range of 10 to 42 kPa (5). Also, while the normal brain tissue is shown to have elastic moduli between 2 to 6 kPa, the elastic modulus for a brain tumor is measured around 35 kPa (6). The detection of the tissue stiffening is used as a method of detection both by patients and clinicians. In addition to the growing tumor, this stiffening has been imputed to the modification of the tumor stroma. In response of growth factors secreted by the tumor cells, such as Transforming Growth Factor-β (TGF-β), the activation of the surrounding fibroblasts is triggered (7). The resulting cells, called Cancer-Associated-Fibroblasts (CAF), lead to the accumulation of overexpress proteins composing the stromal ECM. The resulting ECM accumulation is known as Desmoplasia. In addition, an over-expression of Lysin-Oxydase (LOX) reshapes the ECM structure by catalysing the cross-linking of the fibril proteins (8), which enhance the cancer cell invasion.

The stiffening of the stroma matrix is shown to be critical in order to push toward the host tissue. Mathematical models demonstrate that in order to expend, the tumor must be at least 1.5 stiffer than the surrounding tissue (9).

6.1.2) Growth-induced solid stress

The total solid stress subjected to the tumor is composed of two contributions. First, both the increase in the cell density of cells and ECM stiffening, raise mechanical stress within the tumor called growth-induced solid stress (10). Secondly, the mechanical constraint exerted by the surrounding tissue represents the externally applied solid stress. The tumor growth-induced stress is stored within the tumor as a strain energy (11). Thus induced stress is stored differently between the core and the shell of the tumour: tumor-opening experiments indicate a swelling at the centre whereas a retraction is noticed on the edges of the cut (Figure 6-2). The interpretation is not straightforward as it could both indicates tension at the periphery and/or a compressive state of the core counterbalanced by peripheral tension. Using experimental data and mathematical models, growth-induced stress is estimated in a range of 2 to 20 kPa for various tumors (3) (11) (12).

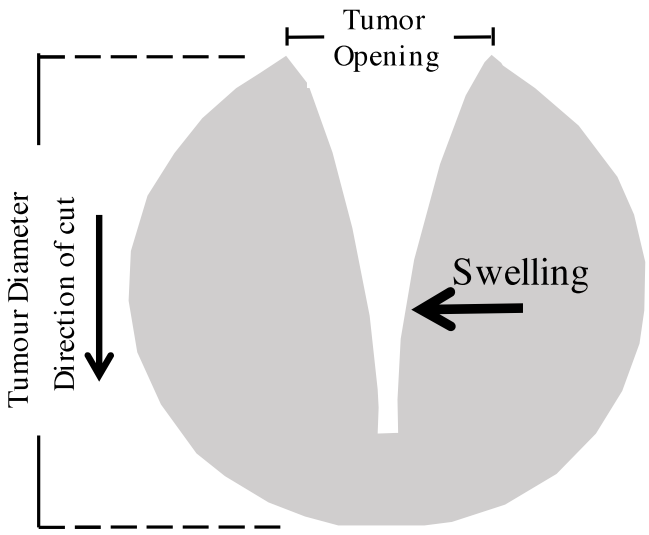

Figure 6-2: Tumor swelling due to the accumulation of growth-induced stress. Scheme of the swelling after a cut inside the tumor. The swelling at the centre indicates a compressive state. The retraction at the surface indicates a circumferential tension. Reproduced from (10).

6.1.3) Effects on the stroma

Conversely, the solid stress induced by the tumor growth is exerted on the surrounding tissue. This stress promotes cancer cell migration through the activation of fibroblasts (13) and favours the tumor growth and spread (14).

6.1.4) Effects of clinical devices

As tumor growth leads to immediate obstructions in existing organs, clinicians developed methods in order to contend these mechanical side effects. In colon cancer treatment for instance, the introduction of a colonic self-expending metal stent (SEMS) is considered as an emergency alternative to avoid laparotomy (15). The surgery consists in expending the stent to re-open the colon lumen, in order to favor a recovery of the patient before removing the tumor. Mature tumor is then compressed, leading to new mechanical stresses whose consequences are still controversial. If some clinical studies present good outcomes of this invasive surgery (16), the long-time benefits are still in question (17) (18). Nevertheless, direct complications due to a SEMS implantation has been shown in mice by co-workers (19). In this study, they injected colon cancer cells (CT26 cell line) in the colon of mice, and they

implanted a SEMS after the colon obstruction. They demonstrated an increase in the death rates due to the compression of the tumor caused by the stent expansion (Figure 6-3).

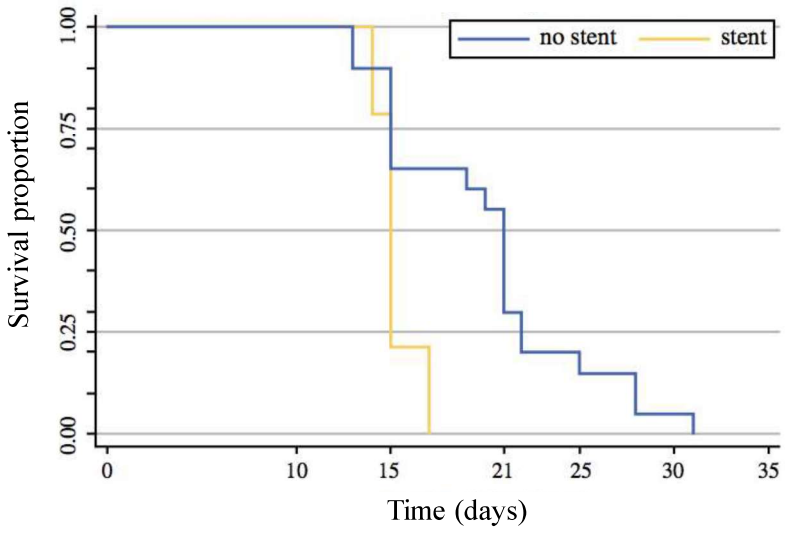

Figure 6-3: Survival curves of mice treated or not with a Self-Expending-Colonic-Stent. 10^5 CT26 cells are injected in the rectal wall. 10 days after the injection, 75% of the colon lumen is obstructed, and a SEMS is inserted. The mice treated with a stent present an average survival time of 20 days, whereas the non-treated present an average survival time of 15 days. Adapted from (19).

The solid stress promotes additional disastrous effects on the host. For instance, using mathematical models, Mascheroni et al. (20) demonstrated that the compression reduces the efficacy of chemotherapeutic agents. Plus, the solid stress induces the compression of blood vessels, impeding the delivery of drugs toward the tumor centre (21). The decrease of the vascularisation induces hypoxia, and favours the development of a necrotic core inside the tumor. Thus induced hypoxia enhances the cancer cell metastatic potency. Indeed, hypoxia leads to the overexpression of the transcription factor family Hypoxia-inducible factors (HIFs) (22), that upregulates TGF-β expression. This activates a cascade of pathways leading to the Epithelial-Mesenchymal Transition EMT (22) (23). During EMT, cancer cells acquire mesenchymal-like features, enhancing their ability to migrate and therefore to create metastasis. Among others, this transition is characterized by a downregulation of E-cadherins (24), and an upregulation of N-cadherins and vimentin (25). These new features, such as the loss of cell-cell adhesion and the increase in the ECM-adhesion, enhance the migration of the cancer cell, enabling them to invade the host (25). Additionally, through the TGF-β activation, hypoxia has been shown to promote the expression of Matrix Metalloproteinases

(MMPs) (26) (27). Such proteins are used by cancer cells to re-shape the surrounding ECM, and an increase in their expression is linked with an enhanced metastatic potency (28).

This hypoxic environment also prevents the tumor from the action of the immune system. The collapse of the vessels prevents the immune system to enter the tumor (2), and hypoxia promotes tolerance towards the cancer cells (29). This condition even leads to the corruption of protumorigenic macrophages (30).

6.1.5) Fluid stresses

The solid stress also affects indirectly the tumor by increasing the interstitial fluid pressure. In order to satisfy the need of the dividing cells, tumor growth is associated with the creation of new vessels. This mechanism, called angiogenesis, is regulated by TGF-β (31). But these vessels are immature, tortuous (32) and result in the leakage of blood plasma in the interstitial space (33). Plus, solid stress collapses blood and lymphatic vessels, leading to an increase in the blood flow resistance, and to an accumulation of fluid in the interstitial space (2) (34). Angiogenesis, and the solid stress favouring the accumulation of interstitial fluid, provokes a pressure difference between the tumor and its environment. This pressure gradient leads to an outward flow from the tumor toward the surrounding tissue. This has been shown to promote cell escaping from the tumor (1). Along with the blood vessel collapse and leakage, the interstitial fluid pressure also decreases the treatment delivery and efficiency (2).

6.1.6) Conclusion

The mechanical map surrounding a tumor is constantly evolving (Figure 6-4). As it is originally triggered by the growth-induced solid stress, understanding its effects on the tumor is an essential matter. To do so, one needs tool to create tumor models, and tools to subject them to controlled mechanical stresses.

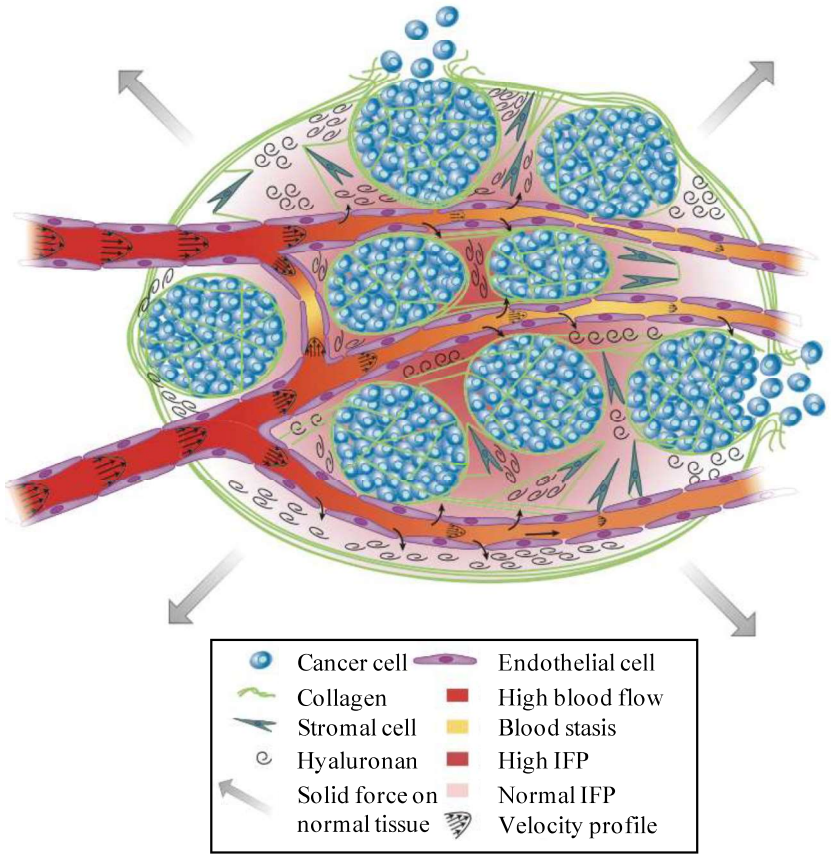

Figure 6-4: A growing tumor is composed of dysfunctioning cancer cells, stroma cells, blood and lymphatic vessels. They are embedded in an ECM mainly composed of Collagen. The stress induced by the growth triggers abnormal blood flow, an accumulation of Interstitial Fluid Pressure (IFP) stocked in hyaluronan and a solid stress on the surrounding tissue. Extracted from (2).

6.2.1) Cancer models

Currently, three cancer models are mainly used:

- (i) 2D monolayers represent the first step that takes into account the collective behaviour of tumor cells. This represents an interesting tool to study migration or invasion.
- (ii) Cells suspensions embedded in a matrix is crucial to highlight the role of the interaction between matrix and cells.
- (iii) The most commonly used system is still the spheroids obtained by aggregation of tumor cells using microwells, hanging drop or agitation. These methods have been addressed in the first chapter of this manuscript.

6.2.2) Tools to compress tumor models

A few methods allow mimicking the effect of the solid stress. The purpose of the methods is to subject cancer cell monolayers or avascular spheroids to controlled compressions (Figure 6-5). Herein, we briefly present these methods, and we will underline some of their limitations.

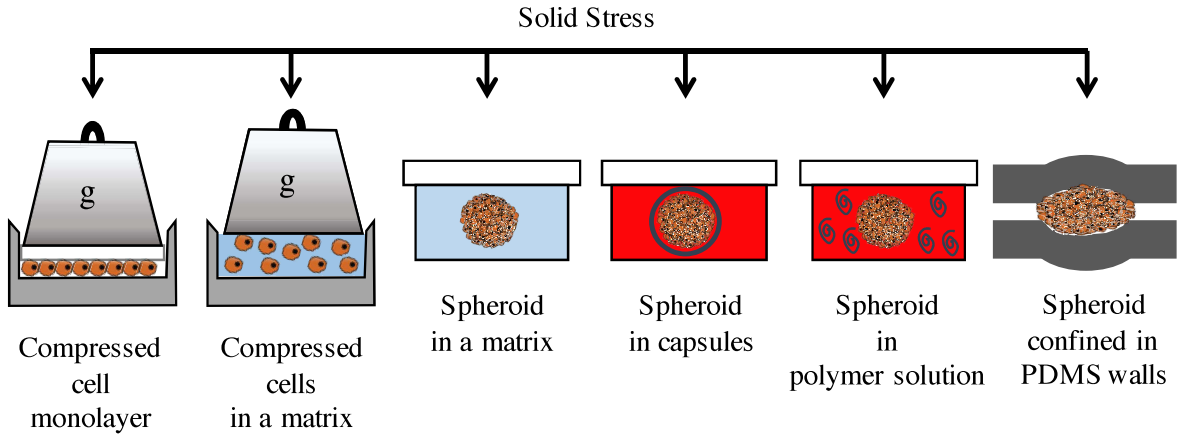

Figure 6-5: Experimental devices used to address the effect of solid stress on cancer cells and tumor models. From left to right: cell monolayers (35) or cells embedded in matrix (36) can be compressed using a piston; avascular spheroids can be embedded in 3D matrices (36); growth confinement can be performed using alginate capsules (37) osmotic pressure (38) or rigid walls (39). Adapted from (40).

Compressing a monolayer: Munn et al. (35) developed a device to compress 2D cancer cell monolayers. The authors grow a cell monolayer in a transwell insert, and applied a control pressure on the cells by tuning the weight of a piston pressing on the cells. Doing so, one is able to apply stresses in a range of 0 to 8 kPa. The compression can be combined with scratch-wound assay using adhesive substrates (41). This device was more recently used with bone osteosarcoma cells (42). If these methods are good tools to apply forces to cancer monolayers, they are by nature limited at the 2D-scale.

Cells embedded in ECM-like 3D matrices: In this method, the gel that hosts the cell suspension drives the compression. Using a piston, gels can be compressed up to 50% of their original volume during several hours. Due to the gel compaction, the resulting stress subjected to the cell decreases from 0.25 kPa to 0.05 kPa (36).

Other tools have been created in order to adapt to the 3D geometry of avascular spheroids.

Confinement of growing spheroids

3D-Gels This method consists in embedding growing multicellular spheroids in agarose or ECM-like gels. The gel stiffness can be tuned by controlling the gel concentration, therefore changing the solid stress subjected to the growing tumor model. Thus applied solid stress is evaluated in a range of 6 to 26 kPa (43). Plus, by growing spheroids in cracks of the agarose gel, this method can also be used in order to apply an anisotropic solid stress (35). Besides, the embedment in agarose gels may have direct effects on their growth. For instance, the growing in gel cracks results in a size limitation and a lack of spheroid maturation (25 μm in (35)).

Confinement without ECM The following methods have been developed in order to confine and to apply controlled solid stress on growing spheroids, without the use of an ECM-like matrices.

- **Alginate capsules:** Alessandri et al (37) developed a microfluidic device to encapsulate mouse colon carcinoma cells in hollow alginate capsules. The capsules are permeable to nutrient and gas, and the elasticity of the spheres, which can be tuned by changing the thickness of the shell, is used to confine the growth of the spheroids. Additionally, the deformation of the capsule, resulting from the spheroid growth, can be used to measure the force applied by the tumor model on the surrounding tissue. Thus resulting pressure is estimated around 2 kPa.
- **Osmotic pressure** applied by polymer solution such as dextran to spheroids directly plunged in solution or in dialysis chamber (38) (44). Thus obtained stress is in a range of 0 to 20 kPa.
- **PDMS rigid walls** are also used to anistropically confine tumor spheroids (39). The confined spheroids present a larger size than with the previous set-ups (the distance between the rigid walls is 300 μm).

6.2.3) Effects of in-vitro solid stress on tumor models

Altogether, these techniques are used to applied solid stress on monolayers, or on growing aggregates limited in sizes. In the later, the resulting stress is applied on the shell of the spheroids, mimicking the impact of the surrounding tissue on a growing tumor. The inhomogeneous applied stress leads to a regionalization of the aggregate, which presents two different compartments: the inner part (the core) and the shell (45). All the noticed changes, such as cell proliferation or apoptosis, are associated to global modification, but also to a change in the localization.

6.2.3.1) Effect on the proliferation

Proliferation is the first changing characteristic of a tumor spheroid under mechanical stresses. This is usually assessed through the labelling of the proliferation marker Ki67, a protein present in 80% of the division cycle (46). However deciphering between the inhibition and the activation of the proliferation is still under debate and seems to depend both on the applied stress, and on the initial state of the spheroids. Numerous experiments on various systems suggest that the mechanical stress due to a confined growth, isotropic or not, results in a drastic decrease of the final spheroid volume. This was linked with an increase in cell apoptosis, and a decrease of the cell proliferation toward the centre of the spheroids. In these experiments, stresses from few kPa (43) to 20 kPa (44) are applied using techniques such as embedment in agarose gels (35), osmotic pressure (44) (38) or alginates capsules (37). The inhibition of the spheroid growth in this confined environment is due both to a decrease in proliferation and an increase in apoptotic cells in the core. This could be correlated with a rise of the pressure in this region (47).

Controversially, anisotropic confinements performed on larger spheroids highlighted an increase of the proliferating cells towards the centre (39), correlated with a change in the hypoxia map.

The effect of the confinement on the proliferation of cancer cell spheroids is not clear yet. These experiments could suggest that the size of the spheroids, and the mode of confinement could trigger different effects on the proliferative behaviour of the spheroids. The Figure 6-6 presents the localization of the proliferation depending on the mode of confinement.

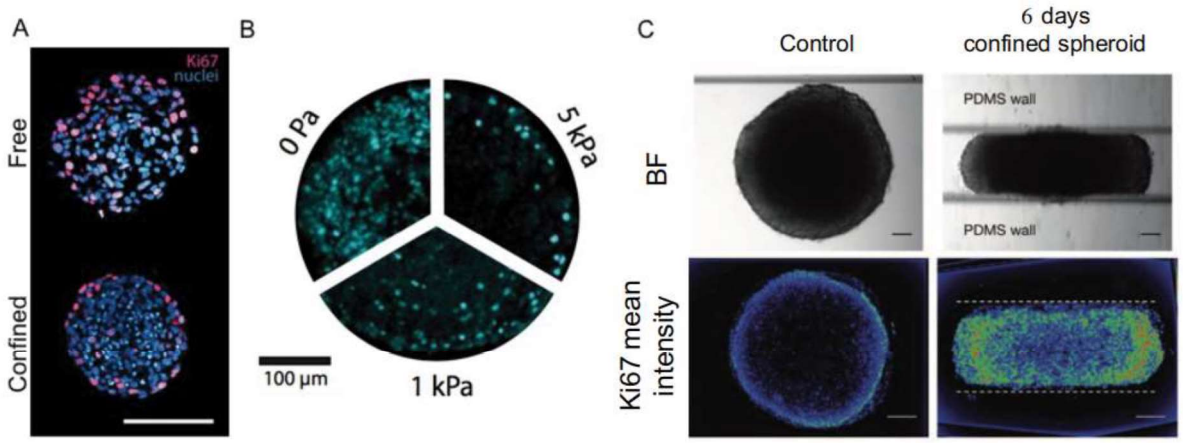

Figure 6-6: The localization of the proliferation depends on the method of confinement of the aggregate. A) CT26 growing spheroids are confined (bottom picture) within an alginate capsule, or let at free growing (up picture). The isotropic growth confinement leads to an increase in the nucleus density, and a decrease in the number of proliferating cells. The nuclei are labeled in blue, and Ki67 (proliferation marker) is labeled in red. Scale bar 100 µm. Adapted from (37). **B)** CT26 growing spheroids are subjected to increasing osmotic pressures from 0 to 5 kPa. The increasing isotropic solid stress leads to a decrease in the number of proliferating cells. Ki67 is labeled in cyan. Adapted from (44). **C)** Anisotropic confinement of large (300 µm) CT26 spheroids. Left and right pictures present respectively a free growing CT26 spheroid and a CT26 spheroid confined between two rigid PDMS walls (distanced of 300 µm). For both, a BF picture (top pictures) and the Ki67 mean intensity (bottom pictures) are presented. Unlike the presented isotropic confinement, the anisotropy of the confinement leads to an increase in the Ki67 mean intensity toward the spheroid center. Adapted from (39).

6.2.3.2) Effect of the cell division cycle

The previous exposed changes in the proliferation of the confined spheroids have been done using Ki67 as a proliferation marker. Additional experiments have refined the effect of the solid stress on the proliferation. Using the osmotic confinement, Delarue et al. (48) demonstrated with various cell lines that the change in the proliferative behaviour was associated with an increase in the expression of the proliferation inhibitor $p27^{Kipl}$, blocking the cells at the G1 checkpoint. Using parallel plate confinement, Desmaison et al. (39) suggested that the mechanical stress could block the cell division before mitosis, due to the non-assembly of the mitotic spindle (49).

Altogether, these results may suggest that the confinement triggers changes in the proliferative behaviour. These experiments suggest that tumor cells are mechanosensitive, and that the stress applied induces different behavior between inner and peripheral cells.

6.2.3.3) Effects on the metastatic potency

If solid stress leads to a change in the proliferating tumor behaviour, it cannot be seen as a benefit for the host (50), as it also triggers an increase in the expression of proteins linked with the metastatic process. First, mechanical compression of cancer monolayers enhances cell invasion by triggering leader-cell phenotypes (41). Plus, modifications in the MMPs expression have been demonstrated (42) (36). In spheroids, the confinement enhances the cell motility on the shell (37).

6.3 - Motivation: anisotropic compression of large tumour spheroids

The previously presented works aim to unravel the consequences of the solid stress on the tumor. If direct compressions have been exerted on monolayers or on suspension of cells embedded in 3D matrices, most of the studies are focused on confined growth of avascular tumor spheroids.

Therefore a lack of knowledge is yet to be filled. As far as we know, no experimental tools are able to assess the effect of a controlled stress applied to a spheroid presenting a size close to mature tumors. This type of mechanical stimulation could unravel some key elements linked with emergency surgical interventions. For instance, co-workers demonstrated an increase in death rate of mice treated with colonic self-expending stents (19). Regarding the in-vitro results obtained by applying isotropic stress on growing tumors, such a result seems controversial. Two key points are at stake: first, SEMS apply mechanical constraints on mature tumors; second, thus applied constraint is anisotropic.

6.4 - Proposed approach

To mimic this in-vivo experiment, we propose a magnetic approach, first to create large mature avascular spheroids of mouse colon cancer cells (CT26 cell line), then to subject them to a volumic magnetic flattening. Both methods of magnetic molding and magnetic flattening have been recently developed in the group in order to measure the surface tension of magnetic Mesenchymal Stem Cells spheroids (51). However, such approaches have never been used on in-vitro cancer spheroids.

The consequences of thus anisotropic constraint on the tumor model behaviour have been addressed. Our approach was not restricted to in-vitro measurements, as we also tried to unravel its impact on the in-vivo metastatic potential.

In particular, I implemented all the in-vitro experiments, from the manufacturing of the tumor model, to the quantification of the effect of a magnetic compression on the tumor spheroid behaviour. The in-vivo model was developed in collaboration with Brice Malgras and Marc Pocard at the Lariboisière Hospital (AP-HP 75010 Paris, France).

References

1. Northcott JM, Dean IS, Mouw JK, Weaver VM. Feeling Stress: The Mechanics of Cancer Progression and Aggression. Front Cell Dev Biol. 2018 Feb 28;6:17.
2. Jain RK, Martin JD, Stylianopoulos T. The Role of Mechanical Forces in Tumor Growth and Therapy. Annu Rev Biomed Eng. 2014 Jul 11;16(1):321–46.
3. Nia HT, Liu H, Seano G, Datta M, Jones D, Rahbari N, et al. Solid stress and elastic energy as measures of tumour mechanopathology. Nat Biomed Eng. 2017 Jan;1(1):0004.
4. Alibert C, Goud B, Manneville J-B. Are cancer cells really softer than normal cells?: Mechanics of cancer cells. Biol Cell. 2017 May;109(5):167–89.
5. Samani A, Zubovits J, Plewes D. Elastic moduli of normal and pathological human breast tissues: an inversion-technique-based investigation of 169 samples. Phys Med Biol. 2007 Mar 21;52(6):1565–76.
6. Angeli S, Stylianopoulos T. Biphasic modeling of brain tumor biomechanics and response to radiation treatment. J Biomech. 2016 Jun;49(9):1524–31.
7. Kalluri R. The biology and function of fibroblasts in cancer. Nat Rev Cancer. 2016 Sep;16(9):582–98.
8. Cox TR, Bird D, Baker A-M, Barker HE, Ho MW-Y, Lang G, et al. LOX-Mediated Collagen Crosslinking Is Responsible for Fibrosis-Enhanced Metastasis. Cancer Res. 2013 Mar 15;73(6):1721–32.
9. Voutouri C, Mpekris F, Papageorgis P, Odysseos AD, Stylianopoulos T. Role of Constitutive Behavior and Tumor-Host Mechanical Interactions in the State of Stress and Growth of Solid Tumors. Singh PK, editor. PLoS ONE. 2014 Aug 11;9(8):e104717.
10. Butcher DT, Alliston T, Weaver VM. A tense situation: forcing tumour progression. Nat Rev Cancer. 2009 Feb;9(2):108–22.
11. Stylianopoulos T, Martin JD, Chauhan VP, Jain SR, Diop-Frimpong B, Bardeesy N, et al. Causes, consequences, and remedies for growth-induced solid stress in murine and human tumors. Proc Natl Acad Sci. 2012 Sep 18;109(38):15101–8.
12. Stylianopoulos T, Martin JD, Snuderl M, Mpekris F, Jain SR, Jain RK. Coevolution of Solid Stress and Interstitial Fluid Pressure in Tumors During Progression: Implications for Vascular Collapse. Cancer Res. 2013 Jul 1;73(13):3833–41.
13. Kalli M, Papageorgis P, Gkretsi V, Stylianopoulos T. Solid Stress Facilitates Fibroblasts Activation to Promote Pancreatic Cancer Cell Migration. Ann Biomed Eng. 2018 May;46(5):657–69.
14. Fernández-Sánchez ME, Barbier S, Whitehead J, Béalle G, Michel A, Latorre-Ossa H, et al. Mechanical induction of the tumorigenic β-catenin pathway by tumour growth pressure. Nature. 2015 Jul;523(7558):92–5.
15. Law WL, Chu KW, Ho JWC, Tung HM, Law SYK, Chu KM. Self-expanding metallic stent in the treatment of colonic obstruction caused by advanced malignancies: Dis Colon Rectum. 2000 Nov;43(11):1522–7.
16. Ho K, Chan K, Kwok S, Lau P ying-yu. Colonic self-expanding metal stent (SEMS) as a bridge to surgery in left-sided malignant colonic obstruction: an 8-year review. Surg Endosc. 2017 May;31(5):2255–62.
17. Small AJ, Coelho-Prabhu N, Baron TH. Endoscopic placement of self-expandable metal stents for malignant colonic obstruction: long-term outcomes and complication factors. Gastrointest Endosc. 2010 Mar;71(3):560–72.
18. Selinger CP, Ramesh J, Martin DF. Long-term success of colonic stent insertion is influenced by indication but not by length of stent or site of obstruction. Int J Colorectal Dis. 2011 Feb;26(2):215–8.
19. Malgras B, Brullé L, Lo Dico R, El Marjou F, Robine S, Therwath A, et al. Insertion of a Stent in Obstructive Colon Cancer Can Induce a Metastatic Process in an Experimental Murine Model. Ann Surg Oncol. 2015 Dec;22(S3):1475–80.
20. Mascheroni P, Boso D, Preziosi L, Schrefler BA. Evaluating the influence of mechanical stress on anticancer treatments through a multiphase porous media model. J Theor Biol. 2017 May;421:179–88.
21. Padera TP, Stoll BR, Tooredman JB, Capen D, Tomaso E di, Jain RK. Cancer cells compress

intratumour vessels. Nature. 2004 Feb;427(6976):695–695.
22. Muz B, de la Puente P, Azab F, Azab AK. The role of hypoxia in cancer progression, angiogenesis, metastasis, and resistance to therapy. Hypoxia. 2015 Dec;83.
23. Tian M, Neil JR, Schiemann WP. Transforming growth factor-β and the hallmarks of cancer. Cell Signal. 2011 Jun;23(6):951–62.
24. Azab AK, Hu J, Quang P, Azab F, Pitsillides C, Awwad R, et al. Hypoxia promotes dissemination of multiple myeloma through acquisition of epithelial to mesenchymal transition-like features. Blood. 2012 Jun 14;119(24):5782–94.
25. Kalluri R, Weinberg RA. The basics of epithelial-mesenchymal transition. J Clin Invest. 2009 Jun 1;119(6):1420–8.
26. Miyazaki Y, Hara A, Kato K, Oyama T, Yamada Y, Mori H, et al. The effect of hypoxic microenvironment on matrix metalloproteinase expression in xenografts of human oral squamous cell carcinoma. Int J Oncol [Internet]. 2008 Jan 1 [cited 2019 Oct 21]; Available from: http://www.spandidos-publications.com/10.3892/ijo.32.1.145
27. Shan Y, You B, Shi S, Shi W, Zhang Z, Zhang Q, et al. Hypoxia-Induced Matrix Metalloproteinase-13 Expression in Exosomes from Nasopharyngeal Carcinoma Enhances Metastases. Cell Death Dis. 2018 Mar;9(3):382.
28. Kessenbrock K, Plaks V, Werb Z. Matrix Metalloproteinases: Regulators of the Tumor Microenvironment. Cell. 2010 Apr;141(1):52–67.
29. Facciabene A, Peng X, Hagemann IS, Balint K, Barchetti A, Wang L-P, et al. Tumour hypoxia promotes tolerance and angiogenesis via CCL28 and Treg cells. Nature. 2011 Jul;475(7355):226–30.
30. Condeelis J, Pollard JW. Macrophages: Obligate Partners for Tumor Cell Migration, Invasion, and Metastasis. Cell. 2006 Jan;124(2):263–6.
31. Carmeliet P, Jain RK. Angiogenesis in cancer and other diseases. Nature. 2000 Sep;407(6801):249–57.
32. Carmeliet P, Jain RK. Principles and mechanisms of vessel normalization for cancer and other angiogenic diseases. Nat Rev Drug Discov. 2011 Jun;10(6):417–27.
33. Hashizume H, Baluk P, Morikawa S, McLean JW, Thurston G, Roberge S, et al. Openings between Defective Endothelial Cells Explain Tumor Vessel Leakiness. Am J Pathol. 2000 Apr;156(4):1363–80.
34. Baxter LT, Jain RK. Transport of fluid and macromolecules in tumors. I. Role of interstitial pressure and convection. Microvasc Res. 1989 Jan;37(1):77–104.
35. Cheng G, Tse J, Jain RK, Munn LL. Micro-Environmental Mechanical Stress Controls Tumor Spheroid Size and Morphology by Suppressing Proliferation and Inducing Apoptosis in Cancer Cells. Blagosklonny MV, editor. PLoS ONE. 2009 Feb 27;4(2):e4632.
36. Demou ZN. Gene Expression Profiles in 3D Tumor Analogs Indicate Compressive Strain Differentially Enhances Metastatic Potential. Ann Biomed Eng. 2010 Nov;38(11):3509–20.
37. Alessandri K, Sarangi BR, Gurchenkov VV, Sinha B, Kiessling TR, Fetler L, et al. Cellular capsules as a tool for multicellular spheroid production and for investigating the mechanics of tumor progression in vitro. Proc Natl Acad Sci. 2013 Sep 10;110(37):14843–8.
38. Montel F, Delarue M, Elgeti J, Malaquin L, Basan M, Risler T, et al. Stress Clamp Experiments on Multicellular Tumor Spheroids. Phys Rev Lett. 2011 Oct 24;107(18):188102.
39. Desmaison A, Frongia C, Grenier K, Ducommun B, Lobjois V. Mechanical Stress Impairs Mitosis Progression in Multi-Cellular Tumor Spheroids. Engler AJ, editor. PLoS ONE. 2013 Dec 3;8(12):e80447.
40. Kalli M, Stylianopoulos T. Defining the Role of Solid Stress and Matrix Stiffness in Cancer Cell Proliferation and Metastasis. Front Oncol. 2018 Mar 12;8:55.
41. Tse JM, Cheng G, Tyrrell JA, Wilcox-Adelman SA, Boucher Y, Jain RK, et al. Mechanical compression drives cancer cells toward invasive phenotype. Proc Natl Acad Sci. 2012 Jan 17;109(3):911–6.
42. Mitsui N, Suzuki N, Koyama Y, Yanagisawa M, Otsuka K, Shimizu N, et al. Effect of compressive force on the expression of MMPs, PAs, and their inhibitors in osteoblastic Saos-2 cells. Life Sci. 2006 Jul;79(6):575–83.
43. Helmlinger G, Netti PA, Lichtenbeld HC, Melder RJ, Jain RK. Solid stress inhibits the growth of 1nulticellular tu1nor spheroids. 1997;15:6.

44. Montel F, Delarue M, Elgeti J, Vignjevic D, Cappello G, Prost J. Isotropic stress reduces cell proliferation in tumor spheroids. New J Phys. 2012 May 9;14(5):055008.
45. Han YL, Pegoraro AF, Li H, Li K, Yuan Y, Xu G, et al. Cell swelling, softening and invasion in a three-dimensional breast cancer model. Nat Phys [Internet]. 2019 Oct 21 [cited 2019 Nov 28]; Available from: http://www.nature.com/articles/s41567-019-0680-8
46. Sun X, Kaufman PD. Ki-67: more than a proliferation marker. Chromosoma. 2018 Jun;127(2):175–86.
47. Dolega ME, Delarue M, Ingremeau F, Prost J, Delon A, Cappello G. Cell-like pressure sensors reveal increase of mechanical stress towards the core of multicellular spheroids under compression. Nat Commun. 2017 Apr;8(1):14056.
48. Delarue M, Montel F, Vignjevic D, Prost J, Joanny J-F, Cappello G. Compressive Stress Inhibits Proliferation in Tumor Spheroids through a Volume Limitation. Biophys J. 2014 Oct;107(8):1821–8.
49. Laurent J, Frongia C, Cazales M, Mondesert O, Ducommun B, Lobjois V. Multicellular tumor spheroid models to explore cell cycle checkpoints in 3D. 2013;12.
50. Trepat X. Forcing Tumor Arrest. Physics. 2011 Oct 24;4:85.
51. Mazuel F, Reffay M, Du V, Bacri J-C, Rieu J-P, Wilhelm C. Magnetic Flattening of Stem-Cell Spheroids Indicates a Size-Dependent Elastocapillary Transition. Phys Rev Lett [Internet]. 2015 Mar 4 [cited 2017 Jan 16];114(9). Available from: http://link.aps.org/doi/10.1103/PhysRevLett.114.098105

7 - Article: *Magnetic compression of tumor spheroids increases the cell proliferation in vitro and the cancer progression in vivo.*

Magnetic compression of tumor spheroids increases the cell proliferation in vitro and the cancer progression in vivo.

Gaëtan Mary[1], Brice Malgras[2], Cynthia Pimpie[2], Atef Asnacios[1], Marc Pocard[2], Myriam Reffay[1], Claire Wilhelm[1]

1: UMR 7057, Paris 5 Diderot University, Laboratoire Matière et Systèmes Complexes (MSC), Paris, France.
2: INSERM U965 Angiogenesis and Translational Research, Department of Digestive Diseases and Pathology, Paris Diderot 7 University, Lariboisière Hospital, AP-HP 75010 Paris, France.

Abstract

A growing tumour is submitted to constantly evolving mechanical stresses, such as growth-induced solid stress, interstitial fluid pressure or ECM stiffening. Besides, surgical procedures such as self-expanding stent implantation in cancer-obstructed colon result in mechanical stresses. Impact of such mechanical forces on cancer progression is still debated.
Herein a set of magnetic methods are proposed to form cancer spheroids and subject them to remote deformation, mimicking the stent-imposed compression. Mouse colon cancer cells (CT26) are labelled with magnetic nanoparticles then magnetically seeded in 1 mm spherical agarose molds. Cohesion of thus formed magnetic multicellular aggregates is reached overnight and the spheroids can be further compressed down to 50% of their initial diameters through the use of a permanent magnet. This large deformation triggers an increase in the spheroid proliferation, correlated with an increase in the number of proliferating cells toward the centre of the compressed spheroids, and with an overexpression of the metalloproteinase-9 (MMP-9) in the spheroids centre. Remarkably, compared to a peritoneal injection with non-stimulated spheroids, thus triggered behaviour translates in vivo into a 50% increase in the peritoneal cancer index (PCI) for mice injected with compressed spheroids.
Altogether, these results demonstrate that a large anisotropic compression of tumor spheroid can be beneficial to cancer progression, by triggering an in-vitro proliferation and an in-vivo increase of the metastatic potential.

Introduction

Cancer comes from continuously dividing cells. In order to grow, the tumor mass has to deform and to disrupt the organization of the surrounding healthy tissue, which in return resists to the expansion. This growth gives rise to a constantly evolving mechanical map (1). Upon growth, the tumor is subjected to mechanical stresses generated both by the increase in the cell density and the extracellular matrix (ECM) stiffening, resulting from the activation of cancer-associated-fibroblasts (CAF) (2) (3). In parallel, the surrounding tissue applies a compressive mechanical resistance toward the centre of the tumor, and tensile on the periphery. The growth-induced stress is stored within the tumor as a strain energy (4) (5), which is measured in a range of 2 to 20 kPa for many tumors (6) (7). Additionally, cancer progression is associated with angiogenesis (8) but new vessels are immature, tortuous (9) and result in the leakage of blood plasma in the interstitial space (10). Plus, solid stress results in the collapse of blood and lymphatic vessels and leads to an increase of blood flow resistance and an accumulation of interstitial fluid (11), ultimately arising additional mechanical stresses (12). Also of importance, surgical acts can subject mature tumors to important mechanical stresses. For instance, the introduction of a colonic self-expending metal stent (SEMS) is considered as an emergency alternative to avoid laparotomy in obstructing colon cancer (13). The surgery consists in expending the stent to re-open the colon lumen, in order to favour the patient recovery before removing the tumor. The tumor is then compressed, leading to additional mechanical stresses. While SEMS insertion leads to immediate therapeutic improvement (14), the long-time benefits are still questioned (15) (16). In particular, SEMS implantation in mice developing an obstructive colon cancer evidenced a decreased of the survival time for treated animals (17). The impact of mechanical stresses on cancer progression has been recently explored in vitro in two-dimensional (2D) or three-dimensional (3D) configurations. 2D cancer cell monolayers (18), cancer cell suspensions (19) and 3D tumor models (20) were subjected to mechanical compressions in the range of a few kPa, in the like of thus experienced in vivo. Isotropic or anisotropic confinements of small growing spheroids (less than 100 μm in diameter) led to the reduction of the final spheroid volume, associated to both an increase of cell apoptosis and a decrease of cell proliferation toward the centre of the confined spheroids (20) (21) (22), which can be related to a pressure rise (23). Controversially, anisotropic confinement performed on larger spheroids (300 μm in diameter) highlighted an increase of proliferating cells toward the spheroid centre, correlated with a change in the hypoxia map (24).

3D spheroids models remain the closest in vitro configuration to mimic in vivo solid tumors (25) (26). Methods for spheroid formation include the use of micro-wells, hanging drop or centrifugation, all based on locally increasing the cell density of an initially small number of cells (1000-10000 cells) (27). Upon cell proliferation, multicellular spheroids are formed within a few days, and present diameters in the range of 250-500 μm. Increasing the spheroid size is then precluded by limited diffusion of dioxygen and nutrients (28), so that typical spheroid sizes remain far from those of mature tumors. Therefore, assessing the effect of a mechanical compression on larger spheroids requires the development of alternative tools, first to create such mature-sized spheroids, then to subject them to controlled forces.

Current methods to mechanically stimulate tumor spheroids include hydrogel embedment (29), microfluidic encapsulation (21), confinement in rigid-walls (24) or the use of osmotic pressures (22). Besides, such methods rely only on the confinement of growing spheroids. If it has been performed through the use of a piston, at the 2D scale or for cell suspension (30), the possibility to apply high deformations on a spheroid without direct contact is still missing.

Herein, we propose a magnetic approach to form and to compress large spheroids of mouse colon cancer cells (CT26 cell line). Magnetic nanoparticles are internalized within CT26 cells via the endocytosis pathways (31) (32), with no impact on cell functions (33). The magnetism granted to each cells not only allows to magnetically mold (34) 1 mm magnetic tumor spheroids, but also to compress them remotely with a permanent magnet. The consequences of this compressive stimulation on the tumor model proliferation in vitro and metastatic potential in vivo were assessed.

Materiel and Methods

Cell culture and magnetic labelling

Mice colon carcinoma cell line (CT26) was used as a model of colon cancer cells. They were cultured in Dulbecco's modified Eagle's medium (DMEM, Gibco), supplemented with 1% Penicillin-Streptomycin (P/S, Thermofisher) and 10% Fetal Bovine Serum (FBS, Gibco). Magnetic nanoparticles were produced by the Massart's procedure of iron salts co-precipitation (35). They consist of an iron oxide core of 8 nm with polydispersity index of 0.35, and were stabilized by citrate surface coating.

Nanoparticles were incubated with the cells overnight, in supplemented DMEM at a concentration [Fe]= 0.6 mM, after optimizing the incubation conditions to obtain a maximal cellular uptake (see Figure S7-1). Cells then incorporated an iron mass of 11 pg per cell, distributed among the cell population with a 35% distribution width. The magnetic labelling had no impact on cell viability and proliferation, as determined using the alamarBlue (Thermofisher) metabolic assay (see Figure S7-2).

Magnetic molding of CT26 spheroids

A 2% agarose (Sigma-Aldrich, Type I-B, A0576) solution was prepared and heated until boiling and homogenization. 2.8mL was deposited onto a 35cm^2 petri dish (TPP), and five 1.0 mm stainless steel beads (CIMAP) were attracted within the liquid agarose by a network of five 6 x 2 mm cylindrical magnets (Supermagnet) placed beneath the dish (Figure 7-1A). Agarose gelation then occurred in a few minutes and semi-spheroidal molds were ultimately obtained by removing the beads. Labelled CT26 were detached from a T75 flask, centrifuged and suspended in supplemented DMEM. 250,000 magnetic cells were seeded inside each well, using exactly the same magnetic configuration than during the formation of the molds. The set-up is then filled with supplemented culture medium was placed overnight within the incubator to allow spheroid formation. The resulting spheroids were removed from the wells the day after (further denoted day 1, corresponding to the end of the formation process).

Magnetic compression

For single spheroid compression experiment, a 6 x 6 mm cylindrical permanent magnet (Supermagnet, B = 520 mT, gradB = 177 $T.m^{-1}$) was glued (Silicon glue, LOCTITE SI 5398) at the bottom of a sterile non-adhesive Petri dish (Grenier bio-one, ref 627102). Multiple dishes were prepared, so every magnetically molded spheroids are seeded on top of a magnet right after formation (day 1). They are then left within for 2 to 3 days (respectively day 3 or day 4), and will be called later on MAG+ spheroids. The same number of spheroids were seeded in the non-adhesive Petri dishes without magnets and left free within (termed MAG- spheroids).

To quantify the deformation of the MAG+ spheroids, they were placed inside a thermally controlled homemade non-adhesive rectangular dish allowing to camera-capture both the profile and the top of the spheroid. The permanent magnet was positioned right below the dish, in the same configuration than for the Petri dishes. The compression of the MAG+ spheroids was video-monitored with CANON- camera. For short times, the deformation was observed at 1 frame per 10 seconds the first minute, at 1 frame per 5 minutes within 10 minutes of deformation, and at 1 frame per 10 minutes until 1h of deformation (see Figure S7-3). Finally, the deformation was captured at 1 frame per hour for 60h. The size of the MAG- spheroids was measured every hour under the microscope (LEICA, 4x objective).

For the compressed spheroids, the resulting deformation is symmetrical along the axis of the magnetic gradient (top and side views of the MAG+ spheroids are shown in Figure S7-4). The volume of the MAG+ spheroids is thus retrieved using the Guldin theorem: $V = 2\pi S_{1/2} d$, with $S_{1/2}$ the area of the semi-surface and d the distance between the centre of mass of the semi-surface and the rotation axis of the spheroid. The MAG- spheroids are spherical in shape, with a volume $V=4\pi R^3/3$, where R is the spheroid radius (respectively n=2, n=9).

AlamarBlue metabolic assay

The metabolic activity of the MAG+ and MAG- spheroids was quantified using the alamarBlue assay. For both conditions, the assay is performed 2 and 3 days after spheroids formation (day 3 and 4, respectively). For both conditions, the assay is performed on single spheroids, for 3h, within 100 μL of solution.

Cryosection and immunofluorescence

Spheroids were fixed with paraformaldehyde (PFA, 4% in PBS, from Alfa Aesar, J61899) for 1h at room temperature (RT), then conserved in PBS at 4°C. MAG+ spheroids are fixed in the presence of the permanent magnet. For cryo-sectioning, they were embedded in Optimal Cutting Temperature compound (O.C.T. compound, from VWR Chemicals, ref 361603E) for 1h at RT, then frozen in iso-Pentane (GPR Rectapur, from VWR, ref 24872.260), cooled down in liquid nitrogen, and stored overnight at -20°C. The day after, 20 μm cryosections were cut at the centre of the spheroids, in the direction of the magnetic compression for the MAG+ spheroids. For immunofluorescence processing, cryosections were permeabilized with Triton (Sigma-Alrich, Triton X-100, dilution 1:1000 in PBS) for 15min at RT. Non-specific interactions were blocked using a solution of 5% Bovine Serum Albumin (BSA, Sigma Life Science, 05479) in PBS, for 1h at RT. MMP9 protein was labelled using primary rabbit polyclonal anti-MMP9 (Abcam, ab38898, dilution 1:200 with 0.5% of BSA, overnight at 4°C), and Cleaved Caspase-3 monoclonal rabbit anti-Cleaved-Caspase-3 antibody (From Cell Signaling, 5A1E, 1:200 with 0.5% BSA in PBS, overnight at 4°C). Both were coupled with anti-rabbit secondary antibody (Molecular Probes, Alexa Fluor 488 goat anti-rabbit IgH (H+L), A11008, dilution 1:200 with 0.5% BSA in PBS, 2h at RT). Ki67 protein was labelled using anti-Ki67 antibody (Abcam, Ab15580, rabbit polyclonal), coupled with an anti-rabbit Polymer Detection System (Leyca, Novolink™ DAB (Polymer) kit). Nuclei were labelled using 4',6-diamidino-2-phenylindole (DAPI, fom Sigma-Aldrich, D9564, 1 μg/mL in PBS, 30min at RT). All the samples were mounted (Sigma-Aldrich, Fluoromount Aqueous Mounting Medium, F4680) and stored at 4°C after gelation of the mounting medium.

Microscopy and image analysis

Microscopy was achieved using spinning-disk confocal microscopy (Olympus JX81/BX61 device, Yokogawa CSU device spinning-disk microscope (Andor Technology), 60X oil objective (Olympus)).

Images were processed using ImageJ open source software (Version 2.0.0-rc-68/1.52i). The stitching of the images was performed using the "Grid/Collection Stitching" plugin (Preibish et al. Bioinformatics (2009)).

The detection and the localization of the Ki67-positive nuclei were performed using the "TrackMate v.3.8.0" plugin (Gaussian Log detection, (36)). The quantification of the normalized distance $\langle R/R_0 \rangle$ used a home-made Matlab Script (MATLAB_R2016a

(9.0.0.341360), License Number: 830200). Briefly, for each cryosection, the coordinates (X,Y) of the boundaries and of the centre of the samples were measured using the Selection tool on ImageJ. Using the coordinates detected for each Ki67-positive nucleus, a vector corresponding to the distance between the Ki67-positive nucleus and the sample was created (R in Figure 7-2C). The R_0 distance corresponds to the average vector of the boundary framing the vector of the Ki67-positive nuclei. $<R/R_0>$ corresponds to the ratio of the norms of the two norms. To quantify the ratio of proliferating cells, the total number of nuclei was assessed by measuring the density of nuclei for 5 to 10 chosen areas per sample. Thus nucleus density was multiply by the sample surface, giving the total number of nuclei.

To quantify the radial expression of MMP-9 (D_{MMP-9}, example shown in Figure S7-5), each image of cryosections was virtually divided in 10 areas, separated by a $\pi/5$ angle. For each angle, D_{mmp-9} was defined as the maximal radial localization from the edge of the sample to its centre.

The number of cells positive to Cleaved Caspase-3 was quantified manually. Again, the ratio of positive cells was assessed by measuring the average nuclear density of each sample, allowing us to measure the total number of nuclei on the slide.

The nuclei density was quantified on cryosections. For each cryosections, the number of nuclei inside 5 to 10 chosen area was quantified. For each samples, the resulting nucleus density is the average density of the chosen areas. Two regions of the cryosections were addressed separately: the centre (spheroid core) and the periphery (40 μm, first fourth cell layers).

Transmission electron microscopy

MAG+ and MAG- spheroids were fixed 2 days after formation, and upon magnet application for the MAG+ spheroids, and processed for TEM analysis. Fixation was performed in 5% glutaraldehyde diluted in 0.1 M cacodylate buffer for 1 hour, and washed with cacodylate buffer. Samples were next contrasted with Oolong Tea Extract (OTE) 0.5% in 0.1 M Na cacodylate buffer, post-fixed with 1% osmium tetroxide containing 1.5% potassium cyanoferrate, dehydrated in ethanol (30% to 100%) and embedded in epoxy resins. Ultrathin sections (70 nm) were observed with a Hitachi HT 7700 TEM operating at 80 kV.

In-vivo experiments

In-vivo experiments were performed with respect to standard European-community-guideline requirements for laboratory-animal care and use. We used five-week-old female Wild Type mice (WT, 8 to 10 mice per groups), previously acclimated for two weeks.

MAG- and MAG+ spheroids were cultured for two days after formation respectively without or with magnet application. To ensure the integrity of the spheroids as well as the absence of additional mechanical stress, the injection was performed using an enlarged tip instead of a syringe. The spheroids were easily manipulated by gently aspiring them inside the pipette. For both conditions, 10 spheroids were suspended in 200 μL of supplemented DMEM. Under anaesthesia, a small incision (close to 1 cm) was performed in the middle of the peritoneum of each mouse, and 10 spheroids per mice were deposited inside the cavity. After the injection, the peritoneum was stitched with medical string. Mice were sacrificed 13 days after the injection, and the Peritoneal Carcinomatosis Index was quantified. To do so, the abdominal cavity was opened and virtually divided in 9 distinct regions (from 0 to 8). The guts represent 4 additional regions. A score from 0 to 3 was allocated for every region, and the sum of the 13 scores gave the total PCI for each mouse (37). A score of "0" corresponds of a complete absence of cancer nodule. "1" corresponds to 1 to 2 nodules in the region, with cumulative sizes from 1 to 2 mm. "2" corresponds to 1 to 2 nodules, with cumulative sizes from 2 to 4 mm. Finally, a score of "3" corresponds to nodules over 4 mm or more than 10 nodules. A PCI below 10 represents a limited carcinomatosis, a PCI between 11 and 20 represents an intermediate carcinomatosis and an advanced carcinomatosis corresponds to a PCI above 20.

Statistical analysis

All quantitative results are represented as Mean Value +/- Standard Deviation (STD). The Wilcoxon rank sum test was used for small sample numbers ($n<5$). For larger number of samples, the homoscedastic or the heteroscedastic of the samples was tested, and the corresponding two-tailed Student Test was performed. p-value is used to indicate the statistical significance of the results ($*p < 0.05$, $**p < 0.01$,$***p < 0.001$).

Results

Tumor spheroid Magnetic Formation and Compression

The magnetic labelling of mouse colon cancer cells (CT26), corresponded to about 11 pg of iron internalized per cell, providing each cell with a magnetic moment at saturation of about $7x10^{-13}$ $A.m^2$. Upon exposure to the permanent magnet used in the set-up (B=520 mT; gradB = 177 $T.m^{-1}$), each magnetic cell then experienced a magnetic force close to 120 pN.

The magnetic molding procedure (34) (Figure 7-1A) then consisted in aggregating in spherical wells 250 000 CT26 cells, as described in details in the Methods section. Thus method delivered overnight spherical tumor spheroids, with a well-defined diameter of 878 ± 54 μm (Figure 7-1B). Such large sizes still gave viable spheroids not presenting apoptotic cells for a typical culture time of 48h (Figure S7-6).

The spheroids magnetic moments, was close to $M=1.7x10^{-7}$ $A.m^2$ at magnetic field saturation. The application of the permanent magnet then results in a magnetic force (F = M.grad(B)) on each spheroid in the range of 30 μN. This force is a volume force, which acts throughout the volume of the spheroid such as gravity, and is close to $9x10^4$ $N.m^{-3}$. This would be equivalent to 110 g, or to a pressure applied to the first layer of the cells forming the spheroid close to 10 Pa.

Figure 7-1B shows two typical spheroids over three days after their formation, either subjected to a permanent field (MAG+) or left at growing free within non-adhesive culture dish (MAG- spheroid). It evidences the very large anisotropic magnetic deformation of the MAG+ spheroid. Electron microscopy was used to observe the impact of the magnetic force on the intracellular magnetic nanoparticles (Figure 7-1C). For both MAG- and MAG+ conditions, the nanoparticles were stored within the endosomes. These magnetic endosomes were spread homogeneously inside the cells for the MAG- condition, whereas a well-defined alignment along the direction of the magnetic field gradient clearly emerged for the nanoparticle-containing endosomes in the MAG+ condition.

Figure 7-1D shows the temporal evolution of average relative diameter and volume (percentage of their value at time zero) of both MAG+ and MAG- spheroids. The MAG+ spheroids experienced first an important and rapid deformation (40% decrease in diameter within 20 minutes, 50% decrease within 30, Figure S7-3), which then stays stable for 35h. This is followed by a longer-term slower deformation. The volume remained constant during the first hours of deformation and slightly decreased afterwards down to 75% of its initial

value. Comparatively, both diameter and volume of the MAG- spheroids slightly rose over time, with a 3% increase in diameter, and 10% in volume.

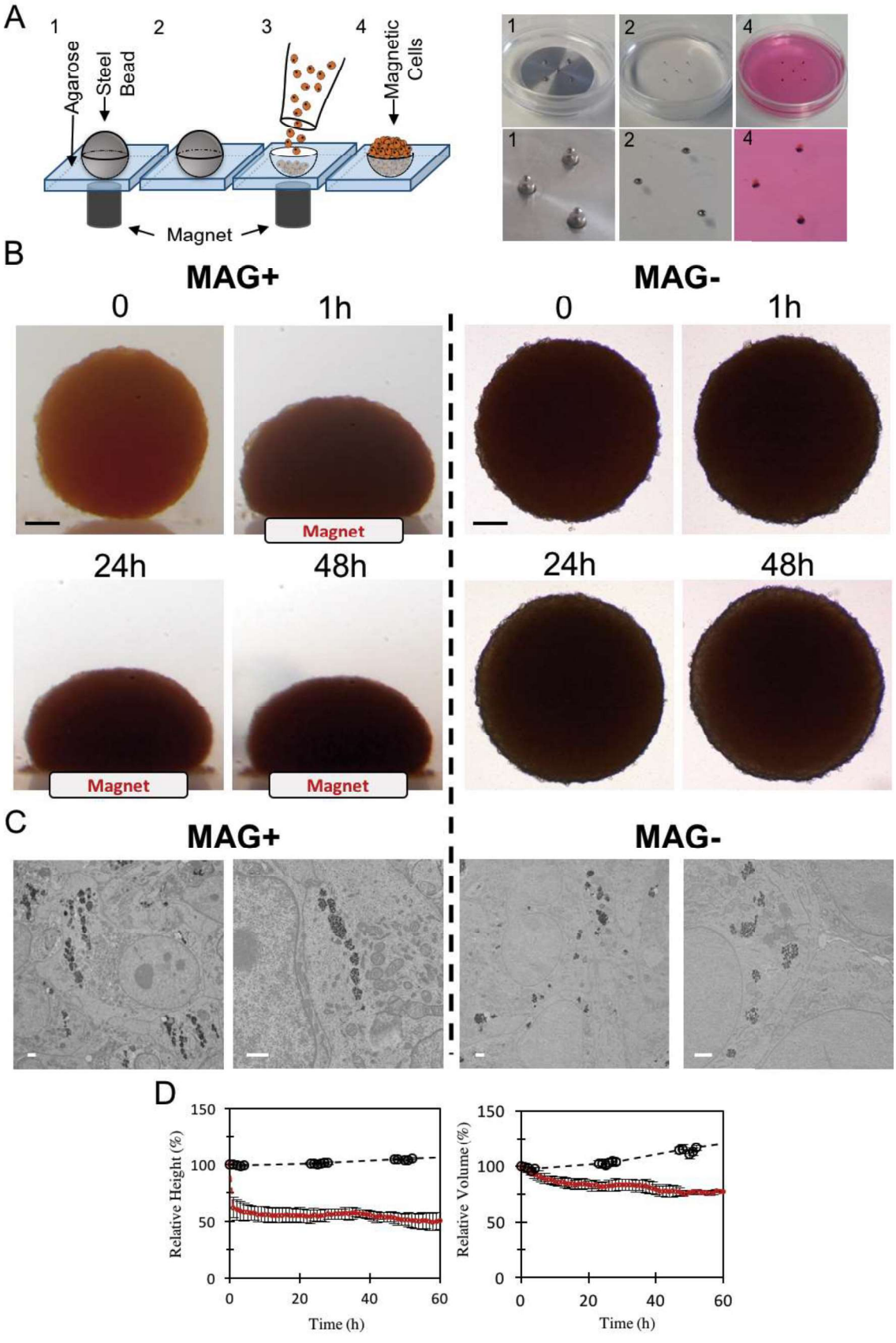

Figure 7-1: Magnetic formation (molding) and compression of CT26 spheroids. A) Principle of spheroids magnetic molding, depicted with a scheme on the left and pictures on the right. 1 mm agarose molds were made using 1 mm magnetic beads (pictures 1 and 2). 250000 magnetically labelled CT26 were deposited on top of the molds and attracted within the molds by the cylindrical magnets placed below each mold. Aggregates were then matured overnight (pictures 3 and 4). **B)** Representative pictures of two molded aggregates. On the left, the spheroid was placed on a top of a permanent magnet (MAG+ condition). On the right, the spheroid was growing without external stimulation (MAG- condition). For both, time-lapse images are shown. Scale bar = 200 μm **C)** Transmission electron microscopy of MAG+ and MAG- spheroids. The magnetic endosomes of the MAG+ spheroids are aligned along the field gradient, whereas the in the MAG- condition, the endosomes containing nanoparticles are homogeneously distributed within the cell cytoplasm. Scale bar = 1000 nm. **D)** Temporal evolution of the relative height and relative diameter of MAG+ (red curve) and MAG- spheroids (black curve). The magnetic compression results in a quick decrease of MAG+ relative height (50% after 2h). The relative volume was stable for the first hour, followed by slow decrease of the relative volume (25% after a few hours). Both relative height and volume of the MAG- spheroids increase slowly (respectively n=2, n=9).

Impact of the magnetic compression on cell proliferation

Both MAG- and MAG+ spheroids were stained for the proliferation marker Ki67 48h and 72h after their formation (corresponding to three-days and four-days matured spheroids). Representative images are presented in Figure 7-2, with nuclei DAPI-labelled in blue and Ki67 antibody-detected in red. Figure 7-2A shows the whole spheroids at day 3 and Figure 7-2B closes up on the periphery region at day 3 and day 4. Qualitatively, the cells with nuclei positive to Ki67 appear more to be found at the centre for the MAG+ spheroids, while they are mainly located at the periphery for the MAG- spheroids. To quantify this, the positions of all nuclei and of Ki67 positive nuclei were detected, as illustrated in Figure 7-2C for typical images at day 3 and day 4. Both the percentage of proliferating nuclei and the localization of the proliferating cells could be extracted from these analyses.

At both day 3 and day 4, the MAG+ spheroids exhibited an increase in the proportion of proliferating nuclei as compared to the MAG- spheroids (Figure 7-3A). As expected, the proportion of proliferating nuclei decreased between 48h and 72h for both conditions.

To overcome the changes in spheroid shape, the normalized distance $\langle R/R_0 \rangle$ was introduced (see Figure 7-2C for their schematic definition), R being the distance from the centre of the spheroid of any Ki67-positive nucleus and R_0 being the distance from the centre to the edge of the spheroid at same angle (equivalent to the local spheroid radius). Therefore $\langle R/R_0 \rangle$ stands for the normalized local position of any Ki67-positive nucleus and was quantified at days 3 and 4 (Figure 7-3B). For both dates, the average $\langle R/R_0 \rangle$ is lower for the MAG+ spheroids

than for the MAG- ones, revealing quantitatively a shift of the proliferation toward the centre of the spheroids, as observed in Figure 7-2.

All individual $<R/R_0>$ values analysed for the same condition were next pooled and the resulting cumulative distributions are presented in Figure 7-3C. At both day 3 and day 4, over 70% of the $<R/R_0>$ for the MAG- spheroids correspond to values between 0.8 and 1, which corresponds to the periphery of the spheroids. On the other hand, for the MAG+ spheroids, the $<R/R_0>$ values are distributed more equally throughout the spheroids, confirming the shift of proliferation toward the centre.

Finally, the proliferation was quantified at the whole spheroid level, by detecting its global metabolic activity using alamarBlue assay (Figure 7-3D). The average proliferation of the MAG- spheroids at day 3 is taken as reference. At day 3, the increase in the metabolic activity of the MAG+ spheroids (n=26) compared to the MAG- ones (n=15) is over 30 % and significant ($p<0.005$). At day 4, the increase reached 60% between the two conditions (n=14 for MAG-, and n=15 for MAG+, $p<0.005$).

Compared to free growing spheroids at Day 3 (48h after the removal from the molds), thus large spheroid deformation was also associated with a small number of cells positive for Cleaved Caspase-3 (less than 5% of the cells, Figure S7-6).

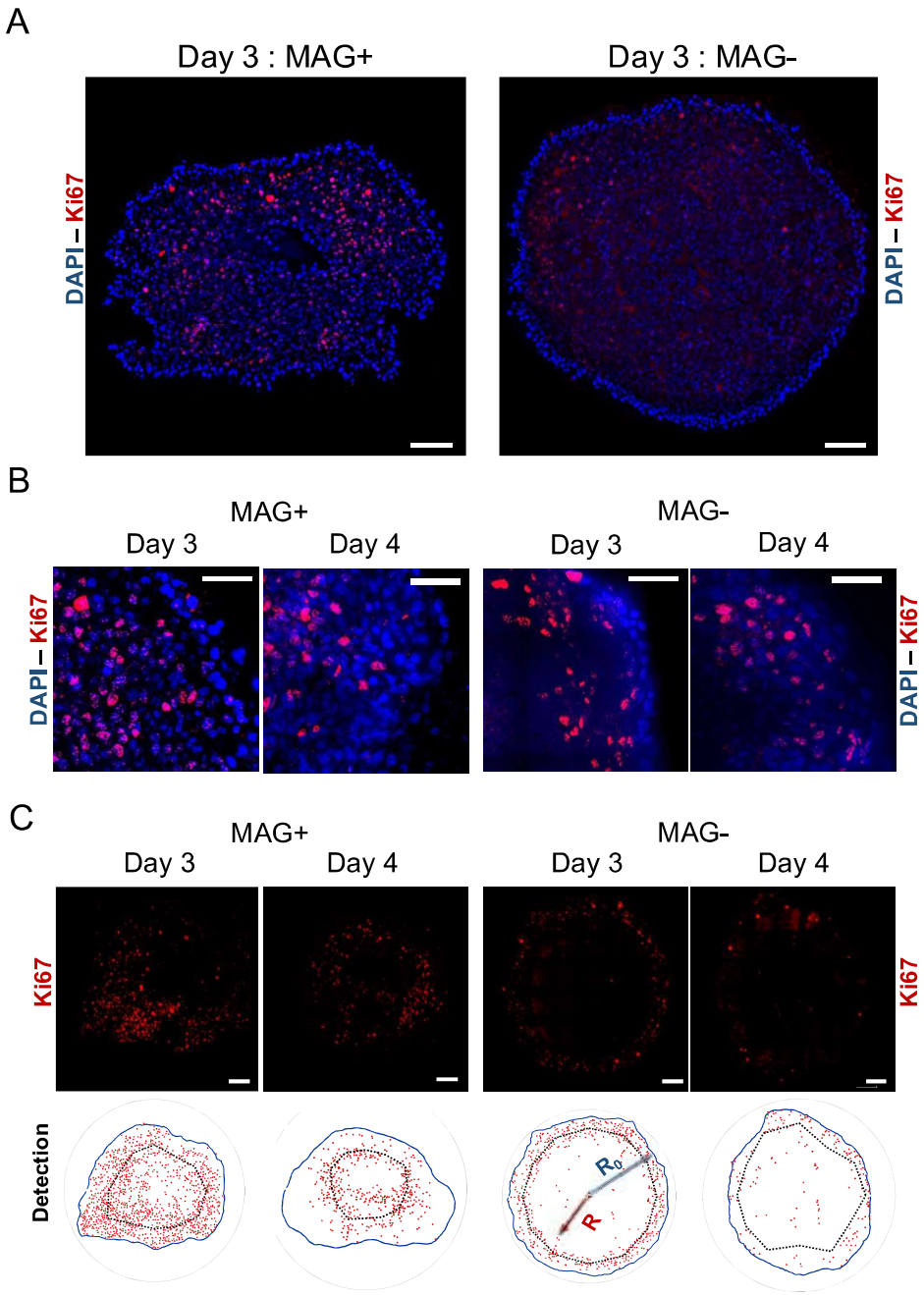

Figure 7-2: Ki67 labelling and detection at day-3 and day-4 for MAG+ and MAG- spheroids. A) Cryosections of CT26 spheroids compressed (MAG+) or let free for two days. The nuclei are labelled in blue (DAPI) and the proliferation marker Ki67 is labelled in red. The proliferative nuclei of the MAG- spheroids are located on the edges, whereas the image evidences proliferation toward the centre of the MAG+ spheroid. Scale bars: 100 μm. **B)** Close up images at the edges of MAG+ and MAG- spheroids cultured for two and three days after formation (day 3 and day 4, respectively). Nuclei are labelled in blue and Ki67 in red. Scale bar = 50 μm. **C)** Cryosections at day-3 and day-4 for MAG+ and MAG- spheroids. Ki67 is labelled in red. The bottom analysis presents typical detection of the Ki67-positive nuclei for the different conditions. The red dots represent the Ki67-positive nuclei, the blue line the edges of the cryosection, and the dashed line represents the average localization of the Ki67-positive nuclei for each cryosection. Scale bar = 100 μm.

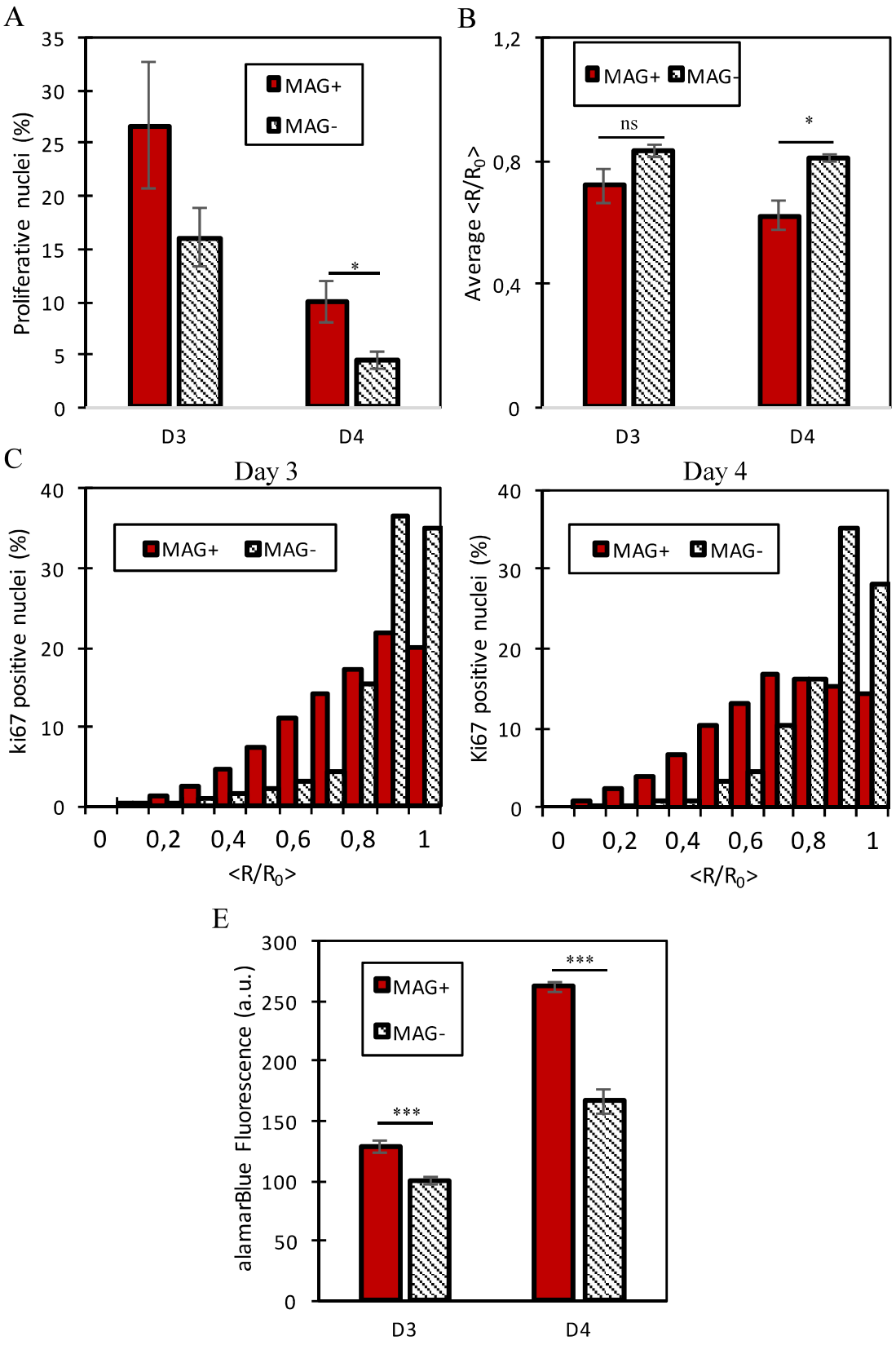
A
Proliferative nuclei (%)
MAG+
MAG-
*
D3
D4
B
Average <R/R0>
MAG+ MAG-
ns
*
D3
D4
C
Day 3
Day 4
ki67 positive nuclei (%)
Ki67 positive nuclei (%)
MAG+ MAG-
<R/R0>
E
alamarBlue Fluorescence (a.u.)
MAG+
MAG-
***
***
D3
D4

Figure 7-3: Quantification of the proliferation for compressed (MAG+) or free (MAG+) spheroids. A) Percentage of proliferating cells for MAG+ and MAG- spheroids (respectively red and striped bars) cultured for two and three days after formation (day 3 and day 4, respectively). MAG+ spheroids presented an increase in the number of proliferating cells for the two times. The resultant proliferation is the ration between the number of Ki67-positive nuclei and the total number of nuclei (At day 3, n=3 for both conditions, at day 4, n=3 for MAG-, n=5 for MAG+, $p<0.05$). **B)** Average of the normalized distance $\langle R/R_0 \rangle$ for the two conditions at the two times. This distance represents the localization from the spheroid centre of a proliferating nucleus. It decreased for the MAG+ spheroids, demonstrating an increase of the proliferative nuclei toward the MAG+ spheroid centre (n=3 spheroids for both conditions at day 3; n=3 and n=5 spheroids at day 4 for MAG+ and MAG- conditions, respectively; $p < 0.05$). **C)** Cumulative distributions of the normalized distance $\langle R/R_0 \rangle$. To obtain such distributions, the Ki67 localizations were pooled for every cryosections of a single condition. These distributions demonstrate a shift of the proliferation toward the centre of the MAG+ spheroids, whereas the MAG- distribution is grouped around 1, which represents nuclei localized at the edge of the cryosection (At day 3: n=1915 Ki67-positive nuclei for the MAG+ spheroids, n =2653 Ki67-positive nuclei for the MAG- spheroids, $p<0.005$. At day 4, n=937 Ki67-positive nuclei for the MAG+ spheroids, n=2359 Ki67-positive nuclei for the MAG- spheroids, $p<0.005$). **D)** Metabolic alamarBlue assay. The relative fluorescence measured is shown for MAG+ and MAG- spheroids (red and striped bars, respectively) for day 3 and day 4. For both times, the proliferation of MAG+ spheroids is increased (At day 3, n=15 for the MAG- spheroids and n=26 for the MAG+ spheroids, $p < 0.005$. At day 4, n=15 for MAG+ and n=14 for MAG-, $p<0.005$).

Impact of the magnetic compression on the metalloproteinase MMP-9

Figure 7-4 shows the staining of MMP-9 on MAG- and MAG+ spheroids labelled at day 3. Whereas the observations of the MAG- spheroids evidenced a MMP-9 localization on the periphery, the images of the MAG+ spheroids revealed the presence of MMP-9 all throughout the spheroid, and in particular at its centre.

For both conditions, the MMP-9 radial localization was quantified (Figure S7-5) and provided the average distance of the MMP-9 expression, from the edge to the spheroids centre, with values of 90.6 ± 18.8 μm and 39.3 ± 3.9 μm for MAG+ and MAG- conditions, respectively. It clearly evidences a relocalization of MMP9 toward the centre of the spheroids upon magnetic compression.

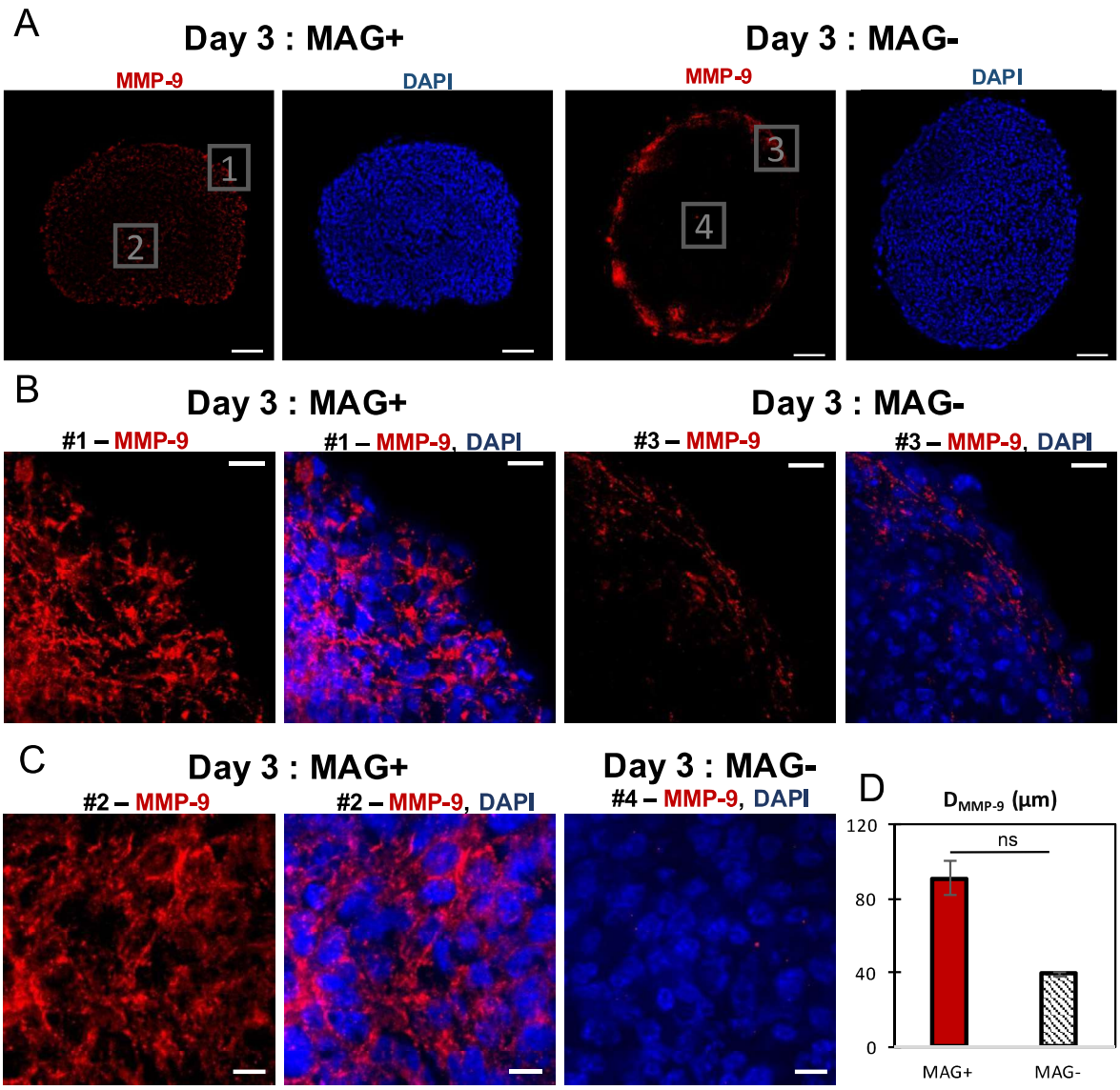

Figure 7-4: MMP-9 labelling of MAG+ and MAG- spheroids at day 3. A) Cryosections of MAG+ and MAG- spheroids cultured for two days after formation. MMP-9 is labelled in red, and the nuclei are labelled in blue (DAPI). For the MAG- spheroid, MMP-9 was mostly expressed on the edges. The MAG+ spheroids showed significant MMP-9 expression toward the centre. Scale bar = 100 µm. **B)** Close up images at the edges of the cryosections: MMP-9 only (red) and merged images (MMP-9 in red, DAPI in blue). Scale Bar = 20 µm. **C)** Close up images for MAG+ (MMP-9 only in red and merge image with DAPI in blue) and MAG- spheroids (merge image of MMP-9 in red and DAPI in blue). Scale bar = 10 µm. **D)** Localization of MMP-9 for the two conditions. The maximal radial MMP-9 localization, from the edges toward the spheroid centre was quantified. The average MMP-9 depth was higher for the three-day MAG+ spheroids (red bar) than for the MAG- spheroids (striped bar), n=2 and n=3, respectively.

In-vivo evaluation of the metastatic potential of the MAG+ and MAG- spheroids

In order to estimate the impact of the magnetic compression on the spheroids behaviour once in a realistic environment, an in-vivo experiment was conducted according to protocol described in Figure 7-5A. Briefly, MAG+ and MAG- spheroids were cultured for two days after their formation, with or without the magnet application, respectively. Then, 10 spheroids of each condition were injected in mouse peritoneum, representing a total of about 2.5 million of injected cells. 4 to 5 mice were injected per condition, and the experiment was repeated twice. The mice were sacrificed 13 days after the injection, and the peritoneal cancer index (PCI) was evaluated as a read out of the cancer propagation (Figure 7-5B). Examples of two different zones for 2 different mice per conditions are shown in Figure 7-5C. On average (Figure 7-5D), mice injected with MAG+ spheroids presented a PCI of 20.8 ± 2.7 whereas mice injected with MAG- spheroids showed a PCI of 13.2 ± 3.7 ($p < 0.005$). Such PCI values correspond to advanced and intermediate carcinomatosis, respectively.

Additionally, hepatic tumors were observed for 40% of mice injected with MAG+ spheroids, while none could be detected within mice injected with the MAG- spheroids. As illustrated in Figure 7-5E, these hepatic tumors were Ki67-positive metastases, demonstrating the proliferation of thus obtained metastases. In addition, Prussian blue staining evidenced the presence of iron oxide nanoparticles located at the center of the hepatic metastasis, confirming that they originate from the injected MAG+ spheroids.

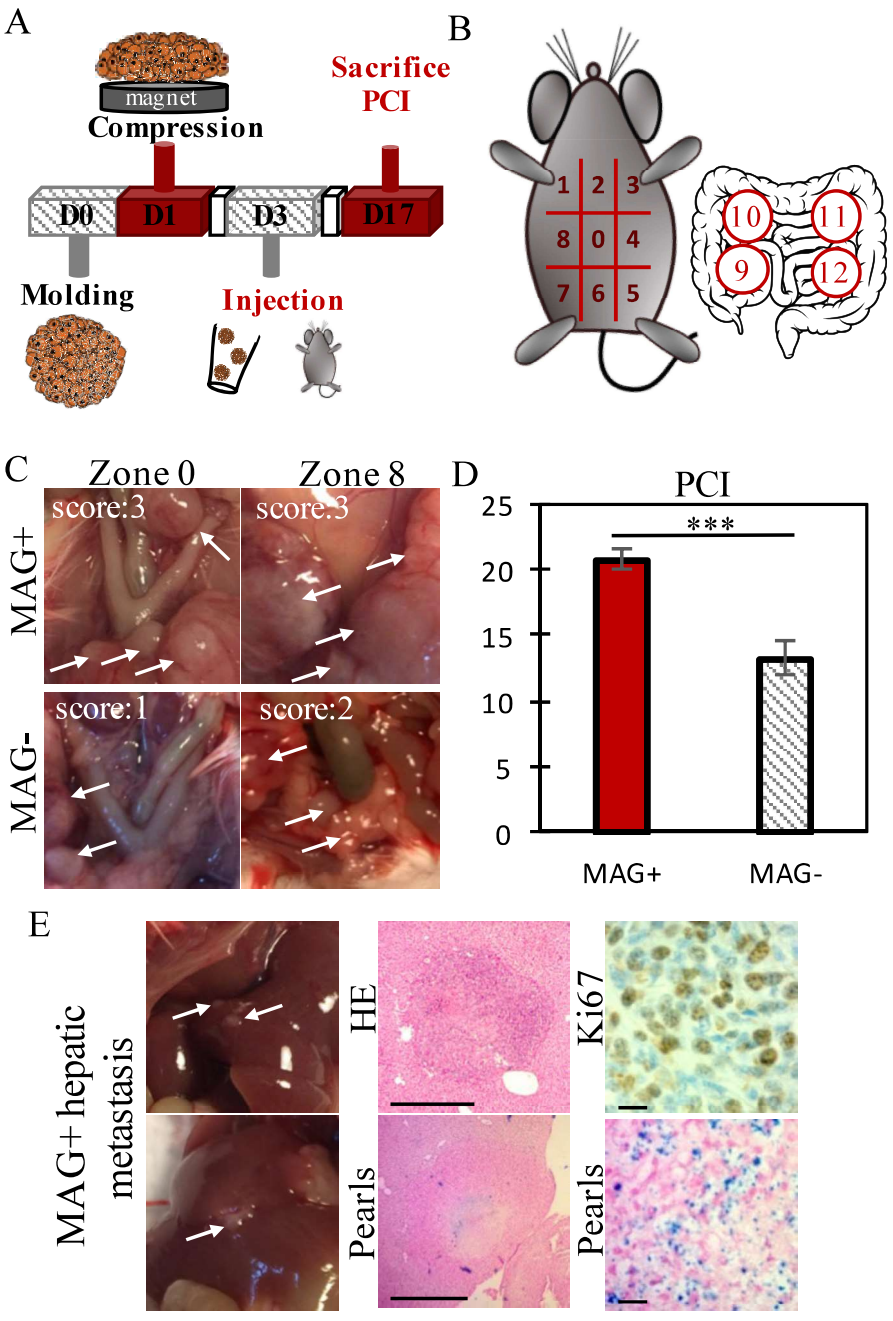
A
magnet
Compression
Sacrifice
PCI
D0
D1
D3
D17
Molding
Injection
B
1
2
3
8
0
4
7
6
5
10
11
9
12
C
Zone 0
Zone 8
MAG+
MAG-
score:3
score:3
score:1
score:2
D
PCI
***
25
20
15
10
5
0
MAG+
MAG-
E
MAG+ hepatic metastasis
HE
Ki67
Pearls
Pearls

Figure 7-5: Evaluation of the carcinomatosis progression in mice injected with MAG+ or MAG- spheroids 3 days after their formation. **A**) Overview of the experiment. Magnetically molded CT26 spheroids were cultured for two days with (MAG+ spheroids) or without (MAG- spheroids) a magnet. Then, for each condition, 10 spheroids per mice were injected in the peritoneum. Mice were sacrificed 13 days later, and the Peritoneal Carcinomatosis Index (PCI) was evaluated. **B)** PCI evaluation: the peritoneum is divided in 13 regions. Depending on the number and the size of tumor nodules, a score between 0 to 3 is allocated for each region. The sum of the scores provides the PCI for each mouse. **C**) Typical images during PCI analysis. The white arrows indicate tumor nodules. For the two regions of the MAG+ mouse, a score of 3 was allocated. Scores of respectively 1 and 2 were allocated for the regions n°0 and n°8 of the MAG- mouse. **D)** Average PCI for mice injected with MAG+ spheroids (red bar) and MAG- spheroids (striped bar). The mice injected with the compressed spheroids (MAG+) experienced an increase in the cancer progression (two different experiments, in total n=8 and n=10 for MAG+ and MAG-, respectively, $p < 0.005$). **E)** Immunohistological staining of hepatic metastasis (white arrows) within mice injected with MAG+ spheroids. The top middle picture shows haematoxylin-eosin staining (HE, cytoplasm and nucleus labelling) of a metastasis section of approximately 800 μm in diameter (scale bar 500 μm). The bottom middle image shows a Prussian blue staining (iron labelling, scale bar = 500 μm). Iron is clearly detected at the centre of the metastasis, indicating that it originates from the injected cells. The right images present a magnification of a Ki67 staining and of a Prussian blue staining. The metastases were proliferating (Ki67-positive) and originated from the injected cells (Prussian blue positive). Scale bar = 20 μm for the right images.

Discussion

Cell magnetic labelling with iron oxides nanoparticles has recently started to be used to form and to mechanically stimulate cellular assemblies (38) (39) (40) (41). The nanoparticles are internalized within the cells through endocytosis pathway, are stored inside the (33), without interfering with cell metabolism and functions, including differentiation (39). Herein, the magnetism conferred to the cells by the incorporation of the magnetic nanoparticles was used to form cancer cells spheroids by magnetic molding (34). Comparatively to common spheroid formation methods, the magnetic molding stands out by delivering overnight spheroids of any size, even large ones up to 2 mm diameter. In the present study, the molds size was chosen at 1 mm to get closer to carcinoma nodule sizes (clinically found between 1mm to few cm) (42). Due to the short in vitro culture time, no necrosis was detected at the core of the spheroids: intact nuclei at the spheroids centre are observed in Figure 7-2 and Figure 7-4, and the labelling of Cleaves Caspase-3 demonstrated no cell apoptosis (Figure S7-6). Additionally, spheroid growth slightly continued in the MAG- conditions (Figure 7-1) and the their compactness still managed to increase at spheroid core over the first days, in the same range than the one obtained with free growing encapsulated smaller aggregates (21).

The magnetic cell labelling next served to mechanically stimulate the spheroids. Combining high magnetic field gradient with high spheroid magnetization resulted in unprecedented spheroid compression. Indeed, other mechanical stimulation studies used smaller spheroids, subjected mostly to growth confinement (20) (21) (22) (43) (24) (29). To the best of our knowledge, there is not yet tested alternative to the proposed approach to impose such a significant anisotropic mechanical stress to large spheroids. Besides, such tumor compression appears clinically relevant with respect to the chirurgical implantation technique of a colonic self-expending metal stent (SEMS). Indeed, this surgery consists in applying a mechanical constraint on one side of a colon-developed tumor, in order to re-open the colon lumen. The magnetic spheroid compression mimicked the deformation experienced by the on-site tumor, where the introduction of a SEMS was evidenced to lead in mice to the re-opening of a lumen obstructed at more than 75% (17).

The compression of the magnetic spheroids triggered an increase in the number of Ki67-positive nuclei, and a delocalization of proliferation toward the centre of the spheroids. This was consistent with an increase of the cells metabolic activity triggered by the magnetic

compression. Proliferation in constrained spheroid remains yet a controversial issue. On one hand, for spheroids confined in isotropic conditions, Ki67 expression decreases in the core, in correlation with an increase of the cell apoptosis (21) (22). On the other hand, the effect of an anisotropic constraint is still debated. Cheng et al. (20) demonstrated a decrease in Ki67 expression while it was increasing in Desmaison et al. (24). Interestingly, the latter applied an anisotropic confinement closer to the magnetic anisotropic compression experienced here: confinement was made on large spheroids (initially 300 μm in diameter), one part of the spheroid remained unconstrained (free surface) and the final shape and size were close to the magnetically compressed spheroids (300x600 μm rod shape). Such differences in the proliferative behaviour could be related to a blocking of the cell division cycle. For instance, Delarue et al. (43) demonstrated that upon confinement, cell division cycle is blocked before the late G1 checkpoint due to an increase of a proliferation inhibitor. Desmaison et al. (24) also demonstrated that despite an increase in Ki67 expression at the core of the spheroids, cell division could be stopped before mitosis. Such cell division cycle alterations caused by mechanical cues have been evidenced in others cell models (44) (45) (46) (47).

This change in the proliferative behaviour was also associated with the presence of a small number of cells positive for Cleaved Caspase-3 (less than 5% of the total number of cells after 48h of compression, Figure S7-6), which is associated with a reversible apoptotic mitochondrial pathway (48). Besides, such number of apoptotic cells was far from the measured proliferating cells (more than 25% for the same date). Also here, the number of Caspase-3 positive cells is far from the one measured in growth confinement experiments (between 40% to 80%) (20) (22).

Finally, a remarkable change in the expression of MMP-9 was evidenced for spheroids subjected to the magnetic compression. During tumor development, cancer cells experience an increased expression of the matrix metalloproteinases MMPs, in order to remodel their surrounding ECM (49). This process participates in the metastatic process, and an increase in MMPs expression is also linked to a hypoxic environment (43) (51) and to a stiffening of the stromal ECM (52) (53). By contrast, the role of mechanical stress on MMPs expression is still open to exploration (54). A compression-triggered increase in MMPs expression was detected with bone cancer cells (30), glyoblastoma and breast cancer cells (19), yet 2D organized as monolayers, or on cells embedded in an ECM-like reconstituted gel. Also worth mentioning, an increase in the expression of MMPs caused by mechanical stress was also demonstrated in fibroblasts (55), or other tissue models such as chondrocyte-like cells (56) and vascular

smooth muscle cells (57). Here, such increase could be related to an enhanced metastatic potency of the cells inside the compressed spheroids, as it is clinically associated with an increase in cancer invasion and a decrease of patient prognosis (58) (59) (60).

Finally the stimulated (MAG+) or free (MAG-) spheroids were injected in mice peritoneal cavities. The PCI was used as a reliable read out of the cancer progression, as previously demonstrated both in animal models (61) and clinical studies (62). Such measurement is commonly performed upon intravenous, subcutaneous or intraperitoneal administration of cell suspensions (63), but more rarely using direct injection of tumor spheroids, which already mimick small cancer nodules. Here, the PCI index measured 13 days after injection demonstrated a significant increase of carcinomatosis in mice injected with the compressed MAG+ spheroids. Besides, several mice injected with compressed spheroids presented hepatic metastasis. The presence of iron in the core these hepatic metastases confirmed that they originate from the initial spheroids. Such organ invasion denotes an increase in the metastatic potency (64).

Finally, the overall results are consistent with what was observed in mice treated with a SEMS, where a decrease of the mouse survival time was observed (40). Clinical studies are still debating on the long-time benefices and the consequences of such a surgical act (65) (66). The results presented here could give insights on the involved mechanism: an anisotropic tumor compression can give rise to an increase in cancer cells proliferation and in the expression of metalloproteases implicated in cancer progression.

Acknowledgment

This work was supported by the European Union (ERC-2014-CoG project MaTissE 648779) for spheroid formation and in vitro evaluation. The in vivo experiment was supported by Lariboisière Hospital. We would like to thank Marylin Favier (Plate-Forme HistIM, Institut Cochin, Paris) for the Ki67 immunolabelling; Christine Péchoux for the TEM imaging (platform TEM, INRA, Jouy-en-Josas); Rachid Kaci for the mouse tumor hepatic histology (Anatomie et cytology pathologiques, Hôpital Lariboisière, Paris).

Supplementary information

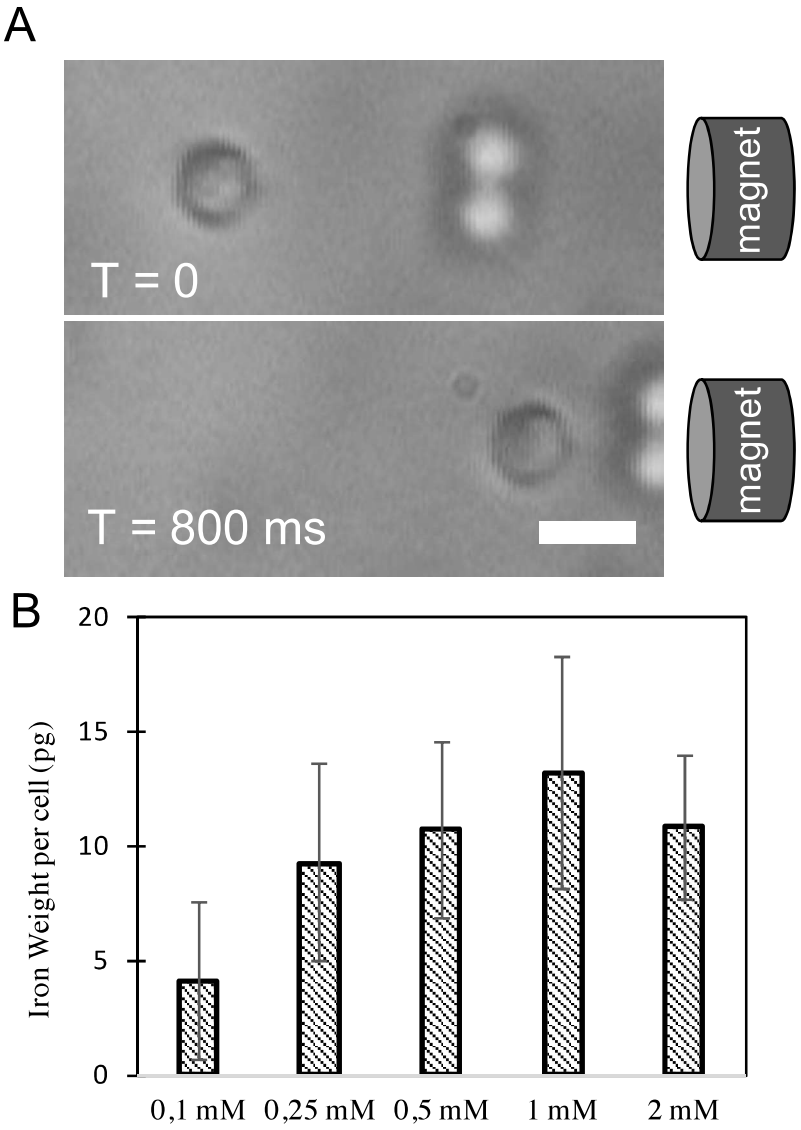

Figure S7-1: Magnetophoresis of magnetic CT26 cells. A) In suspension, a magnetic CT26 was attracted by a permanent magnet (B = 135mT, grad(B) = 17 $T.m^{-1}$). The forces were exerted on the cell: the Stokes law, and the magnetic force ($F = M_{cell}*gradB$). The cell velocity allowed to measure its magnetic iron weight. Scale bar: 20 mm. **B)** Cells were labelled with solutions presenting increasing NPs concentrations during the night (18h). The cells were washed, put at rest and detached to perform magnetophoresis. For the same labelling time, concentrations above [Fe] = 0.5 mM resulted in the same iron weight per cells.

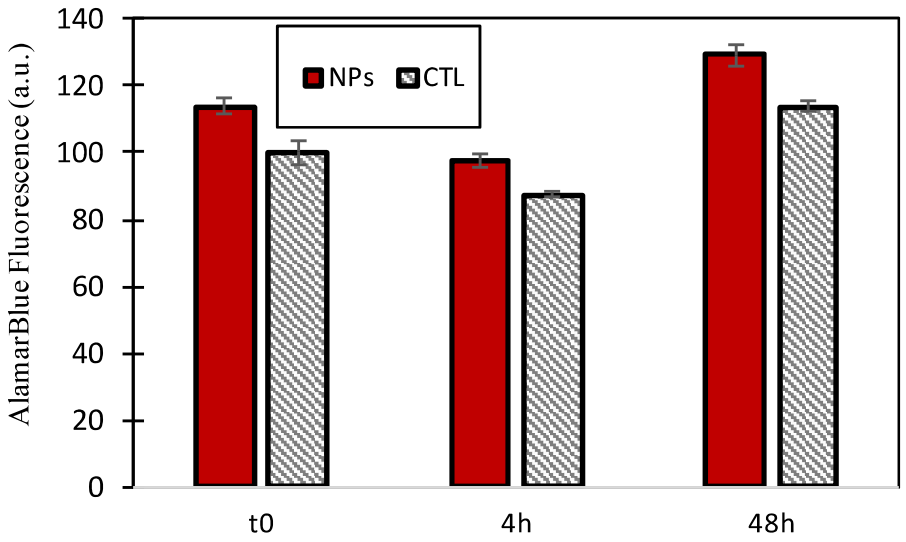

Figure S7-2: Viability of magnetically labelled cells. AlamarBlue assay was performed on control CT26 (CTL) or magnetically labelled CT26 (NPs) ([Fe] = 0.6 mM). Cell viability was tested right after the labelling, 4h and 48h after the labelling. If an increase in the labelled cell metabolism was noticed, cell viability was preserved.

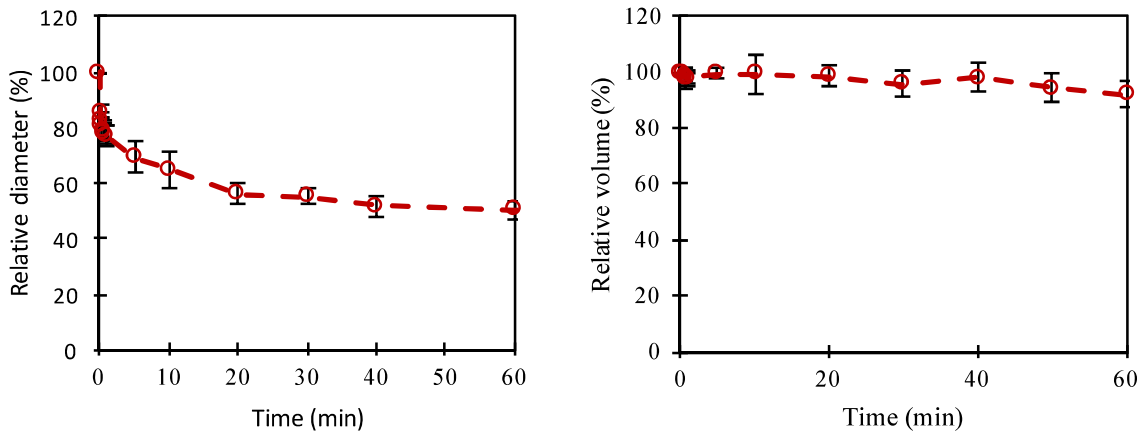

Figure S7-3: Time evolution of relative diameter and relative volume of compressed CT26 spheroids for short-time deformations. The deformation was observed at 1 frame per 10 seconds the first minute, at 1 frame per 5 minutes within 10 minutes of deformation, and at 1 frame per 10 minutes until 1h of deformation. The relative diameter presented a quick deformation, whereas the volume was constant within the first hour of the deformation (n=2).

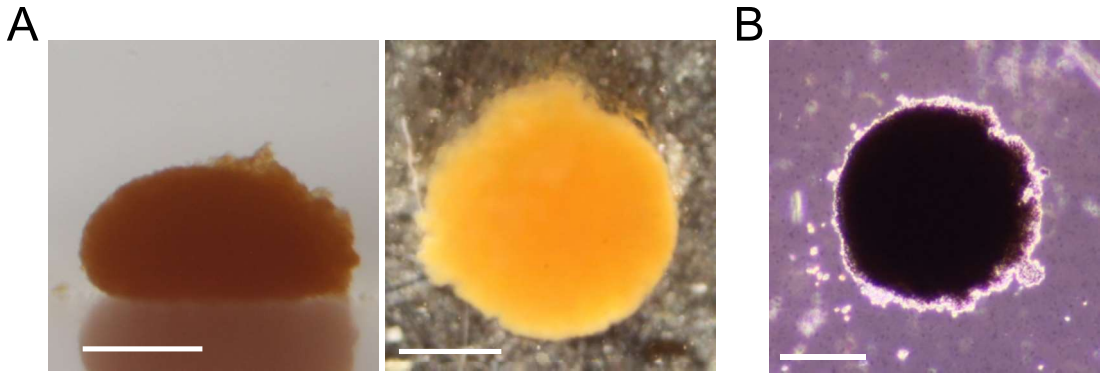

Figure S7-4: Side and top views of magnetically compressed CT26 spheroids. A) A spheroid was subjected to a short magnetic compression (10 min of magnet application). Left picture: side-view of the spheroid without application of the magnet. Middle Picture: side-view of a 1h flattening. Right picture: Top view of a 1h flattening. The flattening results in a symmetric deformation. Scale bars = 500 μm. **B)** Top-views of a CT26 spheroid subjected to a 48h magnetic compression. The resultant deformation was symmetric. Scale bars: 500 μm.

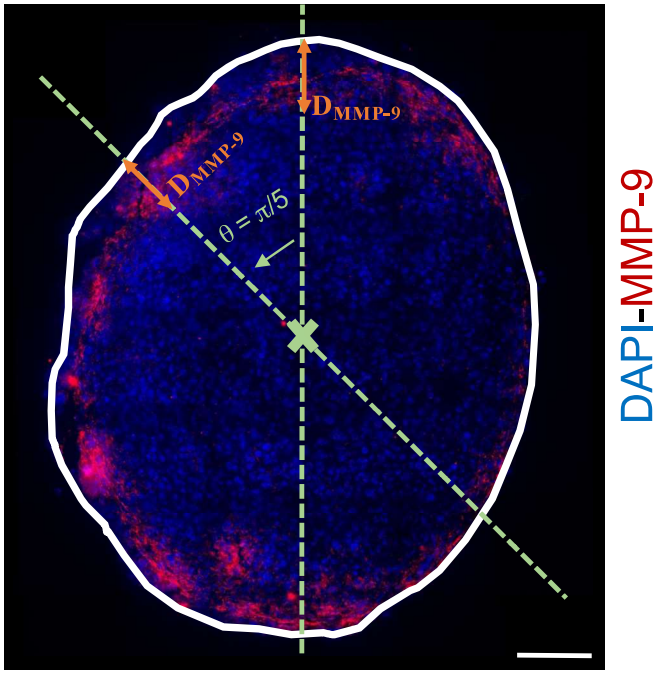

Figure S7-5: Quantification of the MMP-9 radial localization. The sample was virtually divided in 10 areas separated by a π/5 angle. For each angle, the Radial distance of MMP-9 expression was measured, from the edge to the centre of the sample. MMP-9 is labelled in red and the nuclei in blue (DAPI). The white line represents the sample boundary, the green lines represent the delimitation of two regions distanced of π/5. The orange arrows represent two measurement of the MMP-9 radial localization. Scale bar: 100 μm.

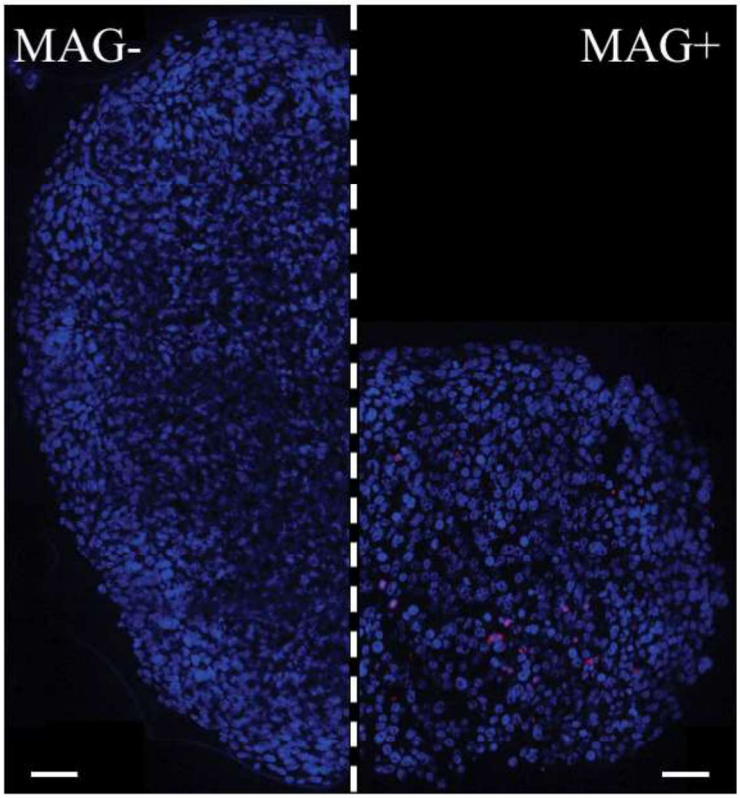

Figure S7-6: Cleaved caspase-3 labelling. Spheroids were fixed 48h after the magnetic molding (Day 3). The figure presents CT26 spheroids at Day 3 (48h after the molding), subjected (MAG+, right picture) or not (MAG-, left picture) to a permanent magnet. No cleaved caspase-3 was noticed for the MAG- conditions (n=3). For the MAG+ spheroids, less than 5% of the cells are positive to cleaved caspase-3 (4.3 ± 0.7%, n=2). Scale bars: 50 μm.

References

1. Kumar S, Weaver VM. Mechanics, malignancy, and metastasis: The force journey of a tumor cell. Cancer Metastasis Rev. 2009 Jun;28(1–2):113–27.
2. Kalluri R. The biology and function of fibroblasts in cancer. Nat Rev Cancer. 2016 Sep;16(9):582–98.
3. Cox TR, Bird D, Baker A-M, Barker HE, Ho MW-Y, Lang G, et al. LOX-Mediated Collagen Crosslinking Is Responsible for Fibrosis-Enhanced Metastasis. Cancer Research. 2013 Mar 15;73(6):1721–32.
4. Nia HT, Liu H, Seano G, Datta M, Jones D, Rahbari N, et al. Solid stress and elastic energy as measures of tumour mechanopathology. Nat Biomed Eng. 2017 Jan;1(1):0004.
5. Stylianopoulos T, Martin JD, Chauhan VP, Jain SR, Diop-Frimpong B, Bardeesy N, et al. Causes, consequences, and remedies for growth-induced solid stress in murine and human tumors. Proceedings of the National Academy of Sciences. 2012 Sep 18;109(38):15101–8.
6. Samani A, Zubovits J, Plewes D. Elastic moduli of normal and pathological human breast tissues: an inversion-technique-based investigation of 169 samples. Phys Med Biol. 2007 Mar 21;52(6):1565–76.
7. Angeli S, Stylianopoulos T. Biphasic modeling of brain tumor biomechanics and response to radiation treatment. Journal of Biomechanics. 2016 Jun;49(9):1524–31.
8. Carmeliet P, Jain RK. Angiogenesis in cancer and other diseases. Nature. 2000 Sep;407(6801):249–57.
9. Carmeliet P, Jain RK. Principles and mechanisms of vessel normalization for cancer and other angiogenic diseases. Nat Rev Drug Discov. 2011 Jun;10(6):417–27.
10. Hashizume H, Baluk P, Morikawa S, McLean JW, Thurston G, Roberge S, et al. Openings between Defective Endothelial Cells Explain Tumor Vessel Leakiness. The American Journal of Pathology. 2000 Apr;156(4):1363–80.
11. Baxter LT, Jain RK. Transport of fluid and macromolecules in tumors. I. Role of interstitial pressure and convection. Microvascular Research. 1989 Jan;37(1):77–104.
12. Northcott JM, Dean IS, Mouw JK, Weaver VM. Feeling Stress: The Mechanics of Cancer Progression and Aggression. Front Cell Dev Biol. 2018 Feb 28;6:17.
13. Law WL, Chu KW, Ho JWC, Tung HM, Law SYK, Chu KM. Self-expanding metallic stent in the treatment of colonic obstruction caused by advanced malignancies: Diseases of the Colon & Rectum. 2000 Nov;43(11):1522–7.
14. Ho K, Chan K, Kwok S, Lau P ying-yu. Colonic self-expanding metal stent (SEMS) as a bridge to surgery in left-sided malignant colonic obstruction: an 8-year review. Surg Endosc. 2017 May;31(5):2255–62.
15. Small AJ, Coelho-Prabhu N, Baron TH. Endoscopic placement of self-expandable metal stents for malignant colonic obstruction: long-term outcomes and complication factors. Gastrointestinal Endoscopy. 2010 Mar;71(3):560–72.
16. Selinger CP, Ramesh J, Martin DF. Long-term success of colonic stent insertion is influenced by indication but not by length of stent or site of obstruction. Int J Colorectal Dis. 2011 Feb;26(2):215–8.
17. Malgras B, Brullé L, Lo Dico R, El Marjou F, Robine S, Therwath A, et al. Insertion of a Stent in Obstructive Colon Cancer Can Induce a Metastatic Process in an Experimental Murine Model. Ann Surg Oncol. 2015 Dec;22(S3):1475–80.
18. Tse JM, Cheng G, Tyrrell JA, Wilcox-Adelman SA, Boucher Y, Jain RK, et al. Mechanical compression drives cancer cells toward invasive phenotype. Proceedings of the National Academy of Sciences. 2012 Jan 17;109(3):911–6.
19. Demou ZN. Gene Expression Profiles in 3D Tumor Analogs Indicate Compressive Strain Differentially Enhances Metastatic Potential. Ann Biomed Eng. 2010 Nov;38(11):3509–20.
20. Cheng G, Tse J, Jain RK, Munn LL. Micro-Environmental Mechanical Stress Controls Tumor Spheroid Size and Morphology by Suppressing Proliferation and Inducing Apoptosis in Cancer Cells. Blagosklonny MV, editor. PLoS ONE. 2009 Feb 27;4(2):e4632.
21. Alessandri K, Sarangi BR, Gurchenkov VV, Sinha B, Kiessling TR, Fetler L, et al. Cellular capsules as a tool for multicellular spheroid production and for investigating the mechanics of tumor

progression in vitro. Proceedings of the National Academy of Sciences. 2013 Sep 10;110(37):14843–8.
22. Montel F, Delarue M, Elgeti J, Malaquin L, Basan M, Risler T, et al. Stress Clamp Experiments on Multicellular Tumor Spheroids. Phys Rev Lett. 2011 Oct 24;107(18):188102.
23. Dolega ME, Delarue M, Ingremeau F, Prost J, Delon A, Cappello G. Cell-like pressure sensors reveal increase of mechanical stress towards the core of multicellular spheroids under compression. Nat Commun. 2017 Apr;8(1):14056.
24. Desmaison A, Frongia C, Grenier K, Ducommun B, Lobjois V. Mechanical Stress Impairs Mitosis Progression in Multi-Cellular Tumor Spheroids. Engler AJ, editor. PLoS ONE. 2013 Dec 3;8(12):e80447.
25. Vinci M, Gowan S, Boxall F, Patterson L, Zimmermann M, Court W, et al. Advances in establishment and analysis of three-dimensional tumor spheroid-based functional assays for target validation and drug evaluation. BMC Biol. 2012;10(1):29.
26. Hirschhaeuser F, Menne H, Dittfeld C, West J, Mueller-Klieser W, Kunz-Schughart LA. Multicellular tumor spheroids: An underestimated tool is catching up again. Journal of Biotechnology. 2010 Jul 1;148(1):3–15.
27. Lin R-Z, Chang H-Y. Recent advances in three-dimensional multicellular spheroid culture for biomedical research. Biotechnol J. 2008 Oct;3(9–10):1172–84.
28. Mehta G, Hsiao AY, Ingram M, Luker GD, Takayama S. Opportunities and challenges for use of tumor spheroids as models to test drug delivery and efficacy. Journal of Controlled Release. 2012 Dec;164(2):192–204.
29. Helmlinger G, Netti PA, Lichtenbeld HC, Melder RJ, Jain RK. Solid stress inhibits the growth of 1nulticellular tu1nor spheroids. 1997;15:6.
30. Mitsui N, Suzuki N, Koyama Y, Yanagisawa M, Otsuka K, Shimizu N, et al. Effect of compressive force on the expression of MMPs, PAs, and their inhibitors in osteoblastic Saos-2 cells. Life Sciences. 2006 Jul;79(6):575–83.
31. Wilhelm C, Billotey C, Roger J, Pons JN, Bacri J-C, Gazeau F. Intracellular uptake of anionic superparamagnetic nanoparticles as a function of their surface coating. Biomaterials. 2003 Mar;24(6):1001–11.
32. Wilhelm C, Gazeau F. Universal cell labelling with anionic magnetic nanoparticles. Biomaterials. 2008 Aug;29(22):3161–74.
33. Mazuel F, Espinosa A, Luciani N, Reffay M, Le Borgne R, Motte L, et al. Massive Intracellular Biodegradation of Iron Oxide Nanoparticles Evidenced Magnetically at Single-Endosome and Tissue Levels. ACS Nano. 2016 Aug 23;10(8):7627–38.
34. Mazuel F, Reffay M, Du V, Bacri J-C, Rieu J-P, Wilhelm C. Magnetic Flattening of Stem-Cell Spheroids Indicates a Size-Dependent Elastocapillary Transition. Physical Review Letters [Internet]. 2015 Mar 4 [cited 2017 Jan 16];114(9). Available from: http://link.aps.org/doi/10.1103/PhysRevLett.114.098105
35. Massart R. Preparation of aqueous magnetic liquids in alkaline and acidic media. IEEE Trans Magn. 1981 Mar;17(2):1247–8.
36. Tinevez J-Y, Perry N, Schindelin J, Hoopes GM, Reynolds GD, Laplantine E, et al. TrackMate: An open and extensible platform for single-particle tracking. Methods. 2017 15;115:80–90.
37. Derrien A, Gouard S, Maurel C, Gaugler M-H, Bruchertseifer F, Morgenstern A, et al. Therapeutic Efficacy of Alpha-RIT Using a 213Bi-Anti-hCD138 Antibody in a Mouse Model of Ovarian Peritoneal Carcinomatosis. Front Med [Internet]. 2015 Dec 21 [cited 2019 Oct 24];2. Available from: http://journal.frontiersin.org/Article/10.3389/fmed.2015.00088/abstract
38. Luciani N, Du V, Gazeau F, Richert A, Letourneur D, Le Visage C, et al. Successful chondrogenesis within scaffolds, using magnetic stem cell confinement and bioreactor maturation. Acta Biomaterialia. 2016 Jun;37:101–10.
39. Du V, Luciani N, Richard S, Mary G, Gay C, Mazuel F, et al. A 3D magnetic tissue stretcher for remote mechanical control of embryonic stem cell differentiation. Nat Commun. 2017 Dec;8(1):400.
40. Yamamoto Y, Ito A, Kato M, Kawabe Y, Shimizu K, Fujita H, et al. Preparation of artificial skeletal muscle tissues by a magnetic force-based tissue engineering technique. Journal of Bioscience

and Bioengineering. 2009 Dec;108(6):538–43.
41. Akiyama H, Ito A, Kawabe Y, Kamihira M. Genetically engineered angiogenic cell sheets using magnetic force-based gene delivery and tissue fabrication techniques. Biomaterials. 2010 Feb;31(6):1251–9.
42. Tateishi S, Arima S, Futami K, Kawahara K, Tachikawa D, Naritomi K, et al. A Clinicopathological Investigation of "Tumor Nodules" in Colorectal Cancer. Surg Today. 2005 Apr 23;35(5):377–84.
43. Delarue M, Montel F, Vignjevic D, Prost J, Joanny J-F, Cappello G. Compressive Stress Inhibits Proliferation in Tumor Spheroids through a Volume Limitation. Biophysical Journal. 2014 Oct;107(8):1821–8.
44. Lancaster OM, Le Berre M, Dimitracopoulos A, Bonazzi D, Zlotek-Zlotkiewicz E, Picone R, et al. Mitotic Rounding Alters Cell Geometry to Ensure Efficient Bipolar Spindle Formation. Developmental Cell. 2013 May;25(3):270–83.
45. Huang S, Chen CS, Ingber DE. Control of Cyclin D1, p27 ^{Kip1} , and Cell Cycle Progression in Human Capillary Endothelial Cells by Cell Shape and Cytoskeletal Tension. Hynes RO, editor. MBoC. 1998 Nov;9(11):3179–93.
46. Fink J, Carpi N, Betz T, Bétard A, Chebah M, Azioune A, et al. External forces control mitotic spindle positioning. Nat Cell Biol. 2011 Jul;13(7):771–8.
47. Sun X, Kaufman PD. Ki-67: more than a proliferation marker. Chromosoma. 2018 Jun;127(2):175–86.
48. Mancini M, Nicholson DW, Roy S, Thornberry NA, Peterson EP, Casciola-Rosen LA, et al. The Caspase-3 Precursor Has a Cytosolic and Mitochondrial Distribution: Implications for Apoptotic Signaling. The Journal of Cell Biology. 1998 Mar 23;140(6):1485–95.
49. Kessenbrock K, Plaks V, Werb Z. Matrix Metalloproteinases: Regulators of the Tumor Microenvironment. Cell. 2010 Apr;141(1):52–67.
50. Miyazaki Y, Hara A, Kato K, Oyama T, Yamada Y, Mori H, et al. The effect of hypoxic microenvironment on matrix metalloproteinase expression in xenografts of human oral squamous cell carcinoma. Int J Oncol [Internet]. 2008 Jan 1 [cited 2019 Oct 21]; Available from: http://www.spandidos-publications.com/10.3892/ijo.32.1.145
51. Shan Y, You B, Shi S, Shi W, Zhang Z, Zhang Q, et al. Hypoxia-Induced Matrix Metalloproteinase-13 Expression in Exosomes from Nasopharyngeal Carcinoma Enhances Metastases. Cell Death Dis. 2018 Mar;9(3):382.
52. Nukuda A, Sasaki C, Ishihara S, Mizutani T, Nakamura K, Ayabe T, et al. Stiff substrates increase YAP-signaling-mediated matrix metalloproteinase-7 expression. Oncogenesis. 2015 Sep;4(9):e165–e165.
53. Haage A, Schneider IC. Cellular contractility and extracellular matrix stiffness regulate matrix metalloproteinase activity in pancreatic cancer cells. The FASEB Journal. 2014 Aug;28(8):3589–99.
54. Jain RK, Martin JD, Stylianopoulos T. The Role of Mechanical Forces in Tumor Growth and Therapy. Annu Rev Biomed Eng. 2014 Jul 11;16(1):321–46.
55. Du G-L, Chen W-Y, Li X-N, He R, Feng P-F. Induction of MMP-1 and –3 by cyclical mechanical stretch is mediated by IL-6 in cultured fibroblasts of keratoconus. Molecular Medicine Reports. 2017 Jun;15(6):3885–92.
56. Tetsunaga T, Nishida K, Furumatsu T, Naruse K, Hirohata S, Yoshida A, et al. Regulation of mechanical stress-induced MMP-13 and ADAMTS-5 expression by RUNX-2 transcriptional factor in SW1353 chondrocyte-like cells. Osteoarthritis and Cartilage. 2011 Feb;19(2):222–32.
57. Grote K, Flach I, Luchtefeld M, Akin E, Holland SM, Drexler H, et al. Mechanical Stretch Enhances mRNA Expression and Proenzyme Release of Matrix Metalloproteinase-2 (MMP-2) via NAD(P)H Oxidase–Derived Reactive Oxygen Species. Circulation Research [Internet]. 2003 Jun 13 [cited 2019 Oct 25];92(11). Available from: https://www.ahajournals.org/doi/10.1161/01.RES.0000077044.60138.7C
58. Zucker S, Vacirca J. Role of matrix metalloproteinases (MMPs) in colorectal cancer. Cancer Metastasis Rev. 2004 Jan;23(1/2):101–17.
59. Yang B, Tang F, Zhang B, Zhao Y, Feng J, Rao Z. Matrix metalloproteinase-9 overexpression is closely related to poor prognosis in patients with colon cancer. World J Surg Onc. 2014;12(1):24.
60. Said AH, Raufman J-P, Xie G. The role of matrix metalloproteinases in colorectal cancer.

Cancers (Basel). 2014 Feb 10;6(1):366–75.
61. Gremonprez F, Willaert W, Ceelen W. Animal models of colorectal peritoneal metastasis. Pleura and Peritoneum [Internet]. 2016 Jan 1 [cited 2019 Oct 26];1(1). Available from: https://www.degruyter.com/view/j/pp.2016.1.issue-1/pp-2016-0006/pp-2016-0006.xml
62. Sadeghi B, Arvieux C, Glehen O, Beaujard AC, Rivoire M, Baulieux J, et al. Peritoneal carcinomatosis from non-gynecologic malignancies. :6.
63. Taibi A, Albouys J, Jacques J, Perrin M-L, Yardin C, Durand Fontanier S, et al. Comparison of implantation sites for the development of peritoneal metastasis in a colorectal cancer mouse model using non-invasive bioluminescence imaging. Bandapalli OR, editor. PLoS ONE. 2019 Jul 31;14(7):e0220360.
64. Okazaki M, Fushida S, Harada S, Tsukada T, Kinoshita J, Oyama K, et al. Establishing a xenograft mouse model of peritoneal dissemination of gastric cancer with organ invasion and fibrosis. BMC Cancer. 2017 Dec;17(1):23.
65. Matsuda A, Miyashita M, Matsumoto S, Matsutani T, Sakurazawa N, Takahashi G, et al. Comparison of Long-Term Outcomes of Colonic Stent as "Bridge to Surgery" and Emergency Surgery for Malignant Large-Bowel Obstruction: A Meta-Analysis. Ann Surg Oncol. 2015 Feb;22(2):497–504.
66. Leite MLLF, Barbosa LER. Endoscopic stent in malignant colonic obstruction: the risk of tumor seeding. Journal of Coloproctology. 2019 Oct;39(4):357–64.

8 - Annexes

Annex 1: Migration of CT26 spheroids

Tse et al. demonstrated that a mechanical compression of cancer cells gives rise to leader-cell phenotypes (1), which present enhanced migration features. For instance, they are able to escape from an adhesive substrate, and to trigger the movement of the non-leading cells. In order to test if our magnetic flattening would trigger such behaviour, we performed two additional experiments. A summary of these experiments is presented in the Annex 8-1(A.1 and B.2).

Migration after magnetic molding

In the first experiment, CT26 spheroids are magnetically molded as described previously. The night after, the spheroids are removed from the molds, and seeded in adhesive cellular culture dishes (one spheroid per dish). The control spheroids (MAG- spheroids) are cultured without magnets. For the others (MAG+), a permanent magnet (B = 520 mT, gradB = 177 $T.m^{-1}$) is glued at the bottom of the culture dishes, mimicking the flattening of the spheroid on an adhesive surface. The spheroids stick to the surface after a few hours (data not shown), and cells start to escape from the spheroids and to migrate on the flat surface of the culture dishes. Typical pictures thus obtained in the two conditions are shown is the Annex 8-1.A.2. For the two chosen dates (24h and 48h of migration), it is clear that the migration corona of the MAG+ spheroid appears larger. The radius of the migration, and the velocity of the migration have been quantified for different migration times, and the resulting histograms are shown in Annex 8-1.A.3. (Three different experiments, all the spheroids are pooled by conditions. In total, n= 22 for the MAG+ spheroids, n= 21 for the MAG- spheroids). For every date, these results show a larger migration corona for the MAG+ spheroids, for every date. But on the other hand, the quantification of the migration velocity does not shown clear differences. Therefore, the larger migration diameter can be imputed to a quicker adhesion of the MAG+ spheroids.

Migration 48h after the molding

Secondly, we try to mimic the migration behaviour of the cells during the in-vivo experiment. To do, magnetic molded aggregates are cultured in non-adhesive culture dishes, with (MAG+) or without (MAG-) magnets. After 48h, the spheroids are seeded in the same conditions (we removed the magnet for the MAG+ spheroids) in adhesive culture dishes (Annex 8-1.B.1). Interestingly, the adhesion of the MAG+ spheroid was slower than the MAG- spheroids, and we had to perform the quantification of the migration 48h hours after the seeding.

Typical pictures such obtained are shown in Annex 8-1.B.2. The figure shows the migration of the cells escaping from the aggregates 48h and 72h after the seeding on the adhesive culture dishes. The presented MAG- spheroid presents clearly a larger migration radius. The radius and the velocity of migration are quantified (one experiment, n= 9 for the MAG+ spheroids, n=15 for the MAG- spheroids). The resulting histograms are shown in Annex 8-1.B.3. These results demonstrate. Again, the results demonstrate a difference in the radius of migration, but no differences are found regarding the velocity. Herein, the difference of radius is imputed to the difference in adhesion.

Quantification of the migration

These two experiments do not show a difference migration velocity for the cells escaping from a flattened spheroid. But, they do demonstrate a difference in the adhesion of the spheroid. This difference is quite understandable in the first experiment, as the MAG+ spheroids are put quickly in contact with the surface by the magnet. Also, the contact surface with the adherent substrate is large for the flattened MAG+ spheroids. But, in the second experiment, MAG- and MAG+ spheroids are seeded in the same way in adhesive culture dishes. Therefore, the previous flattening of the MAG+ spheroids triggers the difference in the adhesive behaviour. Unfortunately, these results are not enough to clarify the in-vivo results.

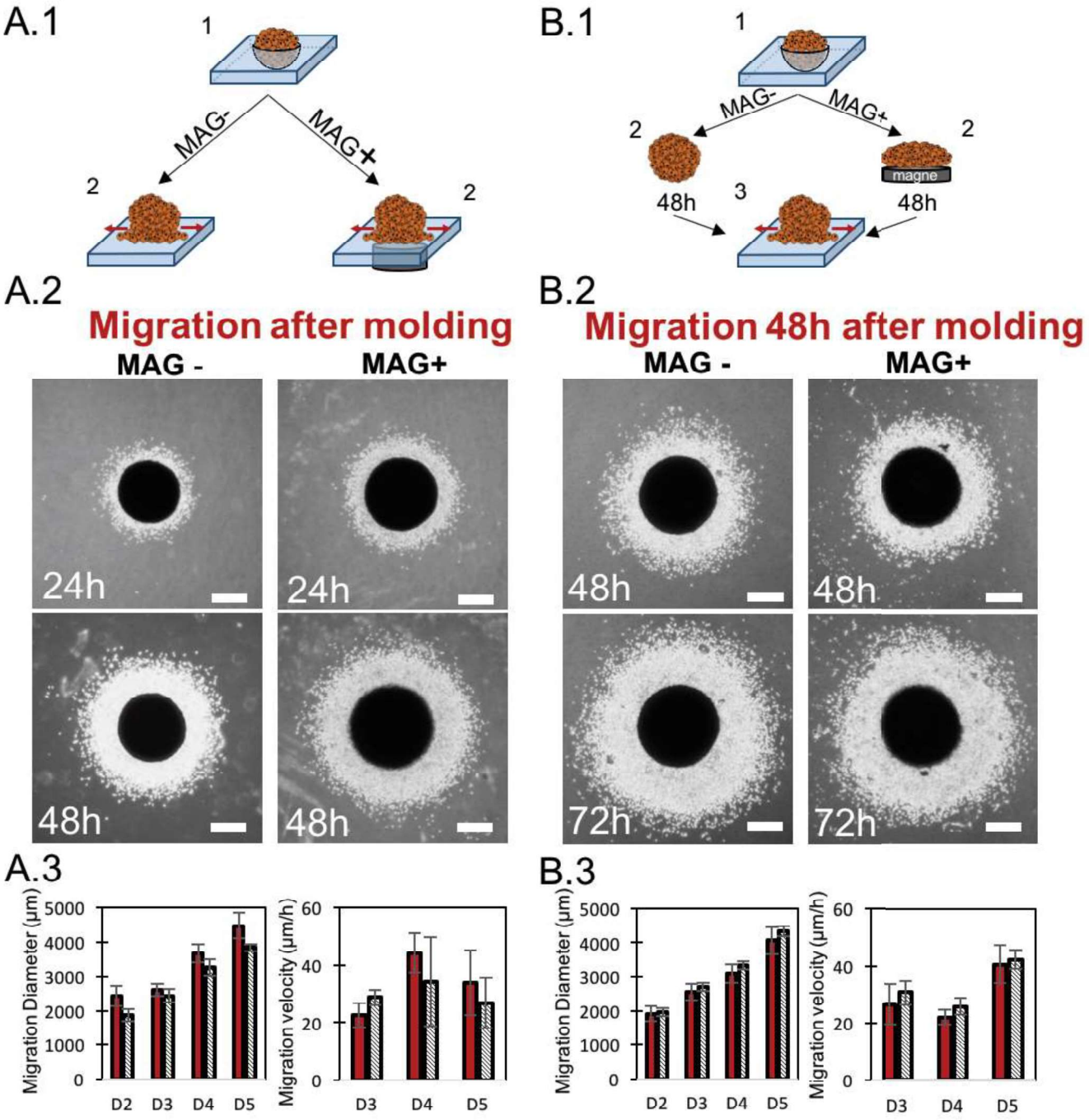

Annex 8-1: Migration of CT26 spheroids on adherent substrates. Two experiments are shown: **A.1-3)** Magnetically molded aggregates were removed from their mold and seeded on adhesive substrate, with (MAG+ spheroids) or without a permanent magnet places below the culture dish. **B.1-3)** Magnetic spheroids were removed from their mold, and kept in culture for 48h with (MAG+ spheroids) or without (MAG- spheroids) the application of a permanent magnet. For both experiments, the figure presents: **A-B.1)** Scheme of the method **A.B-2)** Migration pictures. The seeded spheroids appeared darker than the migrating cells. For the two conditions, the resulting migration is shown 24h and 48h after the seeding (scale bars: 500µm). **A.B-3)** Quantification of the migration diameter and velocity for five days after the spheroid seeding.

Annexe 2: Compression of 0.5 mm CT26 spheroids

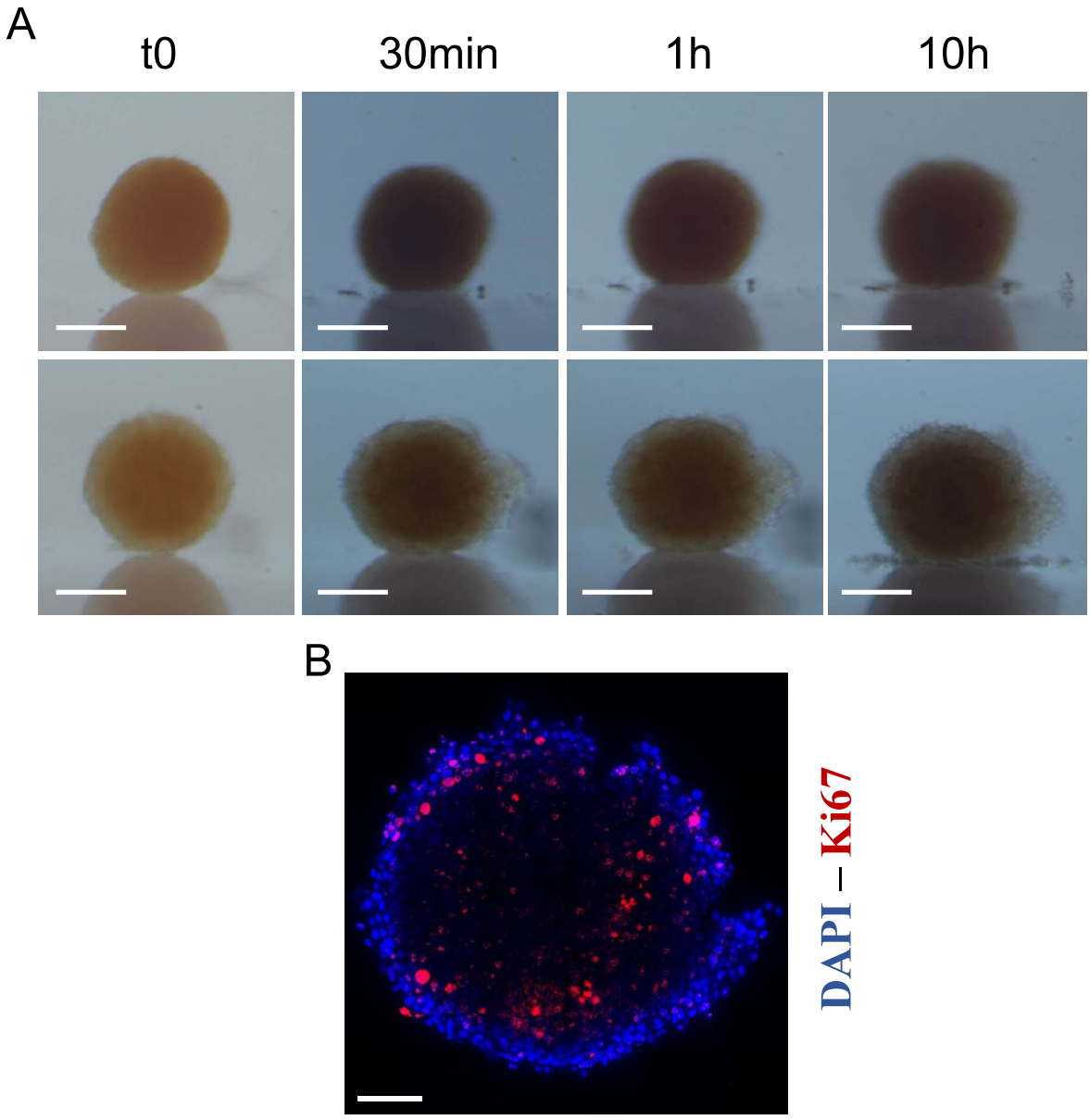

Annex 8-2: Magnetic compression of 0.5 mm CT26 spheroids. A) 0.5 mm CT26 spheroids were obtained using spherical agarose molds formed with beads presenting a diameter of 0.5 mm. Two 0.5 mm spheroids were compressed after their removal from the molds. The resulting deformation was less than 10% of the Initial diameter. Scale bars 250 μm. **B)** Ki67 immunostaining 48h (day 3) after the magnetic molding of a 0.5mm spheroid, without the application of a magnet. The spheroid appeared more proliferative than the 1 mm spheroid at the same date (data not shown). Scale bar: 100 μm.

Annexe 3: Immunostaining of Histone H3

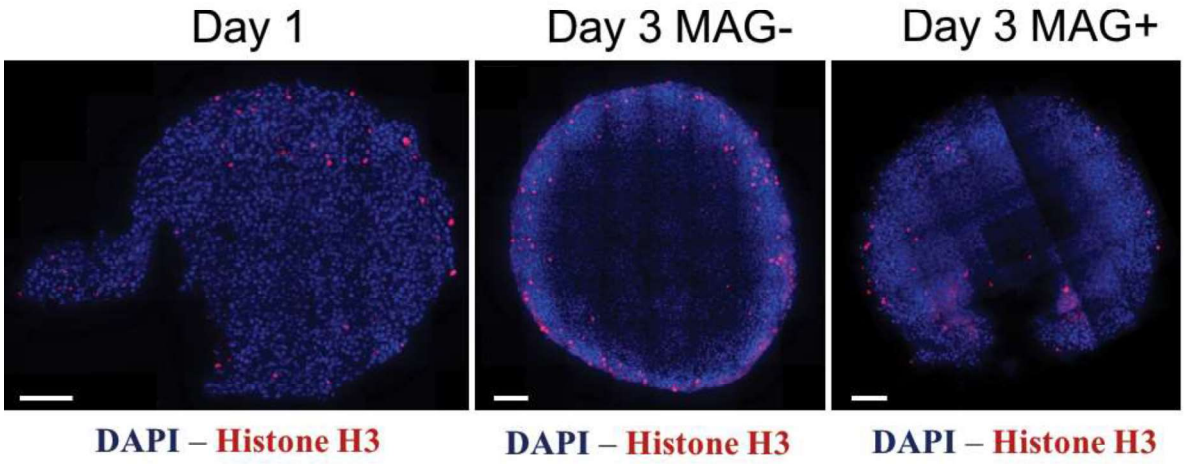

Annex 8-3: Immunostaining of Histone H3. 1 mm CT26 spheroids were labelled for the Histone H3 after they removal from the molds (Day1), or two days after (Day 3) with or without the application of a magnet (MAG+ and MAG-, respectively). At Day 1, 3% of the nuclei or H3-positive, whereas 2.2% and 1.9% or H3-positive respectively for the MAG- and the MAG+ spheroids (n=1 for all the conditions).

9 - Conclusion and perspectives

Herein, we present the magnetic flattening of large (900 μm in diameter) tumor spheroids, produced by using the magnetic molding methods (2). The resulting spheroids present diameters closer to mature tumors than the ones achievable with classic methods. Two conditions are compared. MAG- spheroids are kept for two to three days in free growing conditions, whereas MAG+ spheroids are subjected to a magnetic flattening through the application of a permanent magnet. Briefly, we demonstrate that:

- **The magnetic flattening leads to a quick anisotropic deformation of the spheroids:**
  In the direction of the gradient, a decrease in diameter of almost 40% is measured within 20min. A decrease in the spheroid volume is noticed for longer times (typically a few hours).

- **The magnetic flattening triggers a change in the proliferative behaviour:**
  We demonstrate that the increase in the proliferation, and in the number of proliferating cells is correlated with a change in the localization of the proliferation. While the MAG- spheroids present cells mainly proliferating on the shell, the MAG+ spheroids present a shift of the proliferation toward the core.

- **The Magnetic flattening is associated with a change in the MMP-9 expression:**
  MMP-9 is located on the shell of the MAG-, whereas an increase of MMP-9 is observed toward the centre of the MAG+ spheroids.

- **Thus triggered behaviour increases the in-vitro cancer progression:**
  MAG+ or MAG- spheroids cultured for two days have been injected in mice. We demonstrate that the injection of flattened MAG+ spheroids increases the peritoneal carcinomatosis.

The Conclusion 9-1 presents a graphic summary of the results.

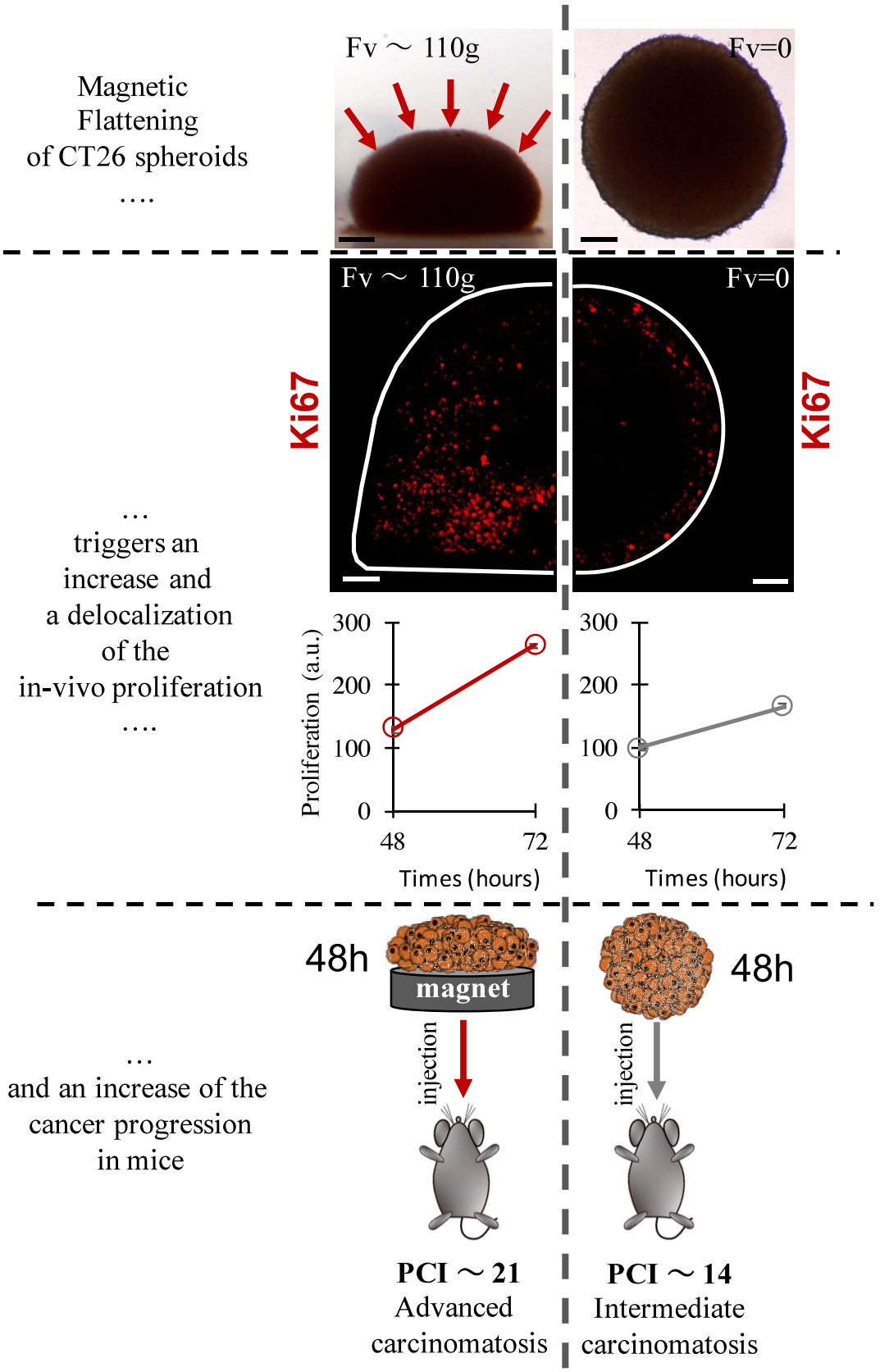

Conclusion 9-1: Conclusion of the chapter 2. The magnetic flattening of CT26 spheroids gives rise to change in the proliferative behaviour, and a change in the MMP-9 expression (not shown in this figure). This triggered behaviour enhanced the in-vivo cancer progression in mice.

This project raises many questions and open many perspectives both in-vitro and in vivo:

In-vitro perspectives

We presented the magnetic flattening of aggregates presenting a size close to mature tumor. One possible following of the project would be to change the size of the spheroids, in order to compare the effect of a large anisotropic deformation on different volumes. In the same line of ideas, it would be possible to modulate the magnetic force (by tuning the magnet and/or the nanoparticles). Indeed, as presented in the introduction of this chapter, an increase of the solid stress (through an increase in the matrix stiffness or in the osmotic pressure) tends to increase the effects on the proliferation. We already tried with spheroids presenting diameters close to 400 μm. But, using the same labelling conditions and the same magnets, the resulting deformation (less than 10% of the initial diameter), seemed not enough for triggering any change in the proliferation (Annex 8-2). A good balance between the spheroid volume and the magnetic force applicable is thus to be found.

Plus, we would like to clarify if our model of compression triggers a change in the in-vitro metastatic potency. First, as a change in the MMPs expression is linked to a hypoxic environment, hypoxia has to be looked in our cancer model. Second, as presented in the Annex of this chapter, the magnetic flattening does not triggers a change in the cell motility on an adhesive substrate (Annex 8-1). Regarding the results, an-other in-vitro model has to be developed. For instance, the migration of compressed spheroid inside an ECM-like matrix is considered.

Our results are controversial regarding thus obtained during a confined growth but agreed the ones observed in clinical tests. We demonstrated the effect of an anisotropic deformation on larger and more mature tumor spheroids. Both the size and the deformation could be responsible, as the anisotropic confinement of small (3) and large spheroids (4) lead to different observations. The mechanism behind such a change in the spheroid behaviour has to be highlighted. In the like of Montel et al. works (5), a mathematical model of mimicking our anisotropic deformation could be an efficient tool for understanding our results. Plus, several studies demonstrated that confinement triggers a blocking in the cell division cycles. This could be tested in our model, for instance by labelling more specific proteins involved in the division cycle, such as the histone H3. Preliminary results of the histone H3 immunostaining

are shown in the Annex 8-3. So far, we observed a small number of CT26 cells positive for histone H3, which may suggest cells blocked before mitosis.

Finally, cancer progression is associated with several mechanotransductional pathways (6). Classically, mechanical cues on cancer cells are linked to the activation of YAP/TAZ or Rho/RAZ signalling pathways. Unravelling the activation of such pathways would be interesting. Preliminary experiments have been performed on the immunostraining of YAP for cryosections of MAG+ and MAG- spheroids, but the staining of the protein is difficult to interpret for 3D configurations (7), and no differences between compressed or free spheroids was observed.

In-vivo perspectives

Following this study, additional in-vivo experiments are already planned with the Marc Pocard's team. This study aims in using magnetic forces in order to compress an in-vitro tumor model. In addition to our study, these experiments could help clarifying the clinical outcomes of surgical acts such as a SEMS implantation. Plus, as iron oxide nanoparticles can be used as contrast agents, Magnetic Resonance Imaging could be used to monitor the potential invasion of the magnetic cells (8). Yet, a more controlled animal model is planned, consisting in an intra-splenic injection of magnetic cells (9). Contrarily to a peritoneal model, thus injected cells are precisely localized in the liver. Through the implantation of a magnet close to liver, this gives us the opportunity of applying magnetic forces in cancer cells constraint inside an organ. As far as we know, such experiments have been carried only on the mouse colonic crypt (10).

References

1. Tse JM, Cheng G, Tyrrell JA, Wilcox-Adelman SA, Boucher Y, Jain RK, et al. Mechanical compression drives cancer cells toward invasive phenotype. Proceedings of the National Academy of Sciences. 2012 Jan 17;109(3):911–6.
2. Mazuel F, Reffay M, Du V, Bacri J-C, Rieu J-P, Wilhelm C. Magnetic Flattening of Stem-Cell Spheroids Indicates a Size-Dependent Elastocapillary Transition. Physical Review Letters [Internet]. 2015 Mar 4 [cited 2017 Jan 16];114(9). Available from: http://link.aps.org/doi/10.1103/PhysRevLett.114.098105
3. Cheng G, Tse J, Jain RK, Munn LL. Micro-Environmental Mechanical Stress Controls Tumor Spheroid Size and Morphology by Suppressing Proliferation and Inducing Apoptosis in Cancer Cells. Blagosklonny MV, editor. PLoS ONE. 2009 Feb 27;4(2):e4632.
4. Desmaison A, Frongia C, Grenier K, Ducommun B, Lobjois V. Mechanical Stress Impairs Mitosis Progression in Multi-Cellular Tumor Spheroids. Engler AJ, editor. PLoS ONE. 2013 Dec 3;8(12):e80447.
5. Montel F, Delarue M, Elgeti J, Vignjevic D, Cappello G, Prost J. Isotropic stress reduces cell proliferation in tumor spheroids. New J Phys. 2012 May 9;14(5):055008.
6. Broders-Bondon F, Nguyen Ho-Bouldoires TH, Fernandez-Sanchez M-E, Farge E. Mechanotransduction in tumor progression: The dark side of the force. J Cell Biol. 2018 May 7;217(5):1571–87.
7. Lee JY, Chang JK, Dominguez AA, Lee H, Nam S, Chang J, et al. YAP-independent mechanotransduction drives breast cancer progression. Nat Commun. 2019 Dec;10(1):1848.
8. Chen J, Ren G, Cai R, Wu X, Gui T, Zhao J, et al. Cellular magnetic resonance imaging: in vivo tracking of gastric cancer cells and detecting of lymph node metastases using microparticles of iron oxide in mice. CMAR. 2019 Aug;Volume 11:7317–26.
9. Goddard ET, Fischer J, Schedin P. A Portal Vein Injection Model to Study Liver Metastasis of Breast Cancer. JoVE. 2016 Dec 26;(118):54903.
10. Fernández-Sánchez ME, Barbier S, Whitehead J, Béalle G, Michel A, Latorre-Ossa H, et al. Mechanical induction of the tumorigenic β-catenin pathway by tumour growth pressure. Nature. 2015 Jul;523(7558):92–5.

CHAPTER 3: CARDIAC AND SKELETAL TISSUE ENGINEERING

10 - Introduction: Strategies for skeletal and cardiac tissue engineering

In the previous chapter, we used magnetic cells in order to form multicellular tumour spheroids, and to mechanically stimulate them using remote controlled magnetic forces. In this case compressed spheroids presented an enhanced cell proliferation and an increased in-vivo metastatic potency, which would arguably raise clinical issues. Herein, we propose also a magnetic approach, employed this time for constructive ends. The purpose is to remotely form aggregates composed of cardiac and muscular precursors, then to induce their differentiation toward functional cardiac and skeletal muscle cells upon a controlled remote magnetic stimulation. By proposing this approach, we integrate the field of tissue engineering, which aims at repairing damaged tissues.

Content

The major challenge of tissue engineering is to properly induce the differentiation of precursor cells, and to recreate a structure close to the native tissue. The development of recent technologies has enable to spatially manipulate the cells, and to create 3D tissue models. On the other hand, the past years have highlighted the contribution of mechanical stimulation one the cell differentiation (1). In this introduction, the two cell precursors used in our approach will first be described. Concurrent technologies used to create 3D functionalized tissues will then be introduced. Among others, we will address how such technologies allow

inducing cell differentiation using mechanical stimuli. Finally, we will stress how magnetic approaches may represent efficient candidates for remote formation and stimulation of 3D engineered tissues, in order to induce a force-triggered differentiation.

10.1 - Muscle cell precursors

First step in a tissue engineering approach for tissue repair is to select the cell type. Herein, we will focus on a precise type of stem cells, and on myogenic skeletal satellite cells.

10.1.1) Skeletal cell precursors

After a muscular damage, myogenic satellite cells migrate toward the injury, differentiate in skeletal myoblasts and fused with the damaged myotubes (2).
These striking features make them natural candidate for skeletal muscle engineering. Primary cells can be extracted and cultured (3), but they are difficult to culture at long time scale and one is not able yet to expend large quantity of primary cell cultures. Therefore, model cell lines have been developed. The C2C12 cell line, an immortalized cell line derived from C3H mouse satellite cells, is considered as a suitable model of myoblast precursors (4).
By contrast, cardiac cells do not present such self-renewing abilities. Therefore, one has to use either primary cardiac cell precursors or differentiated cardiomyocytes which or difficult to culture in mass. Another strategy is the use of pluripotent stem cells, which requires to further trigger the differentiation toward cardiomyogenesis. In the next paragraph, we will present their main features.

10.1.2) Stem cells

Biological tissues are composed of highly specialized cells, with specific phenotypes and function. For instance, neuron cells are able to produce electric signals (action potentials), whereas muscle cells are able to produce mechanical forces through the contraction of the cytoskeleton. Such cells are not able to divide and to self-renew. On the other hand, stem cells are non-functional cells able to replicate and to differentiate. Depending on their location, and the development stage (adult or embryonic stem cells), several stem cell types can be distinguished.

Stem cells was first observed in 1961 by the pioneer works of Till and McCulloch (5). Currently, they are defined according to three specific features: (i) they are able of unlimited or prolonged self-renewal; (ii) they are unspecialized cells; and (iii) depending on their microenvironment, they are able to differentiate in several cell types, through specific steps (6). They can be classified according to different types: Embryonic Stem Cells (ESCs), Adult Stem cells (or somatic stem cells), and Induced Pluripotent Stem Cells (IPS). Whereas the first ones can be found during embryonic development, the seconds can be found in adults, for instance in bone marrow. Such cells present distinct differentiation potency.

10.1.2.1) Stem Cell Differentiation potency

The differentiation potency is defined as the stem cell ability to give rise to specified cell types. Stem cells present different differentiation potencies, and are distinguished in four categories (Figure 10-1) (7) (8):

- **Totipotent cells** These cells are able to differentiate into every specialized cells composing a living organism. By themselves, they are able to build a complete organism. In mammals, the only totipotent cells are the fertilized oocyte and the first 8 cells resulting from the first divisions (blastomeres).
- **Pluripotent cells** They can differentiate in every cell types. In particular, they give rise to three embryonic germ layers: ectoderm, endoderm and mesoderm. These cell layers form during embryonic development, and give rise to the different tissues and organs during organogenesis: (i) Endoderm layer provides organs such as the stomach, the colon or the pancreas; (ii) Ectoderm layer is evolved in a large range of organs such as epidermis, peripheral nervous system and neurones (iii) Finally bones, cartilages and smooth and skeletal muscles arise from the mesoderm.
- **Multipotent cells** These stem cells derive from pluripotent stem cells. If they give rise to multiple specialised cell types, they are limited to a specific tissue or organ. Most adult stem cells are considered as multipotent. Generally, multipotent stem cells differentiate in cells specific to their native tissue.
- **Unipotent stem cells** They derive from multipotent cells, and are able to give rise to a unique cell type. For instance, satellite skeletal cells are considered as unipotent cells, as they can only differentiate in myoblasts (9).

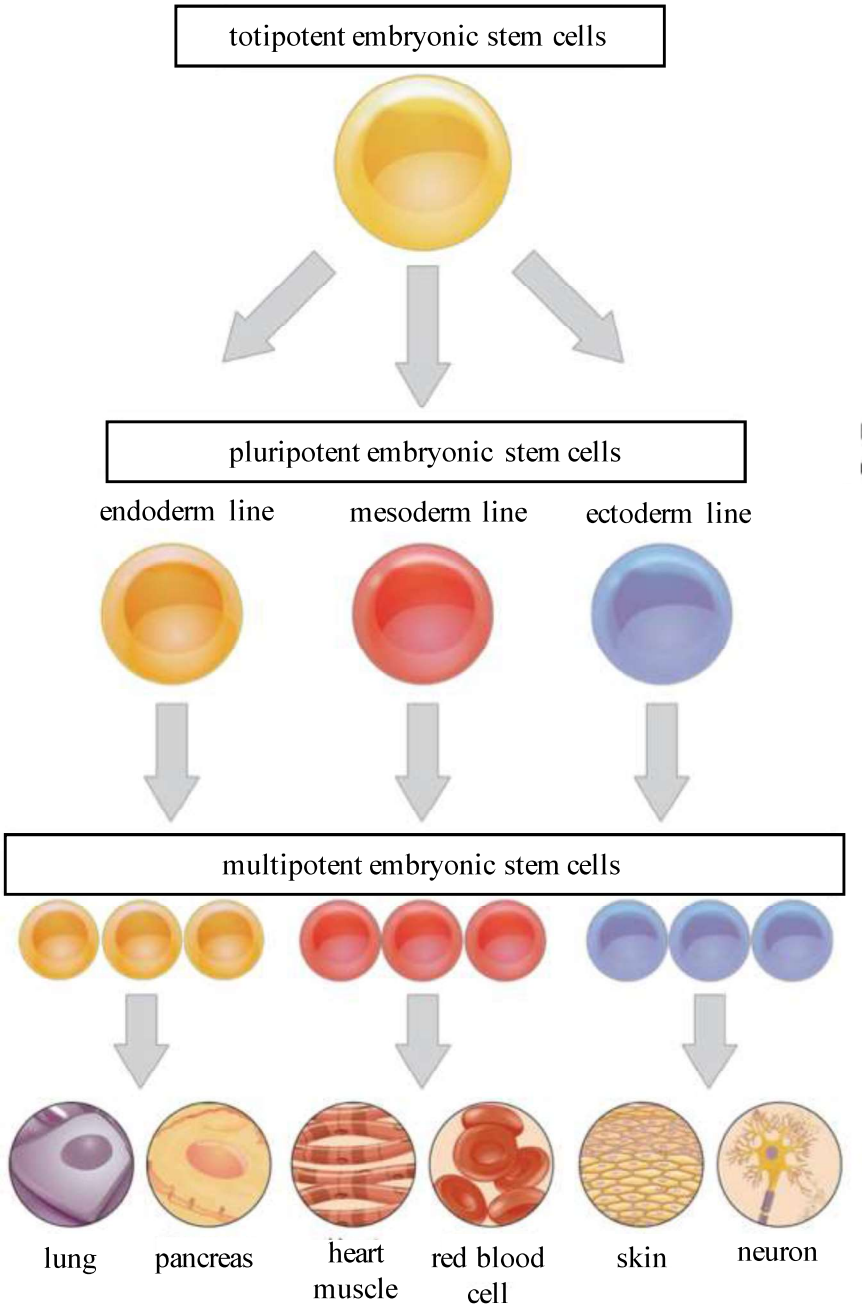

Figure 10-1: Stem cell differentiation potency. Through successive differentiation steps, totipotent stem cells give rise to multipotent stem cells, which give rise to cells composing the different tissues of the living. Unipotent cells are not represented on the scheme. Adapted from (10).

The ESCs are considered as totipotent or pluripotent, whereas Adult Stem cells are more restrictive, and considered as multipotent or even unipotent. Finally, IPS can be considered as pluripotent cells. Due to their large differentiation potency, ESCs were chosen as a stem cell model for cardiomyogenesis.

10.1.2.3) ESCs cardiomyogenesis specific markers

The ESCs differentiation toward cardiomyocyte requires several steps, which are associated to specific genetic markers (11):

- The loss of the pluripotency is associated with a decrease of markers such as OCT4.
- The next differentiation step is linked with an increase in the expression progenitor markers such as Nkx2.5
- Then, an increase in early cardiac markers such as Gata-4, Gata-6 and α-actinin is happening.
- Finally, among others, CMs maturation is associated with the expression of markers specific to the cardiac structural organization such as the Cardiac Troponin T and I (cTnT, cTnI), cardiac myosin heavy chain, the desmin or the Connexin 43.

The second step of tissue engineering is the creation of a tissue model, which will be further differentiated. Yet, such large structures give rise to several issues such as dioxygen and nutrient poor diffusions, which can impact cell viability. Besides, so-obtained tissue needs to be mechanically compatible with the native tissue. To tackle such problems, methods have focused in embedding the cells in an external support structure, called scaffold.

10.2) 3D-Scaffold

Cells can be embedded in a 3D structure called scaffold. Such structures aim at reproducing the mechanical environment of the native tissue, and can be further functionalized or stimulated in order to induce the cell differentiation.

Scaffolds can be designed using ECM-like proteins. Cells are embedded in protein gel close to the natural ECM environment such as collagen (12), gelatin (13), fibrin (14), or decellularized scaffolds (15). The rigidity and shape of these ECM matrices can be finely tuned in order to recreate a proper muscle environment. Additionally, synthetic polymer matrices (16) have been designed, generally allowing a better control of matrix stiffness and shape (17). Thus scaffolds are designed in order to present fibres sizes close to a naturel ECM, promoting the cell colonisation. Moreover, they can be further functionalised in order to direct the cellular differentiation, through adhesion peptides.

However the major drawback of this technology relies on the use of a matrix as they have been reported to trigger inflammatory reactions due to the scaffold biodegradation (18), and the cell-scaffold interactions may change the cell behaviour (19). Yet, such approaches allow the application of mechanical stimuli, which present good outcomes on the cell differentiation.

10.3 - Mechanical stimulation of muscle precursors

By nature, cardiac and skeletal muscles are specialized in order to produce forces. Many studies have been interested in reproducing native stimuli in order to trigger the maturation of myoblasts and myoblast precursors.

10.3.1) Mechanical differentiation through mechanical stimuli

Mechanical stretching of cell monolayers has been widely used to align various cell types. Generally, cells grown on a stretchable elastic substrate tend to align along an applied stretching (20). Cells subjected to a cyclic stimulation tend to align perpendicularly at 2D (21), and parallel to the stretching at 3D (22).

10.3.1.2) 2D- stretching

Such stimuli have been used in order to align myoblasts cultured on 2D elastic substrates. For instance, myoblast cells have been cultured on 2D elastic substrates. Under a permanent uniaxial stretch the myoblasts align parallel to the strain direction (23). Such approach can enhance cardiac cell maturation (24). On the other hand, muscle cells subjected to a cyclic strain stimulation will align perpendicularly (25). Yet, if these methods are interesting for the understanding of myoblast alignment and maturation, they are limited by nature at the 2D scale.

10.3.2.3) 3D mechanical cues

3D scaffolds can be used to subject muscle cell precursors to controlled mechanical stimulations in a 3D configuration.

Skeletal myoblasts embedded in a 3D matrix, and subjected for several days to continuous strain followed by rest periods, demonstrated an increase in genes implicated in myogenesis, an enhanced alignment and fusion (26) (27), and were able to generate forces closer to the native tissue (15). Constant strain has been shown to lead to a better alignment of the scaffold embedding the cells, and therefore leading to an enhanced myotube formation (28).

Plus, cardiac and skeletal muscle cell precursors have been also subjected to quick cyclic stretching (typically 10% stretching between 1Hz to 3Hz) followed by rest periods. These cyclic stimulations allow the alignment and the maturation of C2C12 cells (29) (30). Besides, these stimuli enhance the cardiomyogenesis of Mesenchymal Stem Cells (31), and ESCs cell (32).

Altogether, these studies demonstrate a positive effect on muscle precursors:

- Mechanical continuous or cyclic stimulations enhance the alignment (Figure 10-2.A-B), and the maturation (Figure 10-2.C) of skeletal precursors.
- Cyclic stimulations enhance the cardiomyogenesis of Stem Cells.

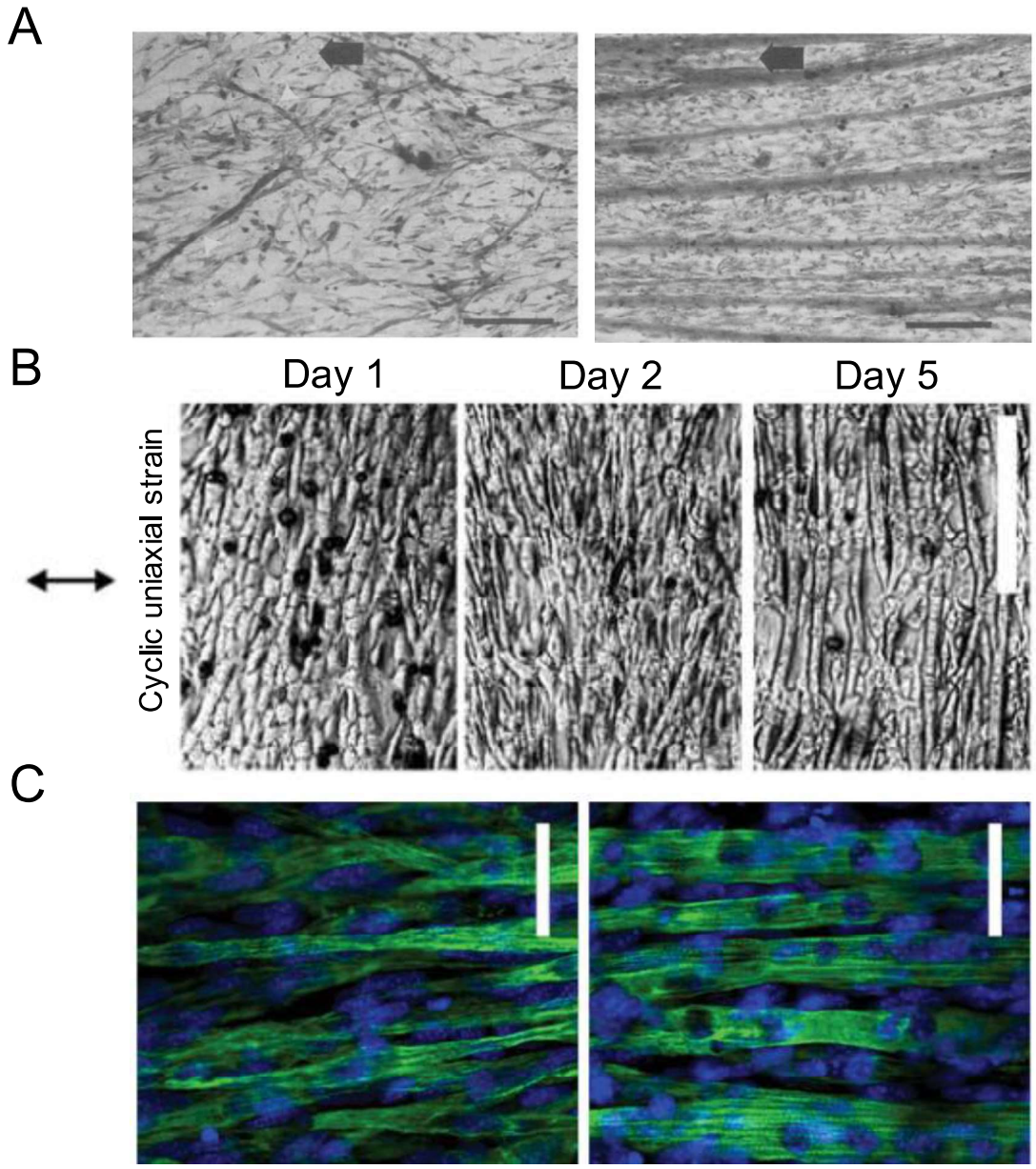

Figure 10-2: Straining or stretching of a 2D or 3D assembly of myotubes progenitors enhances their alignment and differentiation. A) Embryonic skeletal avian muscle cells are subjected to a constant stretching (0.35 mm/h) up to 400% of the initial substrate length. Left picture present the cells after 36h of stretching, and the right picture after 96h of stretching. Dynamic stretching enhanced cell alignment (in the direction of the stretching) and the myoblast differentiation. The arrow represents the stretching direction. Scale bar 50 μm Adapted from (33). **B)** C2C12 subjected to a cyclic strain (15%, 1Hz) align perpendicularly and present an enhanced differentiation Scale bar 50 μm. Adapted from (25). **C**) C2C12 cells embedded in 3D fibrin rings are submitted to a static strain/rest cycles. Left picture presents C2C12 myotubes in a non-stretched scaffold after 6 days of low glucose culture. On the left pictures, the scaffold id submitted to 7 static strain cycles in 6 days. Both maturation and alignment are enhanced by the static strain cycles. The myosin heavy Chain is labelled in green, the nuclei in blue. Scale bar 50 μm. Adapted from (27).

These experiments have been made on cells grown on 2D substrates, or cells embedded in 3D matrixes. Therefore, a gap is yet to be filled. In one hand, one needs to create a 3D tissue without the use of a scaffold, to be closer to the body host tissue. On the other hand, one needs to stimulate the engineered tissue, in order to enhance its differentiation, which is difficult to achieve without a scaffold.

Herein, we propose the use of magnetic approaches to tackle these two issues. Indeed, magnetic forces enable to remotely control the spatial organization of cells, and result in an excitable 3D structure. We will describe first some works available in the literature, and we will focus on a previous work developed in the team.

10.4 - Magnetic Approaches

Magnetic approaches have been developed for tissue engineering. Where are going to briefly describe some available technics.

10.4.1) Magnetic cell sheet

Akira Ito's group developed a magnetic method based on cells magnetically labelled using magnetic liposomes. The so-obtained magnetic cells are attracted using a permanent magnet on a low adhesive surface, and pilled in order to form a cell sheet. Thanks to magnetic forces, these magnetic methods allow to easily implant the tissue at the injury site. The same team used magnetic cell sheet techniques to from cardiac tissue models (34), and skeletal tissue models using the C2C12 cell line. Besides, due to their shrinking, these structures are not stable in time (35).

10.4.2) 3D magnetic engineering

Using magnetic techniques, the same group was able to build 3D C2C12 rings. They seeded magnetic C2C12 around a cylinder, and end up with a structure of 12 mm per 120 μm. The resulting rings were cultured in 3D for days around two anchor pines (Figure 10-3). The shrinking of the ring around the anchor results in a good alignment and functionalization of the model tissue (35). Nevertheless, because of the shrinking, and the ring nature of the resulting tissue, it is difficult to remove the tissue from the anchors.

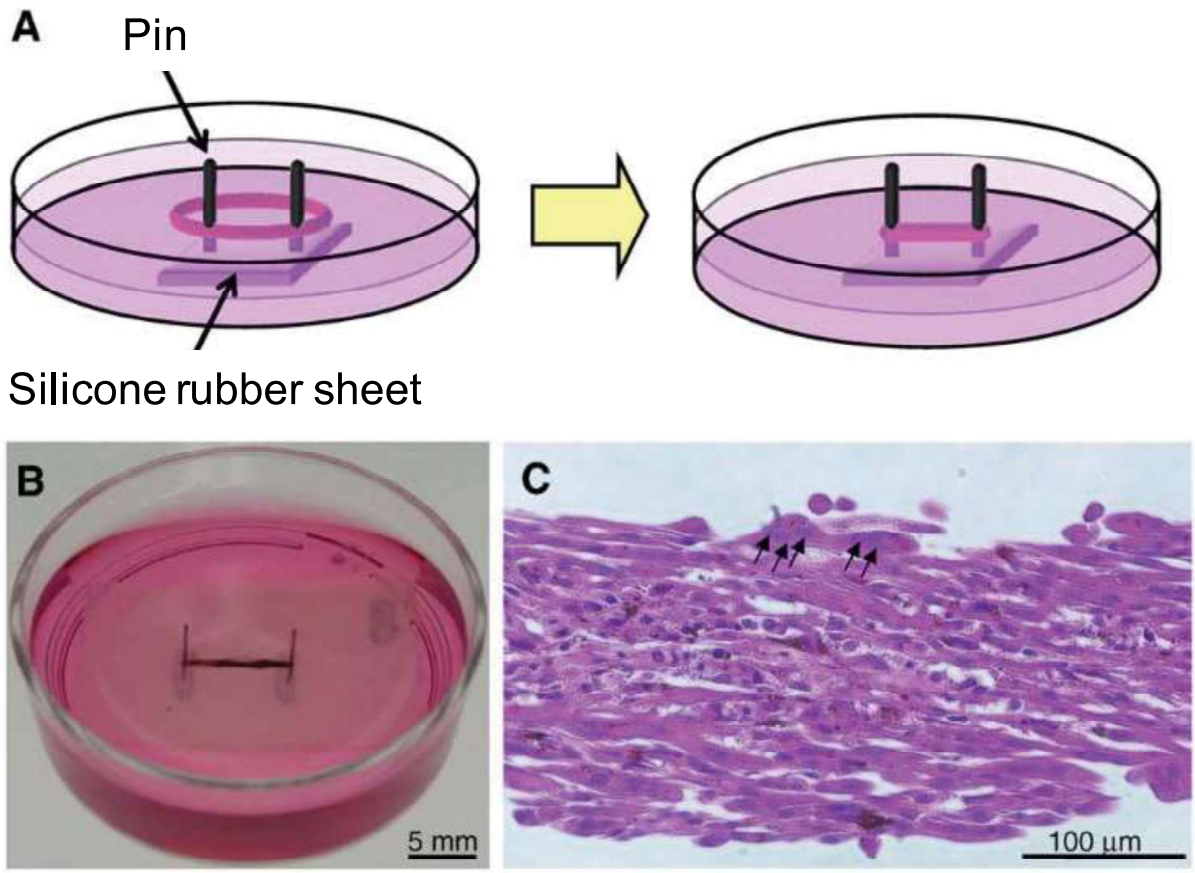

Figure 10-3: Differentiation of C2C12 ring formed using magnetic method. A) Scheme of the differentiation process. C2C12 rings are anchored between two pins (10 mm separation). In differentiation medium, the ring shrinks between the anchors. **B)** BF picture of a 6-day C2C12 ring. The shrinking is visible. The structure is approximately 10 mm per 200 µm **C)** Histological picture of the 6-day ring. The differentiation leads to aligned and fused myotubes in a 3D structure. Adapted from (35).

If the magnetic tissue engineering allows forming 3D tissue models, further differentiation requires the use of chemical or mechanical stimuli. In the following paragraph, we describe an all-in-one method to create 3D-scaffold-free Embryoid Bodies, and to induce the cardiomyogenesis using magnetic stretching.

10.4.3) The Magnetic Stretcher

During my PhD, I have been involved in this project started during the PhD thesis of Vicard Du (36), under the supervision of Claire Wilhelm. The project was the development of a magnetic tissue stretcher for tissue formation and stimulation. The magnetic stretcher was developed as all in on tool first to form embryoïd bodies from ESCs at a 3D scale, then to subject them to controlled mechanical constraints, in order to induce their differentiation using only mechanical stimuli. In particular, I took part in the project as follows:

- I helped to form and stimulate the magnetic EBs inside the Magnetic Stretcher
- I performed immunolabelling on cryosections of EBs formed in the Magnetic Stretcher
- I monitored the cell movements at the surface of EBs subjected to stretching cycles

Herein, I describe the main results of this work. In brief, four methods of EBs formation and differentiation were compared (Figure 10-4):

- Hanging Drop Method This method was used as a Control condition, as it has been widely used in cardiomyogenesis studies (37). Hanging drops containing 10,000 ESCs were used. The resulting EBs were not further mechanically stimulated.

- Magnetic Formation Magnetic ECSs (10 000 cells) were attracted by magnetic actuator (750 μm in diameter) on a non-adhesive surface. Using a magnetic device presenting several arrays of magnetic actuators, this method allows the high- throughput formation of aggregates in a short time (38). Plus, the magnetic actuators allow applying a constant mechanical constraint in the range of 100 pN per EB.

- Constant and cyclic magnetic stretching Briefly, the magnetic stretcher is composed of two opposing magnetic attractors (the same as used in the Magnetic Formation method): one is fixed, whereas one is mobile in one direction. The EBs formation is straightforward. First 10 000 magnetic ESCs were seeded on the fixed actuator, resulting in semi-spheroidal EBs. Second, the mobile actuator was approached, resulting in a stretched cylindrical EBs. Two mechanical stimulations were used. First, EBs were kept in the stretched configuration. Second, the effect of a cyclic stimulation has been investigated: Magnetic EBs were subjected to a 10% compression at 1Hz, 2h twice a day.

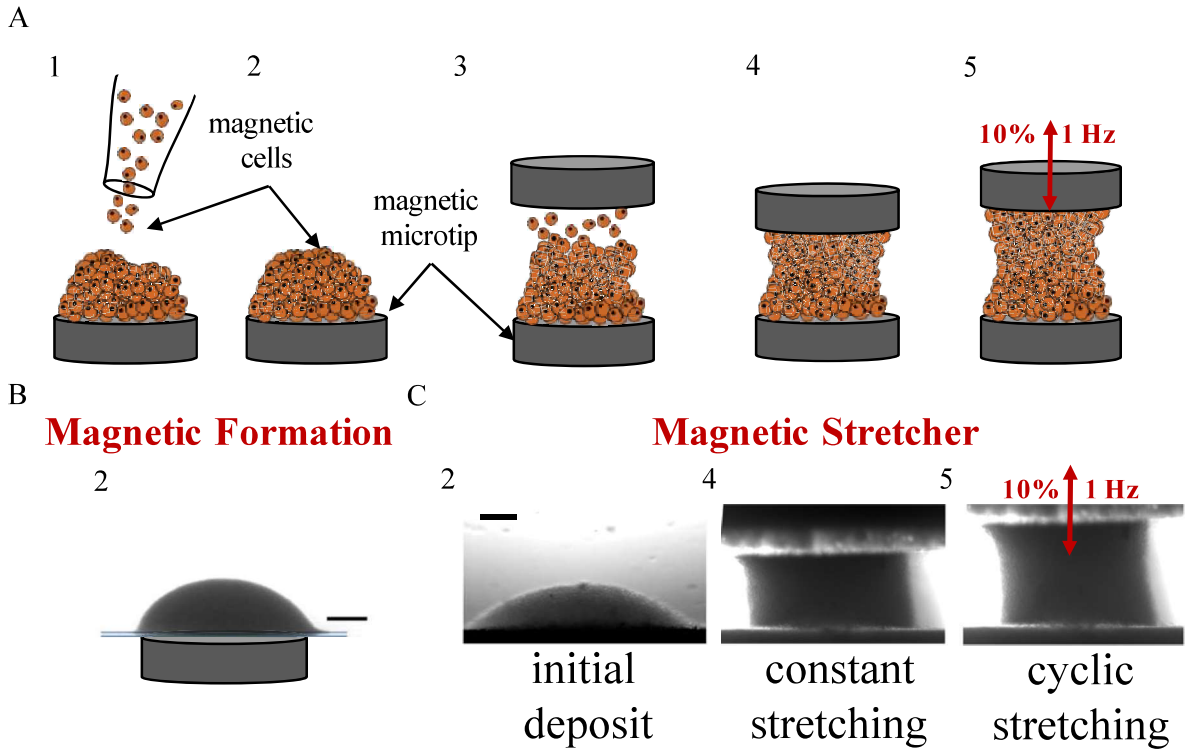

Figure 10-4: EBs formation using magnetic techniques. A) Scheme of the steps required to obtain the Magnetic Formation of EBs, and the Constant and Cyclic Stretching in the Magnetic Stretcher. Magnetic cells are attracted on a non-adhesive surface by a 750 μm magnetic microtip (cartoon 1). The magnetic microtip can be used to form a scaffold-free 3D EB (Magnetic Formation, cartoon 2). In the magnetic stretcher, a second magnetic actuator is approached (cartoon 3), resulting in a cylindrical stretched aggregate. Two conditions are used, a Constant Stretching (cartoon 4), and a Cyclic Stretching (cartoon 4). **B)** Bright Field picture of an aggregate obtained using the Magnetic Formation method. Scale bar 200 μm. **C)** Bright Field picture of an aggregate formed in the magnetic stretcher. The cell deposit, and the resulting aggregate are shown. Scale bar: 200 μm.

EBs were cultured in the different conditions for 3 days, and matured for 2 to 5 days (Day 5 or Day 10) on an adhesive substrate. Following the maturation steps, the genetic expression of specific differentiation markers was assessed:

- Compared to aggregates formed using the Hanging Drop method, the Magnetic Formation did not present an enhanced expression of cardiac markers.
- However, a constant magnetic stretching gave rise to an increase in the genetic expression of early differentiation markers such as Nkx2.5, Gata4 and Gata 6 (at Day

5), and to an increase in the expression of specific cardiac markers such as Troponin T and the myosin heavy chain (at Day 10).

- For both dates, this up-regulation was strikingly enhanced for the EBs subjected to cyclic stretching. Such pattern of up-regulation was consistent with an enhanced cardiomyogenesis.

Therefore, EBs subjected to constant or cyclic magnetic stretching presented enhanced cardiomyogenesis. If such result was described at the 2D scale, or for cells embedded in a 3D scaffold, it was obtained here using a 3D scaffold-free configuration. Such approach was used as the basis for the two projects next presented in this chapter.

10.5 - Proposed approach: Magnetic Engineering of Cardiac and Skeletal tissue

Based on this previous study, we propose a magnetic approach in order enhance the differentiation of muscle precursors toward cardiac and skeletal tissue. Two projects are presented:

- The Magnetic Stretcher allows the enhanced cardiomyogenesis of ESC EBs through cyclic mechanical stimulation. Yet, only a small number of EBs can be produced at the same time. In the next chapter, we propose a magnetic method based on the Magnetic Formation, which allow us to perform a high throughput formation and stimulation 900 EBs at the same time. Then, using an electromagnet (same as the one presented in the Chapter 1), the cyclic stimulation of the obtained EBs can be performed.
- As described above, mechanical stretching enhanced the alignment and the maturation of skeletal muscle precursors. The final chapter of this manuscript will present preliminary results on the 3D alignment of C2C12 cells in the Magnetic Stretcher. The project will be further carried out by Irène Nagle as part of her PhD thesis.

References

1. Engler AJ, Sen S, Sweeney HL, Discher DE. Matrix Elasticity Directs Stem Cell Lineage Specification. Cell. 2006 Aug;126(4):677–89.
2. Relaix F, Zammit PS. Satellite cells are essential for skeletal muscle regeneration: the cell on the edge returns centre stage. Development. 2012 Aug 15;139(16):2845–56.
3. Allen RE, Temm-Grove CJ, Sheehan SM, Rice G. Chapter 8 Skeletal Muscle Satellite Cell Cultures. In: Methods in Cell Biology [Internet]. Elsevier; 1997 [cited 2019 Nov 6]. p. 155–76. Available from: https://linkinghub.elsevier.com/retrieve/pii/S0091679X08603787
4. Dennis RG, Kosnik PE, Gilbert ME, Faulkner JA. Excitability and contractility of skeletal muscle engineered from primary cultures and cell lines. American Journal of Physiology-Cell Physiology. 2001 Feb 1;280(2):C288–95.
5. Till JE, McCULLOCH EA. A direct measurement of the radiation sensitivity of normal mouse bone marrow cells. Radiat Res. 1961 Feb;14:213–22.
6. Chagastelles PC, Nardi NB. Biology of stem cells: an overview. Kidney International Supplements. 2011 Sep;1(3):63–7.
7. Bindu A H, B S. Potency of Various Types of Stem Cells and their Transplantation. J Stem Cell Res Ther [Internet]. 2011 [cited 2019 Dec 2];01(03). Available from: https://www.omicsonline.org/potency-of-various-types-of-stem-cells-and-their-transplantation-2157-7633.1000115.php?aid=3527
8. Weissman IL. Stem Cells: Units of Development, Units of Regeneration, and Units in Evolution. Cell. 2000 Jan 7;100(1):157–68.
9. Seale P, Asakura A, Rudnicki MA. The Potential of Muscle Stem Cells. Developmental Cell. 2001 Sep;1(3):333–42.
10. Biga LM, Dawson S, Harwell A, Hopkins R, Lemaster M, Morrison-Graham K, et al. Anatomy & Physiology. :3038.
11. Habib M, Caspi O, Gepstein L. Human embryonic stem cells for cardiomyogenesis. Journal of Molecular and Cellular Cardiology. 2008 Oct;45(4):462–74.
12. Smith AST, Passey S, Greensmith L, Mudera V, Lewis MP. Characterization and optimization of a simple, repeatable system for the long term in vitro culture of aligned myotubes in 3D. J Cell Biochem. 2012 Mar;113(3):1044–53.
13. Hosseini V, Ahadian S, Ostrovidov S, Camci-Unal G, Chen S, Kaji H, et al. Engineered Contractile Skeletal Muscle Tissue on a Microgrooved Methacrylated Gelatin Substrate. Tissue Engineering Part A. 2012 Dec;18(23–24):2453–65.
14. Huang Y-C. Rapid formation of functional muscle in vitro using fibrin gels. Journal of Applied Physiology. 2004 Oct 15;98(2):706–13.
15. Machingal MA, Corona BT, Walters TJ, Kesireddy V, Koval CN, Dannahower A, et al. A Tissue-Engineered Muscle Repair Construct for Functional Restoration of an Irrecoverable Muscle Injury in a Murine Model. Tissue Engineering Part A. 2011 Sep;17(17–18):2291–303.
16. Choi JS, Lee SJ, Christ GJ, Atala A, Yoo JJ. The influence of electrospun aligned poly(ε-caprolactone)/collagen nanofiber meshes on the formation of self-aligned skeletal muscle myotubes. Biomaterials. 2008 Jul;29(19):2899–906.
17. Green JJ, Elisseeff JH. Mimicking biological functionality with polymers for biomedical applications. Nature. 2016 14;540(7633):386–94.
18. Maleiner B, Tomasch J, Heher P, Spadiut O, Rünzler D, Fuchs C. The Importance of Biophysical and Biochemical Stimuli in Dynamic Skeletal Muscle Models. Front Physiol. 2018 Aug 22;9:1130.
19. Ito A, Kamihira M. Tissue Engineering Using Magnetite Nanoparticles. In: Progress in Molecular Biology and Translational Science [Internet]. Elsevier; 2011 [cited 2019 Nov 6]. p. 355–95. Available from: https://linkinghub.elsevier.com/retrieve/pii/B9780124160200000097
20. Liu C, Baek S, Kim J, Vasko E, Pyne R, Chan C. Effect of Static Pre-stretch Induced Surface Anisotropy on Orientation of Mesenchymal Stem Cells. Cel Mol Bioeng. 2014 Mar;7(1):106–21.
21. Huang C, Miyazaki K, Akaishi S, Watanabe A, Hyakusoku H, Ogawa R. Biological effects of cellular stretch on human dermal fibroblasts. Journal of Plastic, Reconstructive & Aesthetic Surgery.

2013 Dec;66(12):e351–61.
22. Chen K, Vigliotti A, Bacca M, McMeeking RM, Deshpande VS, Holmes JW. Role of boundary conditions in determining cell alignment in response to stretch. Proc Natl Acad Sci USA. 2018 Jan 30;115(5):986–91.
23. Segurola RJ, Sumpio BE, Mills I. Strain-induced dual alignment of L6 rat skeletal muscle cells. In Vitro CellDevBiol-Animal. 1998 Sep;34(8):609–12.
24. Simpson DG, Majeski M, Borg TK, Terracio L. Regulation of Cardiac Myocyte Protein Turnover and Myofibrillar Structure In Vitro by Specific Directions of Stretch. Circulation Research [Internet]. 1999 Nov 12 [cited 2019 Dec 6];85(10). Available from: https://www.ahajournals.org/doi/10.1161/01.RES.85.10.e59
25. Pennisi CP, Olesen CG, de Zee M, Rasmussen J, Zachar V. Uniaxial Cyclic Strain Drives Assembly and Differentiation of Skeletal Myocytes. Tissue Engineering Part A. 2011 Oct;17(19–20):2543–50.
26. Li Y, Huang G, Gao B, Li M, Genin GM, Lu TJ, et al. Magnetically actuated cell-laden microscale hydrogels for probing strain-induced cell responses in three dimensions. NPG Asia Mater. 2016 Jan;8(1):e238–e238.
27. Heher P, Maleiner B, Prüller J, Teuschl AH, Kollmitzer J, Monforte X, et al. A novel bioreactor for the generation of highly aligned 3D skeletal muscle-like constructs through orientation of fibrin via application of static strain. Acta Biomaterialia. 2015 Sep;24:251–65.
28. Matsumoto T, Sasaki J-I, Alsberg E, Egusa H, Yatani H, Sohmura T. Three-Dimensional Cell and Tissue Patterning in a Strained Fibrin Gel System. Isalan M, editor. PLoS ONE. 2007 Nov 21;2(11):e1211.
29. Chang Y-J, Chen Y-J, Huang C-W, Fan S-C, Huang B-M, Chang W-T, et al. Cyclic Stretch Facilitates Myogenesis in C2C12 Myoblasts and Rescues Thiazolidinedione-Inhibited Myotube Formation. Front Bioeng Biotechnol [Internet]. 2016 Mar 21 [cited 2019 Nov 7];4. Available from: http://journal.frontiersin.org/Article/10.3389/fbioe.2016.00027/abstract
30. Bansai S, Morikura T, Onoe H, Miyata S. Effect of Cyclic Stretch on Tissue Maturation in Myoblast-Laden Hydrogel Fibers. Micromachines. 2019 Jun 15;10(6):399.
31. Huang Y, Zheng L, Gong X, Jia X, Song W, Liu M, et al. Effect of cyclic strain on cardiomyogenic differentiation of rat bone marrow derived mesenchymal stem cells. PLoS ONE. 2012;7(4):e34960.
32. Shimko VF, Claycomb WC. Effect of Mechanical Loading on Three-Dimensional Cultures of Embryonic Stem Cell-Derived Cardiomyocytes. Tissue Engineering Part A. 2008 Jan;14(1):49–58.
33. Vandenburgh HH, Karlisch P. Longitudinal growth of skeletal myotubes in vitro in a new horizontal mechanical cell stimulator. In Vitro Cell Dev Biol. 1989 Jul;25(7):607–16.
34. Shimizu K, Ito A, Lee J-K, Yoshida T, Miwa K, Ishiguro H, et al. Construction of multi-layered cardiomyocyte sheets using magnetite nanoparticles and magnetic force. Biotechnol Bioeng. 2007 Mar 1;96(4):803–9.
35. Yamamoto Y, Ito A, Kato M, Kawabe Y, Shimizu K, Fujita H, et al. Preparation of artificial skeletal muscle tissues by a magnetic force-based tissue engineering technique. Journal of Bioscience and Bioengineering. 2009 Dec;108(6):538–43.
36. Du V, Luciani N, Richard S, Mary G, Gay C, Mazuel F, et al. A 3D magnetic tissue stretcher for remote mechanical control of embryonic stem cell differentiation. Nat Commun. 2017 Dec;8(1):400.
37. Chen M, Lin Y-Q, Xie S-L, Wu H-F, Wang J-F. Enrichment of cardiac differentiation of mouse embryonic stem cells by optimizing the hanging drop method. Biotechnol Lett. 2011 Apr;33(4):853–8.
38. Frasca G, Gazeau F, Wilhelm C. Formation of a Three-Dimensional Multicellular Assembly Using Magnetic Patterning. Langmuir. 2009 Feb 17;25(4):2348–54.

11 - Article: *High-Throughput Differentiation of Embryonic Stem Cells into Cardiomyocytes with a Microfabricated Magnetic Pattern and Cyclic Stimulation*

High-Throughput Differentiation of Embryonic Stem Cells into Cardiomyocytes with a Microfabricated Magnetic Pattern and Cyclic Stimulation

*Gaëtan Mary+, Aurore Van de Walle+, Jose Efrain Perez, Tomofumi Ukai, Toru Maekawa, Nathalie Luciani, Claire Wilhelm**

G. Mary, Dr. A. Van de Walle, Dr. J. E. Perez, Dr. N. Luciani, Prof. C. Wilhelm
Laboratoire Matière et Systèmes, Complexes MSC, UMR 7057, CNRS & University of Paris, 75205, Paris Cedex 13, France. + Equal contribution
E-mail: claire.wilhelm@univ-paris-diderot.fr

Dr. T. Ukai, Prof. T. Maekawa
Bio-Nano Electronics Research Centre, Toyo University, Kawagoe, 350-8585, Japan;
Graduate School of Interdisciplinary New Science, Toyo University, Kawagoe 350-8585, Japan.

Keywords (5 maximum): magnetic nanoparticles; stem cell differentiation; cardiomyogenesis; magnetic cell stimulation; microfabrication

Abstract

Pluripotent stem cells are central tools to many regenerative medicine strategies due to their ability to differentiate towards the three embryonic germ layers. One challenge remains in providing control over their differentiation into specific lineage, such as cardiac commitment. Here, the possibility of directing cardiomyogenesis of embryonic stem cells (ESCs) using a microfabricated magnetic pattern is demonstrated. The stem cells are labelled with magnetic nanoparticles, aggregated into embryoid bodies (EBs) onto the pattern, and stimulated with local magnetic force applied by the pattern. The EBs formed on this magnetic device experience the same differentiation profile than the ones created by common hanging drop approach, while it allows high-throughput production of hundreds of EBs. Further on/off cyclic magnetic force stimulation mediated by the same device is sufficient to enhance cardiomyogenesis in a way that almost all EBs develop spontaneous beating, confirmed by the overexpression of a-actin and troponin proteins, and by the upregulation (2 to 5-fold) of

genes involved in mesoderm differentiation (Nkx2.5, Gata4, and Gata6), and more specifically cardiac lineage (Tnnt2, Myh6 and Myl-2). It confirms the importance of mechanical factors in the differentiation of stem cells.

Introduction

The generation of in vitro three-dimensional multicellular assemblies or spheroids has been of recent interest for tissue engineering and regenerative cell therapies and stands as a pivotal biological process to initiate the differentiation of stem cells into specific pathways such as chondrogenesis or cardiomyogenesis. The most common spheroid formation techniques rely on well established procedures that include the aggregation of cells via their culture in suspension[1] or on non-adherent surfaces[2], their pelleting by centrifugation,[3] or their self-assembling by bioprinting.[4] In parallel, material and nanotechnological means have advanced not only to control cell patterning but also to direct cell function such as stem cells differentiation, using for examples nanoparticles or nanoelectrodes,[5] or specific substrates,[6] combined or not with nanomaterials (e.g. graphene, nanoelectrodes, nanofibers, nanowires)[7]. Among them, iron oxide magnetic nanoparticles have recently emerged as magnetic cellular label that has a double advantage. On one hand it can be exploited to promote cell aggregation via localized magnetic forces and organize cells into engineered tissues.[8] As such, it has been employed for the formation of scaffold-free cell-spheroids[8b, 9], combined with standard techniques such as the hanging drop method[10] or agarose-well patterning,[11] and used as well to seed cells within 3D scaffolds.[12] On the other hand, it offers the possibility to control cell functions, including their differentiation.[13]

Spheroids based on embryonic stem cells (ESCs), termed embryoïd bodies (EBs), are particularly relevant as these cells can differentiate into lineages representative of the three embryonic germ layers and their EBs not only mimic early stages of embryonic development but also can be directed into specific organs due to their pluripotency. Despite most recent advances, it is still difficult to control the differentiation of pluripotent stem cells and maintain simultaneously a high production of differentiated or precursors cells, both being of particular relevance for application in regenerative medicine, such as in cardiac regeneration.[14] When stem cells (typically mesenchymal ones[15] or pluripotent ones[16]) were administered after myocardial infarction, cardiac performance was improved, but with low tissue integration and contraction generation.[17] Approaches have been tested to increase contraction, by aligning cardiac cells,[18] however, these approaches are two-dimensional, based on adult cardiac cells, with low output.

The use of magnetic nanoparticles to produce cell-spheroids that can be remotely actuated could provide a valuable solution for the development of next generation of stem cells - based cardiac substitutes, yet the development of high throughputs systems will be required in order to produce a clinically relevant numbers of functional cells.
Herein, we demonstrate the directed cardiomyogenesis of ESCs labelled with magnetic nanoparticles using an all integrated microfabricated magnetic microtips pattern that provides mechano-stimulation and high yield. The micro-pattern allows the controlled formation of a large number of EBs (900 in total with only one seeding) together with the possibility of a mechanical - magnetically induced - stimulation during the first fundamental stages of differentiation. Remarkably, EBs magnetic formation and cyclic stimulation drove the ESCs towards the cardiac mesoderm pathway. Beyond holding high application-level potential, this work confirms that physical forces, and specifically on/off dynamic ones can be sufficient to govern cell function.[19]

Results and Discussion

The photolithography-patterned nickel microtips device was fabricated to achieve a spatially controlled and highly localized magnetic attraction (Figure 1A and Figure S1). The end device accommodates 900 microtips, each 1 μm in height and 1 mm apart (Figure 1B). Magnetic nanoparticles were internalized in the ESCs upon a 30 minutes incubation at [Fe]=2 mM, these same conditions having been previously reported as having no impact on ESC viability or differentiation profiles.[13d] After cellular uptake, the nanoparticles were localized in the cell endosomes (Figure 1C). Magnetically-labelled ESCs were then organized into EBs either by the typical hanging drop method (Figure 1D), with EBs being formed over three days of drop confinement, or under a set of three conditions using the magnetic microtips pattern (Figure 1E-G). For all three conditions, a magnet was placed below the device to magnetize the tips and achieve localized cell attraction and EB formation. In the first case, the magnet was removed after five minutes (MAG-short, Figure 1E), whereas in the second one it was removed after three days (MAG-long, Figure 1F). In the last condition, the magnet was maintained over the three first days, but was replaced with an electromagnet for 6 hours per day, imposing a cyclic magnetic field at a frequency of 1 Hz (MAG-cycl, Figure 1G). It should be stressed that the magnetic stimulation was applied during the first three days of EB formation and growth, when the differentiation pathways are setting up. Besides, in a

more practical term, the cellular magnetic forces are significant only over the first cell divisions within the EBs.

EB formation (1000 ESCs per EB) is immediate when using the magnetic microtips, with cell aggregation taking place within seconds of seeding (Figure 2A). At day 3, the EBs were collected from the drops or from the magnetic pattern. All four tested conditions, the three magnetic ones and the hanging drop, were then transferred in non-adherent dishes and left to mature as spheroids for 2 more days. At day 5, the EBs were transferred to adherent tissue culture wells, and left there to finalize their differentiation pathway. Figure S2 summarizes all steps occurring upon the 10 days of ESCs differentiation, and presents the different analyses performed at various time points. EBs size was measured at days 0, 1, 3, and 5 (only 3 and 5 for the hanging drop condition). After 1 day of magnetic seeding (Figure 2B, 2G), no size difference was observed over the three magnetic conditions. At day 3 and day 5, EBs diameter were similar across all four conditions (including the hanging drop), at approximately 350 and 500 µm, respectively (Figure 2C-F, 2G). At day 7 and day 10, each EB was observed to record the occurrence of spontaneous beatings. Figure 2H-K shows representation illustrations of beating events for each conditions, with spatio-temporal analysis (kymographs). If there is little or no cell displacement (i.e. beating), the cells position in the area selected on the images can be seen as unaltered over time, defined as straight lines along the time axis of the kymographs (vertical in Figures 2H-K); however, if beating takes place, it translates into regular perpendicular lines (at given time interval). Additional analyses are shown in Figures S3-S6. The beating frequency was then systematically extracted from all kymographs, appears distributed in the 1-2 Hz range (Figure 2L), and is very similar across all the conditions, showing that there is no effect of EBs magnetic formation and stimulation on the beating phenomenon itself, once triggered. Finally, the percentage of beating EBs was quantified across all conditions, at days 7 and 10 (Figure 2M). It is remarkably increased for the MAG-cycl condition, at both times, reaching 92% of beating EBs at day 10, percentage rarely achieved even with the use of the most efficient chemical factors for cardiomyogenic differentiation induction of ESCs.[20]

The increase of cardiomyogenesis triggered by the cyclic magnetic stimulation was further confirmed by immunolabeling and gene expression. Two structural proteins located in the sarcomere were labeled with fluorescent antibody: α-actinin, typical of muscular cells, and cardiac troponin T, typically expressed in cardiomyocytes. Figures 3A and 3B show an impressive increase in both labels for the MAG-cycl condition, when compared to the three other conditions, which look similar. Additional analyses are shown in Figures S7-S8 (α-actinin; MAG-long and MAG-cycl conditions), and in Figures S9-S12 (troponin-T; MAG-short, MAG-long, MAG-cycl and DROP conditions) also presenting F-actin labeling with SiR-actin. All images corresponding to the MAG-cycl condition reveal a striated organization for both proteins, representative of the development of sarcomeres, necessary units for cell contraction. It was less marked for observations made at day 7 (Figure S13, MAG-cycl).

The expression of six genes characteristic of the endo/mesoderm (the transcription factor Gata6), and/or more specifically of the cardiac mesoderm (the transcription factors Gata4 and Nkx2.5, and regulating proteins directly specific to cardiac contraction troponin T (Tnnt2), α myosin heavy chain (Myh6), and myosin regulatory light chain 2 (Myl2)) was assessed at days 5, 7 and 10, and normalized to the same gene expression at day 0 (Figure 3C). It first evidences that differentiation of the ESCs toward the cardiac mesoderm is happening for the hanging drop control, with a time-dependent increase of all selected gene expression. This was expected as this technique has specifically been developed for allowing cardiac differentiation of ESCs through aggregation of the cells and their growth in a confined environment.[21] Results show that the EBs formed on the magnetic pattern with no further magnetic compaction (MAG-short) display a similar gene expression than the hanging drop method, sometimes very slightly downregulated, but never more that 1.5-fold. When magnetic compaction was applied all along the first days of differentiation initiation (MAG-long), mesoderm and cardiac mesoderm gene expression was sometimes slightly upregulated, but never more than 2-fold. By contrast, what was highly significant is the upregulation of all genes involved in cardiac differentiation when cells were cyclically stimulated (MAG-cycl), always in the range of a 2 to 5-fold increase.

Conclusion

In summary, high-throughput delivery of EBs could be achieved with the magnetic patterned device, in a single pipetting step, instead of one by one for the common hanging drop method. EBs magnetically formed are homogeneous in size, and contain initially 1000 cells, similar number than the seeding density of the hanging drop approach for optimal differentiation. Without any further stimulation, these EBs have the same differentiation potential toward the mesodermal pathway than when formed with the hanging drop in optimal conditions.

The even more unprecedented advantage of the magnetic pattern device resides in the possibility of further stimulating the EBs magnetically. When dynamic (cyclic), this stimulation drove the EBs towards cardiac differentiation with a remarkable efficiency. Indeed, after 10 days, more than 90% of the EBs were beating, a much higher percentage than with the state-of-the-art hanging drop approach. Also, when comparing with previous studies that used growth factors to increase the differentiation, such as TGF and BMP2, the cardiomyogenesis enhancement obtained here without any additive of any sort seems even more effective.[22] This remarkable result not only indicates applicative relevance of the magnetic device but also beautifully underlines the control that purely mechanical stimulation may have on the differentiation of stem cells.

In conclusion, the magnetic microtips pattern provides a high-throughput approach for EBs formation. It allows their remote mechanical cyclic stimulation, induced magnetically, sufficient to direct almost totally ESCs differentiation towards the cardiac lineage. It could be considered as a next potent platform for high scale production of stem cells-derived cardiomyocytes for regenerative medicine therapies.

Experimental Section

***Magnetic pattern*:** Magnetic pattern was fabricated on a silicon substrate via electroplating and UV photolithography. Titanium and copper films were formed on a silicon substrate using a sputtering system (E-200S-TY, CANON ANELVA Corp.) and reversal patterns of magnetic dots were obtained by a negative tone UV photoresist (KMPR, KAYAKU Advanced Materials, Inc.) via UV lithography. A nickel film was then deposited on the substrate via electroplating and the UV photoresist was removed by Remover PG (KAYAKU Advanced Materials, Inc.). The titanium and copper films were wet-etched and finally silicon oxide was deposited using the sputtering system. The pattern was magnetized by placing it

over either a permanent neodymium magnet (50 mm x 50 mm x 20 mm) creating a 0.2 T magnetic field in the device plane, or over an electromagnet to generate an on/off magnetic field. The electromagnet was composed of a custom-made water-cooled coil (6Ω, 14 mH) wrapped around a soft iron polar piece (diameter 55mm, height 85mm). 4A-on/off current (1Hz) was delivered to the coil using a TGA 1242 signal generator (Aim&TTi) and amplifier (Kebco BOP), creating an on/off 0.15 T magnetic field on the device.

***ESCs and magnetic labeling*:** CGR8 mouse embryonic stem cell were purchased from Sigma (07032901) and were cultured on 0.1% gelatin-coated surfaces in fresh GMEM medium (Sigma, G5154) supplemented with 10% fetal calf serum, 2 mM glutamine, 1% nonessential amino acids, 0.1 mM β-mercaptoethanol, 1 mM sodium pyruvate, 1% penicillin/streptomycin and 1000 U/ml of leukemia inhibitor factor (LIF, Thermo Fisher Scientific). They were passaged every 2 days at a density of 10^4 cells per cm², and were systematically used at passage 5 to 8 (passage zero being initial purchased batch). An older CGR8 cell line was also tested (Figure S14), corresponding to another cell batch, having experienced over 50 passages, and less competent for cardiomyogenesis. The magnetic nanoparticles used were made by aqueous co-precipitation of iron salts, they have a mean diameter of 8 nm, and a polydispersity index of 0.35, and are the most commonly used in biomedicine applications.

***EBs formation and differentiation*:** At day 0, ESCs were labeled with the magnetic nanoparticles (30 min, [Fe]=2mM), then detached and resuspended in differentiation medium (same as culture medium, but with 20% fetal calf serum and without LIF factor). EBs were next formed either by the hanging drop method (DROP, considered as control, seeding of 1000 ESCs in a 30 µL drop, plated on Petri dish cover gently turned over on the dish filled with PBS) or onto the magnetic pattern. ESCs (100 000) were then transferred to 12 mm diameter glass-bottom dishes, previously treated with PLL-PEG (SuSos) diluted in 10 mM HEPES (30min, 10 mg/ml) to prevent adhesion, and placed over the magnetic pattern device. Each dish covers 100 magnetic dots (1000 ESCs available per dot), and multiple dishes can be placed together on the device. The device is then placed over the permanent magnet, and the dishes are left on site for 5 min (MAG-short) or until day 3 (MAG-long). For the MAG-cycl condition, the device is placed on the electromagnet for on/off magnetic stimulation the first 3 days. At day 3, all EBs (hanging drops and magnetically formed ones) are collected and transferred to non-adhesive Petri dishes for 2 days for 2-days maturation before being

individually seeded at day 5 in 0.1% gelatin-coated 24-well plates. Figure S2 illustrates the 10-days differentiation process.

Immunohistology: After paraformaldehyde (4% in PBS) fixation and Triton permeabilization (15 min), cell samples were incubated sequentially with blocking solution (BSA 5%) for 1 hour at room temperature, primary antibodies overnight at 4°C (mouse monoclonal anti-α-actinin, Sigma Aldrich, A7811, dilution 1:400; mouse monoclonal (IgG1) anti cardiac Troponin T, Thermofisher, MA5-12960, dilution 1:200), goat anti-mouse IgG secondary antibody for 2 hours at room temperature (Sigma-Aldrich, 43394, IgG-Atto550, dilution 1:500), and DAPI for 30 min at room temperature (Sigma-Aldrich, D9564, 1 µg/mL), and mounted (Fluoromount, Sigma Aldrich, F4680) on slides. Images were acquired with Olympus JX81/BX61 device/Yokogawa CSU device spinning-disk microscope (Andor Technology) using 60X oil objective (Olympus).

Relative quantification of gene expression by real-time PCR

Samples for PCR were harvested at day 5 (5 EBs per sample), day 7 (3 EBs per sample), and day 10 (2 EBs per sample). At least 4 independent samples were analyzed for each independent data point, and two independent experiments were performed (total of 8-10 samples per condition). Total RNA was isolated using the NucleoSpin RNA kit (Machery-Nagel). Complementary DNA (cDNA) was produced using the SuperScript II Reverse Transcriptase kit (Thermo Fisher Scientific) and random hexamers. Real-time quantitative PCR was conducted using the SYBR Green dye and the StepOnePlus detection system (Thermo Fisher Scientific). The expression of the housekeeping gene of the 60S acidic ribosomal protein P0 (RPLP0) was used as a reference transcript. All primer sequences are provided in Table S1.

Acknowledgements

This work was supported by the European Union (ERC-2014-CoG project MaTissE #648779). We thank Aude Michel (Sorbonne Université, CNRS, PHENIX, UMR8234) for nanoparticles synthesis, Christine Péchoux from Mima2 platform-Inra (Jouy en Josas) for TEM analysis, and Myriam Reffay for discussion.

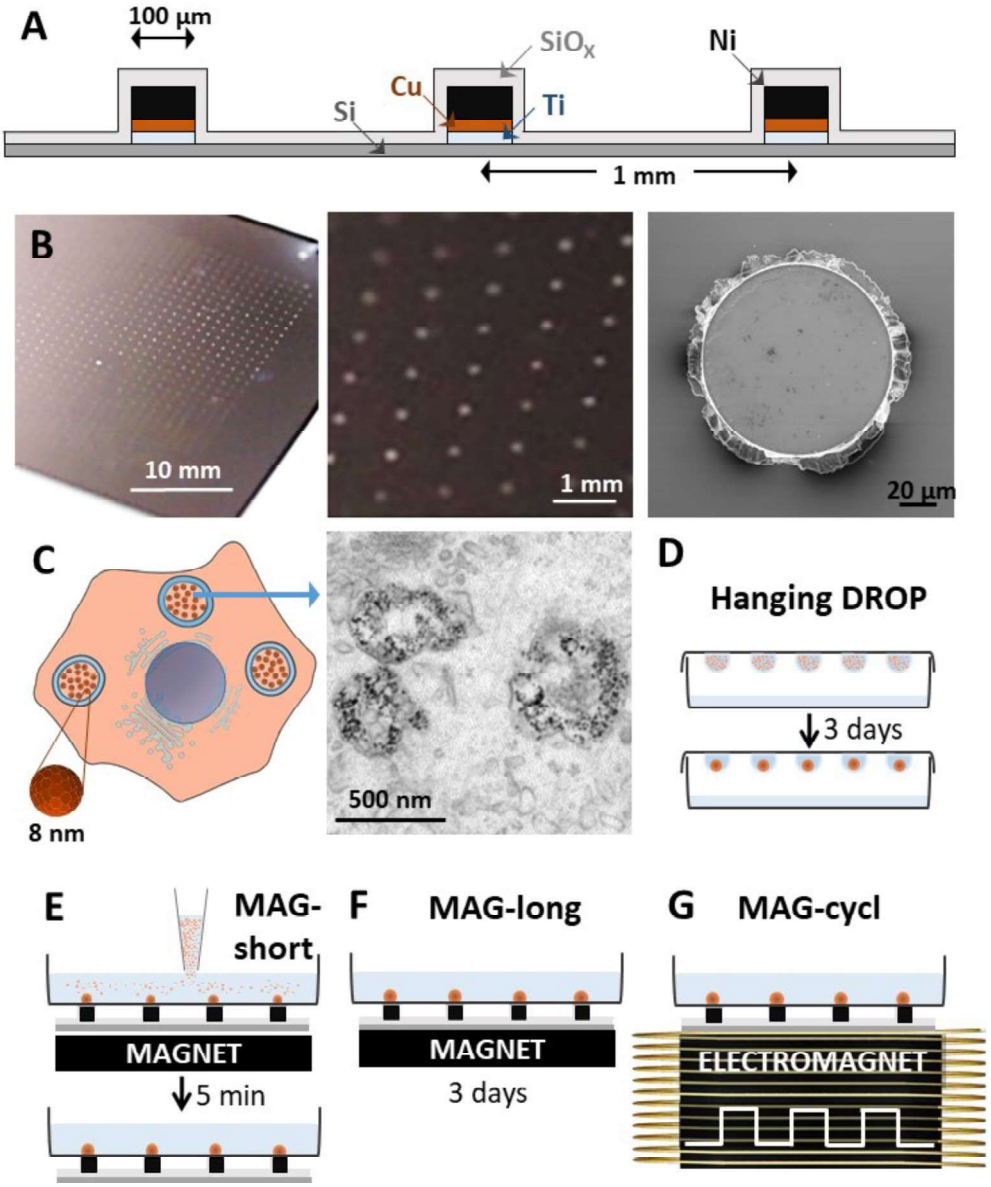

Figure 1. Remote, magnetically actuated, mechanostimulation of ESCs using a microfabricated (A) magnetic device. **B)** Image (left) of the 100 µm diameter microtips pattern composed of 30x30 magnetic nickel dots (900 in total); close-up image in the center showing the 1-mm spacing; and further magnification showing a single microtip observed by scanning electron microscopy. **C)** Magnetic nanoparticles (8 µm in diameter) are internalized in ESCs and localized within endosomes as illustrated on transmission electron microscopy image. D) Spheroids of ESCs are formed via the common hanging drop method (DROP**). E-G)** Spheroids of ESCs are formed by seeding the cells in a dish positioned on top of the microtips-device exposed to a magnetic field (magnet or electromagnet under the device). ESCs are attracted to the magnetic microtips and form cohesive 3D embryoid bodies (EBs). These EBs are then stimulated magnetically following three independent protocols: the spheroids are either compacted magnetically **E)** for a short time-period (5 min; MAG-short) or **F)** for a long one (3 days; MAG-long) by keeping the permanent magnet under the device, or again **G)** the spheroids were cyclically stimulated using an electromagnet (3 days; MAG-cycl).

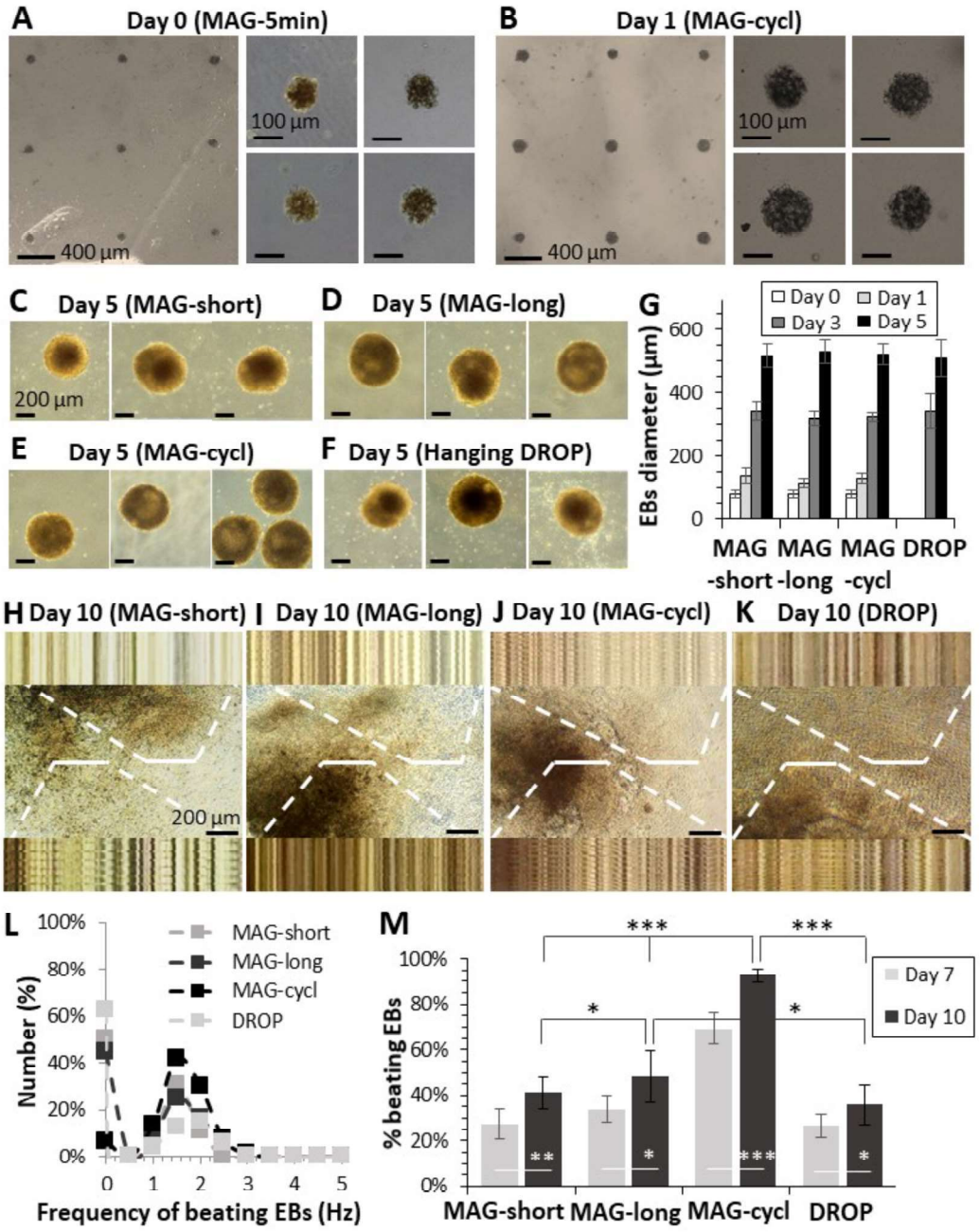

Figure 2. EBs magnetic stimulation. **A-B)** Images of EBs on the magnetic patterns 5 min (A) or 1 day (B; MAG-cycl) after seeding. **C-F)** Representative EBs images for all seeding approaches, 5 days after EBs formation (day 5). **G)** Average size of all EBs for the four seeding protocols. **H-K)** 10 days after seeding (day 10), representative videos of 6 seconds analyzed using Image J, for the four conditions. In each image two defined beating areas (white, full lines) were selected for kymograph analysis (top and bottom raw) which displays the cells beating. **M)** Average frequency of the beating cells for all conditions, analyzed at day 10. **L)** Average percentage of beating EBs, at day 7 and day 10. Statistically significant differences are shown between the conditions with *p<0.1, **p<0.05, ***p<0.01.

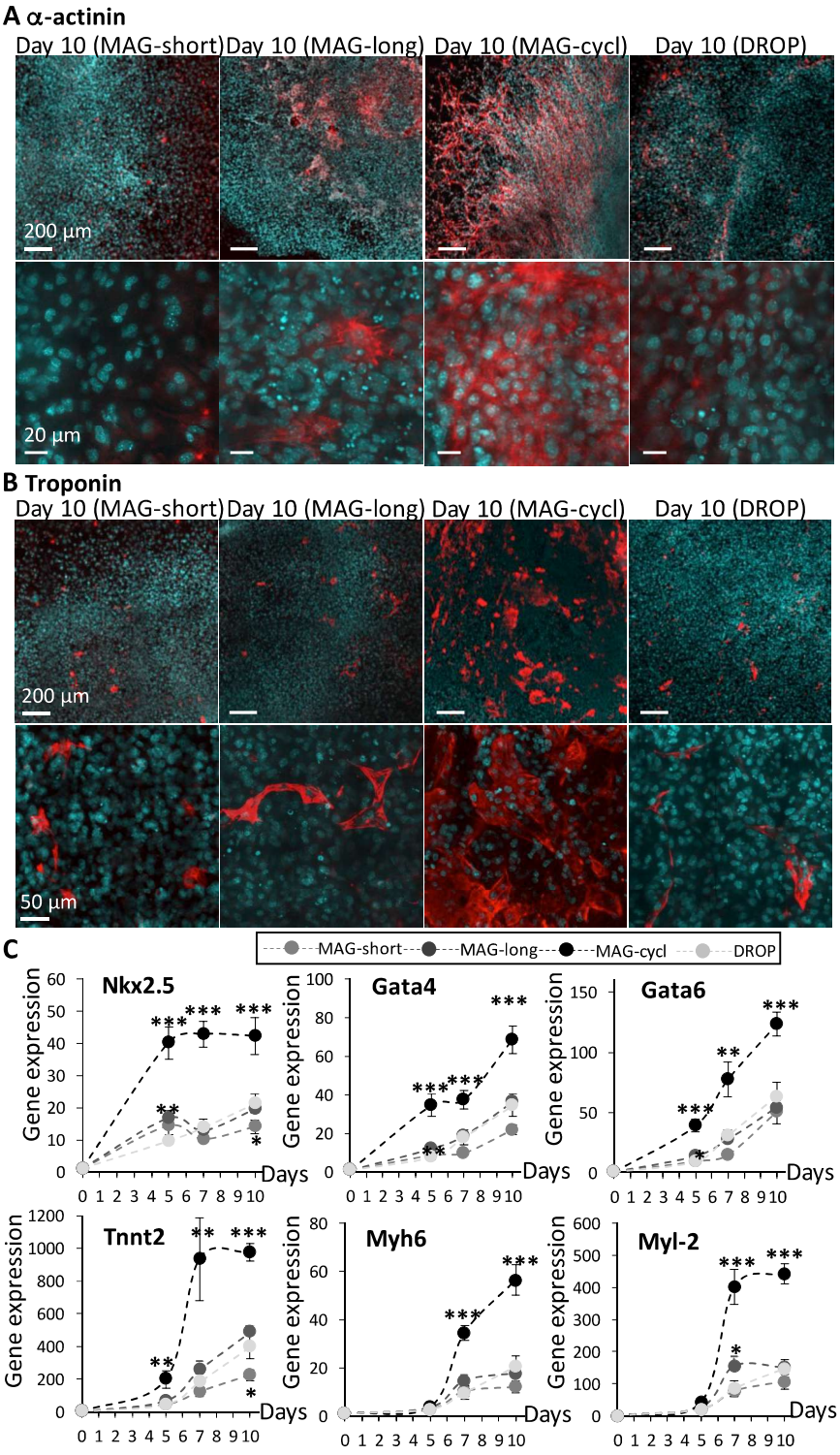

Figure 3. Magneto-mechanical stimulation induced positive expression of the structural proteins **A)** mesoderm α-actinin and **B)** cardiac troponin-T. Immunofluorescence images of the specific antibodies (red) are merged with Dapi (green) for nuclei localization. **C)** Gene expression of proteins involved in mesoderm and cardiac mesoderm differentiation, and in cardiac progenitors, always renormalized by the expression of the same gene at day 0. Statistically significant differences are shown as compared to control (DROP), with *p<0.1, **p<0.05, ***p<0.01.

References

[1] J. M. Kelm, N. E. Timmins, C. J. Brown, M. Fussenegger, L. K. Nielsen, *Biotechnology and bioengineering* **2003**, 83, 173.

[2] J. M. Yuhas, A. P. Li, A. O. Martinez, A. J. Ladman, *Cancer research* **1977**, 37, 3639.

[3] B. Johnstone, T. M. Hering, A. I. Caplan, V. M. Goldberg, J. U. Yoo, *Experimental cell research* **1998**, 238, 265.

[4] a) A. Ovsianikov, A. Khademhosseini, V. Mironov, *Trends in biotechnology* **2018**, 36, 348; b) G. Forgacs, K. Jakab, A. Neagu, V. Mironov, Google Patents, 2015; c) L. Moroni, T. Boland, J. A. Burdick, C. De Maria, B. Derby, G. Forgacs, J. Groll, Q. Li, J. Malda, V. A. Mironov, *Trends in biotechnology* **2018**, 36, 384.

[5] a) H. Rabie, Y. Zhang, N. Pasquale, M. J. Lagos, P. E. Batson, K. B. Lee, *Advanced Materials* **2019**, 31, 1806991; b) T. H. Kim, C. H. Yea, S. T. D. Chueng, P. T. T. Yin, B. Conley, K. Dardir, Y. Pak, G. Y. Jung, J. W. Choi, K. B. Lee, *Advanced Materials* **2015**, 27, 6356.

[6] a) F. A. Pennacchio, C. Fedele, S. De Martino, S. Cavalli, R. Vecchione, P. A. Netti, *ACS applied materials & interfaces* **2017**, 10, 91; b) M. Mahmoudi, S. Bonakdar, M. A. Shokrgozar, H. Aghaverdi, R. Hartmann, A. Pick, G. Witte, W. J. Parak, *ACS nano* **2013**, 7, 8379; c) O. Mashinchian, L.-A. Turner, M. J. Dalby, S. Laurent, M. A. Shokrgozar, S. Bonakdar, M. Imani, M. Mahmoudi, *Nanomedicine* **2015**, 10, 829; d) S. Bonakdar, M. Mahmoudi, L. Montazeri, M. Taghipoor, A. Bertsch, M. A. Shokrgozar, S. Sharifi, M. Majidi, O. Mashinchian, M. Hamrang Sekachaei, P. Zolfaghari, P. Renaud, *ACS applied materials & interfaces* **2016**, 8, 13777.

[7] a) S. Y. Park, J. Park, S. H. Sim, M. G. Sung, K. S. Kim, B. H. Hong, S. Hong, *Advanced materials* **2011**, 23, H263; b) A. Solanki, S. T. D. Chueng, P. T. Yin, R. Kappera, M. Chhowalla, K. B. Lee, *Advanced Materials* **2013**, 25, 5477; c) J. H. Lee, H. K. Choi, L. Yang, S. T. D. Chueng, J. W. Choi, K. B. Lee, *Advanced Materials* **2018**, 30, 1802762; d) M. Kitsara, O. Agbulut, D. Kontziampasis, Y. Chen, P. Menasché, *Acta biomaterialia* **2017**, 48, 20; e) G. Jin, R. He, B. Sha, W. Li, H. Qing, R. Teng, F. Xu, *Materials Science and Engineering: C* **2018**, 92, 995; f) J. E. Perez, T. Ravasi, J. Kosel, *Nanotechnology* **2016**, 28, 055703.

[8] a) S. Hughes, J. Dobson, A. J. El Haj, *Journal of biomechanics* **2007**, 40, S96; b) D. Fayol, G. Frasca, C. Le Visage, F. Gazeau, N. Luciani, C. Wilhelm, *Advanced Materials* **2013**, 25, 2611; c) J. R. Henstock, H. Markides, H. Bin, A. J. El Haj, J. Dobson, in *Nanomagnetic Actuation in Biomedicine*, CRC Press **2018**, p. 205; d) J. P. Armstrong, M. M. Stevens, *Trends in biotechnology* **2019**.

[9] G. R. Souza, J. R. Molina, R. M. Raphael, M. G. Ozawa, D. J. Stark, C. S. Levin, L. F. Bronk, J. S. Ananta, J. Mandelin, M.-M. Georgescu, *Nature nanotechnology* **2010**, 5, 291.

[10] a) V. H. Ho, K. H. Müller, A. Barcza, R. Chen, N. K. Slater, *Biomaterials* **2010**, 31, 3095; b) R.-Z. Lin, W.-C. Chu, C.-C. Chiang, C.-H. Lai, H.-Y. Chang, *Tissue Engineering Part C: Methods* **2008**, 14, 197; c) B. Mattix, T. R. Olsen, Y. Gu, M. Casco, A. Herbst, D. T. Simionescu, R. P. Visconti, K. G. Kornev, F. Alexis, *Acta biomaterialia* **2014**, 10, 623.

[11] B. R. Whatley, X. Li, N. Zhang, X. Wen, *Journal of biomedical materials research Part A* **2014**, 102, 1537.

[12] K. Shimizu, A. Ito, H. Honda, *Journal of bioscience and bioengineering* **2007**, 104, 171.

[13] a) A. Tay, D. Di Carlo, *Nano letters* **2017**, 17, 886; b) P. Tseng, J. W. Judy, D. Di Carlo, *Nature methods* **2012**, 9, 1113; c) D. Liße, C. Monzel, C. Vicario, J. Manzi, I. Maurin, M. Coppey, J. Piehler, M. Dahan, *Advanced Materials* **2017**, 29, 1700189; d) V. Du, N. Luciani, S. Richard, G. Mary, C. Gay, F. Mazuel, M. Reffay, P. Menasche, O. Agbulut, C. Wilhelm, *Nature communications* **2017**, 8, 400; e) M. Ishii, R. Shibata, Y. Numaguchi, T. Kito, H. Suzuki, K. Shimizu, A. Ito, H. Honda, T. Murohara, *Arteriosclerosis, thrombosis, and vascular biology* **2011**, 31, 2210; f) T. Norizadeh-Abbariki, O. Mashinchian, M. A. Shokrgozar, N. Haghighipour, T. Sen, M. Mahmoudi, *Journal of Biomaterials and Tissue Engineering* **2014**, 4, 579.

[14] M. Mahmoudi, M. Yu, V. Serpooshan, J. C. Wu, R. Langer, R. T. Lee, J. M. Karp, O. C. Farokhzad, *Nature nanotechnology* **2017**, 12, 845.

[15] a) M. Cai, R. Shen, L. Song, M. Lu, J. Wang, S. Zhao, Y. Tang, X. Meng, Z. Li, Z.-X. He, *Scientific reports* **2016**, 6, 28250; b) A. D. Celiz, J. G. Smith, A. K. Patel, A. L. Hook, D. Rajamohan, V. T. George, L. Flatt, M. J. Patel, V. C. Epa, T. Singh, *Advanced materials* **2015**, 27, 4006; c) K. Cheng, D. Shen, M. T. Hensley, R. Middleton, B. Sun, W. Liu, G. De Couto, E. Marbán, *Nature Communications* **2014**, 5, 4880; d) A. W. Heldman, D. L. DiFede, J. E. Fishman, J. P. Zambrano, B. H. Trachtenberg, V. Karantalis, M. Mushtaq, A. R. Williams, V. Y. Suncion, I. K. McNiece, *Jama* **2014**, 311, 62.

[16] P. Menasché, V. Vanneaux, A. Hagège, A. Bel, B. Cholley, I. Cacciapuoti, A. Parouchev, N. Benhamouda, G. Tachdjian, L. Tosca, *European heart journal* **2015**, 36, 2011.

[17] G. Vunjak-Novakovic, N. Tandon, A. Godier, R. Maidhof, A. Marsano, T. P. Martens, M. Radisic, *Tissue Engineering Part B: Reviews* **2009**, 16, 169.

[18] a) M. R. Salick, B. N. Napiwocki, J. Sha, G. T. Knight, S. A. Chindhy, T. J. Kamp, R. S. Ashton, W. C. Crone, *Biomaterials* **2014**, 35, 4454; b) W. Bian, B. Liau, N. Badie, N. Bursac, *Nature protocols* **2009**, 4, 1522.

[19] a) C. L. Happe, A. J. Engler, *Circulation research* **2016**, 118, 296; b) V. Panzetta, S. Fusco, P. A. Netti, *Proceedings of the National Academy of Sciences* **2019**, 116, 22004.

[20] a) J. Li, M. Stouffs, L. Serrander, B. Banfi, E. Bettiol, Y. Charnay, K. Steger, K.-H. Krause, M. E. Jaconi, *Molecular biology of the cell* **2006**, 17, 3978; b) P. W. Burridge, G. Keller, J. D. Gold, J. C. Wu, *Cell stem cell* **2012**, 10, 16; c) P. W. Burridge, S. Thompson, M. A. Millrod, S. Weinberg, X. Yuan, A. Peters, V. Mahairaki, V. E. Koliatsos, L. Tung, E. T. Zambidis, *PloS one* **2011**, 6, e18293.

[21] M. Pucéat, *Methods* **2008**, 45, 168.

[22] A. Behfar, L. V. Zingman, D. M. Hodgson, J.-M. Rauzier, G. C. Kane, A. Terzic, M. Pucéat, *The FASEB Journal* **2002**, 16, 1558.

Supporting Information

Genes	Primers sequences
RPLP0	Fwd: GCC-AGC-TCA-GAA-CAC-TGG-TCT-A
	Rev: ATG-CCC-AAA-GCC-TGG-AAG-A
Nkx2.5	Fwd: CTC-CGC-CAA-CAG-CAA-CTT-C
	Rev: GGA-CTC-TGC-ACG-GTG-TTC-AA
Gata4	Fwd: CCT-CCC-GCA-CGA-TTT-CTG
	Rev: CTC-AGG-AAA-AAG-AAA-ATC-CCA-AAT-T
Gata6	Fwd: TCC-CCT-GCC-GAA-GTC-ACA
	Rev: GGC-CAG-AGC-ACA-CCA-AGA-A
TNNT2	Fwd: CGA-CCT-GCA-GGA-AAA-GTT-CAA
	Rev: TCC-GGT-TTC-GCA-GAA-CGT
Myh6	Fwd: CGA-CAT-CAG-TCA-GCA-GAA-CAG
	Rev: GTC-AGA-GCG-CAG-CTT-CTC-C
Myl2	Fwd: CCA-GCA-GGC-TCC-TCG-AAC-T
	Rev: TTT-GGT-GCC-ATG-GTG-TCT-GA

Table S1: Primers sequences used in real-time PCR analysis (5' to 3') for: 60S acidic ribosomal protein P0 (RPLP0), NK2 Homeobox 5 (Nkx2.5), GATA Binding Protein 4 (Gata4), GATA Binding Protein 6 (Gata6), Troponin T Type 2 (Cardiac) (TNNT2), Myosin Heavy Chain 6 (Myh6), Myosin Light Chain 2 (Myl2).

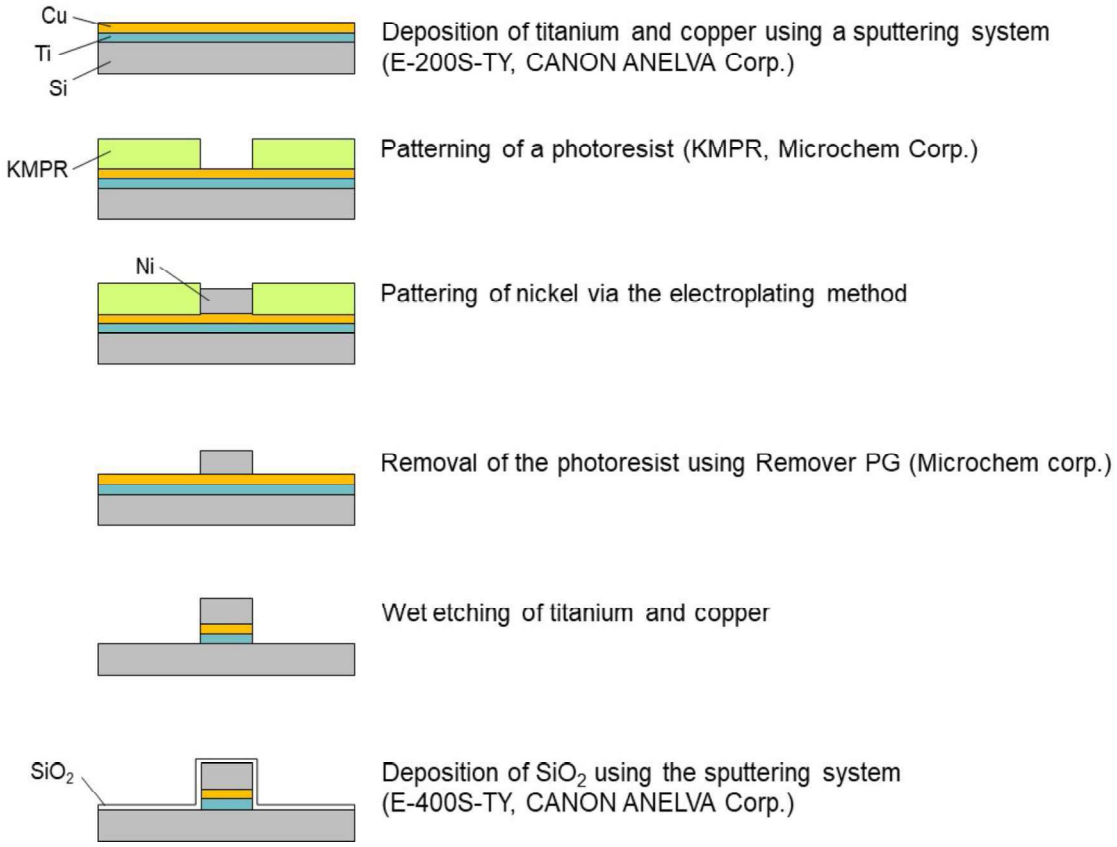

Figure S1: Fabrication procedure of the nickel micropatterns covered with a silica layer using a photolithography method.

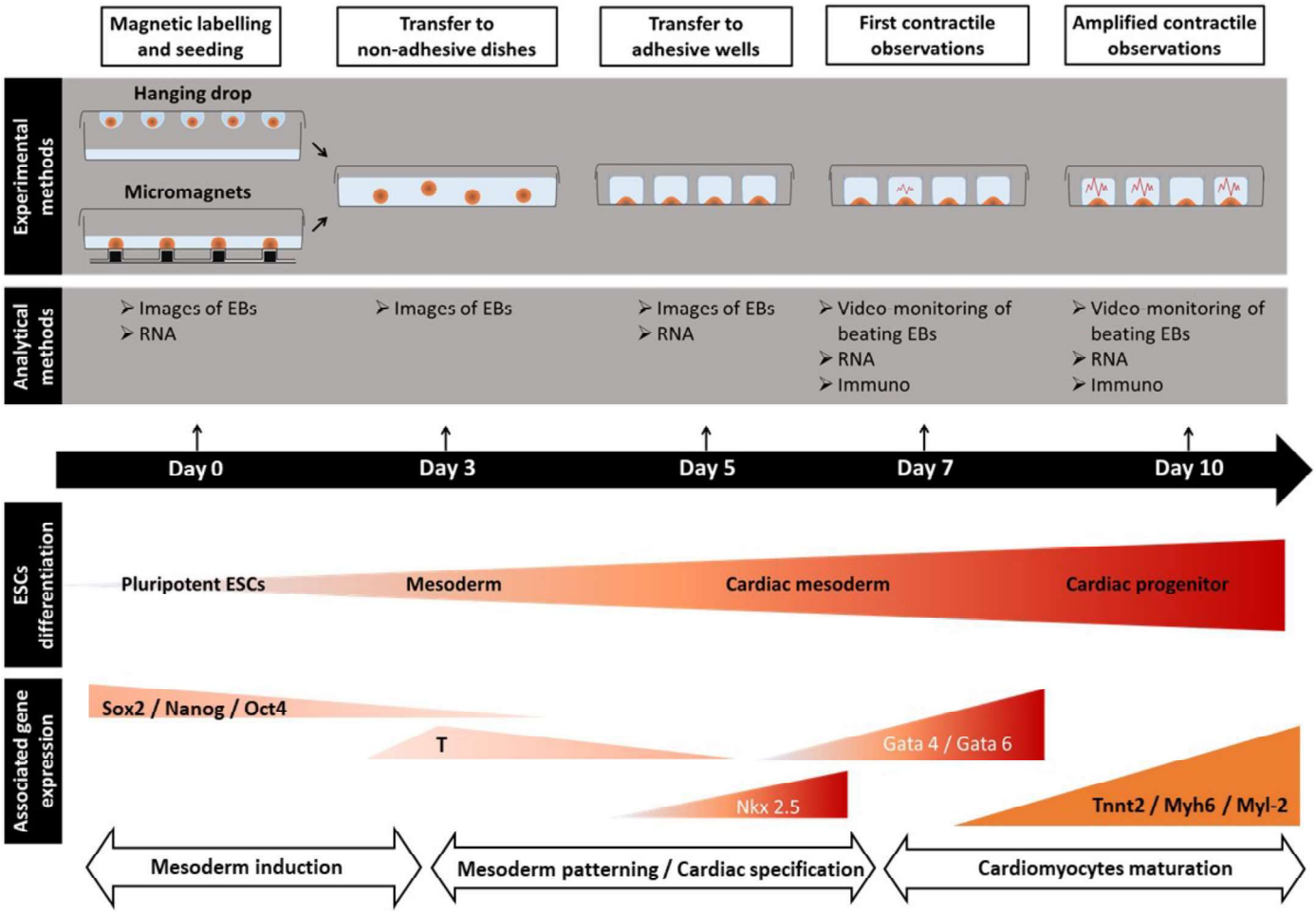

Figure S2: Schematic of the methods employed for the differentiation of embryonic stem cells toward the cardiac lineage (top raws) and of some typical genes expressed over the steps of this differentiation (bottom raws).[1-4]

[1] U. Rutishauser, J. P. Thiery, R. Brackenbury, B. A. Sela, G. M. Edelman, Proc. Natl. Acad. Sci. U.S.A. 1976, 73, 577.

[2] E. Willems, P. J. Bushway, M. Mercola, Pediatr Cardiol 2009, 30, 635.

[3] M. Nakanishi, A. Kurisaki, Y. Hayashi, M. Warashina, S. Ishiura, M. Kusuda-Furue, M. Asashima, FASEB J. 2009, 23, 114.

[4] K. Rajala, M. Pekkanen-Mattila, K. Aalto-Setälä, Stem Cells Int 2011, 383709.

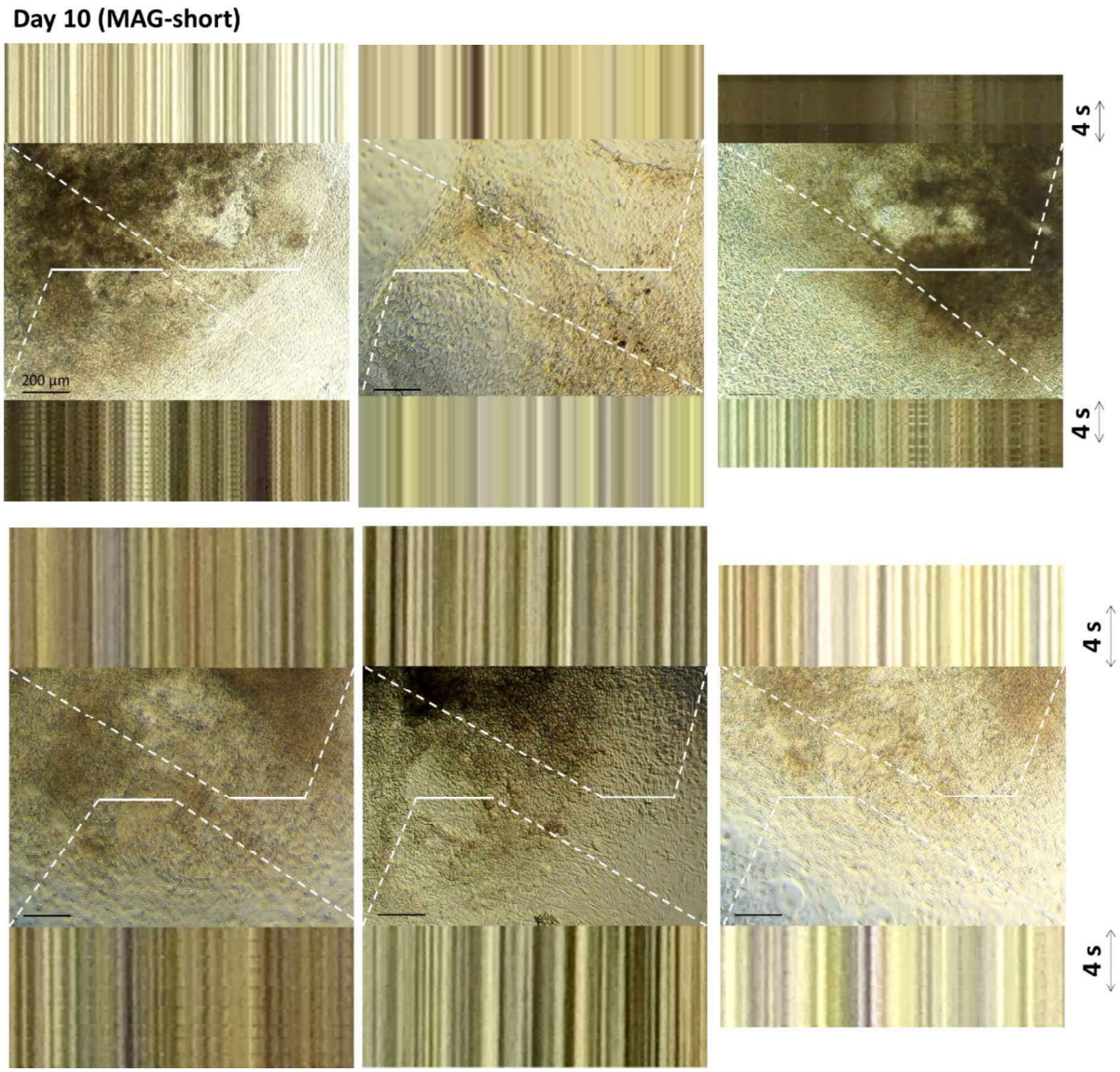

Figure S3: Mag-short condition. Representative illustrations of beating events for MAG-short EBs seeded in gelatin-coated wells, and observed at day 10. Each illustration shows in the center a still image of the movie from which kymographs (top and bottom images) were extracted. Each time, the white plain line corresponds to the portion of image used for kymograph analysis (Fiji resliced function), and the vertical axis represent the elapsed time (same bar for all, shown on the left, equal to 4 s). Horizontal scale bar is 5 µm. Whenever the white line is situated within a beating area, periodic oscillations are seen on the kymographs.

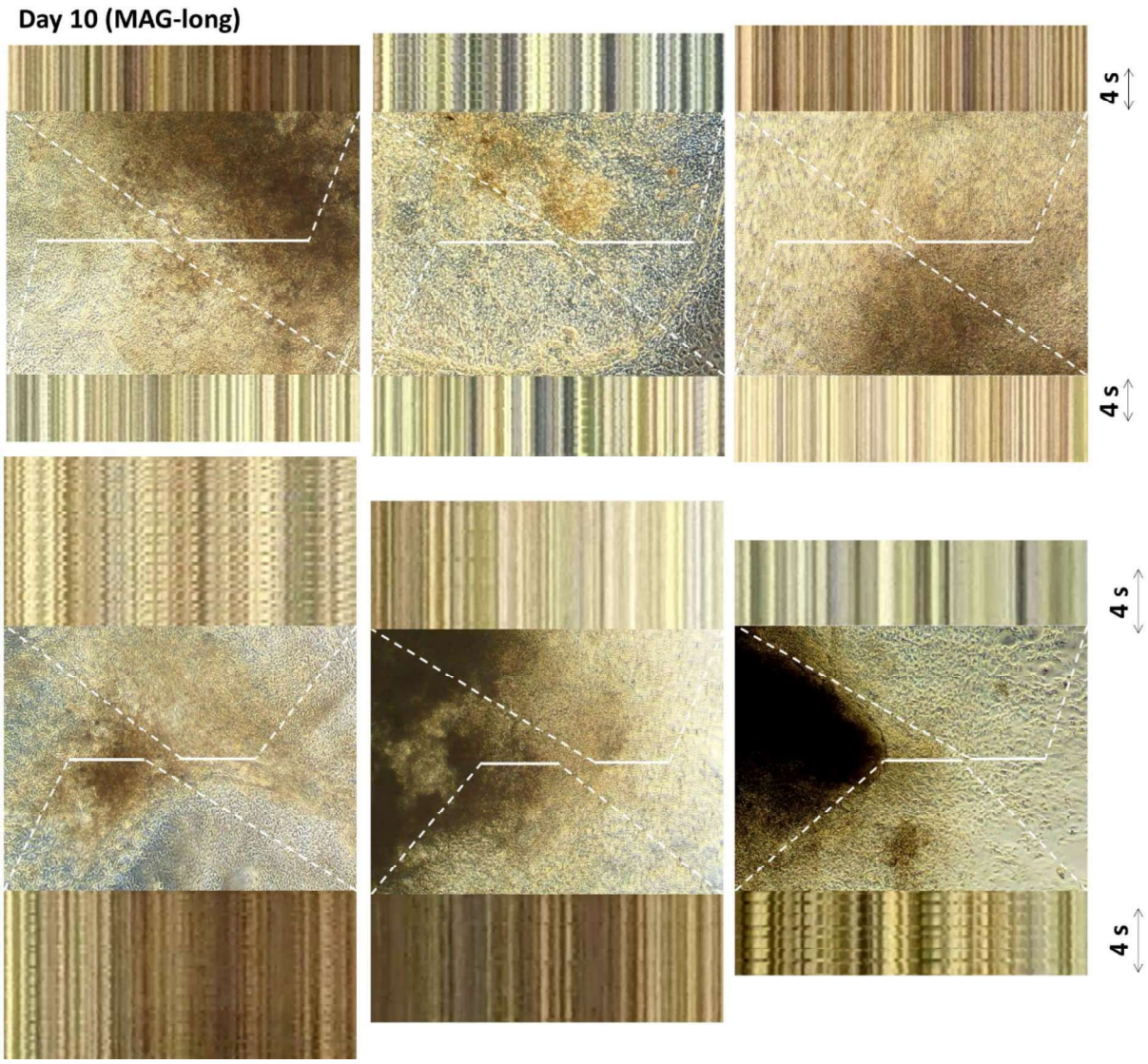

Figure S4: Representation kymographs for the MAG-long condition, extracted from the movies of EBs potential beatings at day 10. See the caption of Figure S1 for more details.

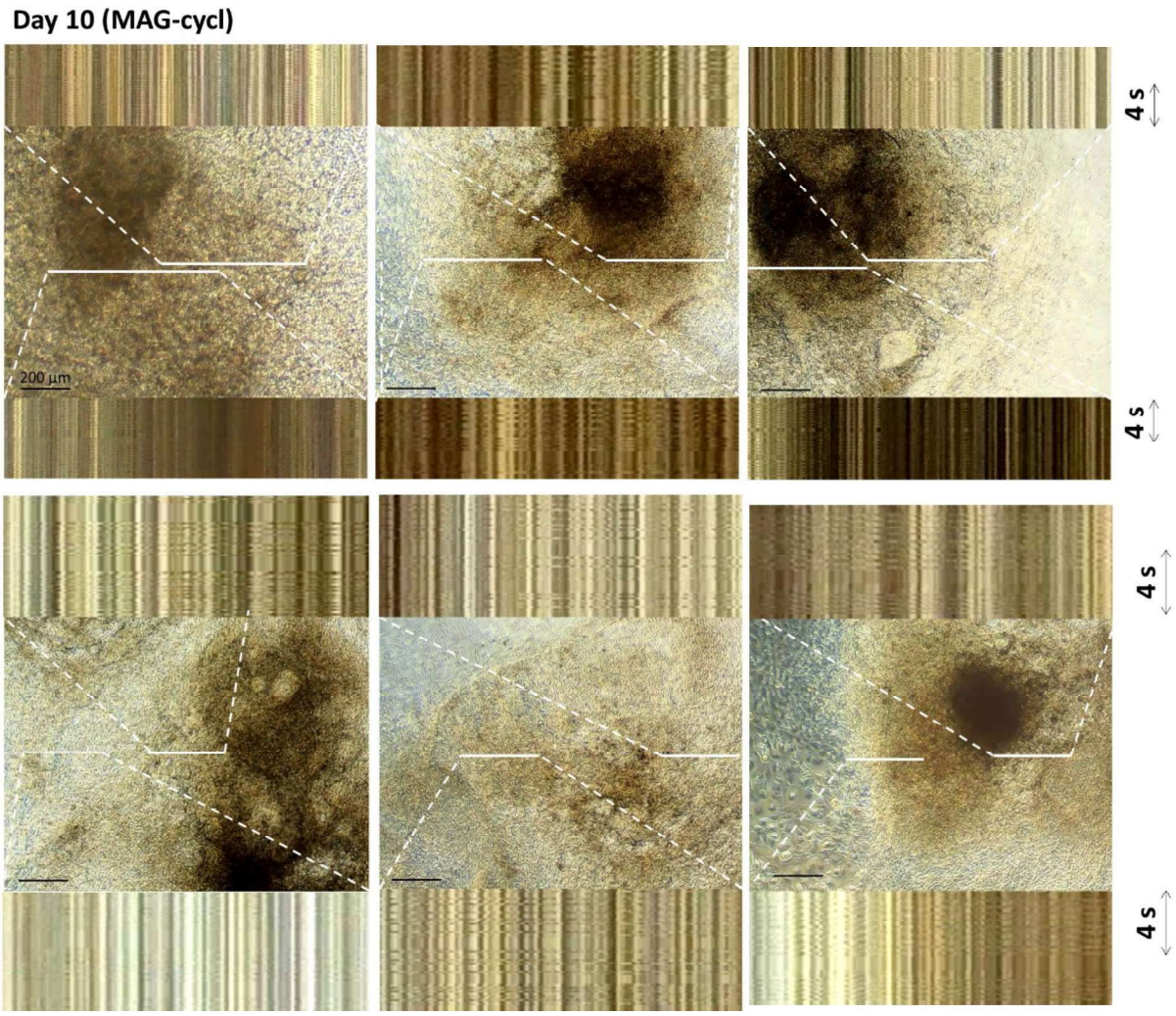

Figure S5: Representation kymographs for the MAG-cycl condition, extracted from the movies of EBs potential beatings at day 10. See the caption of Figure S1 for more details.

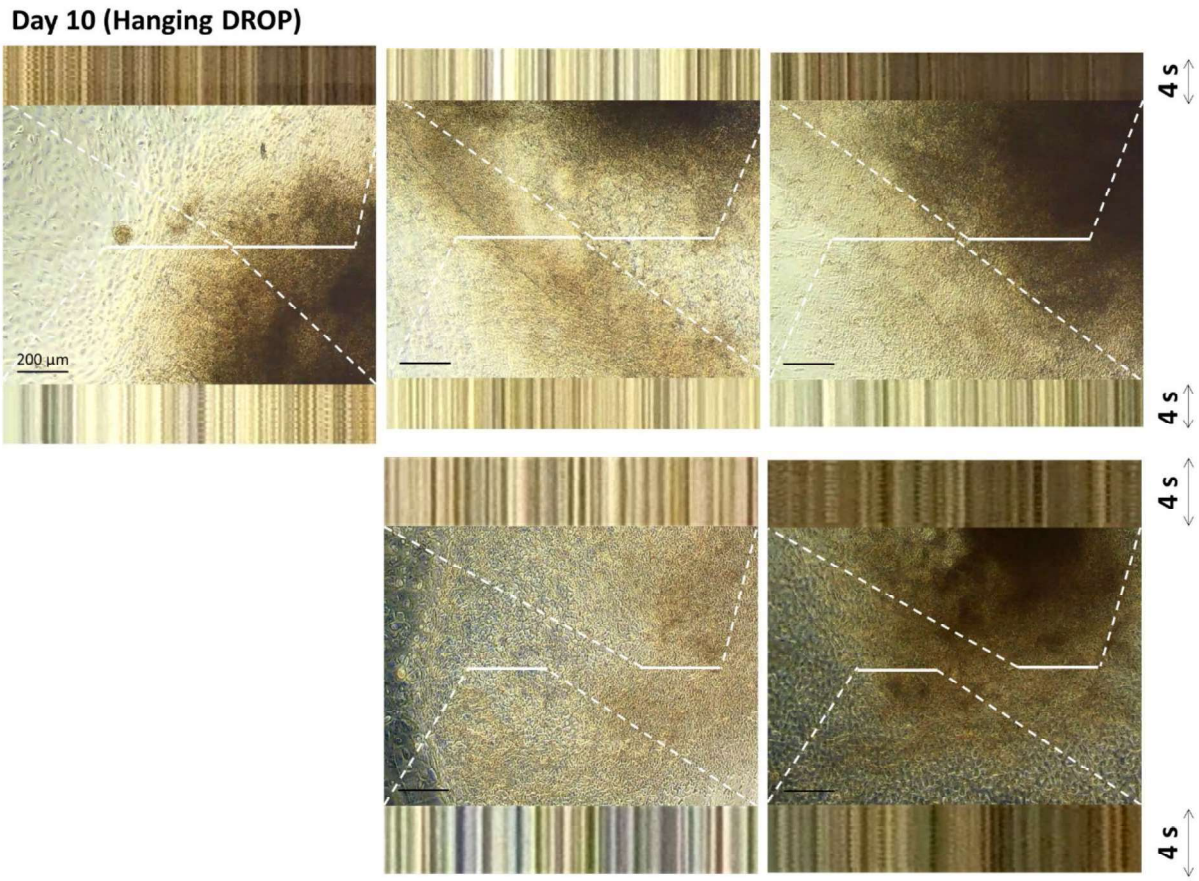

Figure S6: Representation kymographs for the hanging drop condition, extracted from the movies of EBs potential beatings at day 10. See the caption of Figure S1 for more details.

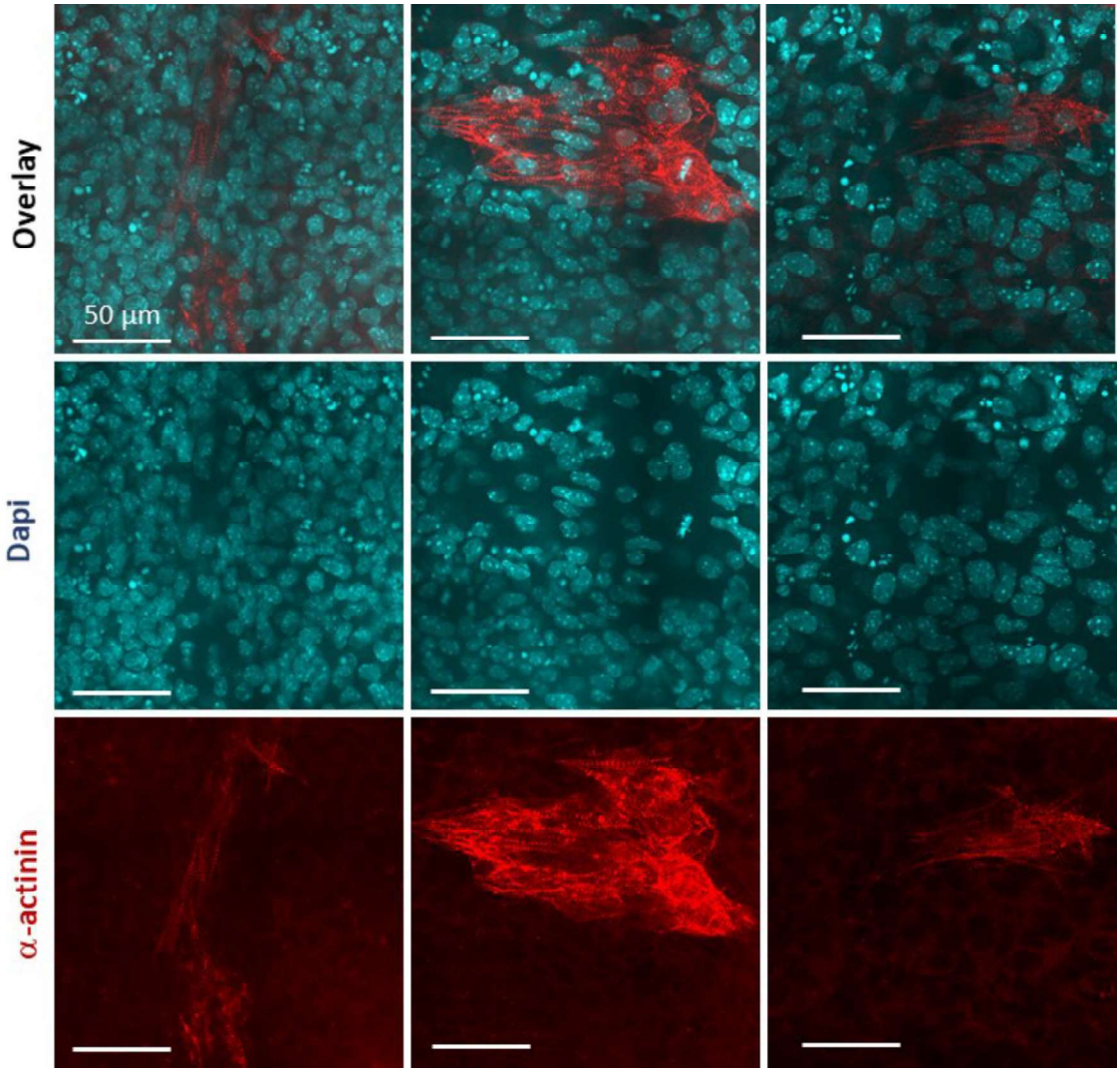

Figure S7: Immunofluorescent analysis of α-actinin for the condition MAG-long, at day 10. Additional images to the ones showed in Figure 3A. Cells were labeled with α-actinin mouse monoclonal antibody, then stained using goat anti-mouse IgG secondary antibody (red, bottom panel) and counterstained with DAPI (blue, middle panel). Top panel is the merged image.

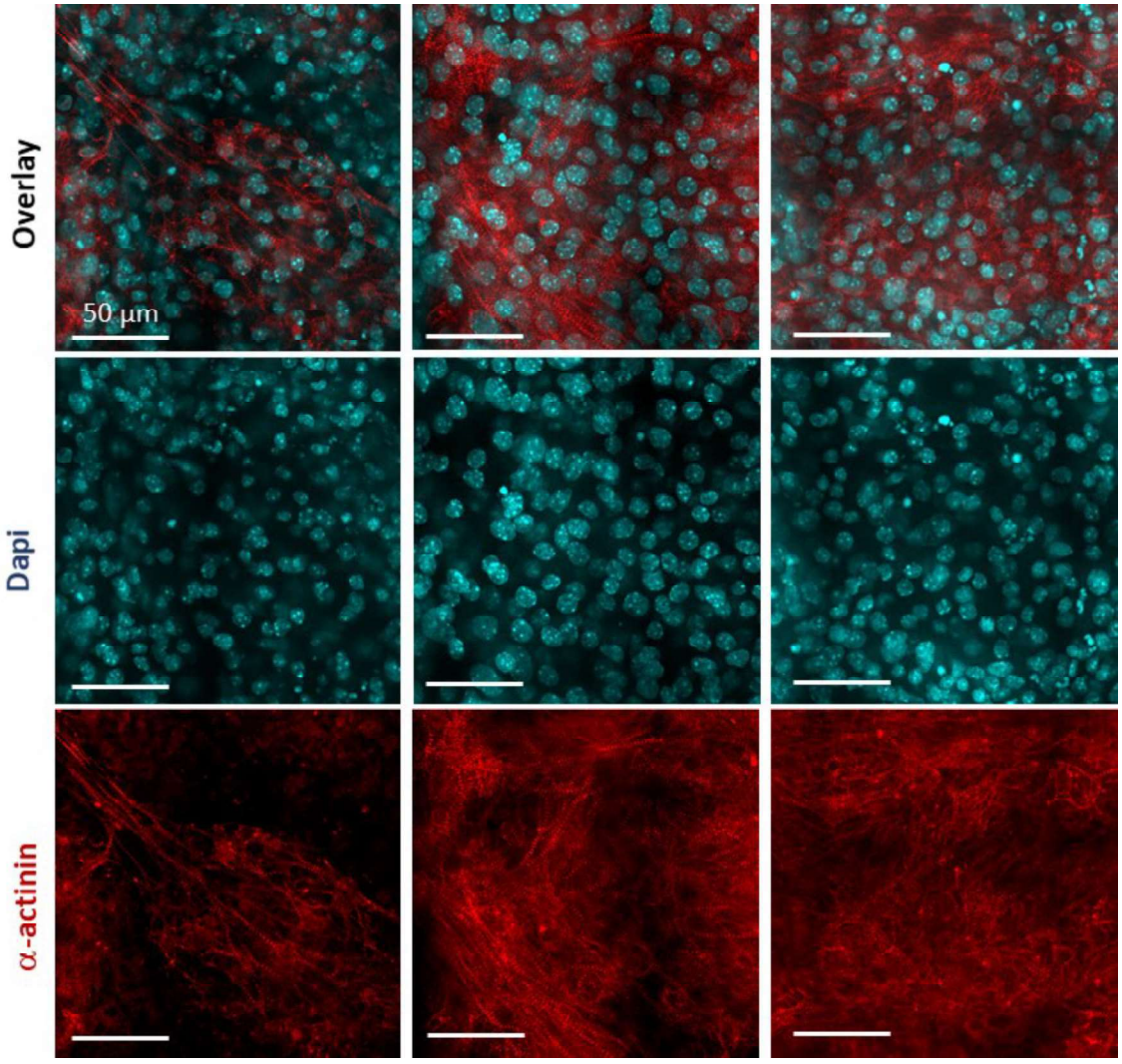

Figure S8: Immunofluorescent analysis of α-actinin for the condition MAG-cycl, at day 10. Additional images to the ones showed in Figure 3A. Cells were labeled with α-actinin mouse monoclonal antibody, then stained using goat anti-mouse IgG secondary antibody (red, bottom panel) and counterstained with DAPI (blue, middle panel). Top panel is the merged image.

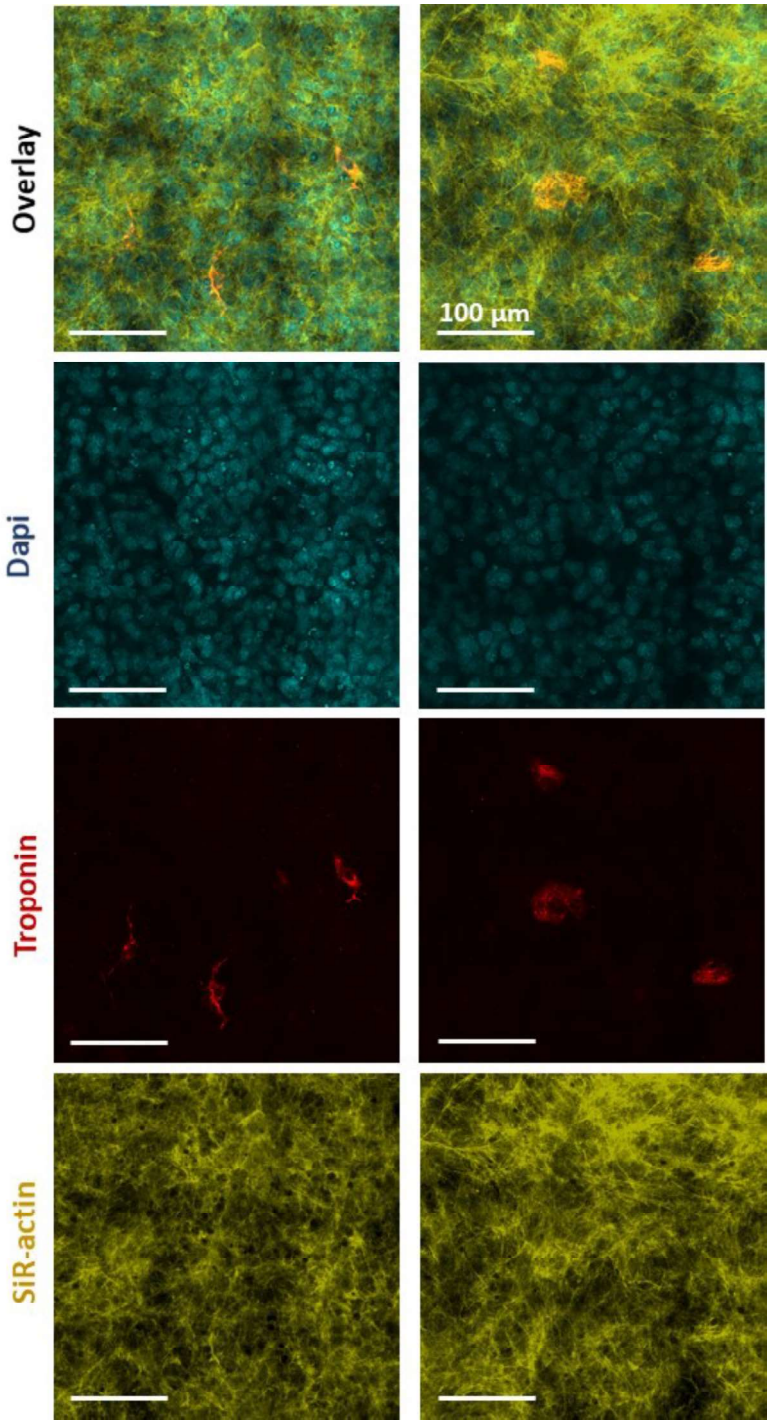

Figure S9: Immunofluorescent analysis of cardiac troponin-T for the condition MAG-short, at day 10. Cells were labeled with cardiac troponin-T mouse monoclonal antibody, then stained using goat anti-mouse IgG secondary antibody (red, second middle panel) and counterstained with DAPI (blue, first middle panel). SiR-actin probe was used (SC001, Spirochrome, 1:1000 in PBS for 2h at room temperature, before DAPI staining) to stain F-actin (yellow, bottom panel). Top panel is the merged image.

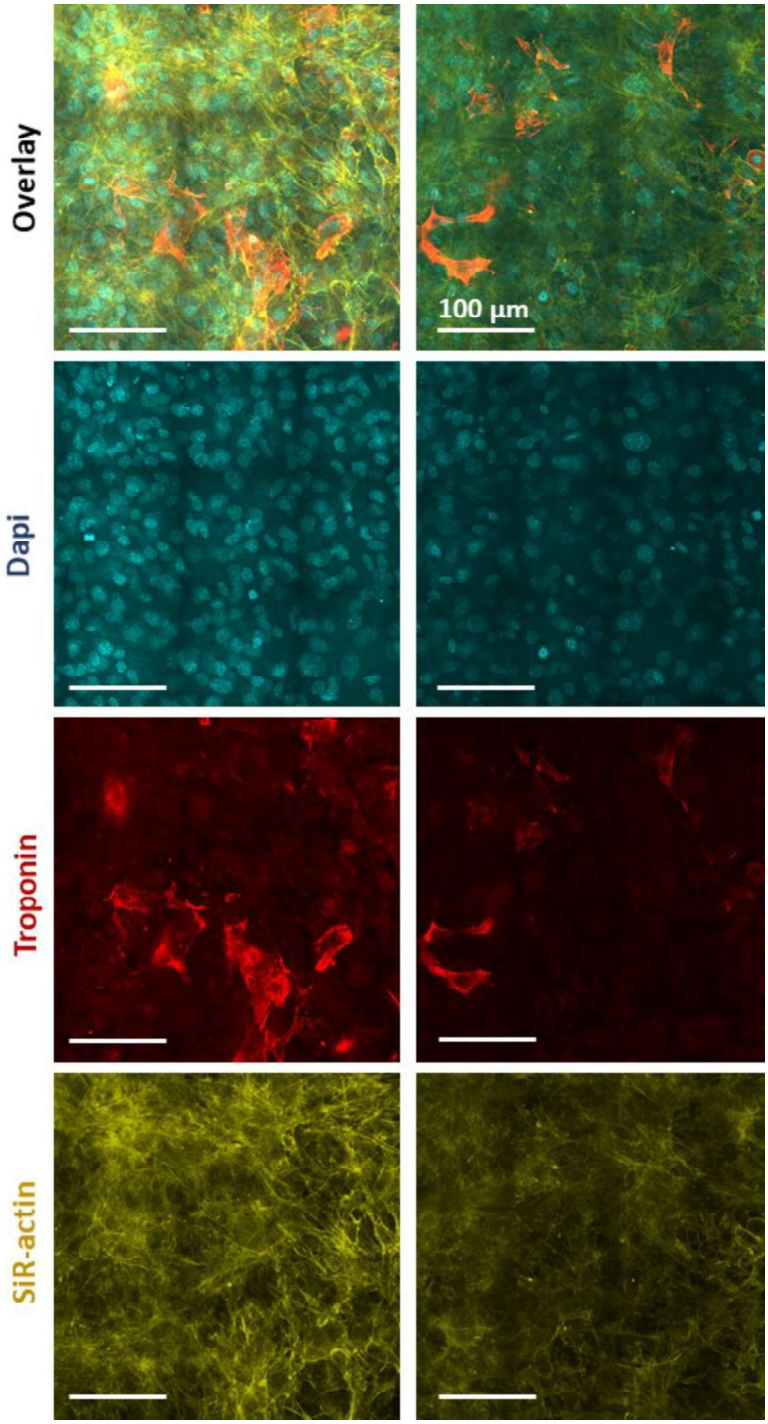

Figure S10: Immunofluorescent analysis of cardiac troponin-T for the condition MAG-long, at day 10. Cells were labeled with cardiac troponin-T mouse monoclonal antibody, stained using goat anti-mouse IgG secondary antibody (red, second middle panel), then stained with SiR-actin probe (yellow, bottom panel) and counterstained with DAPI (blue, first middle panel). Top panel is the merged image.

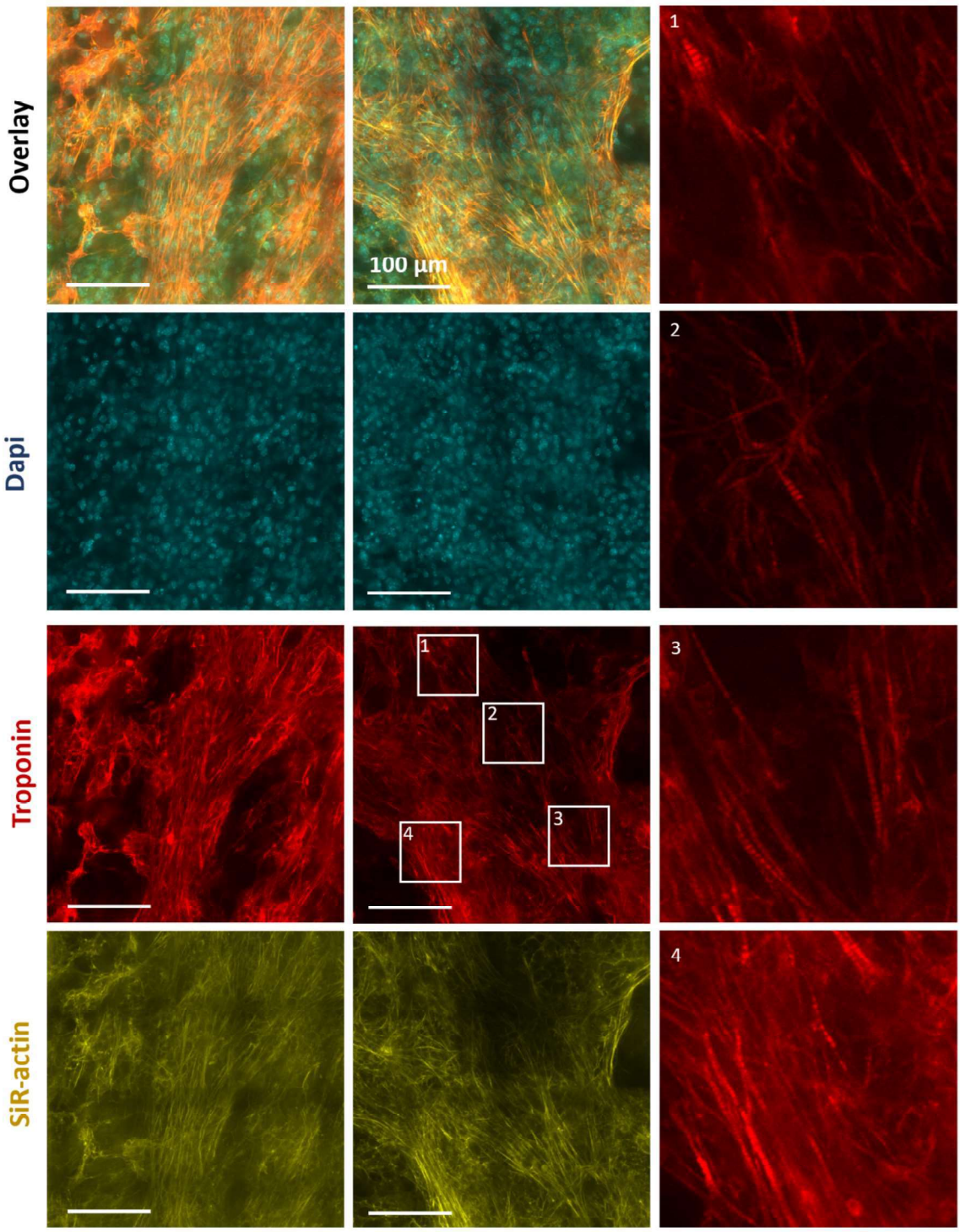

Figure S11: Immunofluorescent analysis of cardiac troponin-T for the condition MAG-cycl, at day 10. Cells were labeled with cardiac troponin-T mouse monoclonal antibody, stained using goat anti-mouse IgG secondary antibody (red, second middle panel), then stained with SiR-actin probe (yellow, bottom panel) and counterstained with DAPI (blue, first middle panel). Top panel is the merged image. In the middle raw image corresponding to the Troponin staining, four sections have been zoomed in and are displayed in the right column, showing the appearance of striated structures.

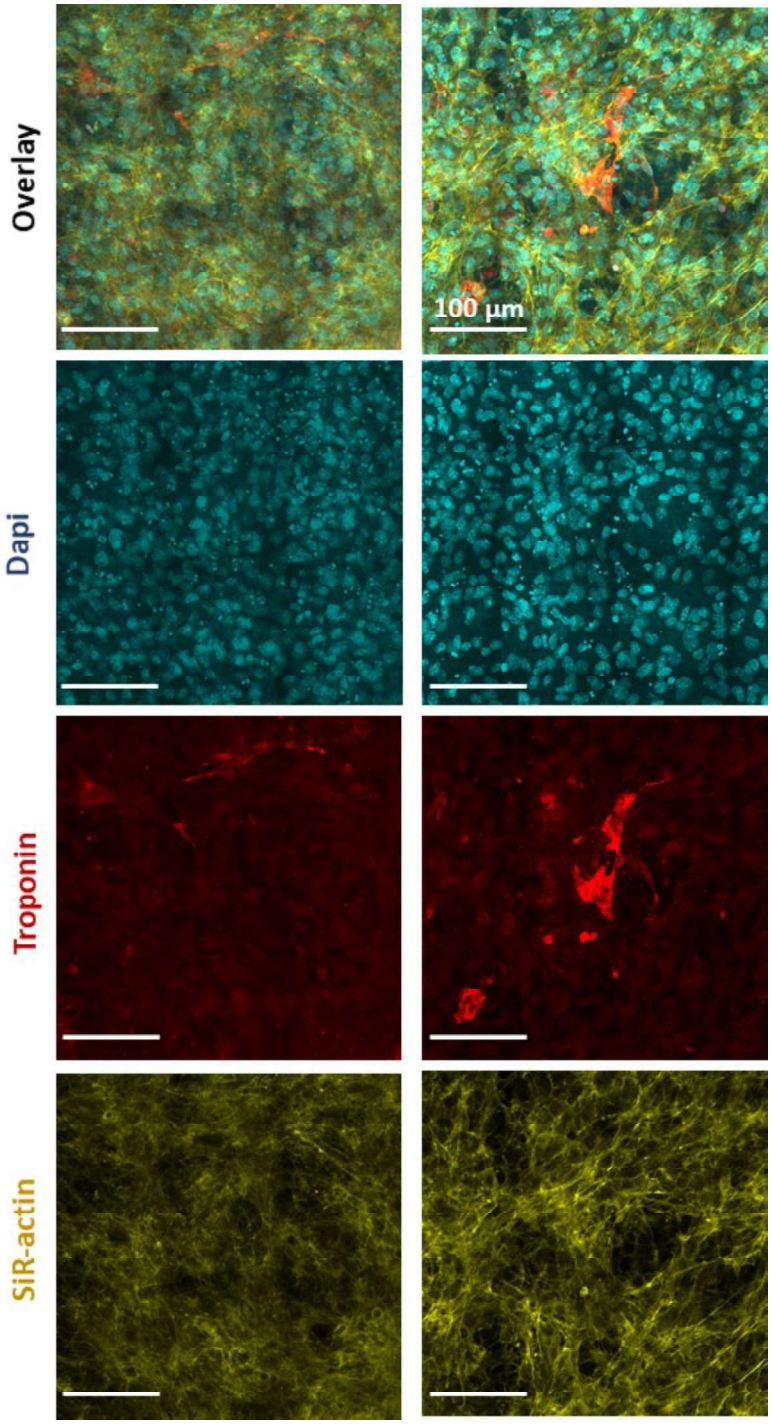

Figure S12: Immunofluorescent analysis of cardiac troponin-T for the condition hanging DROP, at day 10. Cells were labeled with cardiac troponin-T mouse monoclonal antibody, stained using goat anti-mouse IgG secondary antibody (red, second middle panel), then stained with SiR-actin probe (yellow, bottom panel) and counterstained with DAPI (blue, first middle panel). Top panel is the merged image.

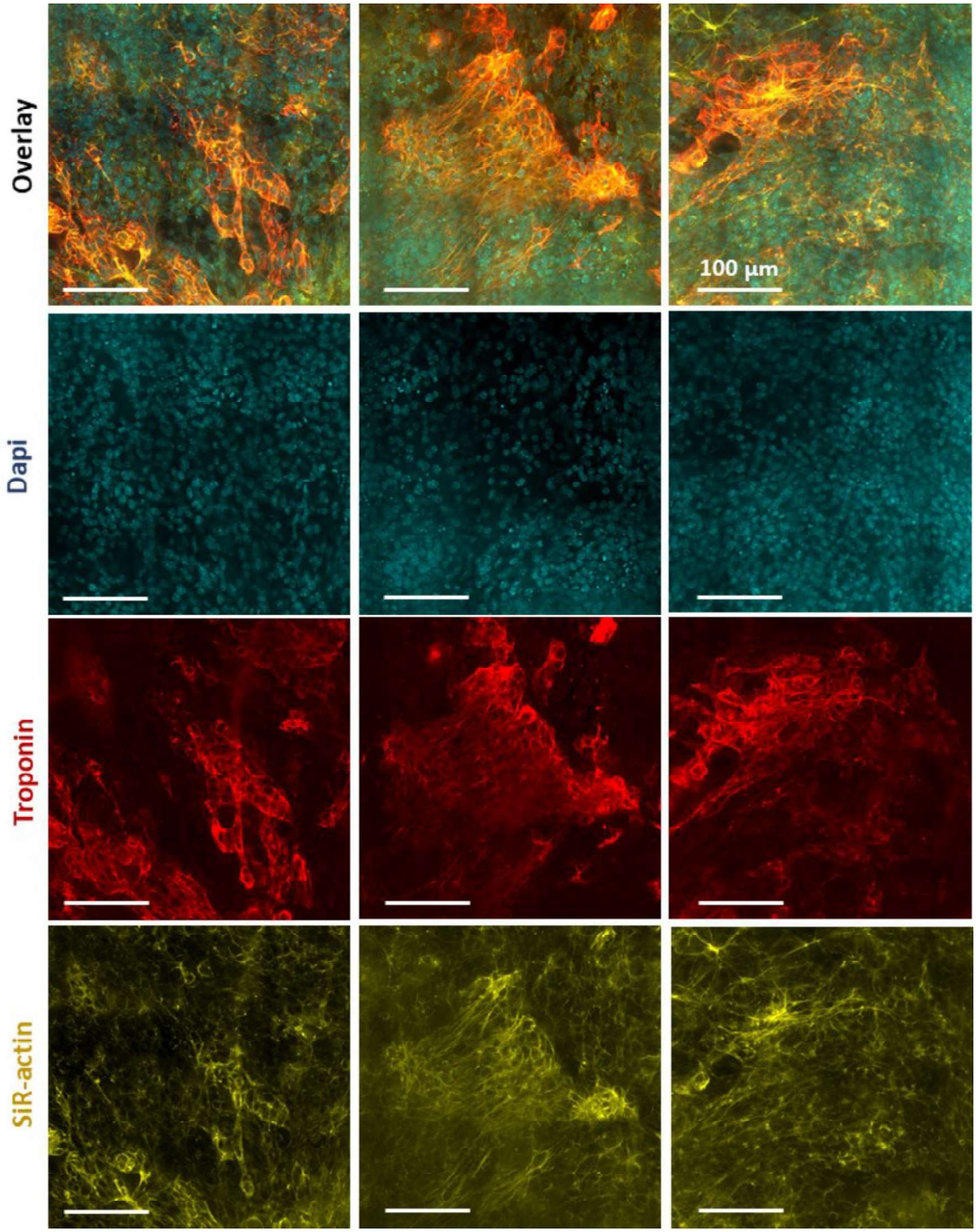

Figure S13: Immunofluorescent analysis of cardiac troponin-T for the condition MAG-cycl, at day 7. Cells were labeled with cardiac troponin-T mouse monoclonal antibody, stained using goat anti-mouse IgG secondary antibody (red, second middle panel), then stained with SiR-actin probe (yellow, bottom panel) and counterstained with DAPI (blue, first middle panel). Top panel is the merged image. As compared to the same condition, at day 10 (previous Figure S11), the troponin staining shows less marked striated muscle fiber localization.

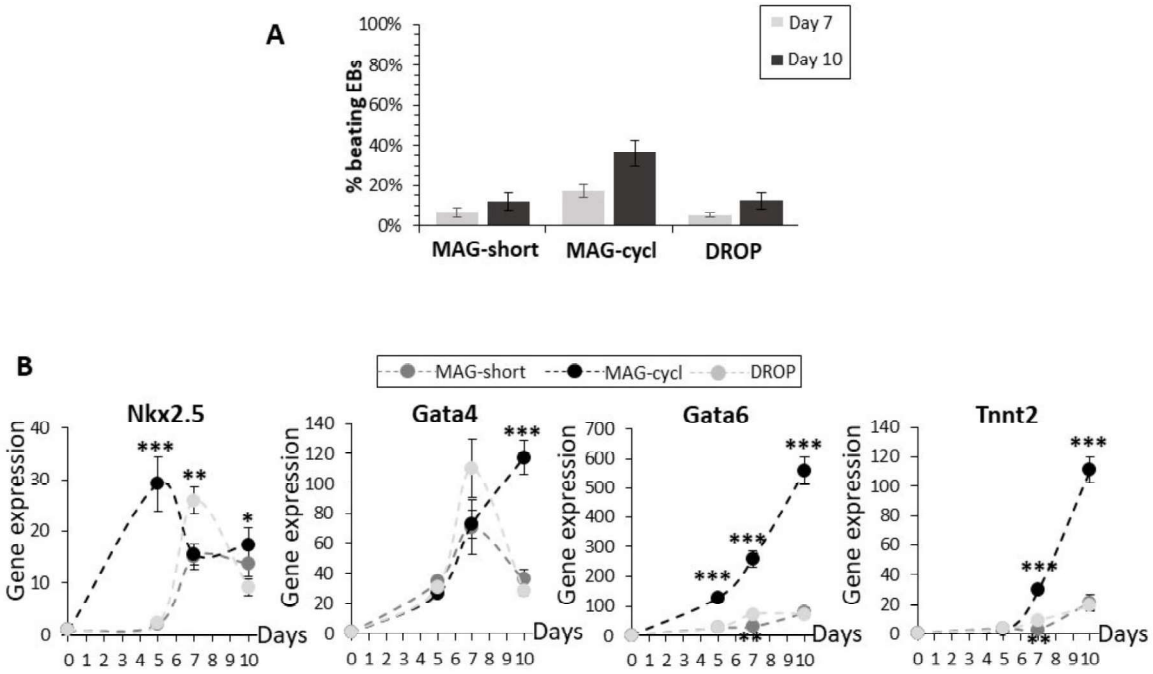

Figure S14: Use of another batch of CGR8 ESCs, having experienced a large number of passages (over 50) prior to use. As shown in A), where the number of beating EBs observed at day 7 and day 10 are plotted for each condition, they were less competent to cardiomyogenesis than the batch newly purchased (Sigma, 07032901) and used in the work. Indeed, less than 20% EBs were beating at day 10 for the control hanging drop condition, as well as for the magnetically patterned EBs without stimulation (MAG-short), while with the new batch, this percent was in the 40% range for both control and MAG-short conditions. Yet, the on/off mechanical cyclic stimulation (MAG-cycl) was again improving greatly cardiomyogenesis, with a more than 2-fold increase in the number of beating EBs at day 10. The positive impact of the cyclic stimulation to direct differentiation was further confirmed with RT-PCR, as shown in B). The mesoderm genes (NKX2.5, Gata4 and Gata6) and cardiac mesoderm Tnnt2 gene were 6 to 10-fold upregulated for the MAG-cycl condition. Note that the level of Tnnt2 expression is much lower than the one reached with the new CGR8 ESCs (see Figure 3C), confirming that this ESC batch was less competent for differentiation to the cardiac lineage. However, these results remarkably evidence that, for two independent ESCs batches used, the cyclic stimulation direct cardiomyogenesis, demonstrating further the robustness of the method.

CHAPTER 3.5: MAGNETIC STRETCHING OF SKELETAL MUSCLE PRECURSORS

12 - C2C12 alignment through the use of magnetic forces

The last chapter of this manuscript presents preliminary results on the use of the Magnetic Stretcher for skeletal tissue engineering. The final goal of this project is to align and to mature skeletal precursors in a 3D scaffold-free configuration, only using a mechanical stretching. First, the impact of the magnetic labelling on the differentiation of C2C12 cells will be addressed. Then, we will present the main features of the Magnetic Stretcher, and how several magnetic configurations were used to optimize the formation of 3D magnetic stretchable C2C12 spheroids. Finally, we will address the main features of thus obtained aggregates, and we will highlight the proof of concept of our magnetic approach to align skeletal muscle precursors.

Content

12.1 - C2C12 magnetic labelling and differentiation

Creating an artificial muscle implies to magnetically label myoblasts precursors, and to optimize the nanoparticle internalization in order to obtain a maximal magnetic force while being able to differentiate them. Within the master internship of Irene Nagle, we demonstrated that the magnetic labelling does not impact neither the differentiation nor the viability of myoblasts with concentrations in a range from 2 to 16 mM in γ-Fe_2O_3 nanoparticles (9 nm, 30% dispersity), and for labelling times in a range of 30 min to 2h. To assess this, cells were magnetically labelled in the chosen condition after reaching 90% of confluency. The cells were put at rest in supplemented medium for 1h after the labelling. Then, the cells were put in low glucose condition in order to trigger the differentiation (1). Bright Field (BF) images were acquired in order to check to C2C12 fusion, and immunolabelling of α-actinin was performed as a way to monitor the maturation of the myotubes.

Figure 12-1 presents typical pictures of the differentiation of C2C12 labelled with high iron conditions. The presented cells were labelled for 30 min with an iron concentration of 16 mM, resulting in 15 pg of iron per cells. Figure 12-1.A presents a BF image of the cells cultured for 5 days in the differentiation medium. If single cells are still visible, a large number of the highly labelled C2C12 achieved to fuse and to form myotubes. As shown in figure 1B, immunolabelling of α-actinin demonstrates the striation of the myotube cytoskeleton. Two different z-position of the same field are presented, and two myotubes are shown. The labelling of the nuclei demonstrates poly-nucleated structures, and the α-actinin labelling shows a partial striation of the cytoskeletons. Besides, at day 5 the maturation was not achieved yet: the cytoskeleton striation was not complete, and the nuclei were not spread along the myotubes. Nevertheless, even in such an important labelling condition, differentiation of the C2C12 cells is not impacted.

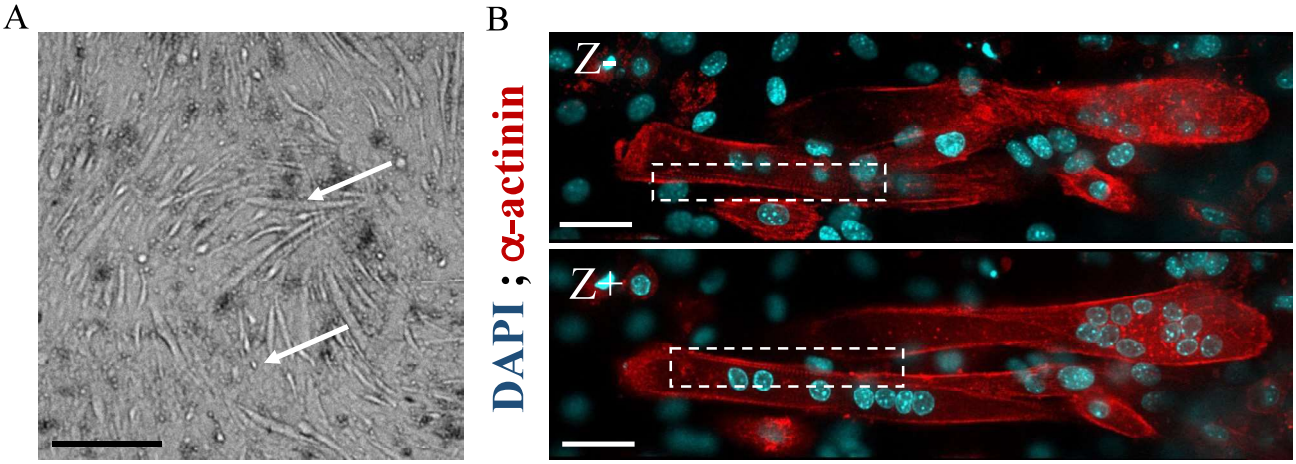

Figure 12-1: C2C12 differentiation after magnetic labelling. A) Bright Field picture of C2C12 cultured for 5 days in low-glucose medium (DMEM, 1% P/S). Before switching to differentiation medium, the cells are magnetically labelled ([Fe] = 16 mM, 30 min) with iron oxide nanoparticles (γ-Fe_2O_3), achieving an internalization of 15 pg of iron per cells. Top white arrow indicates a typical myotube. Bottom white arrow indicates a rounded non-differentiated C2C12 cell. C2C12 fusion is not impacted by a high magnetic labelling. Scale bar: 50 μm **B)** Immuno-fluorescence images of C2C12 labelled in the same condition. The nuclei are show in cyan (DAPI), and the α-actinin in red. Two different z-positions of the same plan are presented, and three myotubes are visible. They presented an early stage differentiation: if the myotubes were poly-nucleated, the nuclei were still gathered. Striation of the cytoskeleton was visible. The maturation of C2C12 myotubes is not impacted by a high magnetic labelling. Scale bar: 50 μm. We warmly thank Irène Nagle for the pictures.

After optimization (data not shown), a 2h labelling using a 2 mM solution was chosen for all results presented next. In this condition, 10 pg of iron were internalized per cells.

12.2 - The Magnetic Stretcher

The Magnetic Stretcher is presented in Figure 12-2.A-B. This is an upgraded version of the device presented in the introduction of this chapter (2). The device is composed of a cell culture chamber, where 2 magnetic actuators hold the cells. The first magnetic actuator is fixed to the culture chamber, and the second is mobile using a motorized actuator (Thorlabs, actuator: " Z806B 6mm Travel DC Servo Motor Actuator", minimal displacement of 1 μm). As the culture chamber and the magnetic parts are 3D printed, the magnetic parts can be tuned in order to obtain different magnetic geometries. Herein, the presented magnetic parts (Figure 12-2.B) are composed of iron needles (750 μm in diameter), magnetised by 6x6 mm permanent magnets (Supermagnet, B = 520 mT, gradB = 180 $T.m^{-1}$).

The magnetic cells were seeded on the fixed actuator, and held by the field gradient. A typical cell deposit is shown in Figure 12-2.C.1. After seeding roughly 1 million of magnetic cells on

the fixed part, the mobile actuator was approached to the formed aggregates. The aggregate was deformed by the second field gradient, and we ended up with a cylindrical aggregates held by the two magnetic gradients (Figure 12-2.C.2-3). Thus, the aggregates can be stretched at will by displacing backward the mobile magnetic part (Figure 12-2.4). In the given example, the aggregate was subjected to a stretching representing 15% of the aggregate initial height.

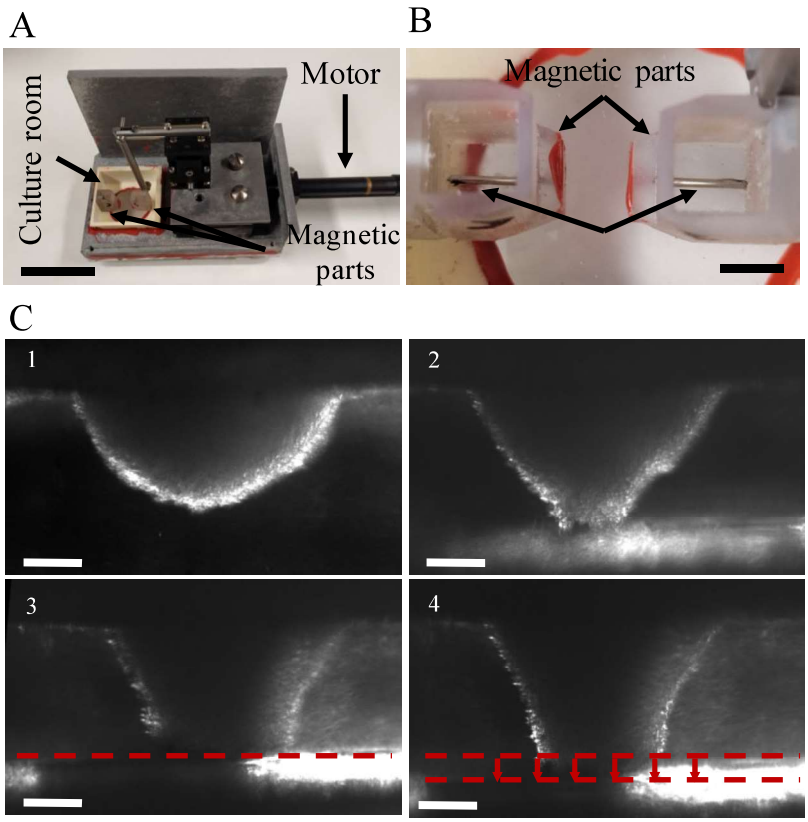

Figure 12-2: The Magnetic Stretcher. A) Pictures of the Magnetic Stretcher. Left picture presents the device composed of: a culture room (white part), a fixed magnet (on the left), and a movable magnet operated by a mechanical actuator (grey and black parts). The right picture presents the device once sealed. Scale bars: 5 mm. **B)** Magnetic Part example. The chosen geometry is composed of a 750 μm needle, magnetised by a 6x6 mm magnet (not shown). Scale bars: 5 mm. **C)** Example of a stretched C2C12 aggregate. 1 million of magnetic C2C12 were held by the fixed magnetic part (picture 1). The mobile magnetic actuator was approached (picture 2), deforming the initial aggregate. Once stabilised, the aggregate presented an almost cylindrical shape (picture 3). On this example, the aggregate was stretched up to 15% of its initial length (picture 4). Scale bars: 250 μm.

The ultimate goal of this project was to manage to stretch an aggregate composed of skeletal muscle precursors, typically in the range of 100% of its initial length. The strategy is therefore different from the one used in the cycling stretching. In order to enhance the magnetic stretching, thanks to the versatility of the 3D printing, we tested different magnetic configurations.

12.3 - Magnetic configurations

As shown in Figure 12-3, different magnetic configurations were tested:

- **Parallelepiped Magnet** This configuration and a resulting aggregate are shown in Figure 12-3A. A permanent parallelepiped magnet (5 x 5 x 1 mm) was embedded in the 3D-printed structure. Roughly 10 million of cells were seeded on the magnetic part, resulting in a large aggregate presenting dimensions close to 5 mm in width, and 1 mm in height. At day 1, the stretched aggregate presented a symmetrical cylindrical shape (dimensions of 5 x 1.4 mm, stretching of almost 50%). Besides, due to the number of cells, the aggregate viability was not assured, and we noticed a loss of the symmetry a day 4, followed by cell death at day 6 (Figure 12-3A, bottom pictures).
- **Magnetic Slide** In this configuration (Figure 12-3B), a soft iron slide was magnetised by a permanent magnet (6x6 mm, B = 520 mT, gradB = 180 $T.m^{-1}$). As the slide is thinner (approximately 500 μm) than the parallelepiped magnet, the purpose was to achieve a high shape factor, and to assure cell viability thanks to the formation of thinner aggregates. On the presented pictures, the cell deposit resulted in a 6 mm x 650 μm aggregate, stretched between day 0 and day 1 at almost 30% (Figure 12-3B, centre picture). At day 1, the aggregate appeared less symmetrical than the one obtained with the previous geometry, but the BF image demonstrates a thinner aggregate (it was not quantified). If the achieved stretching was satisfying, due to its size, the aggregate was too fragile to be cultured more than 4 days (Figure 12-3B, bottom picture).
- **Magnetic Tip** This configuration is the same that the one used before in the group (2). It consists in a 750 μm magnetized microtip (Figure 12-3C). In the given example, one million of magnetic C2C12 were seeded on the fixed part, resulting in a 1 x 0.5 mm aggregate. Between the cell deposit and day 1, we performed a stretching of almost 50% of the initial aggregate height. This geometry allowed us to culture symmetrical

and viable aggregates for longer times than the others geometries. In this example, we achieved at day 4 a stretching of almost 70% of the initial deposit height.

Due to the shape of the parallelepiped magnet, this configuration gave no viable aggregates for long time studies. The Magnetic Slide was tried in order to reduce the thicknesses of the build aggregates, and therefore enhancing the long-time cell viability. But, a stretching larger than 30% of the initial aggregate height was difficult to perform without disrupting the aggregate, probably due to the large number of seeded cells. If this configuration gave interesting shape factors (thin and elongated aggregate), further tuning of the slide needs to be done.

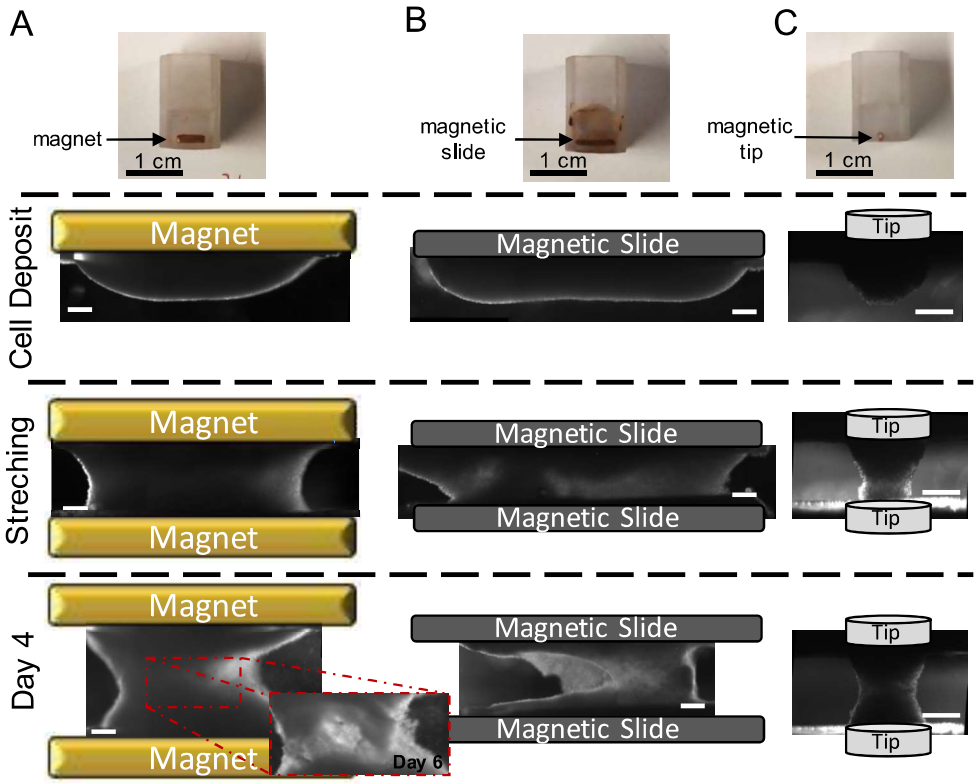

Figure 12-3: Magnetic configurations. A) Magnetic part composed of a 5x5x1 mm parallelepiped magnet. The configuration resulted in a large aggregate (10 million of cells, 5x1 mm aggregate), stretchable up to 50% of the initial height, but not viable in time. The aggregate broke after a few days. The evolution of the aggregate is shown 4 and 6 days after the seeding. Scale bar: 500 μm. **B)** Magnetic parts consisting in a magnetised iron slide (1 cm x 500 mm). Again, this configuration resulted in a large (roughly 6 mm per 500 μm aggregate) but thinner aggregate, stretchable - by almost 30% of its initial height - but not viable in time. Scale bar: 500 μm. **C)** Magnetic configuration composed of a magnetisable needle (see also Figure 12-1). On this example, 1 million of magnetic cells were seeded, and stretched by almost 70% of the initial deposit length. At day 4, the aggregate was still viable. Scale bars: 500 μm.

Nevertheless, regarding these preliminary results, the magnetic microtips were chosen for the entire study. Indeed, this configuration allowed achieving a satisfying stretching of the aggregate, and allowed a long time culture of the stretched aggregates.

12.4 - Long-time culture of stretched aggregates

Using the magnetic microtips, C2C12 aggregates have been kept in the stretcher for up to 10 days. In Figure 12-4, an aggregate composed of 1 million cells was kept for 8 days in a low glucose culture medium. At day 8, we achieved a stretching close to 65% of the initial cell seeding. This long-time stability was satisfying, as it would allow for instance the expression of genes related to late muscle differentiation (3).

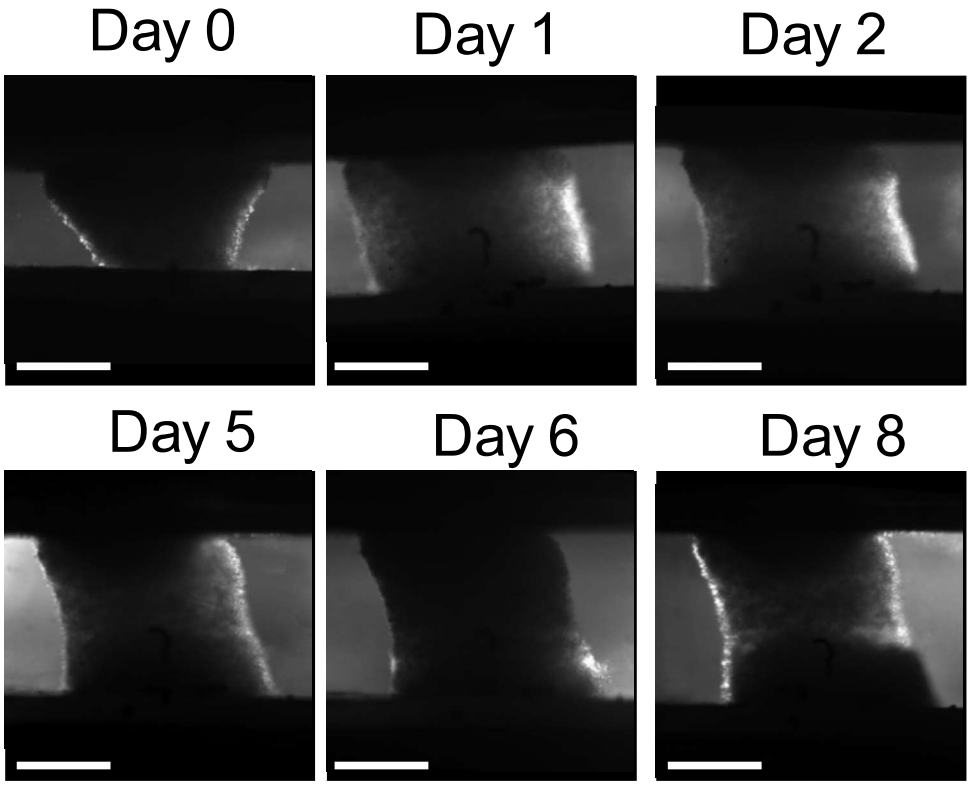

Figure 12-4: Long-time aggregate viability. A magnetic 1 milion-C2C12 aggregate was kept in the magnetic stretcher 8 days after the seeding. The aggregate was stretched everyday using small steps (between 5 to 10% of the current length). Thus final achieved stretching was around 65% of the initial length. Scale bars: 500 μm.

In this example, the conditions were not sufficient to obtain a differentiation of the aggregate despite the large time of culture. But, as shown in figure 4, this aggregate presented large

dimensions, almost 1x2 mm. As necrosis is found in the inner of aggregate larger than 500 μm in diameter, such dimensions might not be compatible with the differentiation of a tissue model. The next step of the project was then to be able to form smaller but still stretchable aggregates, and it raised unexpected issues.

12.5 - A dynamic system

Interestingly, the cell stretching gave rise to a dynamic system of cells moving between the two field gradients. The Figure 12-5 presents aggregates subjected to a fixed stretching, and filmed during a few hours. The Figure 12-5A presents the side of an aggregate stretched between two Magnetic Slides, and the Figure 12-5B and Figure 12-5C present aggregates composed of respectively 100 000 and 50 000 cells held between the magnetic microtips. In the different configurations, cells going back and forth between the two magnetic actuators were observed. The dynamic behaviour stopped after a dozen of hours, consistent with the timescale of the cell-cell adhesion (typically between 10 to 20h) (4), and seemed not to depend on the geometry and on the cell number.

We were not expecting such a dynamic behaviour of a freshly stretched aggregate, and the consequences on the aggregate viability seemed to depend on the initial configuration. For instance, in the presented Magnetic Slide configuration, the movements resulted in a propagation of a crack from the centre of the aggregate toward the edge. The crack propagation stopped after a few hours (roughly 6h). For the same configuration, a change in the cell number gave rise to different aggregate shapes (Figure 12-5.B-C). With 100 000 cells, the cell movements led to an asymmetry (Figure 12-5B) of the aggregates, whereas it resulted in a symmetrisation of the aggregate composed of 50 000 cells (Figure 12-5C). Plus, a larger number of cells led to symmetric aggregates (Figure 12-4).

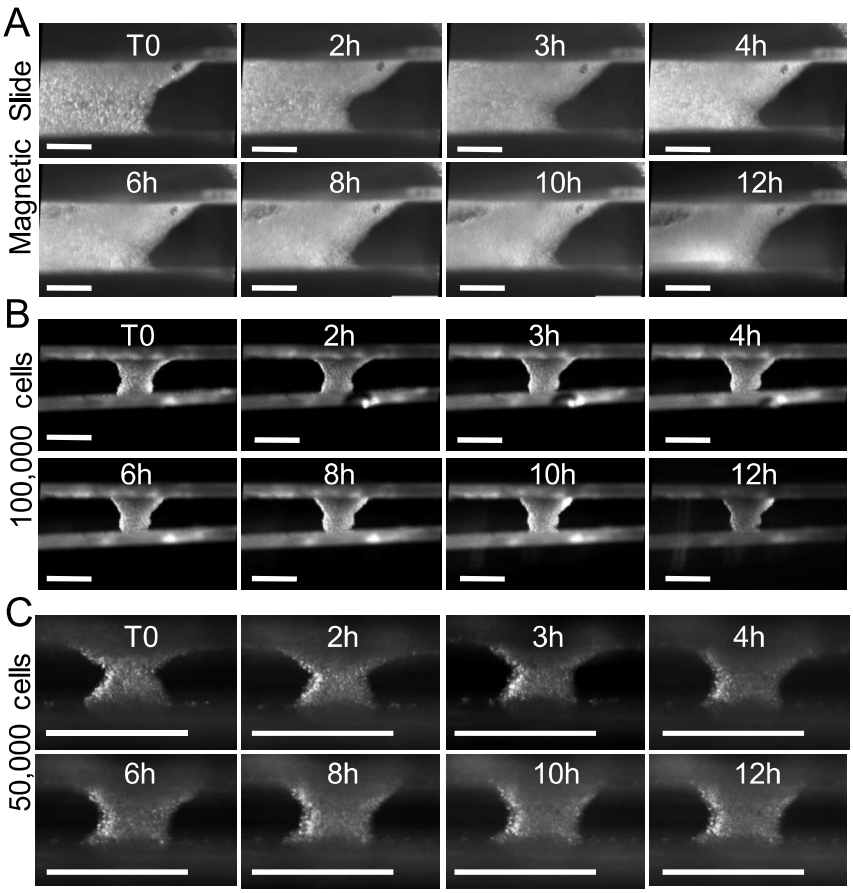

Figure 12-5: A dynamic system. The evolution in time for three aggregates following the approach of the mobile magnet is presented. In each condition, cell movement were observed in the early stages of the approach. **A)** 10 millions of cells were stretched between two magnetic slides. The cell movements, as well as the increase of the cell cohesion, led to the disruption of the aggregate 6h after the magnet approach. The crack increased during the 6 following hours. Scale bars: 500 μm. **B)** 100 000 magnetic C2C12 cells were seeded between two magnetic microtips. Cell movements stopped after about 10h. Due both to cell movements and cell cohesion, the aggregate detached from mobile microtip. Scale bars: 500 μm. **C)** 50 000 C2C12 cells were stretched between two magnetic microtips. Again, the cell movements stopped after about 10h, but here, they resulted in a symmetrisation of the aggregate. Scale bars: 500 μm.

If the effects of the cell number could not be clarified, we are going to stress that the consequences of the cell movement following the magnetic seeding on the aggregate integrity, may critically depend on the initial stretching.

12.6 - Effect of the initial stretching

The aggregate integrity is linked to its initial stretching. Figure 12-6 presents stretched aggregates with different initial number of cells, and with different initial stretching. The aggregates were cultured in low glucose DMEM. The given examples present the deposit of the cells, the approach of the magnet, and the resulting aggregates with or without stretching. The same aggregates were pictured the day following the cell seeding.

First, an aggregate composed of 1 million of cells was slightly stretched up to 13% of the initial deposit height (Figure 12-6A.1). The day after, the aggregate presented a symmetrical shape, and it was further stretchable. A second aggregate was also composed of around 1 million of cells, but it was stretched up to 45% of the initial deposit height (Figure 12-6A.2). The day following the cell seeding, the aggregate was disrupted.

To investigate the effect of a lower cell number, we subjected an aggregate composed of 50 000 cells to the same initial stretching (close to 46% of its initial length, Figure 12-6A.3). This stretching also resulted in a non-symmetrical aggregate, with cells clearly shifted to the fixed magnetic part. Such an aggregate were not further stretchable (Figure 12-6B).

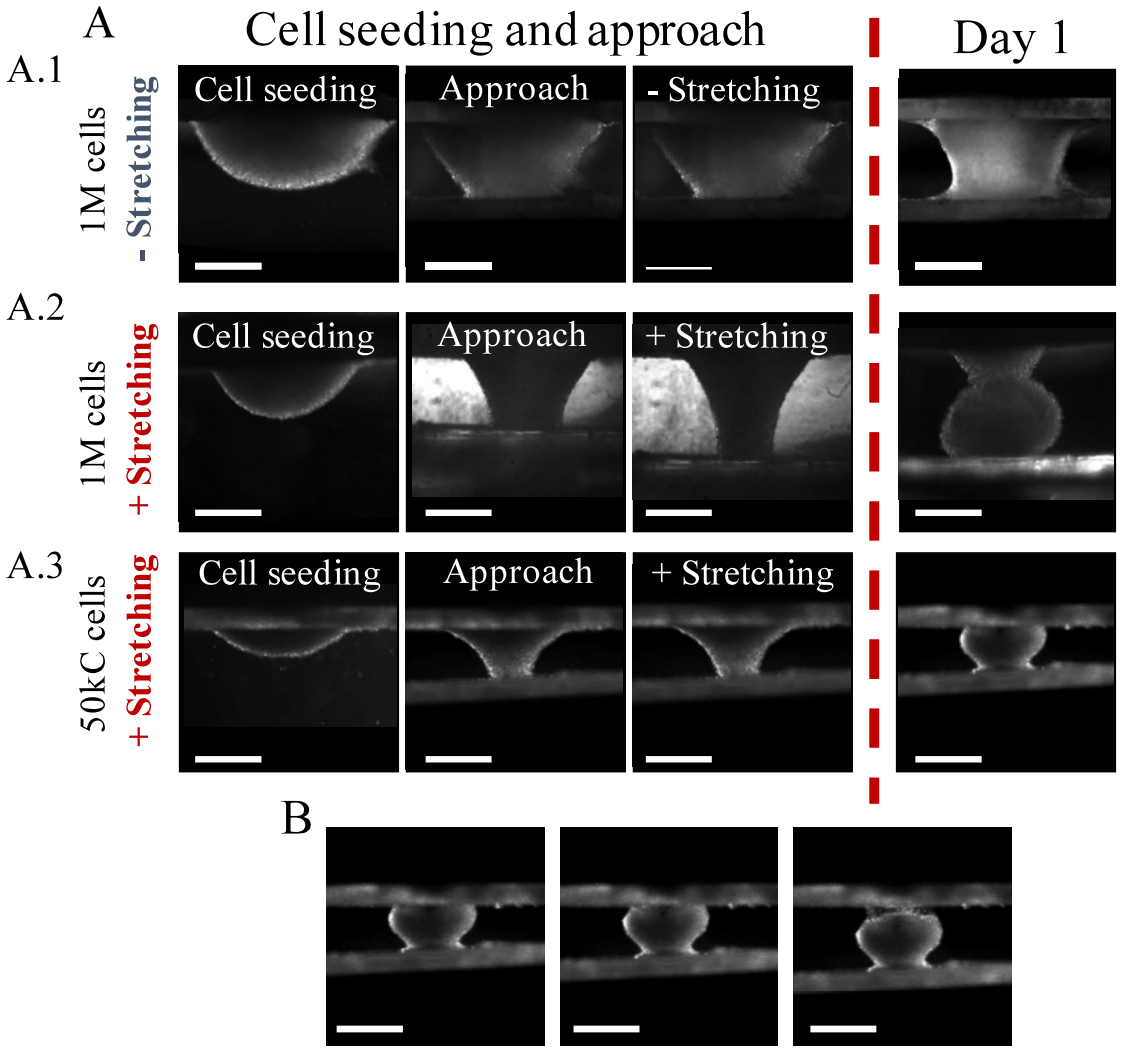

Figure 12-6: Effects of the initial stretching. A) 3 different aggregates presenting different number of cells were seeded between two magnetic microtips, and further stretched, or not stretched. The resulting aggregates are shown the day following the seeding. Scale bars 500 μm. **A.1)** A 1-milion-cell aggregate was slightly stretched by the approach of the second magnet (13% of the initial cell deposit). No further stretching was applied. The day after, the aggregate was viable and stretchable. **A.2)** An aggregate presenting the same number of cells was stretched up to 45% of its initial length. It broke the day after. **A.3)** An aggregate composed of 50,000 cells was stretched up to 46% of its initial height, resulting the day after to a disrupted aggregate. **B)** The Aggregate presented in A.3 was not further stretchable. The displacement of the mobile magnetic microtip resulted in the detachment of the aggregate. Scale bars: 500 μm.

These preliminary experiments suggest that the initial stretching of the aggregates is critical for its stability. Because of the dynamic behaviour of the early stages of the deposit, we are not able to subject the aggregate to a strong initial stretching. If the cell number is critical for the long-time viability of the aggregate, these experiments demonstrate that a compromise

between the cell number and the initial aggregate stretching has to be found in order to obtain stretchable aggregates, which remain stable in time. If the reduction of the number of cells might be promising, we surprisingly found interesting results with aggregates composed of a million of cells.

12.7 - Alignment of skeletal muscle progenitors: Proof of concept

By applying stretching steps roughly close to 5% the aggregate height, we managed to obtain a maximal stretching close to 60% of the initial height after a few days. The stretching then achieved was in the range of maximal stretching obtained with muscle cells embedded in a scaffold (5) (6).

In these conditions, two stretching experiments resulted in interesting observations. These successful experiments are presented as a proof of concept in Figure 12-7. For both experiments, one million cells were held between two magnetic microtips without initial stretching. The cell deposit was initially made in supplemented DMEM, and we shifted to a differentiation medium two days after the cell seeding (low glucose condition). During the days following the magnetic approach, the aggregates were stretched step by step. For the aggregate presented in Figure 12-7A, at day 1, we achieved a total stretching close to 60% of the day-0 height. The aggregate presented a thinner part close to the movable magnetic tip. Strikingly at day 3, this thinner part showed aligned cells in the direction of the stretching. A close up of this alignment is presented (Figure 12-7A, middle pictures). This aligned part represented around 10% of the aggregate surface. Unfortunately, an additional stretching of this aggregated resulted in the rupture of the aggregate.
Figure 12-7B presents another aggregate pictured 4 days after the cell seeding. The aggregate was less stretched than the one presented above (16% of the day-0 aggregate, 60% of the initial cell deposit height), but we ended up in highly stretching a small part of it. Thus stretching resulted in a partial alignment of the C2C12 (around 13% of the surface). Again, this aggregate was fragile, and broke over the day.

These experiments are a proof of concept that the magnetic stretcher can be used as a tool to functionalize an aggregate composed of skeletal muscle precursors. Besides, we only achieved partial alignment on small non-symmetrical, and fragile parts of the aggregates.

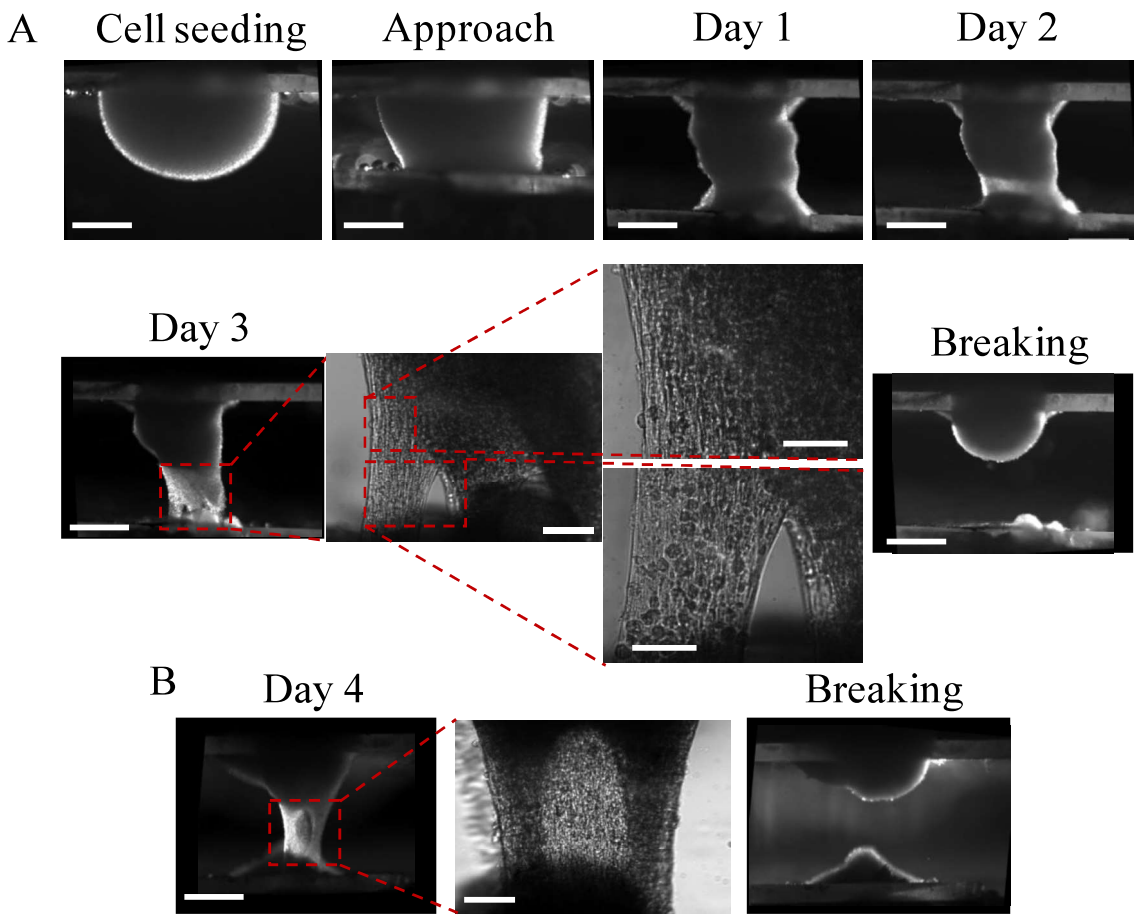

Figure 12-7: Partial alignment of C1C212 aggregates cultured in the Magnetic Stretcher. All the presented pictures are Bright Field images. **A)** A 1-milion-cell aggregate was seeded between the two magnetic microtips. The following days, the aggregate was stretched step by step (5% of the current length), achieving a stretching of 60% four days after the seeding. To trigger the differentiation, the aggregate was placed in low-glucose medium two days after the seeding. At day 3, a partial cell alignment of the cells was observed on a small part of the aggregate (about 10% of the aggregate's surface). The close-up (middle picture) highlights such alignment. The aggregate was fragile, and broke the next day. Scale bars: 50 μm for the close-up, and 500 μm for the other pictures. **B)** Second example of a partially aligned C2C12 aggregate, four days after the cell seeding. Initially 1 million of cells were seeded, and thus obtained stretching was about 60% of the initial deposit length. Cells were aligned in a small region representing roughly 13% of the aggregate's surface. The centre picture presents a close-up of the aligned cells. The day after, the stretching resulted in the disruption of the aggregate (right picture). Scale bars: 50 μm for the magnification, and 500 μm for the other pictures.

To conclude, the Magnetic Stretcher is a promising tool in order to achieve the 3D functionalization of a striated muscle model, and to study the mechanical properties of the stretched aggregates. If a partial C2C12 alignment was shown, the project is far from being achieved. Irène Nagle will carry it as a part of her PhD.

References

1. McMahon DK, Anderson PA, Nassar R, Bunting JB, Saba Z, Oakeley AE, et al. C2C12 cells: biophysical, biochemical, and immunocytochemical properties. American Journal of Physiology-Cell Physiology. 1994 Jun 1;266(6):C1795–802.
2. Du V, Luciani N, Richard S, Mary G, Gay C, Mazuel F, et al. A 3D magnetic tissue stretcher for remote mechanical control of embryonic stem cell differentiation. Nat Commun. 2017 Dec;8(1):400.
3. Du C, Jin Y-Q, Qi J-J, Ji Z-X, Li S-Y, An G-S, et al. Effects of myogenin on expression of late muscle genes through MyoD-dependent chromatin remodeling ability of myogenin. Mol Cells. 2012 Aug;34(2):133–42.
4. Charrasse S, Meriane M, Comunale F, Blangy A, Gauthier-Rouvière C. N-cadherin–dependent cell–cell contact regulates Rho GTPases and β-catenin localization in mouse C2C12 myoblasts. J Cell Biol. 2002 Sep 2;158(5):953–65.
5. Somers SM, Spector AA, DiGirolamo DJ, Grayson WL. Biophysical Stimulation for Engineering Functional Skeletal Muscle. Tissue Engineering Part B: Reviews. 2017 Aug;23(4):362–72.
6. Li Y, Huang G, Gao B, Li M, Genin GM, Lu TJ, et al. Magnetically actuated cell-laden microscale hydrogels for probing strain-induced cell responses in three dimensions. NPG Asia Mater. 2016 Jan;8(1):e238–e238.

13 – Conclusion and perspectives: cardiac and skeletal tissue engineering

The last chapter of this manuscript presented two magnetic approaches to remotely create magnetic multicellular aggregates of muscle precursor cells, and to drive their differentiation through magnetic forces. The first project was presented in the form of an article, and the second one is at the stage of a proof-of-concept of the use of the magnetic stretcher for skeletal tissue engineering. Herein, I present the main results of this tissue-engineering related works (Conclusion 13-1).

Magnetically induced cardiomyogenesis
Magnetic forces were used to induce the differentiation of Embryoid Stem Cells Embryoid Bodies (ESCs EBs) toward cardiac lineage:

- Thanks to a microfabricated magnetic microarray, scaffold-free high-throughput formation of ESCs EBs was achieved (900 spheroids in a single step).
- Compared to the classical Hanging Drop method, the impact of magnetic stimulations on the formation and on the differentiation of the EBs was assessed. In particular, the effects of a constant magnetic compression or a cyclic magnetic compression (1 Hz, 6h per day) were investigated. Importantly, these magnetic stimulations were applied at a distance by the remote magnetic forces.
- After maturation, the EBs gave rise (for all the conditions) at day 7 and day 10 to spontaneous beating regions (with typical frequencies between 1 to 2 Hz), indicating a partial cardiomyogenesis. Strikingly the percentage of beating areas increased for the cyclically stimulated EBs, reaching 92% of the surface of the EBs.
- Such enhanced cardiac differentiation was also assessed through the immunolabelling of the α-actinin (muscle specific marker) and the troponin T (cardiac specific marker). For the cyclically stimulated EBs, the labelling demonstrated larger differentiated regions, consistent with the observed beatings.
- Finally, the genetic expression of cardiac specific markers was compared at day 5, day 7 and day 10. The gene expression of early stage mesoderm markers (Nkx2.5, Gata 4) and cardiac specific markers (troponin T, α myosin heavy chain) were significantly enhanced for the cyclically stimulated EBs.

To conclude, this project presented the use of magnetic approaches to form and to subject remotely a large number of ESCs EBs at the same time. Remarkably, it showed that cyclic remote magnetic stimulations at 1 Hz enhanced the differentiation of the EBs toward cardiac lineage.

Magnetically induced C2C12 alignment

Concerning the skeletal myogenic satellite cells stimulated within the Magnetic Stretcher:

- I first presented the shapes and the stability of C2C12 magnetic aggregates inside the Magnetic Stretcher.
- Then, I demonstrated that the magnetic stretcher can be used as a tool for the long time study of multicellular aggregates.
- I highlighted the fact that a viable stretchable aggregate results in a compromise between the cell number, and the initial stretching.
- Finally, I evidenced partial cell alignments of two stretched aggregates.

To conclude, using the Magnetic Stretcher, we were able to perform partial alignment in a 3D-scaffold free configuration of skeletal precursor cells. Yet, if the presented results demonstrate the proof-of-concept of such a tool, the project requires further developments.

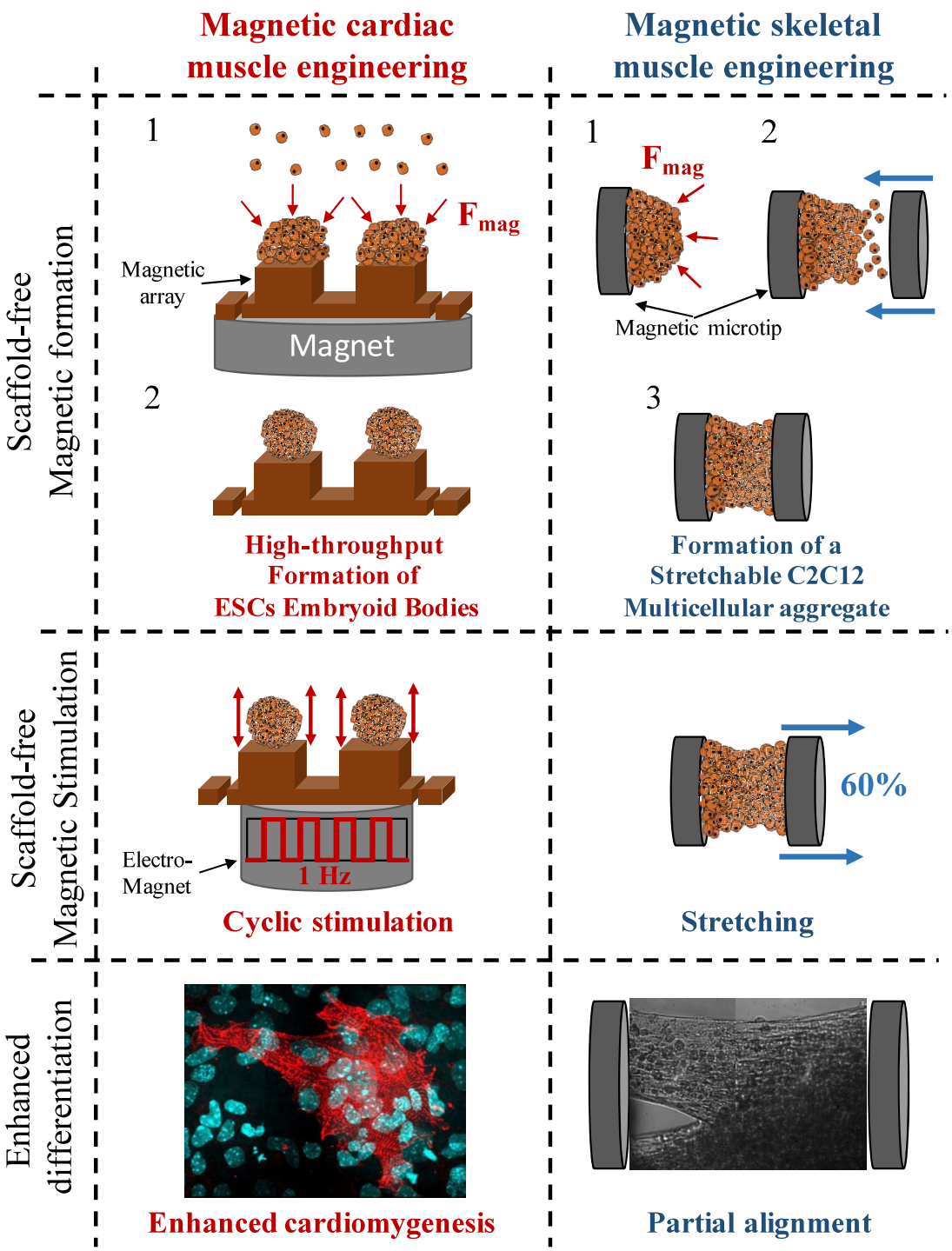

Conclusion 13-1: Cardiac and skeletal muscle tissue functionalization using magnetic forces. Magnetic cells were attracted on magnetic actuators to remotely form precursor cell aggregates. A microfabricated magnetic array allowed the high-throughput formation of hundreds of Embryoid Bodies at the same time, whereas the Magnetic Stretcher allowed the magnetic formation of a stretchable myogenic-satellite-cell aggregate (C2C12 cell line). The magnetic forces allowed the stimulation of the resulting aggregates with cycle compressions (1 Hz) or using a step-by-step stretching, respectively. Such stimulations enhanced the differentiation toward cardiomyocytes, or favoured a partial alignment, respectively.

Perspectives: magnetic tissue engineering

I presented here two magnetic approaches to form muscle precursor cell aggregates and to subject them to several magnetic stimulations: constant compression, cyclic stimulation, and step-by-step stretching. The versatility of the magnetic field application must be emphasized, as it allows multiple stimulations using all-in-one set-ups in scaffold-free configurations. Besides, the observed differentiation and/or alignment were obtained using only mechanical stimulation. Further developments are considered for the two projects.

First, if the magnetic cyclic stimulation of ESCs EBs strikingly enhanced their differentiation toward the cardiac lineage, such stimulations were performed on small aggregates (500 μm in diameter five days after the formation). Yet, repairing a tissue requires the formation of differentiated large structures, most of the time achieved using external scaffolds (1). Thanks to the versatility of the magnetic forces, a possible development of this project would to up-scale the spheroid sizes. Such up-scaling have been proposed by co-culturing precursor cells with endothelial cells, in order to assure the large structure viability (2), which would be easily achieved using magnetic approaches.

Second, the alignments of the C2C12 cells inside the magnetic stretcher only represented small regions of the aggregates, which were more stretched than the rest. Moreover, this gave rise to fragile aggregates that we were not able to collect from the magnetic stretcher. Immunolabelling of proteins expressed during C212 differentiation and maturation represents the next step to evaluate the efficiency of the magnetic stretching on the skeletal muscle precursor functionalization. Besides, the magnetic stretching protocol has to be optimized, for instance by lowering the number of cells, and by implementing a more efficient stretching process. Irène Nagle (PhD student) is currently running experiments consisting in a continuous stretching, with steps close to a few percentages of the aggregate's length. This should enhance the aggregate's stability, as well as allowing higher stretching rates. As described before, a constant strain should also enhance the alignment and the maturation of the C2C12 cells. Finally, the Magnetic Stretcher provides a unique opportunity to study the propagation of a given stress (or deformation) throughout the whole aggregate. Live imaging of the aggregate is the next challenge to explore the mechanics of a stretched aggregate through deep-imaging microscopy (such as bi-photonics). In future experiments, FRET N-cadherin sensors will be inserted in C2C12 cells to map the distribution of the mechanical stress within the overall stretched 3D-strucutre.

References

1. Nguyen AH, Marsh P, Schmiess-Heine L, Burke PJ, Lee A, Lee J, et al. Cardiac tissue engineering: state-of-the-art methods and outlook. J Biol Eng. 2019 Dec;13(1):57.
2. Sekine H, Shimizu T, Hobo K, Sekiya S, Yang J, Yamato M, et al. Endothelial Cell Coculture Within Tissue-Engineered Cardiomyocyte Sheets Enhances Neovascularization and Improves Cardiac Function of Ischemic Hearts. Circulation. 2008 Sep 30;118(14_suppl_1):S145–52.

14 - General conclusion

This PhD presented the use of magnetic forces to apply remote mechanical stimuli on 3D tissue models. The presented works addressed the use of magnetic forces in three different fields: biophysics, cancerology, tissue engineering. The magnetic forces allowed overcoming current limitations in the formation of 3D tissue models, and limitation on their stimulation.

Current limitations of multicellular aggregates arise from the current range of sizes and shape obtainable and controllable. Using innovative magnetic approached previously developed in the group, the magnetic forces were used to overcome these limitations. In the last chapter, the magnetic forces were also used to perform a fully controlled formation of hundreds of spheroids at the same time.

Plus, applying controlled mechanical stresses on tissue models is a challenge on itself. Herein, this was tackled also using magnetic approaches. First, through the use of an electromagnet, we addressed dynamic aspects of the rheology of 3D tissue models. In particular, we demonstrated a power-law behaviour, which has never been highlighted so for at such scale. Second, a constant magnetic constraint was used to induce unprecedented anisotropic deformations on a 3D tumour model. And finally, it can be raised that compared to classic methods used in tissue engineering, magnetic forces were used to subject muscle precursor cell aggregates to remote mechanical stimuli in a scaffold-free manner.

Finally, we can stress that the magnetic forces allowed a gradual understanding of biological tissue models. First, such tools were used to apply mechanical forces on passive multicellular aggregates, allowing to probe the tissue just as any other common material. In the second chapter, magnetic forces were used to trigger a change in the behaviour of a tumour model, leading to results that cannot be seen as a benefit for a patient. Magnetic stimulations were also used to drive the differentiation of precursor cells, this time toward positive outcomes. Herein, the magnetic forces were used at every scale of the understanding of an active material: its mechanics, and its changes in behaviour in response to external stimuli. We cannot avoid here the analogy with tissue engineering and nanomedecine. Indeed in such field, one needs to understand the organization, the mechanics and the force subjected to the tissue that needs to be repaired.

The presented works give rise to further development. The rheology of 3D-tissue models at large deformation needs to be addressed. In-vivo compression experiments of tumour models are considered in mice. Finally, the Magnetic Stretcher needs to be fully optimized for skeletal tissue engineering.

MAGNETIC APPROACHES TO FORM AND TO STIMULATE THREE-DIMENSIONAL TISSUE MODELS

Abstract Français

Cette thèse présente l'utilisation de force magnétiques dans le but de former et de stimuler mécaniquement des agrégats multicellulaires. Ces structures 3D, composées de cellules jointes les unes aux autres, sont considérées comme des bons modèles de tissus biologiques. Ici, des cellules magnétiques sont utilisées afin de créer des agrégats magnétiques présentant des formes et des tailles contrôlées, et de les soumettre à des contraintes mécaniques sans aucune matrice extérieure. Trois sujets sont abordés: (i) le magnétisme induit est utilisé afin de réaliser de la rhéologie tissulaire (ii) le magnétisme induit est utilisé afin d'appliquer une large contrainte anisotropique à des modèles de tumeurs cancéreuses (iii) enfin, le magnétisme induit est utilisé afin d'améliorer la différenciation d'agrégats composés de précurseurs de tissus musculaires squelettiques et cardiaques.

Abstract English

This manuscript presents the use of magnetic forces as a tool to form and to mechanically stimulate multicellular aggregates. These 3D structures, composed of interconnected cells, are considered as relevant models of biological tissues. Herein, magnetic cells are spatially controlled to create magnetic multicellular aggregates presenting specific shapes and sizes, and to subject them to remote mechanical stimuli without any external scaffold. Three different subjects are addressed: (i) the use of magnetic approaches to perform tissue rheology (ii) the use of magnetic forces to apply large anisotropic deformation on tumor models (iii) finally, the use of magnetic forces to enhance the differentiation of multicellular aggregates composed of cardiac muscle and skeletal muscle precursors.